UNIVERSITÉ DE LORRAINE | BIBLIOTHÈQUES UNIVERSITAIRES

AVERTISSEMENT

Ce document est le fruit d'un long travail approuvé par le jury de soutenance et mis à disposition de l'ensemble de la communauté universitaire élargie.

Il est soumis à la propriété intellectuelle de l'auteur. Ceci implique une obligation de citation et de référencement lors de l'utilisation de ce document.

D'autre part, toute contrefaçon, plagiat, reproduction illicite encourt une poursuite pénale.

Contact bibliothèque : ddoc-theses-contact@univ-lorraine.fr
(Cette adresse ne permet pas de contacter les auteurs)

LIENS

Code de la Propriété Intellectuelle. articles L 122. 4
Code de la Propriété Intellectuelle. articles L 335.2- L 335.10
http://www.cfcopies.com/V2/leg/leg_droi.php
http://www.culture.gouv.fr/culture/infos-pratiques/droits/protection.htm

THÈSE

Pour l'obtention du titre de :

DOCTEUR de L'UNIVERSITÉ DE LORRAINE

Spécialité : Chimie

Présentée par :

Luis Fernando PAZ LÓPEZ

Charbons actifs végétaux optimisés pour l'épuration des biogaz

Thèse soutenue publiquement le 23 Septembre 2025 à Epinal devant le jury composé de :

Mme. Conchi ANIA	Directrice de Recherches au CNRS, CEMHTI - Université d'Orléans	Rapportrice
Mme. Cécile VALLIERES	Professeure à l'université de Strasbourg, ECPM-CNRS	Rapportrice
Mme. Camélia GHIMBEU	Directrice de Recherches au CNRS, IS2M - Mulhouse	Examinatrice
M. Michael BADAWI	Professeur à l'université de Lorraine, L2CM - CNRS	Président / Examinateur
Mme. Solène GENTIL	Ingénieur développement électrolyse (H2) chez Axane, Groupe Air liquide	Invitée
M. Cyril Flores	Président de Groupe Bordet, Leuglay	Invité
M. Alain CELZARD	Professeur à l'université de Lorraine, IJL - CNRS	Directeur de thèse
Mme. Vanessa FIERRO	Directrice de Recherches au CNRS, IJL - Université de Lorraine	Co-directrice de thèse

Acknowledgments

Above all, I thank God for guiding me through this journey.

I would like to express my deepest gratitude to my two thesis directors, Pr. Alain Celzard and Dr. Vanessa Fierro, as well as to Solène Gentil, former supervisor at Groupe Bordet, for placing their trust in me and selecting me as a suitable candidate to undertake this project. I am especially proud to have been mentored by Alain and Vanessa, both of whom are highly respected figures in the field of adsorption research internationally. Their continuous support and guidance were invaluable throughout this research journey. I also thank Solène for her support and encouragement during my first two years in the laboratory.

I would also like to thank the members of the thesis jury for their time to read and evaluate this project. I am grateful to the two reviewers, Dr. Conchi Ania and Dr. Cécile Vallières. I also extend my appreciation to the examiners, Dr. Camélia Ghimbeu and Dr. Michael Badawi. Their expertise and perspectives greatly contribute to the depth and rigor of this thesis.

I am grateful to thank the entire IJL team in Épinal. The friendly, supportive and collaborative working environment greatly contributed to the success of this project. Special thanks goes to Philippe Gadonneix for his constant dedication and invaluable assistance in numerous laboratory experiments.

Several others supported me along the way, including Pauline Blyweert and Taher Selmi, to whom I am also grateful for being there when I needed them. I would also like to thank Mr. Cyril Flores, president of Groupe BORDET, for his commitment to expanding the applications of BORDET carbon materials; this research would not have been possible without it.

A particularly memorable moment of this thesis was the testing of materials at the industrial site, where I was warmly welcomed. I am deeply grateful to those individuals who supported me during that time, even though I cannot mention them by name for confidentiality reasons. Thanks, as well to the BORDET and IJL teams for making this possible.

My family in Colombia, though far away, was a constant source of motivation throughout my research work, especially my mother, Claudia López, whose unwavering support inspired me every step of the way. I also thank Valentina Bernal for her valuable company.

Table of contents

Résumé de la thèse **1**

General Introduction **9**

Chapter 1. Biogas purification with adsorbents **13**

1.1 Generalities on biogas 15

1.2 Biogas upgrading 17

1.2.1 CO_2 separation 18

1.2.2 H_2S separation 21

1.3 Use of sorbents in biogas upgrading for CO_2/CH_4 separation 25

1.3.1 Carbon adsorbents 29

1.3.2 Other adsorbents 31

1.4 Use of sorbents in biogas desulfurization 33

1.4.1 Activated carbon (AC) 33

1.4.2 Zeolites 45

1.4.3 Mesoporous silica 47

1.4.4 Metal organic frameworks (MOFs) 49

1.4.5 Metal-based adsorbents 51

1.5 Conclusions 54

1.6 References 55

Chapter 2. Evaluation of adsorbents for CO_2 / CH_4 separation and biogas desulfurization **71**

2.1 CO_2/CH_4 separation by pressure swing adsorption (PSA) systems 73

2.1.1 Performance indicators of adsorbents in PSA systems 74

2.1.2 Parameters for PSA performance evaluation 83

2.1.3 Simulation of PSA systems 83

2.1.4 PSA Performance Evaluation 90

2.2 Biogas desulfurization 98

2.2.1 H_2S separation capacity of different adsorbents 99

2.2.2 Challenges in biogas desulfurization 108

2.2.3 Assessment of adsorbents 109

2.2.4 Simulation of H_2S separation from biogas 111

2.2.5 Sorbent regeneration 115
2.3 Conclusions 121
2.4 References 124
Chapter 3. Tailoring wood-based activated carbons and assessing the role of impregnation and O_2 for efficient H_2S removal from biogas 139
3.1 Introduction 141
3.2 Experimental 142
3.2.1 Materials 142
3.2.2 Impregnation process 143
3.2.3 AC Characterization 144
3.2.4 H_2S dynamic adsorption 145
3.2.5 Mathematical model 147
3.3 Results and discussion 149
3.3.1 Characteristics of synthesized and commercial ACs 149
3.3.2 H_2S adsorption on wood-derived ACs 150
3.4 Performance comparison with commercial activated carbons 157
3.4.1 Effect of H_2S initial concentration 158
3.4.2 Effect of O_2 in the gas feed 159
3.5 Modeling of breakthrough curves 160
3.6 Conclusions 164
3.7 References 164
Chapter 4. Densification and impregnation of wood-based activated charcoal for industrial biogas desulfurization 169
4.1 Introduction 171
4.2 Experimental 172
4.2.1 Materials 172
4.2.2 Densification process 173
4.2.3 Impregnation process 175
4.2.4 Characterization 175
4.2.5 H_2S dynamic adsorption 176
4.3 Results and discussion 177
4.3.1 Binder characteristics 177
4.3.2 AC Characteristics 178
4.3.3 Effect of binder on H_2S separation 181
4.3.4 Selection of best impregnating agent under O_2 presence 183

4.3.5 Selection of best impregnation method with KOH 184
4.3.6 Comparison with commercial activated carbons for biogas desulfurization.... 189
4.4 Mathematical model 191
4.5 Conclusions 193
4.6 References 194
Chapter 5. Biogas purification at pilot scale and regeneration of H_2S-saturated sorbents 197
5.1 Introduction 199
5.2 H_2S and VOCs removal on a pilot scale 199
5.2.1 Sorbent preparation 199
5.2.1 H_2S adsorption test 203
5.2.2 VOCs adsorption test 204
5.3 Regeneration of H_2S saturated activated carbon 205
5.4 Conclusions 208
5.5 References 209
Conclusions and perspectives 211
Annex 1. Complementary data for chapter 2 217
Annex 2. Complementary data for chapter 3 223
Annex 3. Complementary data for chapter 4 235
Annex 4. List of figures and tables 243
Annex 5. Lists of scientific works derived from this thesis 253

Résumé de la thèse

Cette thèse présente une étude sur la purification du biogaz à l'aide de charbons actifs, en mettant particulièrement l'accent sur la séparation du dioxyde de carbone (CO_2) et du sulfure d'hydrogène (H_2S), deux impuretés majeures du biogaz qui limitent son utilisation comme source d'énergie propre. La recherche comprend à la fois une revue étendue des matériaux adsorbants d'une part, et le développement ainsi que l'évaluation d'un charbon actif (AC) optimisé pour une performance accrue de séparation du H_2S d'autre part. L'objectif est de synthétiser un adsorbant à partir de charbon de bois, pouvant être mis à l'échelle pour une purification industrielle du biogaz, tout en offrant une performance concurrentielle par rapport aux charbons actifs commerciaux utilisés pour la même application. Ainsi, la thèse est divisée en les chapitres suivants :

Chapitre 1:

Ce chapitre présente un aperçu de la composition des biogaz, des besoins en épuration, ainsi que du rôle des technologies d'adsorption dans l'élimination de leurs principaux contaminants, en particulier CO_2 et H_2S. Le biogaz, principalement composé de méthane (CH_4) et de dioxyde de carbone (CO_2), contient souvent des impuretés telles que du sulfure d'hydrogène (H_2S), de la vapeur d'eau, des siloxanes, des composés organiques volatils (COV) et d'autres composés en traces. La présence de ces contaminants limite son utilisation directe comme carburant ou son injection dans les réseaux de gaz naturel. Par conséquent, des procédés d'épuration sont essentiels pour améliorer la qualité et le pouvoir calorifique du biogaz (voir **Figure 1**). Le chapitre introduit l'adsorption comme une alternative prometteuse, économe en énergie et adaptable à grande échelle pour la purification du biogaz. Les mécanismes de séparation de H_2S sont également abordés, en soulignant que le processus implique non seulement la physisorption, mais aussi la chimisorption et des réactions d'oxydation de H_2S.

Chapitre 2:

L'attention se porte ensuite sur les matériaux adsorbants utilisés pour l'élimination sélective de CO_2 et H_2S. Divers adsorbants, tels que les charbons actifs, les zéolithes, les tamis moléculaires carbonés et les structures métallo-organiques (MOFs), sont examinés en termes de capacité d'adsorption, de sélectivité et de potentiel de régénération. Pour la séparation CO_2/CH_4, la performance des adsorbants est évaluée sur la base de leur sélectivité et de leur

"work capacity ratio" dans des systèmes d'adsorption modulés en pression (PSA), en utilisant la théorie des solutions adsorbées idéales (IAST) ainsi que des analyses de cycles PSA. Les zéolithes se révèlent être les matériaux les plus prometteurs en raison de leur forte sélectivité (voir **Figure 2**) et de leur "work capacity ratio" élevé. Les cycles PSA intégrant une égalisation de pression et une dépressurisation en dessous de la pression atmosphérique ont permis d'obtenir une efficacité énergétique et une productivité supérieure, fournissant des indications pratiques pour la conception et l'optimisation des procédés PSA. Les charbons activés ne sont pas compétitifs pour la séparation CO_2/CH_4 en raison de leur faible sélectivité vis-à-vis du CO_2.

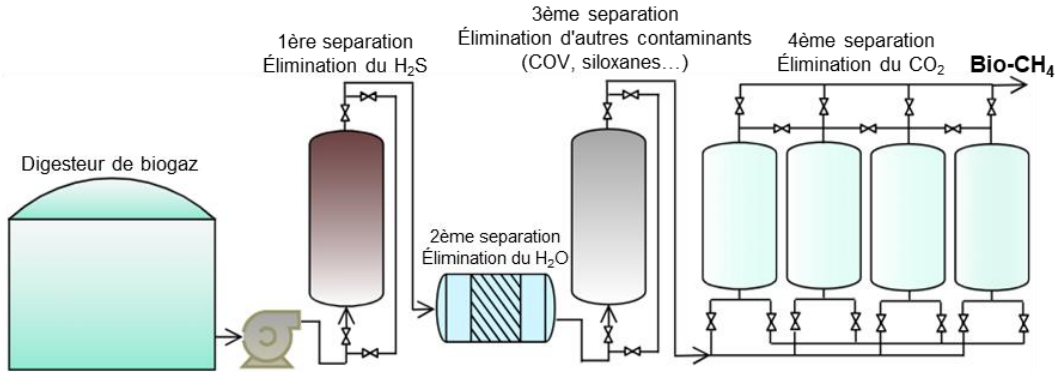

Figure 1. Production de biométhane.

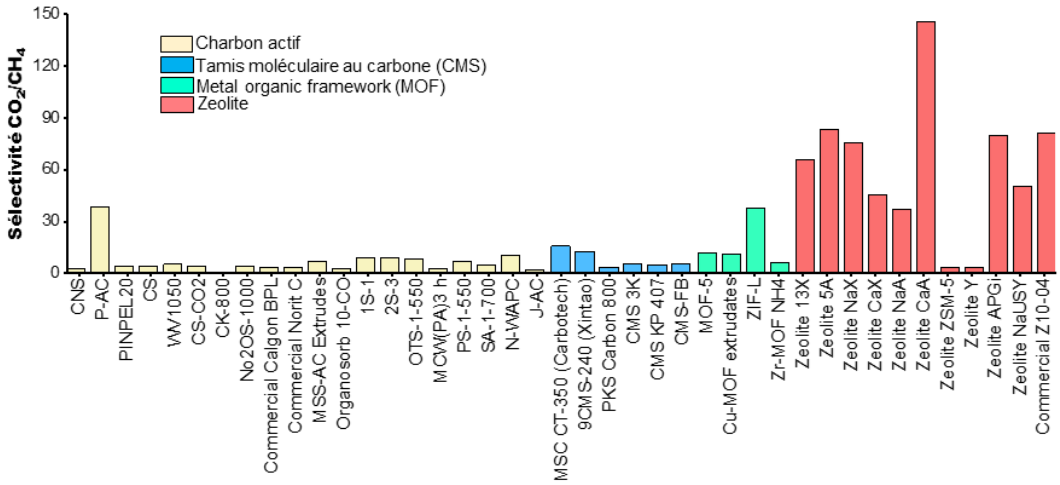

Figure 2. Sélectivité CO_2/CH_4 à l'équilibre, comparée pour différents adsorbants, à une composition gazeuse de 35 % CO_2 et 65 % CH_4 (en volume), sous 1 bar et à température ambiante.

La performance des adsorbants pour l'élimination du H_2S est comparée à celle d'autres matériaux tels que les biochars, les zéolithes, les MOFs et les adsorbants à base de métaux. Les données issues de la littérature sur les capacités de séparation mettent en évidence la grande efficacité des charbons actifs, en particulier lorsqu'ils sont chimiquement imprégnés (voir

Figure 3). Les charbons actifs offrent le meilleur compromis entre efficacité d'élimination et durabilité à long terme, ce qui en fait une option à la fois très efficace et pratique pour la désulfurisation du biogaz.

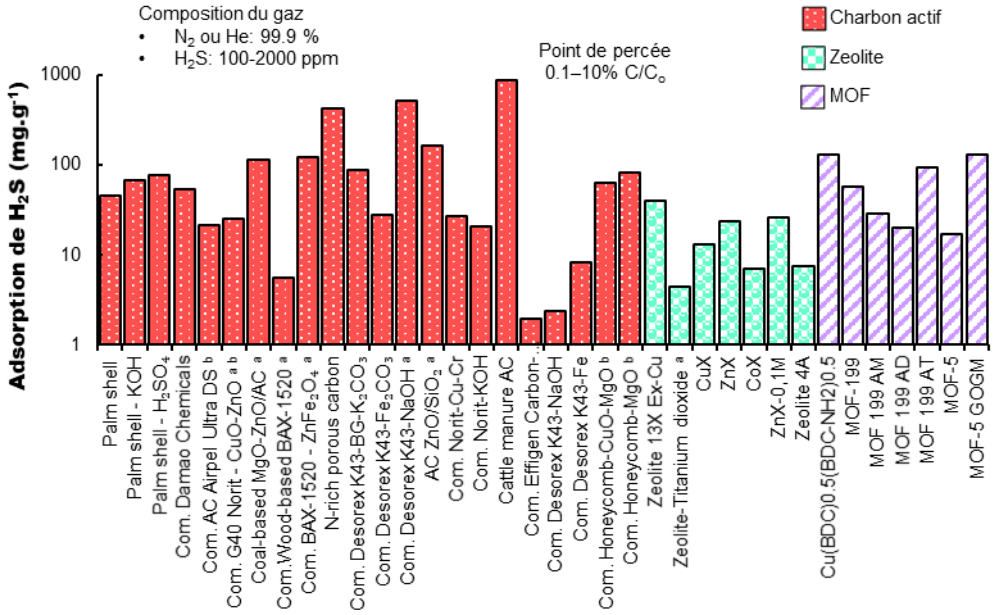

[a] Conditions d'humidité ; [b] Oxygène dans la composition du gaz d'alimentation ; [c] Percée à 0.02%

Figure 3. Capacité d'adsorption de H_2S rapportée dans la littérature en utilisant des mélanges gaz inerte-H_2S.

Chapitre 3:

Ici commence les sections expérimentales de la thèse, qui s'appuient sur les résultats de la littérature par la synthèse, la modification et les tests de charbons activés à la vapeur d'eau, dérivés du bois pour l'élimination de H_2S. Une découverte clé est que l'ultramicroporosité et la microporosité, plutôt que la mésoporosité, sont déterminantes pour une capture optimale du H_2S. Leur imprégnation avec des composés plus ou moins alcalins (KOH, KI, K_2CO_3) à 10 % en masse améliore significativement les performances d'adsorption de H_2S, en particulier dans des conditions humides et oxydantes. Parmi ces agents, KOH s'est révélé être le plus efficace, conduisant aux capacités de séparation les plus élevées. Les expériences ont montré que la présence d'O_2 prolongeait le temps de percée de H_2S jusqu'à un facteur dix et augmentait la capacité d'adsorption jusqu'à huit fois.

Le charbon actif le plus performant, qui présente une ultramicro-, micro- et mésoporosité plus élevée, a démontré une capacité de séparation supérieure par unité de masse par rapport

aux charbons activés commerciaux utilisés pour la désulfurisation du biogaz. Toutefois, sa capacité de séparation par unité de volume est restée faible en raison de sa faible densité apparente (voir **Figure 4**). Par conséquent, une densification est indispensable pour atteindre des performances d'adsorption compétitives.

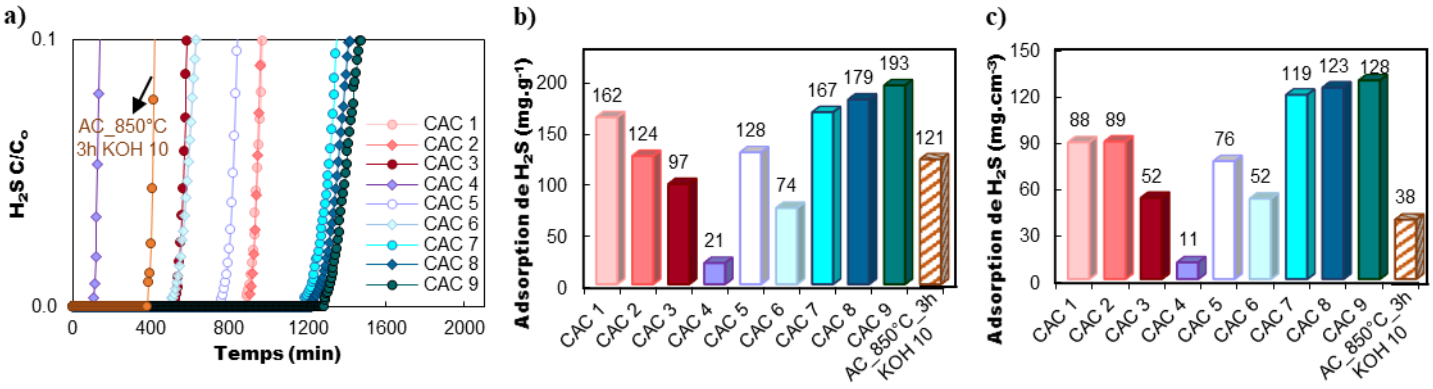

Figure 4. a) Courbes de percée de H_2S, et capacités de séparation des charbons actifs commerciaux et du charbon actif dérivé de bois (850°C_3h_KOH 10) : b) par unité de masse, et c) par unité de volume. - Gaz analysé : N_2 60%, O_2 1,1%, H_2S 4000 ppm et équilibré avec CO_2.

Chapitre 4:

Pour remédier à la faible densité apparente de l'adsorbant, la phase finale de la recherche introduit des stratégies de densification utilisant des liants durables tels que la mélasse de canne à sucre, la mélasse de betterave, et des polyphénols d'origine végétale. Les charbons actifs densifiés et imprégnés ont été évalués dans des conditions réalistes de biogaz (présence de CO_2, N_2 et O_2), et ont surpassé les adsorbants commerciaux en termes de capacité d'élimination du H_2S par unité de masse, tout en atteignant une efficacité volumique compétitive. L'adsorbant optimisé, densifié avec des polyphénols et imprégné à 10 % massique de KOH, a démontré un fort potentiel pour une application à l'échelle industrielle (voir **Figure 5).**

Au cours des études expérimentales, un modèle unidimensionnel d'adsorption dynamique a aussi été développé et validé à partir d'expériences de percée. Le modèle a reproduit avec précision le comportement d'adsorption dans des conditions réalistes et a permis de déterminer les coefficients de transfert de masse et les profils de concentration (voir **Figure 6**), établissant

ainsi une base pour la conception et l'optimisation futures des systèmes de purification du biogaz.

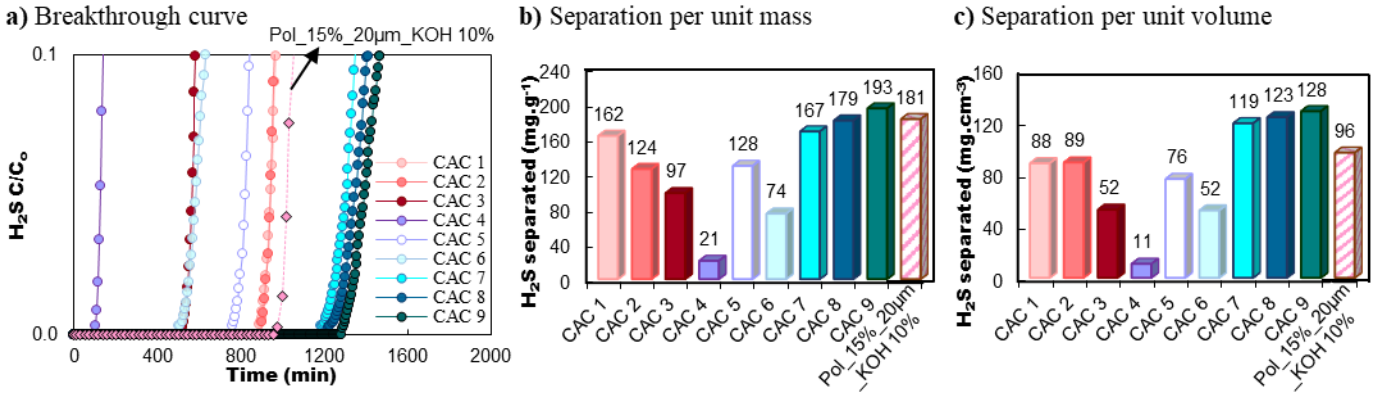

Figure 5. a) Courbes de percée d'adsorption de H_2S, et capacités de séparation des charbons actifs commerciaux et du charbon actif dérivé de bois densifié avec des polyphénols (Pol_15%_KOH 10) et de mélasse de cane à sucre (Can_50%_KOH 10) : b) par unité de masse, et c) par unité de volume. - Gaz analysé : N_2 60%, O_2 1,1%, H_2S 4000 ppm et équilibré avec CO_2.

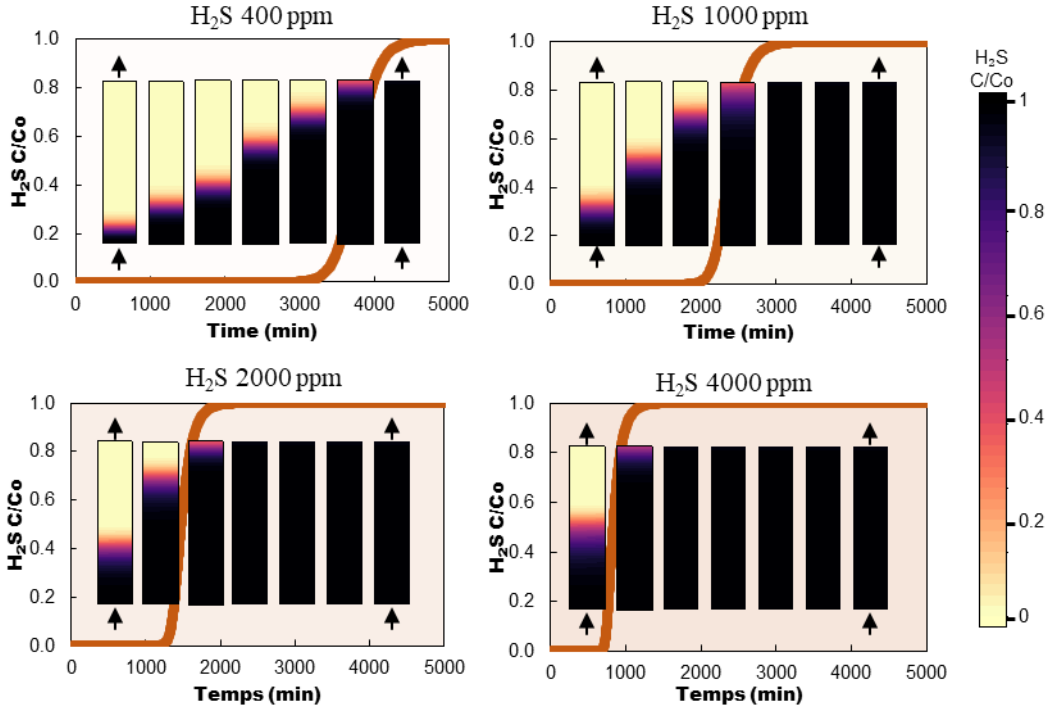

Figure 6. Profils de concentration dans une colonne d'adsorption à différentes concentrations d'entrée de H_2S pour le charbon actif développé densifié avec des polyphénols ajouté à 15 % en masse, et imprégné de KOH à 10 % en masse - Gaz analysé : N_2 60%, O_2 1,1%, H_2S 4000 ppm et équilibré avec CO_2.

Chapitre 5 :

Ici l'attention se porte sur l'application pratique et la mise à l'échelle du matériau adsorbant développé. Ce chapitre présente les résultats des essais d'adsorption à l'échelle pilote réalisés avec du biogaz réel, en utilisant du charbon actif imprégné, afin de valider les performances du charbon de bois activé à la vapeur d'eau pour l'élimination de H_2S et des composés organiques volatils (COV). Bien que les expériences n'aient pas pu être menées à leur terme, faute de disponibilité de l'industriel impliqué, elles offrent une première approche du processus de mise à l'échelle à venir.

Ce chapitre inclut également les résultats des expériences de régénération menées sur des charbons activés densifiés et imprégnés de KOH, préalablement saturés en H_2S. Différentes techniques de régénération, telles que le lavage et les traitements thermiques sous air et azote, ont été évaluées pour leur capacité à restaurer les performances de l'adsorbant. La régénération thermique à 500 °C sous flux d'azote pendant 2 heures a permis une récupération partielle des performances d'adsorption. Bien que la ré-imprégnation avec 10 % en masse de KOH ait légèrement amélioré la capacité de séparation, les performances initiales n'ont pas été totalement rétablies, avec une perte d'environ 50 % par rapport à la capacité d'origine.

General Introduction

Biogas has emerged as a promising clean energy source in the global transition towards sustainable energy systems. Produced through the anaerobic digestion of organic materials, such as agricultural waste, wastewater sludge, and municipal waste, biogas is composed primarily of methane (CH_4) and carbon dioxide (CO_2), along with trace amounts of hydrogen sulphide (H_2S), volatile organic compounds (VOCs), siloxanes, and other impurities. While its high CH_4 content makes biogas an attractive fuel, the presence of impurities limits its direct application and poses challenges for its use in heat and electricity generation, as well as advanced energy systems, such as fuel cells and vehicle fuels.

To exploit the utility of biogas, purification is essential. Removing contaminants like H_2S, VOCs and siloxanes not only protects equipment from corrosion but also enhances combustion efficiency and reduces environmental emissions. One of the most effective and widely researched approaches for biogas purification is adsorption using activated carbons (ACs). These materials, characterized by their high surface area, porosity, and adjustable surface chemistry, offer a cost-effective solution for the selective removal of impurities.

This thesis investigates the application of ACs for biogas purification, evaluating their effectiveness in removing CO_2 and H_2S, the two primary contaminants in biogas, by conducting bibliographical review. Given the widespread industrial use of ACs for H_2S removal, this research focuses on optimizing H_2S adsorption by activating wood-based biochar, thus enhancing its adsorption properties, and applying surface modifications to develop impregnated activated carbons suitable for industrial-scale applications. The separation effectiveness of the ACs is then assessed through breakthrough experiments using a synthetic gas that simulates the composition of biogas.

Most commercial ACs used for biogas desulfurization are derived from mineral coal, a non-renewable resource associated with environmental concerns, including pollution during extraction and processing. In this research, the focus shifts to developing ACs from wood-based biochar, a renewable and environmentally friendly resource. This approach not only reduces the carbon footprint of the adsorbent production process but also offers a cleaner and more sustainable solution for biogas purification.

Despite their promising adsorption properties linked to high levels of micro and meso-porosity, wood-based ACs often face limitations in industrial applications due to their low bulk density, which reduces their efficiency in packed bed systems. To address this challenge, this

research investigates the densification of the carbon materials using eco-friendly binders. This approach aims to improve the physical properties of the activated carbons, making them more suitable for industrial-scale purification processes while maintaining environmental sustainability.

To establish a performance benchmark, several commercial ACs were characterized and tested for biogas desulfurization. These reference materials provided valuable comparative data, allowing us to evaluate the efficiency and adsorption capacity of the developed ACs in relation to industry-standard alternatives. This comparative analysis was essential for assessing the competitiveness and potential advantages of the wood-based activated carbons produced in this research.

In addition to material development, this thesis examines the kinetic characterization of the ACs by simulating breakthrough curves and fitting experimental data. This analysis provides insights into the adsorption mass transfer dynamics. Furthermore, the study investigates the regenerability of the ACs, assessing their capacity for reuse after H_2S saturation. Understanding these properties is essential for evaluating the long-term economic and environmental viability of the proposed purification solutions. The performance of the ACs is further evaluated under real biogas conditions through pilot-scale tests in packed columns. Separate tests were also conducted for H_2S and VOCs removal, allowing for a comprehensive assessment of the materials' efficiency in targeting these distinct contaminants.

Chapter 1. Biogas purification with adsorbents

1.1 Generalities on biogas

Fossil fuels currently account for over 75% of the world's total energy supply[1] and are the primary source of GHG emissions, leading to global warming. In order to fulfill the European Union's (EU) objective of reducing GHG emissions by at least 55% by 2030 and attaining net zero emissions by 2050,[2] the use of biomethane emerges as a promising strategy. Moreover, the EU is currently facing geopolitical challenges associated with natural gas imports, and is striving to reduce its dependence on external suppliers. This underscores the importance of biomethane production, which is anticipated to witness a substantial increase, as suggested in **Figure 1.1**.

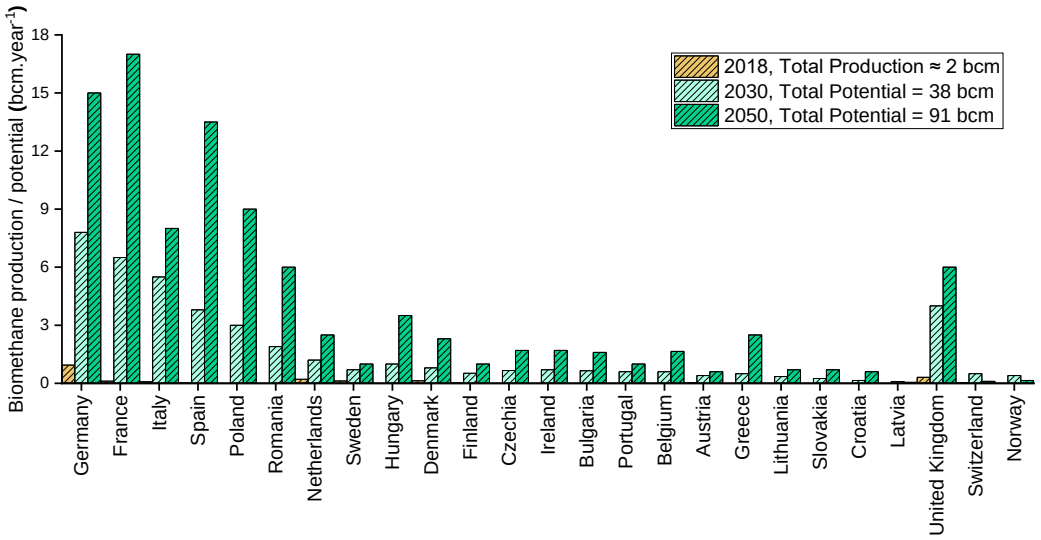

Figure 1.1 Current[3] and potential production in 2030 and 2050[4] of biomethane per country from anaerobic digestion in Europe, expressed in billion cubic meters (bcm). NB: the natural gas consumption in the UE in 2020 was 400 bcm.[4]

Biomethane is mainly obtained from biogas, from which it needs to be separated. Biogas is a byproduct of the anaerobic decomposition of organic matter, including animal manure, plant debris, food waste, biodegradable parts of municipal waste, and sewage sludge. The precise composition of biogas depends on the source of the organic matter undergoing decomposition, as shown in **Table 1.1.**

Since CO_2 can account for up to 50 vol.% of biogas composition, and as it does not undergo combustion, this compound significantly reduces the high heating value (HHV) of biogas (21.5 $MJ \cdot Nm^{-3}$) compared with natural gas (39.8 $MJ \cdot Nm^{-3}$),[6] which is mainly composed of methane.

Upgrading biogas can improve its HHV by up to 30 $MJ \cdot Nm^{-3}$.[7] Additionally, CO_2 hinders biogas compression, a process commonly employed for its storage.[8]

Table 1.1 Typical biogas composition (%).[5]

Components	Agricultural waste	Landfill gas	Industrial waste
Methane, CH_4	50 - 80	50 – 80	50 – 70
Carbon dioxide, CO_2	30 - 50	20 – 50	30 -50
Hydrogen sulfide, H_2S	0.70	0.10	0.80
Hydrogen, H_2	0 – 2	0 – 5	0 – 2
Nitrogen, N_2	0 – 1	0 – 3	0 – 1
Oxygen, O_2	0 – 1	0 – 1	0 – 1
Carbon monoxide, CO	0 – 1	0 – 1	0 – 1
Ammonia, NH_3	Traces	Traces	Traces
Siloxanes	Traces	Traces	Traces
Water, H_2O	Saturation	Saturation	Saturation

Other impurities, such as hydrogen sulfide (H_2S) or ammonia (NH_3), can have various adverse effects. H_2S, for instance, is known for its corrosive impact on internal combustion engines, and it can present serious risks to human health and the environment due to its unpleasant odor and above all its high toxicity. Moreover, when H_2S is burned in combined heat and power (CHP) systems, it can lead to emissions of sulfur oxides (SOx), contributing to environmental pollution.[9] Its impact on human well-being depends on the amount inhaled and the duration of exposure. Effects range from headaches and eye discomfort (from 2 ppm) to loss of consciousness and death (between 1000 and 2000 ppm).[10, 11] As far as industrial applications are concerned, generally accepted maximum levels for H_2S concentration in the final product are 4 ppm for biomethane production.[12] For fuel cells, the tolerance threshold for H_2S is between 0.1 and 10 ppm.[13, 14] Even at concentrations as low as 1 ppm, H_2S has adverse effects on various industrial catalysts, as well as on ceramic membranes used for syngas separations.[15]

On the other hand, the accumulation of NH_3 is a potential issue in the anaerobic digestion of food waste,[16] restricting its application in industrial biogas plants. Its concentration can reach up to 0.05% in biogas composition.[17] It has been reported that its concentration in anaerobic digester biogas can range from 0 to 100 $mg \cdot m^{-3}$, while in landfill gas, it typically varies from 0 to 5 $mg \cdot m^{-3}$.[18] Since a high concentration of NH_3 can lead to a 50% reduction in CH_4 production,[16] NH_3 is normally treated in the anaerobic digester using nitrification/denitrification techniques.

Siloxanes are a prevalent impurity in biogas, particularly when it is produced from sources such as landfills. These impurities arise from the disposal of silicon-rich products such as detergents, cosmetics and sewage sludge, commonly found in landfill sites. The concentration of siloxanes in biogas typically ranges from 0 to 50 $mg \cdot m^{-3}$.[18] When siloxane-containing biogas is burned in an engine, the siloxanes undergo oxidation forming silicon dioxide, which can accumulate on engine components such as spark plugs, valves, and turbo compressors.[18] Finally, the presence of moisture can adversely affect the CO_2 adsorption process on zeolites and MOFs during biogas upgrading. However, the influence of moisture on carbon surfaces remains a subject of debate, as it has been shown to even improve CO_2 adsorption compared to dry conditions.[19] Nevertheless, it is crucial to acknowledge a threshold beyond which the presence of water can exert a negative effect on CO_2 adsorption. Studies indicate that when the water content exceeds 1 % of the total gas volume,[20] or when the relative humidity surpasses 37% in the gas phase (meaning the moisture in the gas reaches 37% of its maximum capacity at a given temperature),[21] CO_2 adsorption experiences a substantial decrease.

When biogas is upgraded to higher CH_4 purity, it is referred to as “renewable natural gas” or “biomethane (Bio-CH_4)”, and can be used in a variety of power generation applications, including heat, electricity and fuel, as shown in **Figure 1.2**. In these processes, biomethane is compressed and burned in a gas turbine or combustion engine, converting chemical energy into mechanical energy, which is then used to power an electric generator that produces electricity. Bio-CH_4 can also serve as a vehicle fuel, similar to natural gas, in either compressed or liquefied form. Furthermore, it can undergo steam reforming to produce hydrogen for fuel cells.[22] When bio-CH_4 is injected into a natural gas grid, the maximum allowable CO_2 content is 2.5 mol.%, in accordance with the regulations set by the European Association for the Streamlining of Energy Exchange (EASEE) for gas injection into the European transport gas grid.[23] A more detailed comparison of biogas applications can be found elsewhere.[24, 25] Overall, the conversion of biogas into Bio-CH_4 emerges as a promising route for the production and transportation of sustainable energy, offering a viable alternative to fossil fuels.

1.2 Biogas upgrading

When upgrading biogas for increased CH_4 purity, the initial focus is typically on eliminating H_2S, given its potential corrosive threat and the need to protect treatment facilities. Subsequently, additional treatment is applied to remove the remaining contaminants in order to obtain a biogas primarily comprising CH_4 and CO_2. Several methods can be used to upgrade

biogas,[26] and the choice of the method depends on several factors, including input composition, desired biogas quality, local market conditions, volume of biogas undergoing treatment, and cost of the upgrading process.

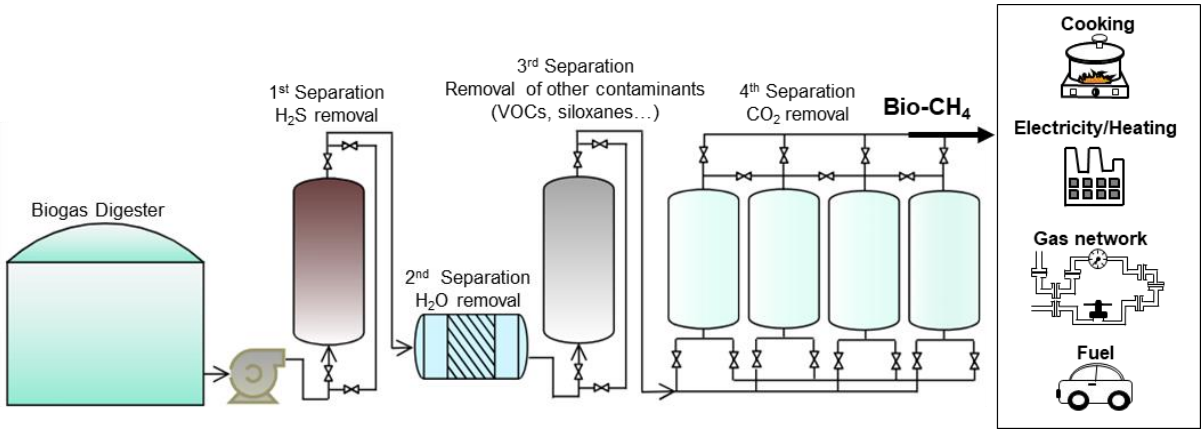

Figure 1.2 Biomethane production and its applications.

1.2.1 CO_2 separation

Notably, water scrubbing (see **Figure 1.3a**) is the most commonly used technology in this regard,[27] with approximately 41% of biogas upgrading plants worldwide incorporating water scrubbing technology.[26] The process involves directing the biogas through a column filled with a water-based scrubbing solution that selectively absorbs impurities. This is due to the fact that the solubility of CH_4 in water is significantly lower than that of CO_2.[28] The biogas ascends through the packed column from the bottom, while the water-based solution flows countercurrently from the top. The purified biogas is then collected at the top of the column. Impure water, containing traces of CH_4, exits the column at the lower end and enters a flash tank with lower pressure than the supply pressure. This lower pressure causes the release of absorbed impurities. In this tank, the small amount of CH_4 is extracted and reintroduced into the scrubbing column for further purification. The aqueous solution is subsequently directed to a desorption column for regeneration, with continuous recirculation through the column. It is worth noting that water scrubbing requires a significant volume of water, a resource that may be scarce in certain regions. Additionally, the process can produce wastewater, necessitating treatment before proper disposal.

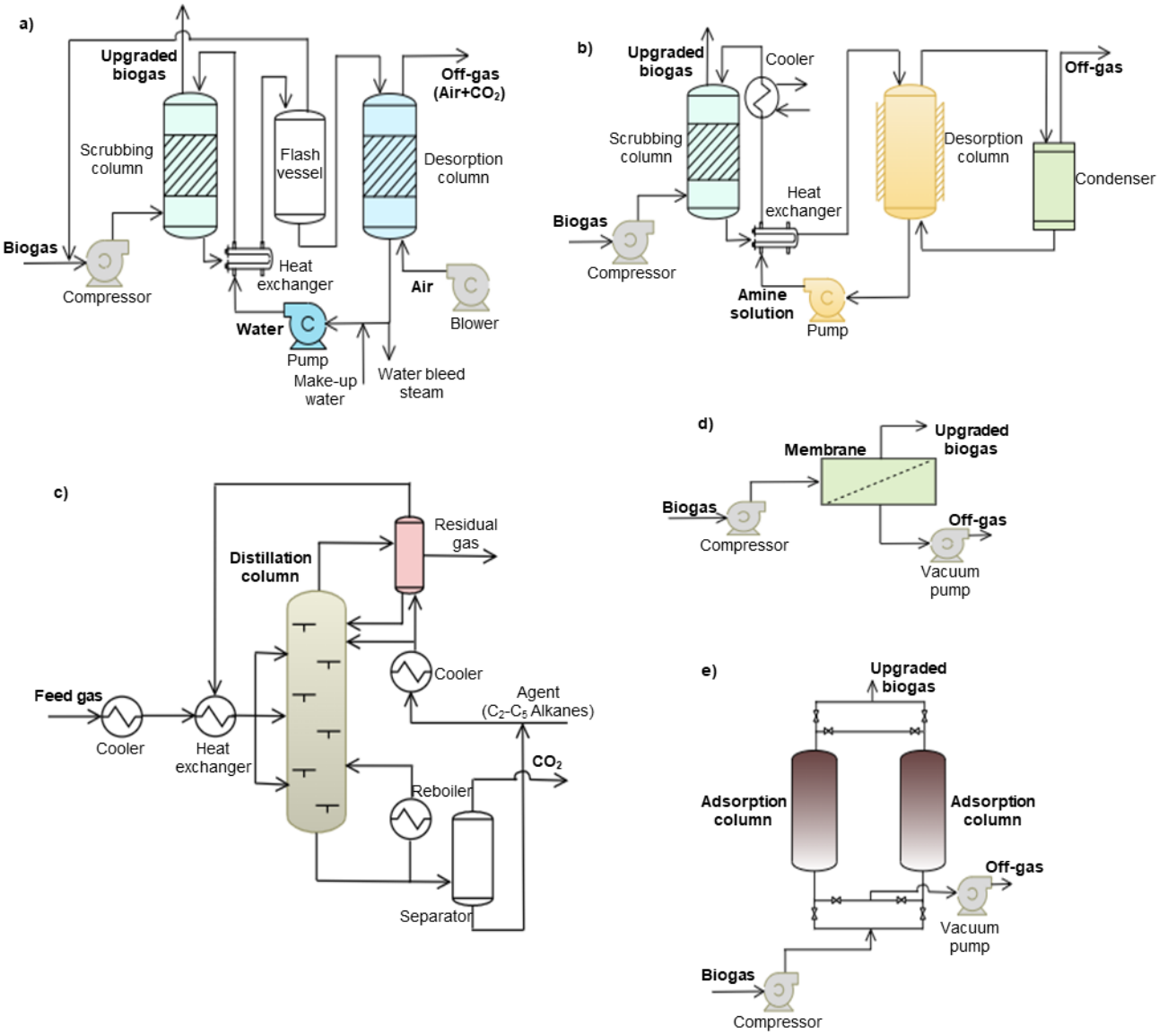

Figure 1.3 Schematic diagrams of biogas upgrading methods: a) water scrubbing; b) chemical scrubbing (amine scrubbing); c) cryogenic distillation; d) membrane separation; e) pressure swing adsorption.

An alternative to water scrubbing for biogas upgrading is chemical absorption (see **Figure 1.3b)**. Instead of using water, a chemical solution such as an amine selectively removes impurities from the biogas. The scrubbing column receives the untreated biogas from the bottom and the amine solution from the top, flowing in opposite direction to the biogas. The amine solution removes impurities from the biogas, and it becomes saturated at the bottom of the column. Following the heat exchanger, the solution proceeds to the desorption/stripping column, where the temperature is raised to between 100 and 180 °C,[27] using the supplied heat. The high temperature effectively breaks the bond between the impurities and the amine

solution, facilitating the regeneration process. The solvent saturated with contaminants is then treated to release the absorbed impurities. Amines are commonly used as a chemical solvent for absorbing CO_2 from biogas due to their selectively reaction with it,[29] without any loss of CH_4.[28] Alternatively, other alkaline salts such as sodium, potassium and calcium hydroxides can also be used to react with CO_2.[27] However, this method has some disadvantages. Firstly, the solvents used can be toxic to both humans and the environment. Secondly, a significant amount of energy is required for regenerating the chemical solutions, as this process demands large amounts of heat and high temperatures. For instance, regenerating the aqueous solution of alkanolamines involves an energy expenditure that accounts for more than 20% of a power plant's total energy production.[30]

Cryogenic separation (see **Figure 1.3c**) is another technique that involves cooling biogas to very low temperatures to liquefy impurities, enabling their separation from the biogas stream according to their boiling point.[31] First, the feed gas undergoes pre-cooling, followed by low-temperature cooling using a refrigeration source through heat exchanger. Next, the cooled feed gas is directed to the distillation column, which includes various vapor-liquid contact devices such as trays or packing materials. In the distillation column, the resulting component stream, i.e., biogas after liquefaction, is primarily divided into two fractions: the top product and the bottom product. The top product, primarily consisting of CH_4, is extracted using a partial condenser. At the bottom of the distillation column, condensed CO_2 accumulates. Part of the CO_2-rich stream is recirculated back into the distillation column via the reboiler, where it supplies the necessary heat for vaporization. The remaining part of the CO_2 stream undergoes further separation, ultimately resulting in the extraction of purified CO_2 product from the separator. However, the use of cryogenic separation for biogas upgrading faces several challenges, including high initial investment and operating costs. Additionally, the process can lead to CH_4 losses, and practical issues may arise, such as the presence of remaining impurities in the biogas stream.[27] Collectively, these factors limit the widespread adoption of this technique in the industry.

Membrane separation (see **Figure 1.3d**) is another common method that involves using a semi-permeable membrane, allowing CH_4 to pass through while retaining impurities such as CO_2 and water vapor.[32] However, this technology comes with major disadvantages, including the high cost of the membranes and their fragility.[27] Additionally, the economic viability of membrane separation processes has proven to be challenging for small-scale plants (< 100 $Nm^3 \cdot h^{-1}$ biogas flowrate).[26]

The last method is pressure swing adsorption (PSA) (see **Figure 1.3e**), which uses adsorbent materials to separate CO_2 and other impurities from the biogas stream. The adsorbent material is regenerated by reducing the pressure, releasing the impurities and leaving behind a concentrated CH_4 stream.[7] The popularity of PSA technology in biogas upgrading is on the rise due to its energy efficiency, minimal operational and installation costs, compact equipment design, and user-friendly operation.[33]

1.2.2 H_2S separation

Usually, due to its corrosive nature, and to safeguard treatment facilities, H_2S is removed prior to biogas treatment. For example, it has been shown that desulfurization is a prerequisite for entering the PSA process unless the H_2S concentration remains below 300 ppm.[34] Various methods such as chemical scrubbing, physical adsorption in column filters, aerobic and anaerobic biotrickling filters, and anoxic desulfurization can effectively remove H_2S.[35] H_2S removal is recommended for amine scrubbing to reduce the high energy demand during the regeneration of the amine solution.[26] Similarly, the presence of siloxanes in biogas can lead to the formation of white deposits on engine components (such as engine heads, spark plugs and valves) and other units (such as boiler tubes and intercooler radiators).[36] Several methods, including adsorption filters, physical and chemical absorption, cryogenic distillation and membrane separation, can be used to remove siloxanes from biogas.[37]

The choice of H_2S removal technology must rely on the current conditions of the purification system, for instance: site conditions in terms of gas flow operating parameters, composition of the H_2S to be treated, temperature, pressure and concentration of other contaminants present. In addition, final gas requirements must be taken into account. CAPEX and OPEX must also be considered to achieve the best financial results. While an expensive technology may involve lower operating and maintenance costs, choosing a cheaper solution may result in higher ongoing expenses. **Figure 1.4** has been proposed to guide the choice of the correct separation technology according to the quantity of H_2S to be separated and the total quantity of gas to be treated.[38] The adsorption process (non-regenerable dry medium) is often recommended for high biogas flow rates with moderate H_2S concentrations, or for low flow rates with high H_2S concentrations. **Table 1.2** provides an overview of conventional technologies widely used in industry.

The absorption process for H_2S removal from biogas (see **Figure 1.5a**) involves the use of a scrubbing solution that reacts with and/or absorbs H_2S, separating it from the biogas stream. The biogas enters the scrubbing tower from the bottom, and the scrubbing solution is distributed through the tower in a countercurrent flow. The scrubbing solution can be common physical solvents for physical absorption (i.e., without chemical reaction), but also alkanolamines, ionic liquids, deep eutectic solvents or hybrid blends.[39] As the biogas rises in the tower, it enters into contact with the scrubbing solution. The H_2S gas interacts with the alkaline solution, forming a water-soluble compound that remains dissolved in the scrubbing solution. Once the biogas has passed through the absorption tower, it is free of H_2S and scrubbing solution. The solution leaving the scrubbing tower contains dissolved H_2S, which is then regenerated for reuse by air stripping, biological oxidation or other methods. The collected H_2S concentrate can then be treated or processed further for disposal or utilization. The use of amines in an aqueous solution for H_2S removal becomes impractical at low concentrations due to the high operational costs, corrosive nature and loss of solution due to its chemical degradation.[40]

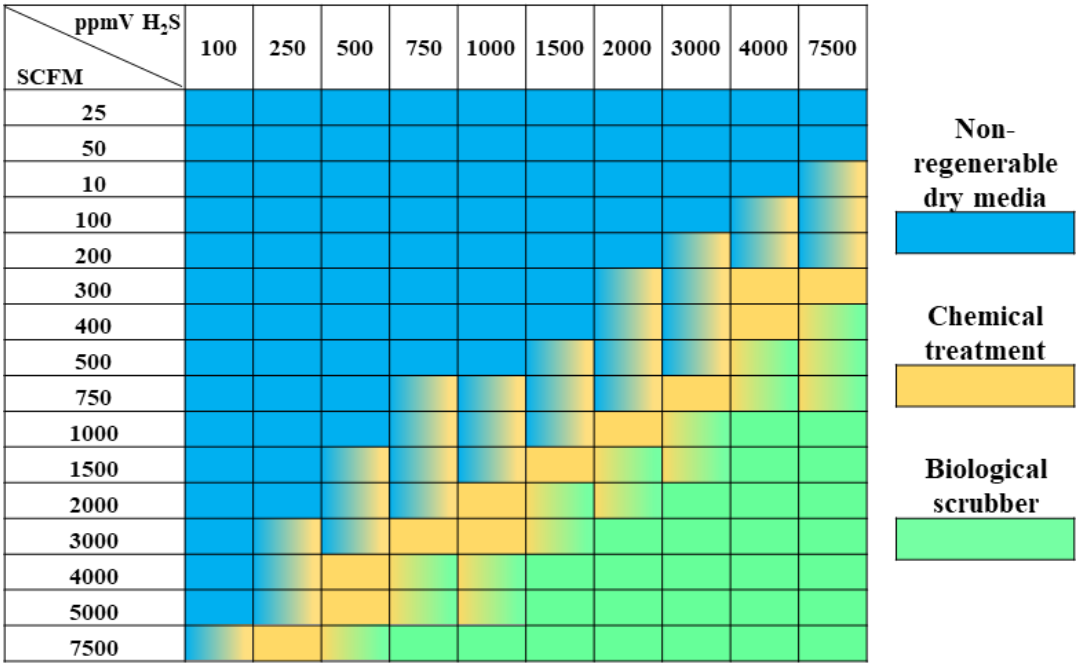

Figure 1.4 Efficient H_2S abatement technology according to the amount of H_2S and biogas in SCFM (standard cubic feet per minute).[38]

The adsorption process (see **Figure 1.5b**) involves a column filled with a bed of sorbent, which may include activated carbon, zeolite and/or metal oxide. These sorbents bind H_2S molecules to their surface or, if modified by metal loading or chemical impregnation, oxidize H_2S to elemental sulfur. The operating principle of the column involves biogas passing through

the sorbent bed, where the H_2S molecules enter into contact with the surface of the sorbent material and then stick to its surface through chemical or physical interactions. The adsorption process continues until the sorbent bed becomes saturated with H_2S, or until the desired level of H_2S removal is achieved. At this point, the sorbent must be regenerated or replaced to restore its adsorption capacity. Regeneration is generally carried out at high temperatures, up to 500 °C, using air or nitrogen. However, the sorbent's separation capacity diminishes after each cycle of use, as discussed below.

Table 1.2 Comparative table of gas desulfurization methods.

	Membrane separation	**Absorption**	**Biological separation**	**Adsorption**
Application	Natural gas	Biogas, natural gas and syngas	Biogas mainly	AC for biogas; Metal oxides for syngas and fuel gas
Operating temperature	< 60 °C [39]	-70 °C to 60 °C [39]	Near ambient	Near ambient for biogas; up to 850 °C for fuel gas.
Operating pressure	25 to 100 bar [39]	Ambient to > 50 bar [39]	Ambient to 15 bar [39]	Near ambient for biogas
Advantages	No hazardous chemicals; Suitable for remote or offshore applications [41]	Solvent can be regenerated	No hazardous chemicals; Mild operation conditions	Energy efficiency; Easy operation; Simple design [42]
Drawbacks	High-pressure requirement; Low H_2S selectivity when CO_2 is present [42]	Water presence in outlet gas [42] – Energy intensive due to solvent regeneration	Sensitive to environmental conditions; Space limitations	Difficult regeneration; Spent sorbent is hazardous waste
Commercial technologies	SLB Cynara; UOP Separex™; Air Liquide MEDAL™	**Physical solvents**: Rectisol; Selexol; Purisol; Morphysorb **Alkanolamines**: ADIP; FLEXORB™SE; OASE®sulfexx™; UOP Benfield™; UCARSOL; GASSPEC	**Biotrickling filter**: Biogasclean QSR; Sulfurex BF or BR – BIOSULFEX; **Bioscrubber**: Sulfothane;THIOPAQ	**Activated carbon**: Desorex K43, PI; Jacobi AddSorb™; Desotec RPure 25DS – Chemviron ENVIROCARB STIX, SOLCARB KS3 – SILCARBON – EUROCARB SAC460 KIC, C4, KP, HR5 **Metal oxides**: SLB SULFATREAT; PuriStar® R3-22; Selexsorb®
Unit desulphurization cost (US $·m^{-3}) [a]	-	2.421 [43]	Bioscrubber: 0.185; [43] Biofilter: 0.123; [43] Biotrickling fiter: 1.534[43]	1.245 [43]

[a] Cost of the entire technology, considering the annualized capital cost (C), the annual operating cost (P) and the volume of biogas desulfurized (V) in 2019, according to the following equation: (C+P)/V. [43]

Membrane separation is a relatively recent new method compared with more traditional technologies such as absorption and adsorption (see **Figure 1.5c**), as its industrial applications only began in the second half of the 20th century.[39] Gas separation applications are currently dominated by polymer membranes, as the higher costs and production difficulties of inorganic membranes limit their use.[39] Membranes have specific pore sizes to retain H_2S molecules (retentate) while allowing other gases such as CH_4 to pass through (permeate). The permeate stream is desulfurized, while the retentate stream, enriched with H_2S, is discharged from the membrane separation unit for further treatment or disposal. Although membranes alone cannot achieve high levels of purification for H_2S removal, their role as a pretreatment step can significantly improve the efficiency of other technologies, particularly when dealing with streams containing high concentrations of H_2S. They are mainly used for natural gas purification, especially when H_2S concentrations are between 10% and 20% or even higher.[39]

Other processes are also used in industry, such as biological methods, which can include biofilters, bioscrubbers and biotrickling filters (see **Figure 1.5d, 1.5e and 1.5f**, respectively). In biofilters, biogas is introduced into the system, which contains a porous support that can consist of a mixture of compost (pig manure + sawdust), wood-based substrate, granulated sludge, expanded schist, aerated concrete waste, vermiculite[44] and various other materials, providing a favorable environment for microorganisms to settle and grow as a biofilm.[39] As biogas passes through the substrate, microorganisms naturally colonize its surface, forming a diverse community of bacteria in the biofilm, which can convert H_2S to sulfuric acid and water[39] in a process known as biological oxidation. To ensure a healthy population of microorganisms, these are first grown in bioreactors before being transferred to the bed filter using a counter-current flow, while the treated biogas is simultaneously discharged from the top of the biofilter.[45]

Bioscrubbing technology consists of two main components: an absorption/separation chamber and a bioreactor column. The former involves a physical mechanism, while the latter operates as a biological process. In the initial stage, the gas mixture containing the pollutant passes through the absorption chamber, where an absorbing solution facilitates transfer of the contaminant from the gaseous phase to the aqueous phase. This aqueous phase is then directed to the bioreactor, where treatment is carried out by suspended heterotrophic or autotrophic sulfur-oxidizing bacteria.[39] The operating mechanism of a biotrickling filter is similar to that of a biofilter, except that a continuous stream of aqueous-phase nutrient solution flows dropwise over the packed bed.[45]

At present, adsorption is a highly efficient method for removing H_2S. Its simple design, ease of operation and the extensive experience in this consolidated technology make it the preferred choice for biogas desulfurization. Furthermore, ongoing advances in this technology and continuing research efforts are aimed at improving the development of even more efficient sorbents. The following section explores the mechanisms of H_2S adsorption in sorbents, explaining why this technology is ideally suited for biogas purification.

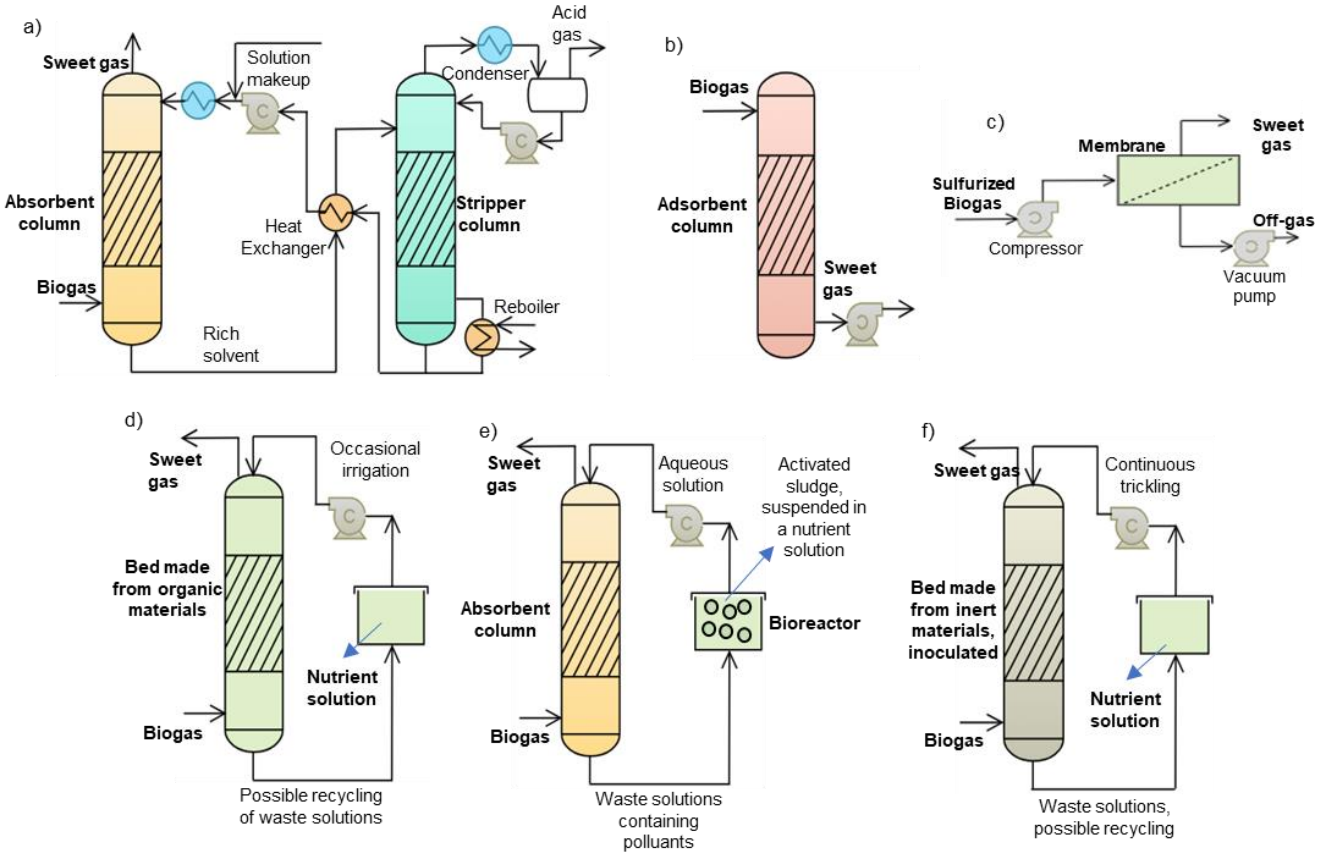

Figure 1.5 Conventional technologies for H_2S removal: a) absorption; b) adsorption in a column filter; c) membrane separation; d) biofilter: e) bioscrubber; f) biotrickling filter.

1.3 Use of sorbents in biogas upgrading for CO_2/CH_4 separation

Nanoporous materials are frequently considered the most suitable for biogas upgrading involving adsorption processes. Research on the removal of H_2S from biogas has primarily concentrated on ACs[46–48] and zeolites.[49–51] In addition, other adsorbents, including alumina, silica gel, along with ACs[52–54] and zeolites once more, have been used to eliminate siloxanes. CO_2, the most common contaminant in biogas streams, has been mainly studied with ACs,

CMSs, MOFs and zeolites. **Table 1.3** gives an overview of some of the characteristics of these materials.

Table 1.3 Comparison of the properties of ACs, carbon molecular sieves, metal organic frameworks and zeolites. AC and CMS images were taken with permission from [55] and [56].

	Activated carbon	**Carbon molecular sieve**	**Metal organic framework**	**Zeolite**
		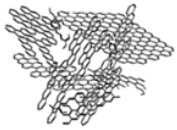	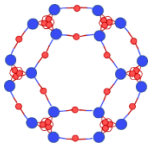	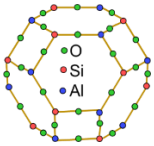
Nature	Carbonaceous	Carbonaceous	Organic ligands and metal ions	Crystalline aluminosilicates
Pore size distribution (PSD)	Wide PSD: micropores (<2 nm) and mesopores (2-50 nm)	Narrow PSD (<1 nm)	Tailorable PSD	Uniform and narrow PSD (<1 nm)
Adsorption mechanism	Presence of micropores and active sites	Well-defined micropores	Well-defined micropores	Well-defined micropores
Surface area	High due to micropores and mesopores	High due to micropores	High due to micropores	High due to micropores

- ACs are a subject of extensive research due to their remarkable characteristics, including a large surface area, high micropore volume and appropriate pore size distribution (PSD).[22] ACs exhibit a relatively low heat of adsorption, translating to low energy requirements for regeneration. Additionally, ACs are generally cost-effective.[57]
- CMSs, as implied by their name, consist primarily of carbon, and they have demonstrated effectiveness in separating CO_2 from CH_4 due to their small pore size, enabling kinetically preferential adsorption for CO_2 (see details two-four pages further down). However, their production is expensive, and their performance may be restricted by a low adsorption capacity.[58]
- MOFs have recently emerged as a promising class of materials, due to their high surface area and pore volume, which allow efficient gas adsorption and separation. MOFs can be tailored with specific pore sizes and shapes, enabling selective adsorption of CO_2 over CH_4. However, a drawback of MOFs is their relatively low stability under certain conditions, such as high temperatures or humid environments.

- Zeolites, as porous crystalline aluminosilicates, exhibit a high selectivity for CO_2 and possess high CO_2 adsorption capacities. This can be attributed to their PSD and surface chemistry. Additionally, zeolites also have good thermal and chemical stability, making them durable and suitable for prolonged usage. However, they also have some disadvantages with regard to the substantial adsorption heat of CO_2, leading to challenges in adsorbent regeneration.[58]

In the literature, the evaluation of adsorbents typically involves assessing their adsorption equilibrium with pure gases (e.g. CH_4 and CO_2) or conducting breakthrough curve experiments using a synthetic gas mixture that mimics biogas composition (e.g. CH_4 = 65 vol. %, CO_2 = 35% vol. %). When considering the separation of CO_2 and CH_4 using a PSA process, it is important to consider not only the properties of the adsorbent but also the operational parameters of the PSA unit. Indeed, the adsorption capacity of the adsorbent and the efficiency of the separation process can be influenced by various factors such as feed gas flow rate, pressure, temperature, cycle time, as well as the type and amount of adsorbent used. A recommended approach for selecting an optimal adsorbent/PSA system configuration is to select adsorbents based on equilibrium isotherms and dynamic measurements to identify the most promising candidates. Subsequently, the chosen adsorbent undergoes evaluation in a PSA system to establish a set of baseline performance data. Finally, a reliable numerical model of the PSA process can be validated using experimental PSA data, enabling exploration of additional cycles and operating windows.[59]

The preferential selectivity of the components of a gas mixture for a given adsorbent is the fundamental principle behind adsorption/separation processes. Ideally, a high selectivity is needed, but a large working capacity ratio in the adsorption column is also desirable as it determines the size and cost of the bed separation system.[60] In addition to the aforementioned selection criteria concerning adsorption and separation performance, various other factors associated with an adsorbent are of significant importance. These include aspects such as ease of synthesis, density, scalability, sustainability, availability, physicochemical stability, cost, hydrophobicity, and toxicity.[30] The strength of the interaction between adsorbent and adsorbate is determined by the adsorption enthalpy. The adsorption enthalpy of CO_2 lies between -25 and -50 $kJ \cdot mol^{-1}$ for physisorption and is below -60 $kJ \cdot mol^{-1}$ for chemisorption. A higher enthalpy in absolute value requires more energy for CO_2 desorption, which increases

regeneration costs. However, too low an enthalpy in absolute value results in low CO_2 adsorption capacity.[61]

The surface of an adsorbent material attracts gas molecules through a combination of Van der Waals interactions and electrostatic forces from more or less polar or quadrupolar species. CO_2 is a molecule with a quadrupole moment of 13.4×10^{-40} cm^2, whereas CH_4 has no polarity. Due to this significant difference in polarity, the presence of polar functional groups on the adsorbent surface proves highly beneficial in enhancing the selectivity for CO_2.[62] These interactions vary in strength, enabling different substances to be adsorbed to varying extents. Separation of CO_2 based on this kind of electrostatic interactions with the adsorbent is called equilibrium separation.[61] When selectivity results from significant variations in the diffusivity of the different molecules in the micropores, the separation is called kinetic separation.

To identify the optimum adsorbent for selectively capturing CO_2 from biogas streams, various parameters can be considered, including BET area, micropore volume, adsorbent capacity at different CO_2 partial pressures for biogas upgrading, and CO_2/CH_4 selectivity. Porous materials used in CO_2/CH_4 separation by PSA units can be classified into carbonaceous materials such as ACs and CMSs, or other inorganic or hybrid materials such as zeolites or MOFs, respectively, see **Table 1.4**.

Table 1.4 Main properties of adsorbents for CO_2/CH_4 separation.

	Activated carbon	**Carbon molecular sieve**	**Metal organic framework**	**Zeolite**
				
CO_2 adsorption capacity	High	Medium	Medium	High
CH_4 adsorption capacity	High	Medium	Low	Low
CO_2/CH_4 equilibrium selectivity	Low	Low	Medium	High
CO_2/CH_4 kinetic selectivity	Low	High	Medium	High
PSA regeneration	Feasible	Feasible	Not documented	Feasible at $P<P_{tam}$
Cost (USD·kg^{-1})	0.6 – 2.4 [63]	6.0 – 15.0	10.0 – 70.0 [64, 65]	0.6 – 5.0

1.3.1 Carbon adsorbents

ACs can be synthesized from a variety of precursors, including coal, char, peat, petroleum coke, lignite, wood and other biomass materials.[66] Additionally, industrial waste can serve as a viable source, provided it contains a high carbon content and minimal levels of inorganic compounds, commonly referred to as ashes.[67] The preparation of ACs involves enriching the raw material with carbon through heat treatment and developing and opening porosity, which corresponds to the activation process itself. There are two primary activation processes: physical activation, which involves carbon dioxide[22, 57, 67–69] and/or water vapor[22] as gasifying agents, and chemical activation, which involves the use of substances such as phosphoric acid (H_3PO_4),[70–72] potassium hydroxide (KOH),[70, 73–77] or potassium carbonate (K_2CO_3),[72, 78] amongst others.

Physical activation enhances the textural characteristics of the resulting carbon by creating micropores, thereby increasing its adsorption capacity. Furthermore, physical activation can enlarge existing porosity by making micropores wider and introducing some mesoporosity into the carbon structure, which facilitates molecules diffusion within carbon.[79] Finally, it also facilitates the emergence of oxygenated functional groups, including phenolic, ketonic, and carboxylic groups,[66] which may enhance carbon surface interaction with molecules. Physical activation processes involve progressive carbon gasification, limiting control over micropore size distribution. In contrast, chemical activation methods offer a good alternative, as they enable porosity development to be precisely controlled and modified. Through well-controlled activation conditions, the porosity characteristics of the carbon material can be significantly altered, leading to tailored and optimized PSDs.[79] Nevertheless, chemical activation is often considered detrimental to the environment, given the use of water to dissolve reagents, extract and wash products, separate mixtures, clean reaction apparatus, and disperse products for practical applications.[67] It is important to recognize, however, that the surface area of chemically and physically activated carbons can be influenced by a variety of factors, including the precursor material and other activation conditions.

The incorporation of heteroatoms such as nitrogen, phosphorus, and sulfur has been investigated to further enhance the properties of activated carbons.[77] Nitrogen-functionalized ACs, in particular, have shown improved CO_2 adsorption capacity and selectivity through mechanisms such as acid-base interactions and hydrogen bonding.[30] Incorporating heteroatoms, such as nitrogen, into the carbon framework can significantly enhance adsorption

efficiency by improving interactions between gas molecules and carbon. Reported nitrogen-doped activated carbons with very high surface areas, exceeding 1400 $m^2 \cdot g^{-1}$, have confirmed the improvement achieved by this approach.[30, 80]

It is feasible to create carbon adsorbents with tightly controlled PSDs in their porous structures. These materials, known as CMSs, possess narrow, uniformly sized micropores that are able to sieve molecules based on their differences in diffusion rate, size and shape.[81] The CMS production process can be similar to the preparation of ACs, but with an additional step involving pore shrinkage. This is achieved by controlled deposition of carbon obtained by high-temperature cracking of molecules such as benzene or acetylene.[60] CMSs can also be produced by controlled pyrolysis of synthetic polymers such as polyvinylidene chloride, polyimide and phenol-formaldehyde resin.[82] By carefully adjusting the preparation conditions, a highly homogeneous PSD can be obtained.[60]

CMSs exhibit uniform, slit-shaped pore openings, similar in size to those of small molecules (N_2, O_2, CO_2 or CH_4). It is essential for a CMS to possess pore sizes between 3.2 and 3.7 Å to ensure the sieving effect,[7] which implies that small gas molecules pass through the narrow channels and pores more easily than larger molecules. For instance, since the CH_4 molecule (3.8 Å) is larger than that of CO_2 (3.3 Å), the latter is more adsorbable. The main difference between ACs and CMSs lies in their PSD. ACs exhibit a disordered and widely distributed range of pore sizes, from 0.4 to 4 nm and often extending far beyond this range. This characteristic renders them unsuitable for the kinetic separation of gas mixtures, as their broad PSD hampers their kinetically-based selectivity.[7] CMSs have the potential to facilitate highly effective kinetic separation, relying on differences in sorption rates rather than sorption equilibrium. Nonetheless, CMS synthesis requires the modification of the pores of the carbon precursor, involving energy-intensive and complex techniques such as chemical vapor deposition (CVD). Consequently, conventional CMSs may not be suitable for household biogas upgrading systems due to their cost-effectiveness limitations.[8]

If ACs exhibit stronger surface interactions with CO_2, allowing them to adsorb larger quantities of this gas compared to CH_4, CMSs are kinetic-based adsorbents. CMSs control the diffusion rate thanks to their narrow micropore size, resulting in greater CO_2 retention per unit time.[83] Due to these kinetics restrictions, CMSs use only a fraction of their total adsorption capacity.

1.3.2 Other adsorbents

MOFs are produced by the self-assembly of organic ligands consisting of carboxylate, phosphonate, pyridyl and imidazolate or other azolate functional groups and metal oxide clusters (e.g. Cu^{2+}, Mg^{2+}, Al^{3+}, Cr^{3+} or Zn^{2+}),[84] resulting in the formation of crystalline structures with exceptionally high surface areas and pore volumes. MOFs have a very regular porous structure with adjustable pore sizes and chemical functionalities that can be customized by modifying the metal groups or organic ligands.[85]

MOFs typically exhibit surface areas exceeding 4000 $m^2 \cdot g^{-1}$,[86] surpassing those observed in conventional porous materials. Within MOFs, CO_2 adsorption is enhanced by the metal sites, capable of inducing local electric field effects, thereby increasing the affinity for CO_2 in comparison to CH_4.[87] Furthermore, strategic functionalization, such as incorporating polyamines to introduce CO_2-binding sites through physical means, or integrating carbon nanotubes and chemically decorating them with amine groups have allowed to further increase CO_2 adsorption selectivity over CH_4.[87] Thus, CO_2-MOF interactions can be adjusted through the use of functionalized ligands. Among the functional groups most commonly incorporated into MOF ligands are thiols, carbonyls, carboxyls, cyano groups and amines.[84]

One of the primary drawbacks of MOFs is their limited stability to water at moderate to high temperature,[88] which can, however, be improved by both post-synthetic modifications and material compounding.[87] While MOFs have proven effective, their complex preparation methods often make the process uneconomical. It is therefore necessary to develop new, economically viable compounds that can be synthesized by solvent-free reactions or by simple precipitation reactions under ambient conditions.[84]

Among all the MOFs, the most remarkable and cutting-edge one for CO_2 adsorption is a zinc-based one developed at the University of Calgary, known as CALF-20. This MOF exhibits a high capacity for adsorbing CO_2 while also showcasing selectivity over water. CALF-20 demonstrates competitive separations by favoring CO_2 physisorption at relative humidity levels below 40%. Computational modeling supports this observation. CALF-20 imposes a low enthalpic regeneration penalty and demonstrates robustness against steam (> 450,000 cycles) and wet acid gases. Notably, its preparation involves a single-step process, enabling formation of composite materials, and its synthesis can be scaled up to produce multikilogram batches.[89]

MOFs have attracted attention for their remarkable CO_2 adsorption capacities, reaching values as high as 33.5 $mol \cdot kg^{-1}$ at 35 bar. However, for applications such as biogas upgrading,

good adsorption capacity is best achieved at lower pressures (< 10 bar). Indeed, compression up to 35 bar requires more expensive equipment and increases energy costs. MOFs with high adsorption capacity at high pressures are less suited to the lower pressure ranges (< 5 bar), where zeolites generally have higher adsorption capacities.[61] One area of ongoing research in MOFs is CO_2 diffusion, which has been reported to be poor,[90] for instance with MIL-53,[91] where reduced diffusion has been attributed to the presence of hydroxyl groups within its structure. On the other hand, in another study, it was reported that, in the case of MIL-53, there were no significant mass transfer limitations.[92]

Zeolites are crystalline, microporous materials composed of hydrated aluminosilicates with a three-dimensional framework structure. They consist of a network of tetrahedra (aluminum, silicon, and oxygen) that create cavities and channels of a uniform size and shape. These materials possess a high surface area and regularly spaced pores, allowing them to selectively adsorb and desorb molecules based on size and polarity.[88] Renowned for their molecular sieving capabilities, zeolites possess highly selective properties, effectively excluding molecules beyond a critical size and restraining the diffusion of molecules nearing this threshold. This separation mechanism, commonly referred to as steric separation, along with the effects of kinetic separation, offers reliable and predictable gas separation.[60] Medium- and large-pore zeolites achieve equilibrium separation. On the other hand, the selectivity of the separation process in small-pore zeolites is generally affected by the diffusion rate of adsorbates in the pores. Due to its smaller kinetic diameter than CH_4, CO_2 exhibit higher diffusion rates than CH_4 through several small-pore zeolites. This difference may have an impact on the diffusion through narrow pores more than on the interaction of the molecules with the zeolite surface, particularly in low-Al zeolites.[61]

The efficiency of zeolites for CO_2 capture also depends on their chemical composition and charge density.[88] In general, the separation capability improves as the electrostatic field in the zeolite cavities intensifies, which is mainly influenced by the charge of the framework and can be altered by the type of charge-compensating cations or the Al content in the zeolite framework.[93] Zeolite performance is also adversely affected by the presence of moisture, which can significantly decrease the amount of CO_2 adsorbed on the zeolite surface. Indeed, moisture can react with adsorbed CO_2 molecules to form an adsorbed layer that prevents access to other CO_2 molecules.[94]

SAPO-56 (Silicoaluminophosphate-56), ZSM-5 (Zeolite Socony Mobil-5) and Sodalite-based Zeolites, like Na-X and Na-A, among others, have been studied for their potential in CO_2 separation processes due to their versatile pore structures and adsorption properties. The adsorption capacity of zeolite NaX, also called zeolite X, NaX, Linde X and molecular sieve 13X, is among the highest for zeolites (6.3 $mmol \cdot g^{-1}$), and this can be further improved by ion exchange.[61] However, zeolite NaX strongly interacts with water molecules, to the extent that it is marketed as a desiccant.[95] When water is adsorbed close to its saturation point, its CO_2 capacity decreases significantly, being an order of magnitude lower compared to dry material.[96] The working capacities and CO_2/CH_4 selectivities of some of these zeolites, when used in PSA systems, will be examined in section 2.1.

1.4 Use of sorbents in biogas desulfurization

Selection of the appropriate material for H_2S adsorption is influenced by the constituents present in the feed mixtures. For instance, biogas often requires H_2S to be separated from non-polar molecules, such as CH_4, so a surface with polar adsorption properties is often preferred.[39, 97] Separation relies on other adsorbent properties, such as the introduction of base functionalization. However, the presence of CO_2 brings additional complexities, as both CO_2 and H_2S are acidic, imposing further limitations on the process.[39]

The regenerability of the sorbent is important as it enables the implementation of a cyclic swing adsorption process, thereby enhancing energy efficiency. Conversely, the consumption of single-use adsorbents is accompanied by considerable environmental costs. Spent sorbents have to be disposed of, incinerated or regenerated using expensive and hazardous chemicals, which raises safety concerns. An ideal sorbent material should thus not only have high breakthrough capacity and selectivity for H_2S, but also chemical and thermal stability, and regenerability.

1.4.1 Activated carbon (AC)

- Commercial ACs for biogas desulfurization

ACs are generally chosen for to their high surface area and pore volume. **Table 1.5** lists typical commercial ACs for biogas desulfurization, mostly coal-based, some from renewable resources such as coconut shell or wood. Available in granular or pellet form, pelletized ACs are preferred because of their higher density, which is advantageous on an industrial scale. All

ACs are impregnated with alkaline chemicals, with a basic pH (>8) and surface areas of 800–1100 $m^2 \cdot g^{-1}$. One of the disadvantages of chemically impregnated ACs is their low ignition temperature, which can lead to dangerous working conditions.

AC micropores allow the storage of highly adsorbed sulfur molecules, an important feature in terms of removal capacity. To facilitate the adsorption of H_2S, the latter must undergo oxidation, resulting in the formation of elemental sulfur or sulfuric acid. Furthermore, the sulfur that accumulates can act as a catalyst for H_2S oxidation.[98] The degree of oxidation depends on the surface pH of the AC, which is attributed to its inorganic fraction.[99]

The surface of ACs thus exhibits catalytic sites that facilitate a variety of reactions, including oxidation.[100] This catalytic behavior arises from the existence of heteroatoms, mainly oxygen chemisorbed onto the carbon surface, or nitrogen, such as the pyridine-like forms observed in ammonia-modified ACs.[101] It imparts basic characteristics to the carbon surface, making it suitable for promoting catalytic reactions, such as the dissociation and oxidation of H_2S in the water film adsorbed on the carbon surface.[102] ACs can also be conventionally functionalized by doping with heteroatoms or via impregnation.

Table 1.5 Properties of commercial activated carbons for biogas desulfurization.

Origin	Particle size	Impregnation	Bulk density ($kg.m^{-3}$)	pH	Surface area ($m^2.g^{-1}$)	Commercial producers	Commercial ACs
Coal	Granular (2.4 – 4.8 mm) or Pellets (Ø = 3 – 4 mm; L = 7 – 9 mm)	1-10 wt.% of: KI, NaOH, K_2CO_3, KOH	430 - 660	8 – 9.7	830- 1150	Chemviron; Silcarbon; Desotec, Eurocarb	Solcarb KS3; Envirocarb Stix; KC10; R-Pure 25DS-1; SAC 460 C4; SAC 460 KP
Coconut shell	Granular (2.36 - 4.75 mm)	KOH 5 wt.%	600-660	9	1100	Eurocarb	HR5 4X8 C4
Wood	Pellets (Ø = 3 – 4 mm)	Unknown	470	10.5	1050	AdFIS	Dopetac Sulfo 100

- H_2S sorption mechanisms on ACs

The H_2S removal process in ACs is primarily governed by two competing adsorption mechanisms. The first is micropore saturation with, for the strongest adsorption forces, pores ideally around 0.36 nm in size, corresponding closely to the size of H_2S molecules (0.33 nm),[103] and also, for the preferential deposition of elemental sulfur during H_2S oxidation,[104]

pores smaller than 1.2 nm. The second mechanism is the catalytic oxidation of H_2S to elemental sulfur. Usually, ACs used for H_2S adsorption are modified by: (1) caustic substances such as KOH [105–107] or NaOH [102, 107, 108] to promote acid-base interactions; (2) oxidizing agents such as CuO,[109, 110] $ZnFe_2O_4$, [111] ZnO, [112, 113] MgO, [110, 112, 114] Fe_2O_3, [115] $KMnO_4$[116] for redox reactions, or (3) catalysts such as KI,[98] urea[54] or transition metals like Cu, [118] Zn [119] and Fe[119, 120] to promote H_2S oxidation in the presence of oxygen. The catalytic effect of urea comes from the incorporation of nitrogen groups into the carbon matrix, which activates oxygen to form superoxide ions. These ions in turn promote oxidation reactions.[117] On the other hand, the catalytic effect of metals in their elemental form derives from their strong affinity for oxygen, which accelerates the oxidation of H_2S. Experimental evidence has demonstrated that the introduction of KI as a catalyst increases the reaction rate and limits sulfuric acid formation,[98] however, the specific mechanisms and roles of KI as a catalyst are not well documented in the literature.

The reactions, involving H_2S dissociation (see **Figure 1.6**), can be expressed as follows:[116]

- Adsorption onto the carbon surface:

$$H_2S_{gas} \rightarrow H_2S_{ads} \quad (1.1)$$

- Dissolution in a water film adsorbed:

$$H_2S_{ads} \rightarrow H_2S_{ads-liq} \quad (1.2)$$

- Dissociation in the adsorbed state in a water film:

$$H_2S_{ads-liq} \rightarrow HS^-_{ads} + H^+ \quad (1.3)$$

When moisture is present in the AC, it leads to the generation of a water film adsorbed on the porous surface, which facilitates the dissociation of H_2S molecules and, consequently, their interaction with the basic active sites on the carbon surface.[102] Suppliers of commercial ACs generally suggest maintaining a relative humidity of 40% to 80% for optimum efficiency.[13]

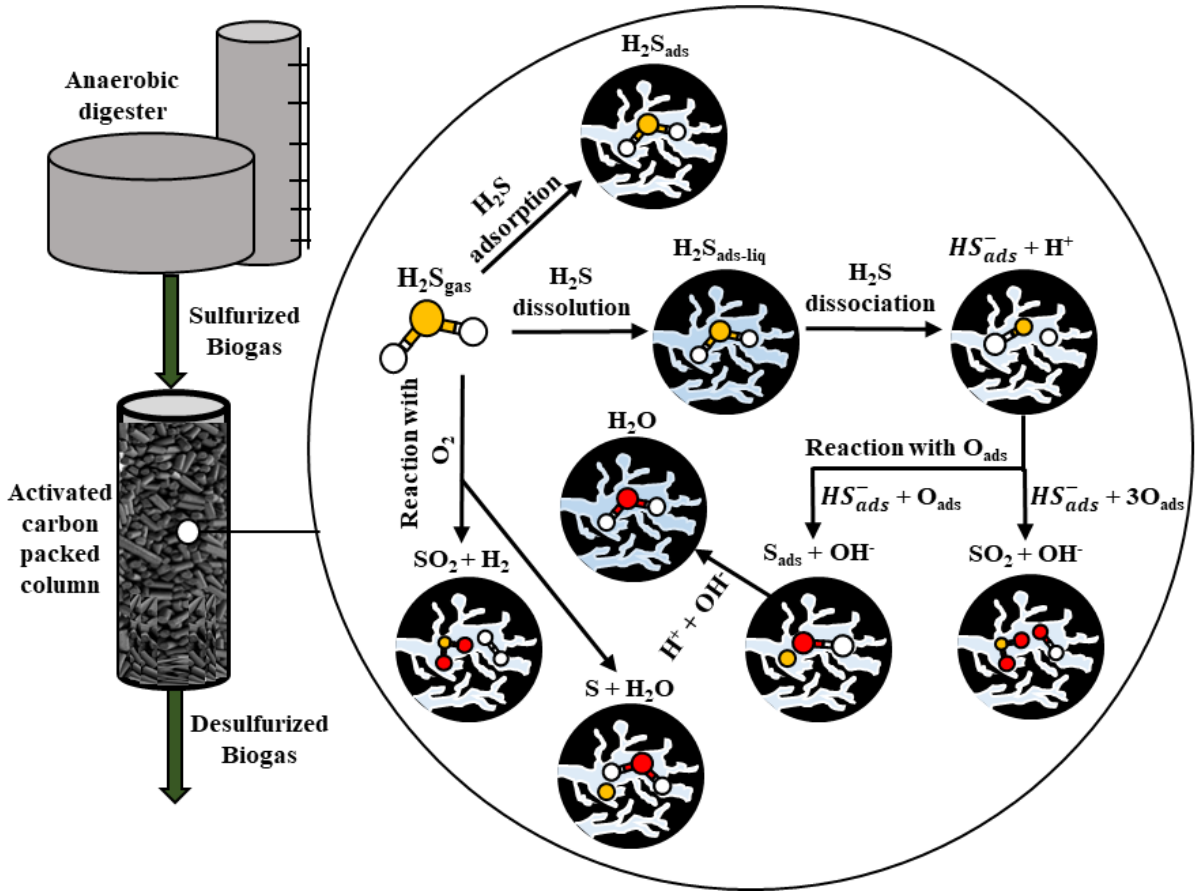

Figure 1.6 Reaction mechanisms for H_2S separation in activated carbons. The role of the impregnating agent is not shown.

If adsorbed oxygen is present, the following reactions can occur:

$$HS^-_{ads} + O^*_{ads} \rightarrow S_{ads} + OH^- \quad (1.4)$$

$$HS^-_{ads} + 3O^*_{ads} \rightarrow SO_{2\,ads} + OH^- \quad (1.5)$$

$$H^+ + OH^- \rightarrow H_2O \quad (1.6)$$

where H_2S_{gas}, $H_2S_{ads\text{-}liq}$, and H_2S_{ads} correspond to H_2S in gas, liquid and adsorbed phases, respectively, O^*_{ads} is dissociated adsorbed oxygen and S_{ads} represents sulfur as the final product of the surface oxidation reaction in the adsorbed state.[116]

- Oxidation in the gas phase with oxygen in the inlet gas:[98]

$$H_2S_{gas} + O_2 \rightarrow SO_2 + H_2 \quad (1.7)$$

The presence of H_2S on AC surfaces can undergo oxidation, resulting in the formation of solid sulfur (S, S_8) and/or sulfur dioxide (SO_2), with consequent H_2O release, as indicated by the following reactions:[98]

$$H_2S_{gas} + \frac{1}{2}O_2 \rightarrow S + H_2O \quad (1.8)$$

$$2H_2S_{gas} + O_2 \rightarrow \frac{1}{4}S_8 + 2H_2O \quad (1.9)$$

Further oxidation (side reactions) of the deposited solid sulfur is possible, forming sulfur dioxide:

$$S + O_2 \leftrightarrow SO_2 \quad (1.10)$$

$$\frac{1}{4}S_8 + 2O_2 \leftrightarrow 2SO_2 \quad (1.11)$$

Conversely, elemental sulfur (S_x) or polysulfides (HS_xSH) that adhere to carbon surfaces could serve as active sites to catalyze H_2S oxidation. Consequently, the following reactions become possible on these sulfur-active sites located on the surface of AC, whether in the form of H_2S molecules or hydrogen sulfide ions (HS^-):[102]

$$S_x + H_2S_{gas} \rightarrow HS_xSH \quad (1.12)$$

The polysulfide (HS_xSH) decomposes to form radical species ($HS_xS\bullet$) and a hydrogen atom (H).

$$HS_xSH \rightarrow HS_xS\bullet + H \quad (1.13)$$

The sulfur radicals serve as intermediates that react with O_2, forming chemisorbed oxygen species $HS_xS(O)$:

$$HS_xS\bullet + \frac{1}{2}O_2 \rightarrow HS_xS(O) \quad (1.14)$$

Alternatively, an elemental sulfur site, fixed at the surface (S_f), can react with O_2 to produce oxidized sulfur species, S(O).

$$S_f + \frac{1}{2}O_2 \rightarrow S(O) \quad (1.15)$$

The S(O) species react with H_2S, forming H_2O and a longer-chain polysulfide ($HS_{x+1}S\bullet$)

$$HS_xS(O) + H_2S \rightarrow HS_{x+1}S\bullet + H_2O \quad (1.16)$$

S(O) can also react with H_2S to produce the original sulfur S_f, sulfur (S_x) and H_2O :

$$S(O) + H_2S \rightarrow S_f + S + H_2O \quad (1.17)$$

- Effect of alkaline impregnates

ACs impregnated with strong bases exhibit adsorption capacities far superior to those of their unmodified counterparts (see **Figure 1.7**).[102] Potassium, for instance, acts as a catalyst in the formation of intermediate compounds such as KHS, which may then decompose into HS^- ions and eventually undergo oxidation to give sulfur. On the other hand, when a promoter of H_2S oxidation is used, such as KI, the main reaction product is elemental sulfur.[102]

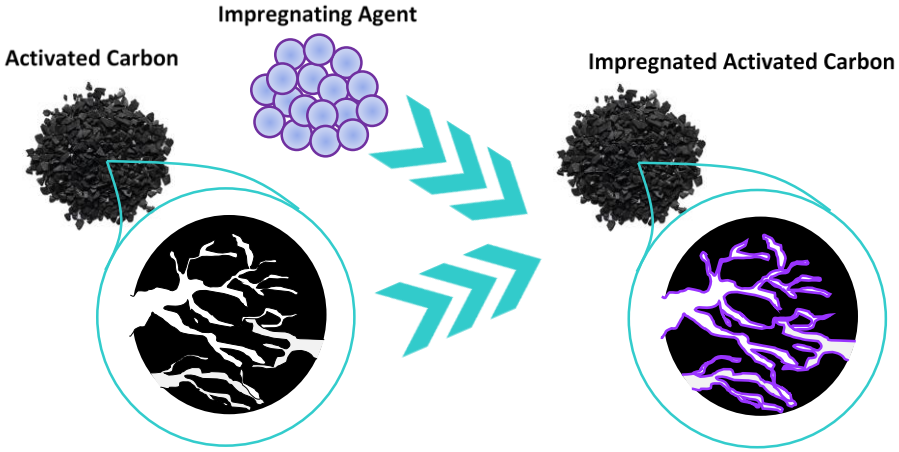

Figure 1.7 Impregnated activated carbon.

In the presence of an alkaline medium such as KOH or NaOH, H_2S reacts with the OH^- group. Since H_2S is a diproton acid, it reacts with hydroxides as follows,[121] A being either Na^+ or K^+.

$$H_2S + AOH \rightarrow AHS + H_2O \quad (1.18)$$

$$H_2S + 2AOH \rightarrow A_2S + 2H_2O \quad (1.19)$$

Since the adsorption ratio of H_2S is nearly one mole of H_2S per mole of AOH, Eq. (1.18) is the predominant reaction.[121] For the case of carbonates:

$$H_2S + A_2CO_3 \rightarrow AHS + AHCO_3 \quad (1.20)$$

$$H_2S + A_2CO_3 \rightarrow A_2S + H_2CO_3 \quad (1.21)$$

By raising the pH of the AC, NaOH causes an increase in the concentration of HS^- ions. These ions can then undergo oxidation, forming either elemental sulfur or sulfuric acid, as indicated by changes in pH levels at the surface. These reactions continue until all of the NaOH reacts with H_2SO_4 or CO_2, produced from surface reactions or present in the surrounding atmosphere, and the basic environment is no longer maintained.[102]

The study of Bagreev and Bandosz proposes the following mechanisms for the role of NaOH.[102] The carbon surface contains chemisorbed oxygen, as well as deposited sodium hydroxide, probably dissolved in the water film adsorbed in the pores:

$$NaHS + \frac{1}{2}O_2 \rightarrow S + NaOH \quad (1.22)$$

$$Na_2S + \frac{1}{2}O_2 + H_2O \rightarrow S + 2NaOH \quad (1.23)$$

with side reactions:

$$NaOH + CO_2 \rightarrow NaHCO_3 \quad (1.24)$$

$$2NaOH + CO_2 + H_2O \rightarrow Na_2CO_3 + 2H_2O \quad (1.25)$$

$$Na_2CO_3 + H_2S \rightarrow NaHCO_3 + NaHS \quad (1.26)$$

where CO_2 can originate from the atmosphere or from partial gasification of the carbon surface.

Removal of H_2S by efficient acid-base reaction with KI can occur at high temperatures (≈ 550 °C), to produce KHS and K_2S, as shown in Eq. (26) and (27):[122]

$$H_2S + KI \rightarrow KHS + HI \quad (1.27)$$

$$H_2S + 2KI \rightarrow K_2S + HI \quad (1.28)$$

Impregnation of ACs can reduce their adsorption capacity, as it can lead to blockage of pore entrances, making the micropores inaccessible. Furthermore, the reactivity of alkaline carbons in H_2S oxidation ceases once the alkaline component is depleted and the carbon pores are blocked by sulfur, sodium or potassium salts. Chemical modification of the adsorbent by impregnation or doping also leads to a significant increase in its cost, due to the additional materials and processing required.[116]

However, there is an optimum between the amount of impregnating agent and the intrinsic adsorption capacity of the AC, which is determined experimentally. For most commercial carbons, the optimum point corresponds to an impregnation of around 10 wt.% (see again **Table 1.5**).

Oxidation of H_2S on strongly basic ACs is a rapid reaction, while oxidation on unmodified carbon is kinetically limited.[116] It has been noted that when the H_2S concentration in the inlet gas is low, which ensures the completeness of the reaction occurring at the carbon surface, non-impregnated ACs can exhibit substantial capacities that are comparable to those of alkali-impregnated materials.[102, 116] In the work of Frilund et al.[123] for non-impregnated AC, major kinetic limitations were overcome at an H_2S inlet concentration of 70 ppm for their experiment. This value is well below the H_2S concentration, in the order of thousands of ppm, found in most biogases.[13]

The amount of impregnating agent applied to the AC depends on the chemical reaction that takes place. When the impregnating agent is reactive, its quantity must align stoichiometrically with the number of contaminants targeted for adsorption. In this case, the impregnating agent may occupy a substantial proportion of the pore volume of the AC, thus decreasing its surface area and potentially limiting physical adsorption. Conversely, when the impregnating agent catalyzes a reaction, its quantity may be minimal, provided it is well dispersed on the surface.[102] Thus, to achieve effective H_2S removal, it is essential to strike the right balance between the AC's surface chemistry and its porosity.

H_2S removal on AC is mainly influenced by several key factors, namely oxygen concentration, AC acidity and basicity, water amount in the adsorption process[124] and pore volume, where oxidation products can be stored.[100] The pH of the AC plays an important role in H_2S adsorption, influencing both the overall removal capacity and the composition of oxidation byproducts. Specifically, a low pH environment inhibits H_2S dissociation, favoring the generation of sulfur oxides and sulfuric acid,[11, 116, 125] while elevated pH lead to the

formation of elemental sulfur and polysulfides, resulting in higher removal capacities.[98, 123] It has been reported that pH must be above 5 for effective H_2S removal from the gas phase.[116]

- Experiments from literature

Tables 1.6 and **1.7** provide a list of ACs and waste-derived materials, respectively, documented in the literature for H_2S separation. This list includes sample names and an explanation of their source and nature. Many of these carbons are commercially available, with a suffix in the Tables indicating the compounds used for modification. These Tables also detail the experimental conditions under which H_2S separation capacity was determined, including the breakthrough point (BTP) at which the measurement was made and the composition of the gas used during the experiment. In addition, the surface area of each sorbent is presented.

Table 1.6 Activated carbons used for H_2S separation by dynamic adsorption and their H_2S removal properties.

Sample	BTP, C/C_0 (%)	Gas composition	Impregnating agent	BET area ($m^2 \cdot g^{-1}$)	H_2S adsorption @BTP ($mg \cdot g^{-1}$)	Ref.
Coconut husk AC	30	H_2S 10000 ppm; CH_4 60%; CO_2 40%	Non-impregnated	604	38.7	[126]
Cow dung AC				131	38.2	
Pig manure AC				126	16.5	
Chicken manure AC				24	8.0	
Com. coal-based I-1 - KOH	0.5	H_2S 10000 ppm; Air 74.7%; N_2 24.3%; Moisture	KOH	639	211.0	[106]
Com. coal-based II - KOH				777	200.0	
Com. G55C (Pica)	0.5	H_2S 10000ppm; Air 99%; Moisture	Non-impregnated	950	56.3	[102]
Com. BAX 500				2245	92.9	
Com. S208C				991	54.2	
Com. RB4 (Norit)				1063	72.7	
Com. G55C - NaOH			NaOH 10 wt.%	878	272.2	
Com. BAX 500 - NaOH				1340	321.9	
Com. S208C - NaOH				803	196.4	
Com. RB4 - NaOH				799	200.0	
Com. coconut shell-based S-208	0.5	H_2S 10000ppm; Air 99%; Moisture	-	877	36.0	[100]
Com. STIX			Caustic	779	201.0	
Com. Centaur (NI)				987	176.0	
Com. Midas			-	1110	608.0	
Sewage-sludge-derived SC				98	79.0	
Com. AC (Jacobi) - MgO	0.5	H_2S 10000 ppm; Air 99%; Moisture	MgO nanocomposite 1.2 wt. %	1358	275.0	[114]
Com. AC Effigen Carbon - $ZnAc_2$/ZnO	0.02	H_2S 5000 ppm; N_2 99,5%	$ZnAc_2$/ZnO		1.9	[113]
Com.coal-based IAC - Chemviron	1.25	H_2S 80ppm; N_2 100%; Moisture	Unknown	1120	46.0	[13]

	0.02	Biogas: H_2S 4020ppm; CH_4 42.5%; CO_2 41.1%; O_2 2.2%; H_2O 1.3%			383.0	
Com. S208C coconut shell-based Waterlink Barnebey Sutcliffe	17	H_2S 3000 ppm; Air 99.7%; Moisture	-	880	125.0	[127]
Com. S208C Com. S208C-Fe	16.7	H_2S 3000 ppm; Air 99.7%; Moisture	Non-impregnated Fe 5 wt. %	880 933	48.8 104.5	[120]
Wood based AC Wood based AC - Urea Com. Calgon centaur - urea	16.7	H_2S 3000 ppm; Air 99.7%; Moisture	Non-impregnated Urea Urea	1400 1024 630	298.0 276.0 104.0	[128]
Com. Wood based Westvaco BAX-1500 Com. Wood based Westvaco WVA 1100	16.7	H_2S 3000 ppm; Air 99.7%; Moisture	H_3PO_4 activation	1400 1110	295.0 230.0	[129]
AC - bentonite AC - bentonite - Fe AC - bentonite - Fe - Zn AC - bentonite - Fe - Cu AC - Zn AC - Fe AC - Cu	3.3	H_2S 3000 ppm; Air 99.7%; Moisture	bentonite bentonite-Fe bentonite-Fe-Zn bentonite-Fe-Cu Zn Fe Cu	1554 1290 1460 1410 1470 1430 1470	9.4 9.6 12.5 47.0 30.9 39.6 496.6	[119]
Com. Sigma-aldrich	10	H_2S 2045 ppm; CH_4 65.2 %; CO_2 34.8%; Moisture	-	-	610.0	[9]
Palm shell Palm shell - KOH Palm shell - H_2SO_4 Com. Coconut shell, Damao Chemicals and Chemical Apparatus	5	H_2S 2000 ppm; He 100%	Non-impregnated KOH activation H_2SO_4 activation -	1062 1148 1014 1183	46.0 68.0 76.0 53.0	[105]
Com. AC Norit Anaerobic digestion fiber - AC 750	10	H_2S 2000ppm; CH_4 65%; CO_2 34%; Moisture	- Non-impregnated	372 305	23.1 51.2	[99]
Granular activated carbon	6,7	Biogas: H_2S 1500 ppm; CH_4 57.3±2.0%; CO_2 24.7±3.3%; O_2 1.57±0.29%	-	-	1266.0	[130]
Maize cob waste AC	2,8	Biogas: H_2S:1100-1800 ppm; CH_4: 51%; CO_2 49%; O_2:<1%; H_2:160 ppm; CO 15 ppm; NH_3: 18 ppm	Non-impregnated	820	15.5	[131]
Cattle manure AC	8,3	H_2S 1200 ppm; N_2 99.6%; $O_2 \approx 0.3\%$	Non-impregnated	408	868.5	[132]
Com. wood-based BAX-1520 Com. wood-based BAX-1520 - $ZnFe_2O_4$	10	H_2S 1000 ppm; N_2 100%; Moisture	- $ZnFe_2O_4$ loading at 10 wt. %	2158 1403	5.6 122.5	[111]
Com. wood-based BAX-1500 - Urea Com. wood-based BAX-1500 - Melanine	10	H_2S 1000 ppm; CH_4 60%; CO_2 40%	Urea Melanine	1364 1435	51.6 64.1	[117]

Spent coffee-based AC	10	H_2S 1000 ppm; Air 99.9%; Moisture	$ZnCl_2$ activation	905	127.0	[133]
Com. Desorex K43-BG-K_2CO_3	5	H_2S 1000 ppm; N_2 99.9%	K_2CO_3 5 wt. %	1005	88.0	[108]
Com. Desorex K43-Fe_2O_3			Fe_2O_3	952	28.0	
Com. Desorex K43-NaOH		H_2S 1000 ppm; N_2 99.9%; Moisture	NaOH 10 wt. %	815	156.2 520.4	
Coal-based MgO-ZnO/AC	0,02	H_2S 730ppm; N_2 100%; Moisture H_2S 730ppm; N_2 100%	MgO-ZnO metal oxide loading at 20 wt.%	653	113.4 96.5	[112]
Com. Norit-Cu-Cr	20	H_2S 200 ppm; N_2 100%	Cu-Cr	1599	27.2	[118]
Com. Norit RB1			Non-impregnated	1101	1.7	
Com. AC Airpel Ultra DS			KOH-KI	1042	6.6	
Com. Norit-KOH			KOH	817	20.4	
Com. AC Darco G40 Norit - CuO-ZnO	5	H_2S 100 ppm; N_2 99.75%; O_2 0.25% H_2S 100ppm; N_2 100%; Moisture H_2S 100ppm; N_2 99.75%; O_2 0.25%; Moisture	CuO and ZnO metal oxide loading at 10 wt. %	570	13.1 16.6 25.0	[109]
Com. Desorex K43	10	H_2S 100 ppm; He 100%	-	1003	0.3	[115]
Com. Desorex K43-Na			NaOH	952	2.4	
Com. Desorex K43-Fe			Fe_2O_3	815	8.2	
Com. AC honeycomb - CuO-MgO	5	H_2S 100 ppm; O_2 2500ppm; N_2 100%	CuO-MgO metal oxide loading at 5 wt. %	640	63.1	[110]
Com. AC honeycomb - MgO			MgO metal oxide loading at 5. wt %	670	82.9	
AC	6,3	H_2S 8ppm; He 100%	-	1110	49.8	[107]
AC NaOH			NaOH	1039	57.6	
AC KOH			KOH	1322	56.9	
AC Na_2CO_3			Na_2CO_3	1106	83.9	

BTP: Breakthrough point
Com.: Commercial

The non-activated form of carbon demonstrates lower H_2S separation capacities, underlining the need to develop materials with high microporosity. This is corroborated by the higher surface areas observed in ACs. Commercial AC BAX 500 (Wetsvaco) has the highest surface area at 2245 $m^2.g^{-1}$, which is substantially greater than the highest surface area found in non-AC, represented by Japanese oak biochar at 476 $m^2 \cdot g^{-1}$. Considerable efforts have been made to produce biochar from a variety of sources, including agricultural residues,[134, 138] industrial waste,[137] wastewater by-products,[137] animal manure,[126] and other plant-based materials,[126, 134] for biogas desulfurization purposes. Biochar has also been modified, for example by iron (Fe) loading,[138] or with an impregnation of Na_2CO_3 [9] and spent car oil,[135] to improve H_2S separation. Adsorbent modification increases the amount of H_2S that can be separated compared

with non-modified carbons. For example, in the study by Bagreev and Bandosz,[102] various commercial ACs were impregnated with 10 wt. % NaOH, resulting in a more than threefold increase in the amount of H_2S separated compared with non-modified carbon, such as the commercial AC RB4-Norit, which, after impregnation, saw its performance increase from 72.7 $mg.g^{-1}$ to 200.0 $mg.g^{-1}$.

Table 1.7 Waste-derived materials used for H_2S separation by dynamic adsorption and their H_2S removal properties.

Sample	BTP, C/C_0 (%)	Gas composition	Impregnating agent	BET area ($m^2 \cdot g^{-1}$)	H_2S adsorption @BTP ($mg \cdot g^{-1}$)	Ref.
Coconut husk biochar	30	H_2S 10000ppm; CH_4 60%; CO_2 39%	Non-impregnated	0	30.4	[126]
Cow dung biochar				7	29.8	
Pig manure biochar				7	13.8	
Chicken manure biochar				12	11.0	
Perilla leaf biochar	5	H_2S 3000ppm; CH_4 59.7 %; CO_2 40 %; Moisture	Non-impregnated	473	7.1	[134]
Soybean stover biochar				420	2.5	
Commercial Korean oak biochar				271	0.8	
Japanese oak biochar				476	0.6	
Sewage sludge SC950	16.7	H_2S 3000 ppm; Air 99.7%; Moisture	Non-impregnated	122	82.6	[120]
Sewage sludge-Spent car oil-950	16.7	H_2S 3000 ppm; Air 99.7%; Moisture	Spent car oil	117	115.0	[135]
Anaerobic digestion fiber - T600*60	10	H_2S 2045 ppm; CH_4 65.2 %; CO_2 34.8%; Moisture	Non-impregnated	142	542.0	[9]
Anaerobic digestion fiber - T600*60I			Na_2CO_3 3 wt. %	-	652.0	
Sewage sludge LG 700 PA	10	H_2S 2000 ppm; CH_4 60%; CO_2 39.8%	Non-impregnated	90	8.6	[136]
Metal sludge CT650	10	H_2S 1000 ppm; CO_2 60%; CH_4 39.9%	Non-impregnated	48	20.2	[137]
Sewage sludge CS950			Non-impregnated	113	19.8	
Sewage/metal sludge CST950C			Non-impregnated	105	19.5	
Corn stover biochar-Fe	50	H_2S 1000 ppm; CH_4 59.9%; CO_2 40%	Fe	60	16.8	[138]
$ZnFe_2O_4$-loaded biochar	90	H_2S 300 ppm; N_2 100%	$ZnFe_2O_4$ metal loading	1065	228.3	[139]

BTP: Breakthrough point

Similar experiments comparing non-modified and modified carbons have shown a significant improvement in separation. Bagree et al. demonstrated this with a commercial Fe-loaded carbon,[120] Yang et al. used a commercial wood-based carbon loaded with $ZnFe_2O_4$,[111]

Sisani et al. modified commercial AC Norit RB1 by KOH impregnation and Cu-Cr loading,[118] and Micoli et al. impregnated AC with NaOH, KOH, and Na_2CO_3.[107] Nevertheless, some modifications did not improve sorbent performance. In their study, Nguyen-Thanh and Bandosz[119] mixed AC with bentonite containing 10 wt. % iron, zinc or copper salts. Performance improved only for the AC+bentonite+Fe^{3+}+Cu^{2+} combination, which showed an adsorption capacity of 47.0 $mg \cdot g^{-1}$, compared with 17.3 $mg.g^{-1}$ for non-modified AC. However, for the AC+bentonite+Fe^{3+} and AC+bentonite+Zn^{2+} combinations, H_2S adsorption capacity decreased to 9.6 $mg \cdot g^{-1}$ and 12.5 $mg \cdot g^{-1}$, respectively. The modification led to a decrease in porosity, particularly in micropore volume, caused by the combined effect of mass dilution and the metal adsorption/re-adsorption in small pores. In another study by Adib et al.,[128] modification of AC with urea led to a reduction in H_2S separation capacity, from 298 $mg \cdot g^{-1}$ for unmodified AC to 276 $mg \cdot g^{-1}$. This decrease is due to a reduction in surface area and microporosity.

1.4.2 Zeolites

Zeolites are crystalline aluminosilicates in which silicon and aluminum atoms interconnect by oxygen atoms and form a three-dimensional lattice with a system of micropores or channels.[140] Their properties, including a relatively high surface area, with values of the order of 500 $m^2.g^{-1}$,[141] make certain zeolites effective for H_2S separation. Furthermore, a pore size of about 0.36 nm, corresponding to the kinetic diameter of H_2S, is important. Zeolites 4A (pore size ≈ 0.4 nm) and zeolite 3A (pore size ≈ 0.3 nm)[14] are thus recommended for H_2S separation. Moreover, the presence of numerous cationic active sites, such as K^+, Ca^{2+} and Mg^{2+},[142] enhance their efficiency. In terms of structure (see **Figure 1.8**), they consist primarily of a three-dimensional arrangement of TO_4 tetrahedra, where T represents elements such as Si, Al, P and other tetrahedrally coordinated elements. These units are interconnected by sharing their vertex O atoms, leading to the formation of various structures due to the different bonding methods between these fundamental building blocks.[39] These structures are usually anionic. To maintain electrical neutrality, they contain alkali or alkaline-earth metals as charge-compensating cations. In addition to the type of structure, additional framework elements, porous structure and chemical composition (Si/Al ratio) significantly influence the suitability of a zeolite material for adsorption purposes.

The sorption behavior of fluid components in zeolitic molecular sieves is determined by their mutual interactions, in particular the interactions between fluid and solid. In addition to the van

der Waals-type dispersion forces that occur between all molecules and the solid zeolite, zeolite ion-dipole interactions must be taken into account for H_2O and H_2S, as well as zeolite ion-quadrupole interactions for CO_2.[140] Zeolites have large hollow spaces or "cages" within their structures, enabling them to accommodate big cations such as sodium, potassium, barium and calcium, as well as relatively large molecules and molecular ions, including H_2O, NH_3, carbonate and nitrate ions,[12] which leads to improved adsorption capacities, reactivity and selectivity towards desired analytes.

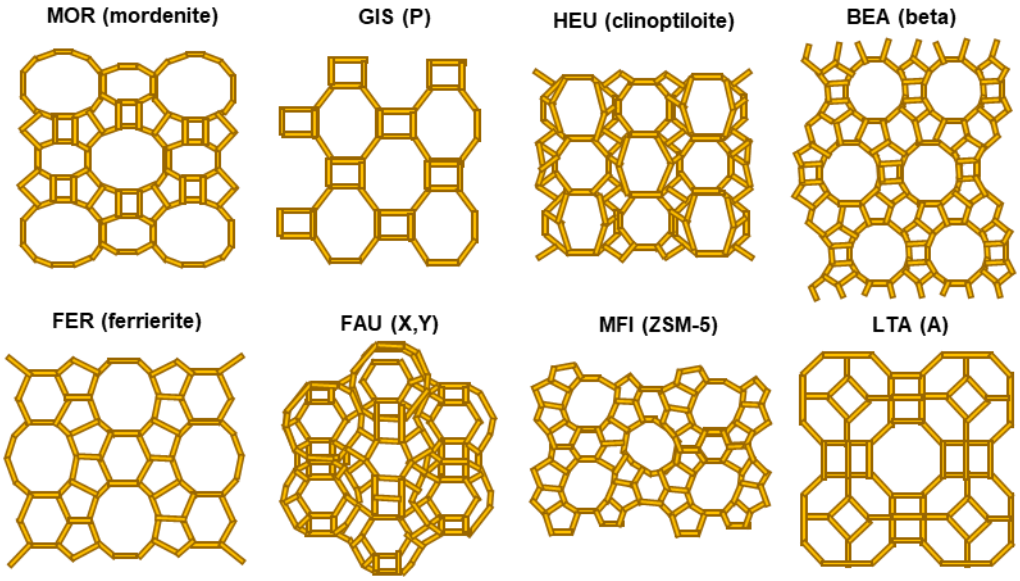

Figure 1.8 Front view of the main pores of selected zeolites. The three-letter codes above each image are the official structure names from the International Zeolite Association, with common names in parentheses.

Natural zeolites, found in volcanogenic sedimentary rocks,[143] contain aluminum and exhibit a notable water affinity, displaying excellent adsorption capacities for polar compounds such as water and water-soluble elements. Thus, the removal of aluminum makes zeolites less attractive to water, improving their ability to adsorb non-polar substances.[12] Although natural zeolites exist, their commercial use is not viable due to their low purity, expensive purification processes and limitations in certain applications. In contrast, synthetic zeolites, manufactured on a pilot scale, can be produced by hydrothermal, alkaline fusion and microwave-assisted methods.[103] However, while there is considerable research into H_2S removal, as shown in **Table 1.8**, no concrete evidence of their use for biogas desulfurization in commercial applications has been found.

The literature available on this topic is more limited than the information available on carbon materials. Most studies have focused on low H_2S concentrations, with only one example

exceeding 1000 ppm,[13] where real biogas was analyzed at an H_2S concentration of 4020 ppm. Additionally, while low H_2S concentrations are common in the literature, only limited attention has been to examining the influence of CO_2 in the gas composition, with only a few examples addressing this factor.[13],[142] Zeolites with pore sizes exceeding 0.36 nm, corresponding to the kinetic diameter of H_2S, are capable of adsorbing H_2S. However, the presence of CO_2 in the biogas, with a kinetic diameter of 0.33 nm, can lead to a reduction in separation efficiency due to competitive adsorption.[103] H_2S separation is similar as in the process using AC, with H_2S molecules first adsorbed onto the zeolite surface and then dissociated to form HS^-,[142] (see Eq. (1) – (3)). Simultaneously, H_2S chemisorption can occur on the sorbent through an acid-base reaction involving the cations present in the zeolite. While Eq. (29) below simplifies this process by considering Na^+ ions, it should be noted that other cations Z such as K^+, Ca^{2+} and Mg^{2+} are viable options, following different mechanisms such as:[142]

$$HS^-_{aq} + H_3O^+_{aq} + NaZ \rightarrow HZ + NaHS + H_2O \quad (1.29)$$

Research also focused on the modification of zeolites, which have been modified with Cu,[107],[142],[145] Zn,[107],[145],[146], Ag,[14],[146] and Mn,[145]. As expected, the modifications led to higher H_2S separation compared to the original zeolite. For instance, in the work of Micoli et al.,[107] zeolite 13X was modified by ion exchange and impregnation methods with Cu and Zn. In all cases, these modifications resulted in an increase in H_2S separation capacity. The most effective modification was achieved by ion exchange with Cu, which resulted in a separation capacity of 39.9 $mg \cdot g^{-1}$, ten times greater than the 3.07 $mg \cdot g^{-1}$ capacity of the original zeolite.

1.4.3 Mesoporous silica

Other sorbents have attracted attention in the literature for their H_2S separation potential. This is the case of mesoporous silica, which represents a distinct category of silica materials with uniform channels featuring large pore sizes, high surface area, high porosity, precise pore size distributions, good mechanical and thermal stability, and a modifiable structure.[147] There are several types of mesoporous silica structures characterized by variations in pore organization. Synthesis under different conditions yields a variety of mesostructures, including hexagonal ordered nano-channels such as MCM-41 [148] and SBA-15,[149–151] cubic 3D structures with interconnected short channels such as MCM-48,[148] and lamellar structures such as MCM-50.[152] The frameworks of mesoporous silica materials have poor affinity for H_2S.

Consequently, their functionalization by incorporation of active/reactive components such as amine modification is required.[153]

Table 1.8 Zeolites used for H_2S separation by dynamic adsorption and their H_2S removal properties.

Sample	BTP, C/C_0 (%)	Gas composition	BET area ($m^2 \cdot g^{-1}$)	H_2S adsorption @BTP ($mg \cdot g^{-1}$)	Ref.
13X	1.3	H_2S 80 ppm; N_2 100%; Moisture	700	105	[13]
	0.02	Biogas; H2S 4020 ppm; CH_4 42.5%; CO_2 41.1%; O_2 2.2%; H_2O 1.3%		76	
Zeolite-Titanium dioxide	10	H_2S 1000 ppm; CH_4 65%; N_2 35%	62	3.4	[144]
	10	H_2S 1000 ppm; CH_4 65%; N_2 35%; Moisture		4.4	
13X Ex-Cu	0.05	H_2S 1000ppm; N_2 99%	239	18.91	[142]
	0.25	H_2S 200ppm; N_2 100%		39.43	
		H_2S 200ppm; CO_2 100%		14.24	
		H_2S 200ppm; CO_2 40%; CH_4 60%		18.17	
		H_2S 200ppm; CH_4 100%		23.4	
Zeolite 4A	10	H_2S 860ppm; N_2 100%	50	7.45	[40]
NaX	10	H_2S 100 ppm; N_2 100%	492	0.9	[145]
CuX			111	13.1	
ZnX			427	23.5	
CoX			-	6.9	
MnX			-	0.9	
NiX			-	0.8	
CaX			-	0.4	
ZnX-0,1M			-	26.0	
Com. 4A	6.7	H_2S 15ppm; N_2 100 %	-	3.2	[14]
NaA nano zeolite			263	14.0	
AgNaA nano zeolite			202	33.2	
Cu-ETS-2	10	H_2S 10ppm; He 100%	250	29.7	[15]
13X	6.3	H_2S 8ppm; He 100%	582	3.07	[107]
13X-Im-Cu			370	6.82	
13X-Im-Zn			356	5.12	
13X-Ex-Cu			575	39.90	
13X-Ex-Zn			585	7.50	

BTP: Breakthrough point

Examples of mesoporous silica used for H_2S adsorption are presented in **Table 1.9**. Experiments with mesoporous silica are also questionable because in the absence of CO_2 in the corresponding H_2S separation studies, which is not representative of research for biogas desulfurization. The results apply more to natural gas desulfurization, where CO_2 levels are significantly lower than in biogas. To improve performance, various chemicals such as amines and metals have been used in conjunction with mesoporous silica. For instance, polyethyleneimine (PEI) supported on mesoporous silica SBA-15 increased its separation capacity from 0.6 $mg \cdot g^{-1}$ to 26.9 $mg \cdot g^{-1}$.[148] Similarly, methyldiethylamine improved separation from 0.3 $mg \cdot g^{-1}$ to 3.7 $mg \cdot g^{-1}$.[149] Metal oxides like ZnO and Fe_2O_3 were also used.

SBA-15 loaded with ZnO achieved a remarkable separation capacity of 436 $mg \cdot g^{-1}$ at an optimum ZnO loading of 3.06 wt. %.[150] Impregnation of SBA-15 with Fe_2O_3 resulted in even higher adsorption of 701 $mg \cdot g^{-1}$,[151] although the optimal metal oxide loading is much higher at 31.3 wt.%. However, the use of very high impregnation levels can be costly for industrial applications.

Table 1.9 Mesoporous silica used for H_2S separation by dynamic adsorption and their H_2S removal properties.

Sample	BTP, C/C_0 (%)	Gas composition	H_2S adsorption @BTP ($mg \cdot g^{-1}$)	Ref.
MSU-1 - CuO	2	H_2S 5000 ppm; CH_4 99.5%	19.4	[154]
MSU-1 - ZnO			42.3	
SBA-15	0.05	H_2S 4000 ppm; H_2 20%; N_2 79.6 %	0.6	[148]
SBA-15 - Polyethyleneimine			26.9	
MCM-48 - Polyethyleneimine			27.6	
MCM-41 - Polyethyleneimine			15.7	
SBA-15 - ZnO	0.01	H_2S 1000ppm; Air 99.9%; Moisture	436.0	[150]
SBA-15 - Fe_2O_3	0.01	H_2S 1000ppm; Air 99.9%; Moisture	701.0	[151]
SBA-15-ZnO/Al	5	H_2S 1000 ppm; Air 99.9%	103.2	[155]
SBA-15	0.5	H_2S 210 ppm; CH_4 100%	0.3	[149]
SBA-15 - Methyldiethylamine			3.7	
3D-ZnO-silica composite	0.2	H_2S 429ppm; N_2 100%; Moisture	135.0	[156]

1.4.4 Metal organic frameworks (MOFs)

MOFs are hybrid materials in which metal ions or small metallic nano-clusters are bound in one, two or three dimensions in the structures by multifunctional organic linkers.[12] These materials have a crystalline structure characterized by exceptionally high porosity, reaching up to 90% free volume. They exhibit large internal surface areas, ranging from 1000 to 10,000 $m^2 \cdot g^{-1}$, combined with remarkable thermal stability (e.g. 300-500 °C).[157] Moreover, these structures present a good level of flexibility.[39] H_2S has the ability to chemisorb on metals through the creation of sulfides. In addition, it can engage with incompletely coordinated metal sites via Lewis acid-base interactions, interact with basic linkers via acid-base interactions, or undergo physisorption via dipolar interactions.[158]

Capturing H_2S using MOFs has proved challenging, primarily due to the development of a strong and sometimes irreversible bond. This bond can break other coordination bonds between metal centers and linkers, leading to breakdown of the MOF structure. Moreover, in humid

conditions, the generation of acidic species can accelerate structural degradation. Specifically, the H_2S/H_2O reaction may give rise to HS^- and H_3O^+ species. Hence, it is important to regulate the interactions governing the binding between MOFs and H_2S. [158]

Some studies on H_2S capture using MOFs draw attention to their structural instability.[159, 160] In general, the possibility of addressing this property lies in the ability to modulate it by altering the nature of the metal sites. MOFs based on Cu, Zn and Fe are commonly used, but they exhibit instability in H_2S adsorption. In contrast, MOFs based on Al, Mg, Ni, V, Zr and Ti are more resistant to H_2S environments. Beyond the aspect of chemical stability, the high cost of MOFs also poses a challenge to their large-scale industrial adoption.[39]

MOFs are not used at the industrial scale for biogas desulfurization, and their application is still limited at the lab-scale. **Table 1.10** summarizes experiments on H_2S removal using MOFs. Notably, these experiments do not involve CO_2 in the feed gas, with the exception of one study using ZIF-8;[161] however, the CO_2 concentration was 7.3%, significantly lower than typical levels found in biogas (see again **Table 1.1**). Additionally, even if it included CH_4, its concentration was 88.8%, much higher than levels typical of biogas. As with zeolites, H_2S adsorption is evaluated without CO_2 competing for adsorption sites. In this scenario, H_2S is mixed with either N_2 or air, ensuring that most of micropores are dedicated solely to H_2S adsorption.

Various MOFs for H_2S removal have been synthesized by methods such as solvothermal synthesis[162],[163] and rapid ultrasonication.[164] Several of these MOFs have undergone structural modifications to improve their properties. For instance, the Cu-based MOF, HKUST-02,[165] initially demonstrated a separation capacity of 56.3 $mg \cdot g^{-1}$ for H_2S and its separation capacity remained almost unchanged at 55.9 $mg \cdot g^{-1}$ after hybridization with graphene oxide (GO). This contrasts with the results of Petit et al.,[166] who demonstrated that a composite of HKUST and graphite oxide significantly increased the separation of H_2S, achieving an adsorption capacity of 199.0 $mg \cdot g^{-1}$, more than double that of the non-composite MOF, which exhibited a capacity of 92.0 $mg \cdot g^{-1}$. Another successful example of a nanocomposite can be found in the work of Daraee et al.,[167] where the MOF UiO-66 initially adsorbed 95.5 $mg \cdot g^{-1}$ of H_2S, but the composite with GO increased its separation capacity to 296.7 $mg \cdot g^{-1}$. Similar positive results were observed using a composite of MOF-5 and GO.[163]

MOFs have also been modified by amine impregnation. For example, MOF-199 was successfully impregnated with triethanolamine, increasing its separation capacity from 56.9

$mg \cdot g^{-1}$ to 93.4 $mg \cdot g^{-1}$. [162] However, the same MOF showed no improvement when impregnated with monoethanolamine and diethanolamine, with separation capacities of 28.3 $mg \cdot g^{-1}$ and 19.8 $mg \cdot g^{-1}$, respectively. The authors concluded that primary and secondary amines could damage the structure of MOF-199 due to strong interactions. In another work, MOF-199 was modified by incorporating 2 wt.% of AC during its synthesis under hydrothermal conditions,[169] which enhanced the final H_2S separation capacity from 55.9 $mg \cdot g^{-1}$ to 84.6 $mg \cdot g^{-1}$. This improvement was attributed to the formation of additional micropores and, in particular, to the increase in the number of unsaturated copper metal sites.

MOFs have shown their potential for industrial applications, in particular for CO_2 capture from industrial emissions and for CO_2/CH_4 separation in biogas upgrading.[171] Commercially available products, such as Svante and novoMOF, illustrate their effectiveness in these areas. However, despite their success in CO_2 capture, MOFs have yet to demonstrate the same level of efficiency in H_2S removal. As H_2S removal involves different chemical interactions and sulfur species, further research is needed to modify and optimize MOFs for this purpose. The advances already presented in this field could lead to the development of new solutions for H_2S removal in various industrial applications.

1.4.5 Metal-based adsorbents

Metal-based adsorbents have been the most widely used for high-temperature desulfurization, thanks to their strong chemical affinity for H_2S. They comprise a wide range of materials derived from oxides of metals such as Zn, Cu, Fe, Mn, Co, Mo, and Ca.[39] The mechanism of H_2S removal by metal oxides involves physisorption on the surface of a solid sorbent or a liquid water film present on it. This is followed by reaction with the active phase to produce sulfides, or interaction with surface oxygen species via a redox reaction, leading to the formation of sulfates or elemental sulfur.[152] The latter mechanism, chemisorption, is the predominant capture mechanism.

Recent research has also focused on H_2S removal at lower operating temperatures. Compared with the high-temperature process, desulfurization at temperatures below 400 °C offers significant cost advantages. In addition, high temperatures can cause sintering of metal oxides, which reduces their activity. However, low temperatures also slow down sulfidation kinetics, reducing the adsorption reaction of H_2S with metal oxides and increasing diffusion resistance.[152] Iron oxide, copper oxide and zinc oxide are the most widely used sorbents for hydrogen sulfide removal at low temperatures.[153]

Table 1.10 MOFs used for H_2S separation by dynamic adsorption and their H_2S removal properties.

Sample	BTP, C/C_0 (%)	Gas composition	BET area ($m^2.g^{-1}$)	H_2S adsorption @ BTP ($mg.g^{-1}$)	Ref.
UiO-66 Uio-66-Graphen oxide	50	H_2S 4500 ppm; N_2 100%	1351 -	95.5 296.7	[167]
HKUST-1-E HKUST-Graphite oxide	10	H_2S 1000ppm; Air 100%; Moisture	301 141	92.0 199.0	[166]
Cu-BTC-Sulfanilic acid modified graphite oxide	5	H_2S 1000 ppm; Air 99.9%	234	133.0	[168]
Cu-BTC-Polystyrene sulfonate modified graphite oxide		H_2S 1000 ppm; Air 99.9%; Moisture	447	241.0	
MOF-199	1	H_2S 515ppm; N_2 %100	1459	56.9	[162]
MOF-199-Amine monoethanolamine			18	28.3	
MOF-199-Amine diethanolamine			4	19.8	
MOF-199-Amine triethanolamine			187	93.4	
MOF-199 MOF-199-Activated carbon	1	H_2S 500 ppm; Air 100%; Moisture	1351 1415	55.9 84.6	[169]
Cu(BDC)0.5(BDC-NH2)0.5	10	H_2S 500ppm; N_2 100%	19.4	128.4	[164]
IRMOF-3	5	H_2S 100 ppm; N_2 99.9%	-	10.6	[170]
MOF-5	1	H_2S 100 ppm; N_2 100%	812	16.7	[163]
MOF-5-Graphene oxide-Glucoso modified			1062	130.1	
HKUST-02	5	H_2S 99.6ppm; N_2 100%	1380	56.3	[165]
HKUST-Polyethyleneimine			38	10.2	
HKUST-Graphene oxide			1096	55.9	
HKUST-Polyethyleneimine-Graphene oxide			489	55.6	

Tables 1.11 and **1.12** show metal-based adsorbents used at room (≈ 25 °C) and high (500 °C) temperatures, respectively. The majority of these adsorbents are iron-based and exhibit high separation capacities, particularly at high temperatures where many achieve separation capacities exceeding 95 $mg \cdot g^{-1}$. It is worth noting that high-temperature desulfurization processes mainly target gases containing H_2 (10%), CO (18%) and CO_2 (5%), as they are designed for coal gas desulfurization.

Cu–Zn–Al metal oxide demonstrated the highest performance, achieving a separation capacity of 257.0 $mg \cdot g^{-1}$.[172] This performance was achieved at 40 °C, above the usual 25 °C for ACs, but well below high-temperature adsorbents. While separation capacity increases with temperature, 40 °C remains in the low-temperature range. The gas used was H_2S with N_2, unlike

the adsorbents listed in **Table 1.12**, which were evaluated with gas mixtures containing additional contaminants that compete for sorption sites. This difference in testing conditions probably explains the superior performance observed.

Table 1.11 Metal-based adsorbents used for H_2S separation by dynamic adsorption and their H_2S removal properties at room temperature (≈ 25 °C).

Sample	BTP, C/C_0 (%)	Gas composition	H_2S adsorption @BTP ($mg \cdot g^{-1}$)	Ref.
Cu–Zn–Al metal oxide[a]	0.003	H_2S 3000ppm; N_2 100%	257.0	[172]
$Fe(OH)_3$	5	H_2S 2000 ppm; H_2O 5%; N_2 95%	103.0	[173]
Com. Fe-based			12.0	
α-FeOOH[a]		Biogas: H_2S 205-350 ppm; CH_4: Not reported; CO_2 45-55%; H_2O 5%; O_2 <1 ppm	49.0	
Fe_2O_3-bentonite	10	H_2S 1200 ppm; N_2 100%	0.9	[174]
Fe-Cu-Al-O[a]	0.01	H_2S 1000 ppm; CO_2 99.9%	96.7	[175]
Cu-Al-O[a]			86.0	
Cu-based (3DOM-SC-43)	0.01	H_2S 500ppm; N_2 100%	147.0	[176]
3DOM γ-Fe_2O_3/SiO_2	0.2	H_2S 500 ppm; N_2 100 %	6.5	[177]
Com. HXT-1 (amorphous hydrated iron oxide)			21.0	
Coral-like Mn_2O_3/Fe_2O_3	80	H_2S 500 ppm; N_2 100%	10.5	[178]

Com: Commercial adsorbent
[a] Temperature of test = 40 °C

Table 1.12 Metal-based adsorbents used for H_2S separation by dynamic adsorption and their H_2S removal properties at high temperatures.

Sample	BTP, C/C_0 (%)	Gas composition	T (°C)	H_2S adsorption @BTP ($mg \cdot g^{-1}$)	Ref.
Fe_2O_3 crystal	Saturation	H_2S 2500 ppm; N_2 100%	500	113.6	[179]
Fe_2O_3 arenaceous clay	20	H_2S 2500 ppm; H_2 39%; CO 27%; CO_2 12%; N_2 22%	500	98.8	[180]
Zn@MnOx porous carbon nanofiber	90	H_2S 1000 ppm; H_2 10%; CO 18%; CO_2 5%; N_2 67%	500	96.3	[181]
Fe-doped Carbon nanofibers	30	H_2S 1000 ppm; H_2 10%; CO 18%; CO_2 5%; N_2 67%	500	72.1	[182]
Si-doped Carbon nanofibers				141.8	
Fe-doped carbon nanofiber	30	H_2S 1000 ppm; H_2 10%; CO 18%; CO_2 5%; N_2 67%	500	38.1	[183]
$Zn_xCo_{3-x}O_4$ Carbon nanofiber	30	H_2S 1000 ppm; H_2 10%; CO 18%; CO_2 5%; N_2 67%	500	124.0	[184]

The highest performance for high-temperature sorbents was achieved by Si-doped carbon nanofibers (Si-CNFs), separating 141.8 $mg \cdot g^{-1}$ of H_2S, which were synthesized through a sequential process involving electrospinning, template method and microwave carbonization. This approach effectively disperses Si nanoparticles through CNFs, a key factor contributing to

its success.[182] Similarly, exceptional performance was observed with $Zn_xCo_{3-x}O_4$ Carbon Nanofibers, fabricated by a combination of electrospinning, in situ hydrothermal growth and carbonization. This adsorbent demonstrated a separation capacity of 124.0 $mg \cdot g^{-1}$ for H_2S.[184]

Alternative techniques for dispersing metal oxides on porous structural supports have also been successfully demonstrated. For example, microwave heating has proved effective, as it improves the O^{2-} content of the sorbents surface,[179] and leads to a better inner structure of the sorbent and a more uniform distribution of the active component with a smaller particle size, facilitating chemical reaction and mass transfer.[180, 182]

As with impregnated ACs, the performance of metal-based adsorbents is highly dependent on the content of active component. In general, performance improves as the active component content increases, up to a certain threshold. Beyond this point, further increases may not improve performance, and can even lead to a decline, due to limitations in the pore structure and mechanical strength of the sorbent. It is therefore essential to determine the optimum content of active components.[179] For metal-based adsorbents, the amount of metal can be higher than that generally used for ACs, where the optimum content is less than or equal to 10 wt.%. For example, in Fe_2O_3 crystals[179] and Fe_2O_3 arenaceous clay,[180] the optimum Fe content has been found to be 30 wt.%.

1.5 Conclusions

Chapter 1 provided an overview of biogas as a clean energy source, its composition, and the necessity of purification for efficient use. Biomethane is expected to play a significant role as a substitute for fossil fuels, with production projected to grow substantially. In Europe alone, production is estimated to rise from 2 billion cubic meters (bcm) in 2018 to 38 bcm by 2030. Among the purification methods, adsorption is a practical and competitive technology, its well-known technique and increasing develop of more optimal adsorbents will make of it a more practical solution for the coming years.

Various sorbents were examined for CO_2 separation, including ACs, MOFs, zeolites, and CMSs. Each material offers distinct advantages depending on adsorption capacity, selectivity, and operational conditions. ACs are valued for their high surface area and tunable properties, while MOFs exhibit structural flexibility and high adsorption capacities. Zeolites with their crystalline structures, along with CMSs provide excellent molecular selectivity due to their controlled pore structures.

The removal of H_2S from biogas was also discussed, highlighting the performance of different sorbents, including ACs, zeolites, MOFs, and metal-based adsorbents. ACs remain a popular choice due to their high affinity for sulfur compounds and adaptability for surface modifications. The reaction mechanisms for H_2S separation indicate that the presence of both H_2O and O_2 positively influences the overall separation efficiency. The most effective ACs for H_2S separation are those impregnated with alkaline substances, a technique employed in all commercial activated carbons for biogas desulfurization.

Overall, this chapter set the foundation for understanding the potential of various adsorbent materials in biogas purification, enclosing the research focus on ACs for CO_2 and H_2S separation. The literature contains extensive experimental research on removing these biogas contaminants using different adsorbents. However, a comprehensive evaluation is necessary to identify the most effective adsorbents and their key preparation procedures for developing higher-performance materials. This evaluation will be presented in Chapter 2.

1.6 References

[1] INTERNATIONAL ENERGY AGENCY. *Key World Energy Statistics 2021*; Statistics; 2021; p 6.

[2] A European Green Deal https://commission.europa.eu/strategy-and-policy/priorities-2019-2024/european-green-deal_en (accessed Dec 13, 2022).

[3] Abdalla, Nabil; Bürck, Silvana; Fehrenbach, Horst; Köpen, Susanne; Staigl, Tim Janosch. *Biomethane in Europe*; Prepared on behalf of the European Climate Foundation; ifeu: Heidelberg, 2022.

[4] Alberici, Sacha; Grimme, Wouter; Toop, Gemma. *Biomethane Production Potentials in the EU - Feasibility of REPowerEU 2030 Targets, Production Potentials in the Member States and Outlook to 2050*; A gas for climate report; Guidehouse, 2022.

[5] Chen, X. Y.; Vinh-Thang, H.; Ramirez, A. A.; Rodrigue, D.; Kaliaguine, S. Membrane Gas Separation Technologies for Biogas Upgrading. *RSC Adv.*, **2015**, *5* (31), 24399–24448. https://doi.org/10.1039/C5RA00666J.

[6] How much energy in biogas Inoplex https://inoplex.com.au/information/how-much-energy-is-in-biogas/ (accessed Dec 13, 2022).

[7] Bahrun, M. H. V.; Bono, A.; Othman, N.; Zaini, M. A. A. Carbon Dioxide Removal from Biogas through Pressure Swing Adsorption – A Review. *Chemical Engineering Research and Design*, **2022**, *183*, 285–306. https://doi.org/10.1016/j.cherd.2022.05.012.

[8] Seo, D.-J.; Gou, Z.; Fujita, H.; Fujii, T.; Sakoda, A. Simple Fabrication of Molecular Sieving Carbon for Biogas Upgrading via a Temperature Controlled Carbonization of Phyllostachys Pubescens. *Renewable Energy*, **2016**, *86*, 693–702. https://doi.org/10.1016/j.renene.2015.09.006.

[9] Pelaez-Samaniego, M. R.; Smith, M. W.; Zhao, Q.; Garcia-Perez, T.; Frear, C.; Garcia-Perez, M. Charcoal from Anaerobically Digested Dairy Fiber for Removal of Hydrogen Sulfide within Biogas. *Waste Management*, **2018**, *76*, 374–382. https://doi.org/10.1016/j.wasman.2018.03.011.

[10] Becker, C. M.; Marder, M.; Junges, E.; Konrad, O. Technologies for Biogas Desulfurization - An Overview of Recent Studies. *Renewable and Sustainable Energy Reviews*, **2022**, *159*, 112205. https://doi.org/10.1016/j.rser.2022.112205.

[11] Sawalha, H.; Maghalseh, M.; Qutaina, J.; Junaidi, K.; Rene, E. R. Removal of Hydrogen Sulfide from Biogas Using Activated Carbon Synthesized from Different Locally Available Biomass Wastes - a Case Study from Palestine. *Bioengineered*, **2020**, *11* (1), 607–618. https://doi.org/10.1080/21655979.2020.1768736.

[12] Peluso, A.; Gargiulo, N.; Aprea, P.; Pepe, F.; Caputo, D. Nanoporous Materials as H_2S Adsorbents for Biogas Purification: A Review. *Separation & Purification Reviews*, **2019**, *48* (1), 78–89. https://doi.org/10.1080/15422119.2018.1476978.

[13] Sigot, L.; Fontseré Obis, M.; Benbelkacem, H.; Germain, P.; Ducom, G. Comparing the Performance of a 13X Zeolite and an Impregnated Activated Carbon for H_2S Removal from Biogas to Fuel an SOFC: Influence of Water. *International Journal of Hydrogen Energy*, **2016**, *41* (41), 18533–18541. https://doi.org/10.1016/j.ijhydene.2016.08.100.

[14] Bahraminia, S.; Anbia, M.; Koohsaryan, E. Hydrogen Sulfide Removal from Biogas Using Ion-Exchanged Nanostructured NaA Zeolite for Fueling Solid Oxide Fuel Cells. *International Journal of Hydrogen Energy*, **2020**, *45* (55), 31027–31040. https://doi.org/10.1016/j.ijhydene.2020.08.091.

[15] Rezaei, S.; Jarligo, M. O. D.; Wu, L.; Kuznicki, S. M. Breakthrough Performances of Metal-Exchanged Nanotitanate ETS-2 Adsorbents for Room Temperature Desulfurization. *Chemical Engineering Science*, **2015**, *123*, 444–449. https://doi.org/10.1016/j.ces.2014.11.041.

[16] Sheng, K.; Chen, X.; Pan, J.; Kloss, R.; Wei, Y.; Ying, Y. Effect of Ammonia and Nitrate on Biogas Production from Food Waste via Anaerobic Digestion. *Biosystems Engineering*, **2013**, *116* (2), 205–212. https://doi.org/10.1016/j.biosystemseng.2013.08.005.

[17] Deublein, Dieter; Steinhauser, Angelika. *Biogas from Waste and Renewable Resources. An Introduction*; WILEY-VCH, 2008.

[18] Nyamukamba, P.; Mukumba, P.; Chikukwa, E. S.; Makaka, G. Biogas Upgrading Approaches with Special Focus on Siloxane Removal—A Review. *Energies*, **2020**, *13* (22), 6088. https://doi.org/10.3390/en13226088.

[19] Wang, X.; Wang, D.; Song, M.; Xin, C.; Zeng, W. Tetraethylenepentamine-Modified Activated Semicoke for CO_2 Capture from Flue Gas. *Energy Fuels*, **2017**, *31* (3), 3055–3061. https://doi.org/10.1021/acs.energyfuels.6b03177.

[20] Irani, M.; Jacobson, A. T.; Gasem, K. A. M.; Fan, M. Modified Carbon Nanotubes/Tetraethylenepentamine for CO_2 Capture. *Fuel*, **2017**, *206*, 10–18. https://doi.org/10.1016/j.fuel.2017.05.087.

[21] Liu, Y.; Lin, X.; Wu, X.; Liu, M.; Shi, R.; Yu, X. Pentaethylenehexamine Loaded SBA-16 for CO_2 Capture from Simulated Flue Gas. *Powder Technology*, **2017**, *318*, 186–192. https://doi.org/10.1016/j.powtec.2017.06.002.

[22] Álvarez-Gutiérrez, N.; Gil, M. V.; Rubiera, F.; Pevida, C. Adsorption Performance Indicators for the CO2/CH4 Separation: Application to Biomass-Based Activated Carbons. *Fuel Processing Technology*, **2016**, *142*, 361–369. https://doi.org/10.1016/j.fuproc.2015.10.038.

[23] Scholwin, Frank; Grope, Johan; Clinskscales, Angela; Bowe, Stephan. Biomethane Production and Grid Injection: German Experiences, Policies, Bsiness Models and Standards., 2020.

[24] Kadam, R.; Panwar, N. L. Recent Advancement in Biogas Enrichment and Its Applications. *Renewable and Sustainable Energy Reviews*, **2017**, *73*, 892–903. https://doi.org/10.1016/j.rser.2017.01.167.

[25] Kabeyi, M. J. B.; Olanrewaju, O. A. Technologies for Biogas to Electricity Conversion. *Energy Reports*, **2022**, *8*, 774–786. https://doi.org/10.1016/j.egyr.2022.11.007.

[26] Khan, M. U.; Lee, J. T. E.; Bashir, M. A.; Dissanayake, P. D.; Ok, Y. S.; Tong, Y. W.; Shariati, M. A.; Wu, S.; Ahring, B. K. Current Status of Biogas Upgrading for Direct Biomethane Use: A Review. *Renewable and Sustainable Energy Reviews*, **2021**, *149*, 111343. https://doi.org/10.1016/j.rser.2021.111343.

[27] Angelidaki, I.; Treu, L.; Tsapekos, P.; Luo, G.; Campanaro, S.; Wenzel, H.; Kougias, P. G. Biogas Upgrading and Utilization: Current Status and Perspectives. *Biotechnology Advances*, **2018**, *36* (2), 452–466. https://doi.org/10.1016/j.biotechadv.2018.01.011.

[28] Sun, Q.; Li, H.; Yan, J.; Liu, L.; Yu, Z.; Yu, X. Selection of Appropriate Biogas Upgrading Technology-a Review of Biogas Cleaning, Upgrading and Utilisation. *Renewable and Sustainable Energy Reviews*, **2015**, *51*, 521–532. https://doi.org/10.1016/j.rser.2015.06.029.

[29] Cavaignac, R. S.; Ferreira, N. L.; Guardani, R. Techno-Economic and Environmental Process Evaluation of Biogas Upgrading via Amine Scrubbing. *Renewable Energy*, **2021**, *171*, 868–880. https://doi.org/10.1016/j.renene.2021.02.097.

[30] Yuan, B.; Wang, J.; Chen, Y.; Wu, X.; Luo, H.; Deng, S. Unprecedented Performance of N-Doped Activated Hydrothermal Carbon towards C_2H_6/CH_4, CO_2/CH_4, and CO_2/H_2 Separation. *J. Mater. Chem. A*, **2016**, *4* (6), 2263–2276. https://doi.org/10.1039/C5TA08436A.

[31] Song, C.; Liu, Q.; Deng, S.; Li, H.; Kitamura, Y. Cryogenic-Based CO2 Capture Technologies: State-of-the-Art Developments and Current Challenges. *Renewable and Sustainable Energy Reviews*, **2019**, *101*, 265–278. https://doi.org/10.1016/j.rser.2018.11.018.

[32] Baena-Moreno, F. M.; le Saché, E.; Pastor-Pérez, L.; Reina, T. R. Membrane-Based Technologies for Biogas Upgrading: A Review. *Environ Chem Lett*, **2020**, *18* (5), 1649–1658. https://doi.org/10.1007/s10311-020-01036-3.

[33] Abd, A. A.; Othman, M. R.; Shabbani, H. J. K.; Helwani, Z. Biomethane Upgrading to Transportation Fuel Quality Using Spent Coffee for Carbon Dioxide Capture in Pressure Swing Adsorption. *Journal of Environmental Chemical Engineering*, **2022**, *10* (2), 107169. https://doi.org/10.1016/j.jece.2022.107169.

[34] Chen, Y.-F.; Lin, P.-W.; Chen, W.-H.; Yen, F.-Y.; Yang, H.-S.; Chou, C.-T. Biogas Upgrading by Pressure Swing Adsorption with Design of Experiments. *Processes*, **2021**, *9* (8), 1325. https://doi.org/10.3390/pr9081325.

[35] Becker, C. M.; Marder, M.; Junges, E.; Konrad, O. Technologies for Biogas Desulfurization - An Overview of Recent Studies. *Renewable and Sustainable Energy Reviews*, **2022**, *159*, 112205. https://doi.org/10.1016/j.rser.2022.112205.

[36] Tansel, B.; Surita, S. C. Managing Siloxanes in Biogas-to-Energy Facilities: Economic Comparison of Pre- vs Post-Combustion Practices. *Waste Management*, **2019**, *96*, 121–127. https://doi.org/10.1016/j.wasman.2019.07.019.

[37] Shen, M.; Zhang, Y.; Hu, D.; Fan, J.; Zeng, G. A Review on Removal of Siloxanes from Biogas: With a Special Focus on Volatile Methylsiloxanes. *Environ Sci Pollut Res*, **2018**, *25* (31), 30847–30862. https://doi.org/10.1007/s11356-018-3000-4.

[38] Knapke, M. Technologies for Hydrogen Sulfide Removal (Selection of a Potential H_2S Removal Technologies), 2022.

[39] Pudi, A.; Rezaei, M.; Signorini, V.; Andersson, M. P.; Baschetti, M. G.; Mansouri, S. S. Hydrogen Sulfide Capture and Removal Technologies: A Comprehensive Review of Recent Developments and Emerging Trends. *Separation and Purification Technology*, **2022**, *298*, 121448. https://doi.org/10.1016/j.seppur.2022.121448.

[40] Liu, X.; Wang, R. Effective Removal of Hydrogen Sulfide Using 4A Molecular Sieve Zeolite Synthesized from Attapulgite. *Journal of Hazardous Materials*, **2017**, *326*, 157–164. https://doi.org/10.1016/j.jhazmat.2016.12.030.

[41] Chan, Y. H.; Lock, S. S. M.; Wong, M. K.; Yiin, C. L.; Loy, A. C. M.; Cheah, K. W.; Chai, S. Y. W.; Li, C.; How, B. S.; Chin, B. L. F.; et al. A State-of-the-Art Review on Capture and Separation of Hazardous Hydrogen Sulfide (H_2S): Recent Advances, Challenges and Outlook. *Environmental Pollution*, **2022**, *314*, 120219. https://doi.org/10.1016/j.envpol.2022.120219.

[42] Aminuddin, M. S.; Bustam, M. A.; Johari, K. Latest Technological Advances and Insights into Capture and Removal of Hydrogen Sulfide: A Critical Review. *RSC Sustain.*, **2024**, 757–803. https://doi.org/10.1039/D3SU00484H.

[43] Okoro, O. V.; Sun, Z. Desulphurisation of Biogas: A Systematic Qualitative and Economic-Based Quantitative Review of Alternative Strategies. *ChemEngineering*, **2019**, *3* (3), 76. https://doi.org/10.3390/chemengineering3030076.

[44] Ramírez-Sáenz, D.; Zarate-Segura, P. B.; Guerrero-Barajas, C.; García-Peña, E. I. H_2S and Volatile Fatty Acids Elimination by Biofiltration: Clean-up Process for Biogas Potential Use. *Journal of Hazardous Materials*, **2009**, *163* (2–3), 1272–1281. https://doi.org/10.1016/j.jhazmat.2008.07.129.

[45] Huynh Nhut, H.; Le Thi Thanh, V.; Tran Le, L. Removal of H_2S in Biogas Using Biotrickling Filter: Recent Development. *Process Safety and Environmental Protection*, **2020**, *144*, 297–309. https://doi.org/10.1016/j.psep.2020.07.011.

[46] Bagreev, A.; Bandosz, T. J. A Role of Sodium Hydroxide in the Process of Hydrogen Sulfide Adsorption/Oxidation on Caustic-Impregnated Activated Carbons. *Ind. Eng. Chem. Res.*, **2002**, *41* (4), 672–679. https://doi.org/10.1021/ie010599r.

[47] Guo, J.; Luo, Y.; Lua, A. C.; Chi, R.; Chen, Y.; Bao, X.; Xiang, S. Adsorption of Hydrogen Sulphide (H2S) by Activated Carbons Derived from Oil-Palm Shell. *Carbon*, **2007**, *45* (2), 330–336. https://doi.org/10.1016/j.carbon.2006.09.016.

[48] Yan, R.; Liang, D. T.; Tsen, L.; Tay, J. H. Kinetics and Mechanisms of H_2S Adsorption by Alkaline Activated Carbon. *Environ. Sci. Technol.*, **2002**, *36* (20), 4460–4466. https://doi.org/10.1021/es0205840.

[49] Sigot, L.; Ducom, G.; Benadda, B.; Labouré, C. Comparison of Adsorbents for H_2S and D4 Removal for Biogas Conversion in a Solid Oxide Fuel Cell. *Environmental Technology*, **2016**, *37* (1), 86–95. https://doi.org/10.1080/09593330.2015.1063707.

[50] Cruz, A. J.; Pires, J.; Carvalho, A. P.; De Carvalho, M. B. Physical Adsorption of H2S Related to the Conservation of Works of Art: The Role of the Pore Structure at Low Relative Pressure. *Adsorption*, **2005**, *11* (5–6), 569–576. https://doi.org/10.1007/s10450-005-5614-3.

[51] Bak, C.; Lim, C.-J.; Kim, Y.-D.; Kim, W.-S. Multi-Stage Adsorptive Purification Process for Improving Desulfurization Performance of Biogas. *Separation and Purification Technology*, **2019**, *227*, 115702. https://doi.org/10.1016/j.seppur.2019.115702.

[52] Gong, H.; Chen, Z.; Fan, Y.; Zhang, M.; Wu, W.; Wang, W. Surface Modification of Activated Carbon for Siloxane Adsorption. *Renewable Energy*, **2015**, *83*, 144–150. https://doi.org/10.1016/j.renene.2015.04.004.

[53] Tran, V. T. L.; Gélin, P.; Ferronato, C.; Mascunan, P.; Rac, V.; Chovelon, J.-M.; Postole, G. Siloxane Adsorption on Activated Carbons: Role of the Surface Chemistry on Sorption Properties in Humid Atmosphere and Regenerability Issues. *Chemical Engineering Journal*, **2019**, *371*, 821–832. https://doi.org/10.1016/j.cej.2019.04.087.

[54] Tran, V. T. L.; Gélin, P.; Ferronato, C.; Chovelon, J.; Fine, L.; Postole, G. Adsorption of Linear and Cyclic Siloxanes on Activated Carbons for Biogas Purification: Sorbents Regenerability. *Chemical Engineering Journal*, **2019**, *378*, 122152. https://doi.org/10.1016/j.cej.2019.122152.

[55] Moseley, P. T.; Rand, D. A. J.; Davidson, A.; Monahov, B. Understanding the Functions of Carbon in the Negative Active-Mass of the Lead–Acid Battery: A Review of Progress. *Journal of Energy Storage*, **2018**, *19*, 272–290. https://doi.org/10.1016/j.est.2018.08.003.

[56] Cosey, W. K.; Balkus, K. J.; Ferraris, J. P.; Musselman, I. H. Reduced Aging in Carbon Molecular Sieve Membranes Derived from PIM-1 and MOP-18. *Ind. Eng. Chem. Res.*, **2021**, *60* (27), 9962–9970. https://doi.org/10.1021/acs.iecr.1c01727.

[57] Vilella, P. C.; Lira, J. A.; Azevedo, D. C. S.; Bastos-Neto, M.; Stefanutti, R. Preparation of Biomass-Based Activated Carbons and Their Evaluation for Biogas Upgrading Purposes. *Industrial Crops and Products*, **2017**, *109*, 134–140. https://doi.org/10.1016/j.indcrop.2017.08.017.

[58] Grande, C. A.; Rodrigues, A. E. Layered Vacuum Pressure-Swing Adsorption for Biogas Upgrading. *Ind. Eng. Chem. Res.*, **2007**, *46* (23), 7844–7848. https://doi.org/10.1021/ie070942d.

[59] Jiang, Y.; Ling, J.; Xiao, P.; He, Y.; Zhao, Q.; Chu, Z.; Liu, Y.; Li, Z.; Webley, P. A. Simultaneous Biogas Purification and CO2 Capture by Vacuum Swing Adsorption Using Zeolite NaUSY. *Chemical Engineering Journal*, **2018**, *334*, 2593–2602. https://doi.org/10.1016/j.cej.2017.11.090.

[60] Ruthven, Douglas M; Farooq, Shamsuzzaman; Knaebel, Kent S. *Pressure Swing Adsorption*; VCH Publishers, Inc, 1994.

[61] Boer, D. G.; Langerak, J.; Pescarmona, P. P. Zeolites as Selective Adsorbents for CO_2 Separation. *ACS Appl. Energy Mater.*, **2023**, *6* (5), 2634–2656. https://doi.org/10.1021/acsaem.2c03605.

[62] Greco, G.; Canevesi, R. L. S.; Di Stasi, C.; Celzard, A.; Fierro, V.; Manyà, J. J. Biomass-Derived Carbons Physically Activated in One or Two Steps for CH4/CO2 Separation. *Renewable Energy*, **2022**, *191*, 122–133. https://doi.org/10.1016/j.renene.2022.04.035.

[63] León, M.; Silva, J.; Carrasco, S.; Barrientos, N. Design, Cost Estimation and Sensitivity Analysis for a Production Process of Activated Carbon from Waste Nutshells by Physical Activation. *Processes*, **2020**, *8* (8), 945. https://doi.org/10.3390/pr8080945.

[64] Peng, P.; Anastasopoulou, A.; Brooks, K.; Furukawa, H.; Bowden, M. E.; Long, J. R.; Autrey, T.; Breunig, H. Cost and Potential of Metal–Organic Frameworks for Hydrogen Back-up Power Supply. *Nat Energy*, **2022**, *7* (5), 448–458. https://doi.org/10.1038/s41560-022-01013-w.

[65] DeSantis, D.; Mason, J. A.; James, B. D.; Houchins, C.; Long, J. R. Techno-Economic Analysis of Metal-Organic Frameworks for Hydro- Gen and Natural Gas Storage. *Energy & Fuels*, **2017**, *31*, 2024–2032. https://doi.org/10.1021/acs.energyfuels.6b02510.

[66] Abd, A. A.; Othman, M. R.; Kim, J. A Review on Application of Activated Carbons for Carbon Dioxide Capture: Present Performance, Preparation, and Surface Modification for Further Improvement. *Environ Sci Pollut Res*, **2021**, *28* (32), 43329–43364. https://doi.org/10.1007/s11356-021-15121-9.

[67] Abdeljaoued, A.; Querejeta, N.; Durán, I.; Álvarez-Gutiérrez, N.; Pevida, C.; Chahbani, M. Preparation and Evaluation of a Coconut Shell-Based Activated Carbon for CO2/CH4 Separation. *Energies*, **2018**, *11* (7), 1748. https://doi.org/10.3390/en11071748.

[68] Vivo-Vilches, J. F.; Pérez-Cadenas, A. F.; Maldonado-Hódar, F. J.; Carrasco-Marín, F.; Faria, R. P. V.; Ribeiro, A. M.; Ferreira, A. F. P.; Rodrigues, A. E. Biogas Upgrading by Selective Adsorption onto CO2 Activated Carbon from Wood Pellets. *Journal of Environmental Chemical Engineering*, **2017**, *5* (2), 1386–1393. https://doi.org/10.1016/j.jece.2017.02.015.

[69] Surra, E.; Ribeiro, R. P. P. L.; Santos, T.; Bernardo, M.; Mota, J. P. B.; Lapa, N.; Esteves, I. A. A. C. Evaluation of Activated Carbons Produced from Maize Cob Waste for Adsorption-Based CO2 Separation and Biogas Upgrading. *Journal of Environmental Chemical Engineering*, **2022**, *10* (1), 107065. https://doi.org/10.1016/j.jece.2021.107065.

[70] Yang, H.; Gong, M.; Chen, Y. Preparation of Activated Carbons and Their Adsorption Properties for Greenhouse Gases: CH4 and CO2. *Journal of Natural Gas Chemistry*, **2011**, *20* (5), 460–464. https://doi.org/10.1016/S1003-9953(10)60232-0.

[71] Munusamy, K.; Somani, R. S.; Bajaj, H. C. Breakthrough Adsorption Studies of Mixed Gases on Mango (Mangifera IndicaL.) Seed Shell Derived Activated Carbon Extrudes. *Journal of Environmental Chemical Engineering*, **2015**, *3* (4), 2750–2759. https://doi.org/10.1016/j.jece.2015.05.010.

[72] Sun, Y.; Webley, P. A. Preparation of Activated Carbons with Large Specific Surface Areas from Biomass Corncob and Their Adsorption Equilibrium for Methane, Carbon Dioxide, Nitrogen, and Hydrogen. *Ind. Eng. Chem. Res.*, **2011**.

[73] Zhang, Y.; Zhang, P.; Yu, W.; Wang, J.; Deng, Q.; Yang, J.; Zeng, Z.; Xu, M.; Deng, S. Facile and Controllable Preparation of Ultramicroporous Biomass-Derived Carbons and

Application on Selective Adsorption of Gas-Mixtures. *Ind. Eng. Chem. Res.*, **2018**, *57* (42), 14191–14201. https://doi.org/10.1021/acs.iecr.8b02139.

[74] Rattanaphan, S.; Rungrotmongkol, T.; Kongsune, P. Biogas Improving by Adsorption of CO2 on Modified Waste Tea Activated Carbon. *Renewable Energy*, **2020**, *145*, 622–631. https://doi.org/10.1016/j.renene.2019.05.104.

[75] Yang, F.; Wang, J.; Liu, L.; Zhang, P.; Yu, W.; Deng, Q.; Zeng, Z.; Deng, S. Synthesis of Porous Carbons with High N Content from Shrimp Shells for Efficient CO2 Capture and Gas Separation.

[76] Ahmadi, R.; Ardjmand, M.; Rashidi, A.; Rafizadeh, M. High Performance Novel Nanoadsorbents Derived - Natural Cellulose Fibers for Superior CO2 Adsorption and CO2 / CH4 Separation. *Energy Sources, Part A: Recovery, Utilization, and Environmental Effects*, **2020**, *0* (0), 1–19. https://doi.org/10.1080/15567036.2020.1845878.

[77] Li, Y.; Xu, R.; Wang, B.; Wei, J.; Wang, L.; Shen, M.; Yang, J. Enhanced N-Doped Porous Carbon Derived from KOH-Activated Waste Wool: A Promising Material for Selective Adsorption of CO2/CH4 and CH4/N2. *Nanomaterials*, **2019**, *9* (2), 266. https://doi.org/10.3390/nano9020266.

[78] Saadi, W.; Rodríguez-Sánchez, S.; Ruiz, B.; Najar-Souissi, S.; Ouederni, A.; Fuente, E. From Pomegranate Peels Waste to One-Step Alkaline Carbonate Activated Carbons. Prospect as Sustainable Adsorbent for the Renewable Energy Production. *Journal of Environmental Chemical Engineering*, **2022**, *10* (1), 107010. https://doi.org/10.1016/j.jece.2021.107010.

[79] Marsh, H.; Rodríguez-Reinoso, F. *Activated Carbon*, 1st ed.; Elsevier: Amsterdam ; Boston, 2006.

[80] Arami-Niya, A.; Rufford, T. E.; Zhu, Z. Nitrogen-Doped Carbon Foams Synthesized from Banana Peel and Zinc Complex Template for Adsorption of CO_2, CH_4, and N_2. *Energy Fuels*, **2016**, *30* (9), 7298–7309. https://doi.org/10.1021/acs.energyfuels.6b00971.

[81] Masruroh, K.; Cahyono, R. B.; Prasetyo, I.; Ariyanto, T. The Effect of Amine Types on Breakthrough Separation of Methane on Biogas. *IJRED*, **2021**, *10* (2), 149–155. https://doi.org/10.14710/ijred.2021.33514.

[82] Prasetyo, I.; Rochmadi, R.; Wahyono, E.; Ariyanto, T. Controlling Synthesis of Polymer-Derived Carbon Molecular Sieve and Its Performance for CO2/CH4 Separation. *EJ*, **2017**, *21* (4), 83–94. https://doi.org/10.4186/ej.2017.21.4.83.

[83] Santos, M. P. S.; Grande, C. A.; Rodrigues, A. E. Pressure Swing Adsorption for Biogas Upgrading. Effect of Recycling Streams in Pressure Swing Adsorption Design. *Ind. Eng. Chem. Res.*, **2011**, *50* (2), 974–985. https://doi.org/10.1021/ie100757u.

[84] Khan, A.; Qyyum, M. A.; Saulat, H.; Ahmad, R.; Peng, X.; Lee, M. Metal–Organic Frameworks for Biogas Upgrading: Recent Advancements, Challenges, and Future Recommendations. *Applied Materials Today*, **2021**, *22*, 100925. https://doi.org/10.1016/j.apmt.2020.100925.

[85] Liang, Z.; Marshall, M.; Chaffee, A. L. CO_2 Adsorption-Based Separation by Metal Organic Framework (Cu-BTC) versus Zeolite (13X). *Energy Fuels*, **2009**, *23* (5), 2785–2789. https://doi.org/10.1021/ef800938e.

[86] Kim, J.; Lee, Y.-R.; Ahn, W.-S. Dry-Gel Conversion Synthesis of Cr-MIL-101 Aided by Grinding: High Surface Area and High Yield Synthesis with Minimum Purification. *Chem. Commun.*, **2013**, *49* (69), 7647. https://doi.org/10.1039/c3cc44559c.

[87] Shen, J.; Wang, X.; Chen, Y. Adsorbents for Adsorption Separation of CO_2 and CH_4: A Literature Review. *Can J Chem Eng*, **2023**, *101* (12), 7115–7133. https://doi.org/10.1002/cjce.24942.

[88] Sharma, H.; Dhir, A. Capture of Carbon Dioxide Using Solid Carbonaceous and Non-Carbonaceous Adsorbents: A Review. *Environ Chem Lett*, **2021**, *19* (2), 851–873. https://doi.org/10.1007/s10311-020-01118-2.

[89] Lin, J.-B.; Nguyen, T. T. T.; Vaidhyanathan, R.; Burner, J.; Taylor, J. M.; Durekova, H.; Akhtar, F.; Mah, R. K.; Ghaffari-Nik, O.; Marx, S.; et al. A Scalable Metal-Organic Framework as a Durable Physisorbent for Carbon Dioxide Capture. *Science*, **2021**, *374* (6574), 1464–1469. https://doi.org/10.1126/science.abi7281.

[90] Fujiki, J.; Kajiro, H.; Takakura, Y.; Yajima, T.; Kawajiri, Y. Breakthrough Analysis for Parameter Estimation of CO2 Adsorption on Pelletized Flexible Metal–Organic Framework. *Chemical Engineering Journal*, **2023**, *460*, 141781. https://doi.org/10.1016/j.cej.2023.141781.

[91] Salles, F.; Jobic, H.; Ghoufi, A.; Llewellyn, P. L.; Serre, C.; Bourrelly, S.; FØrey, Gø.; Maurin, G. Transport Diffusivity of CO2 in the Highly Flexible Metal–Organic Framework MIL-53(Cr)*. *Angew. Chem.*, **2009**.

[92] Ferreira, A. F. P.; Ribeiro, A. M.; Kulaç, S.; Rodrigues, A. E. Methane Purification by Adsorptive Processes on MIL-53(Al). *Chemical Engineering Science*, **2015**, *124*, 79–95. https://doi.org/10.1016/j.ces.2014.06.014.

[93] Palomino, M.; Corma, A.; Rey, F.; Valencia, S. New Insights on CO_2 −Methane Separation Using LTA Zeolites with Different Si/Al Ratios and a First Comparison with MOFs. *Langmuir*, **2010**, *26* (3), 1910–1917. https://doi.org/10.1021/la9026656.

[94] Abd, A. A.; Naji, S. Z.; Hashim, A. S.; Othman, M. R. Carbon Dioxide Removal through Physical Adsorption Using Carbonaceous and Non-Carbonaceous Adsorbents: A Review. *Journal of Environmental Chemical Engineering*, **2020**, *8* (5), 104142. https://doi.org/10.1016/j.jece.2020.104142.

[95] Hou, Y.; Vidu, R.; Stroeve, P. Solar Energy Storage Methods. *Ind. Eng. Chem. Res.*, **2011**, *50* (15), 8954–8964. https://doi.org/10.1021/ie2003413.

[96] Wang, Y.; LeVan, M. D. Adsorption Equilibrium of Binary Mixtures of Carbon Dioxide and Water Vapor on Zeolites 5A and 13X. *J. Chem. Eng. Data*, **2010**, *55* (9), 3189–3195. https://doi.org/10.1021/je100053g.

[97] Georgiadis, A.; Charisiou, N.; Goula, M. Removal of Hydrogen Sulfide From Various Industrial Gases: A Review of The Most Promising Adsorbing Materials. *Catalysts*, **2020**, *10* (5), 521. https://doi.org/10.3390/catal10050521.

[98] Barelli, L.; Bidini, G.; De Arespacochaga, N.; Pérez, L.; Sisani, E. Biogas Use in High Temperature Fuel Cells: Enhancement of KOH-KI Activated Carbon Performance toward H_2S Removal. *International Journal of Hydrogen Energy*, **2017**, *42* (15), 10341–10353. https://doi.org/10.1016/j.ijhydene.2017.02.021.

[99] Ayiania, M.; Carbajal-Gamarra, F. M.; Garcia-Perez, T.; Frear, C.; Suliman, W.; Garcia-Perez, M. Production and Characterization of H_2S and PO_4^{3-} Carbonaceous Adsorbents

from Anaerobic Digested Fibers. *Biomass and Bioenergy*, **2019**, *120*, 339–349. https://doi.org/10.1016/j.biombioe.2018.11.028.

[100] Bagreev, A.; Bandosz, T. J. On the Mechanism of Hydrogen Sulfide Removal from Moist Air on Catalytic Carbonaceous Adsorbents. *Ind. Eng. Chem. Res.*, **2005**, *44* (3), 530–538. https://doi.org/10.1021/ie049277o.

[101] Biniak, S.; Szymański, G.; Siedlewski, J.; Świątkowski, A. The Characterization of Activated Carbons with Oxygen and Nitrogen Surface Groups. *Carbon*, **1997**, *35* (12), 1799–1810. https://doi.org/10.1016/S0008-6223(97)00096-1.

[102] Bagreev, A.; Bandosz, T. J. A Role of Sodium Hydroxide in the Process of Hydrogen Sulfide Adsorption/Oxidation on Caustic-Impregnated Activated Carbons. *Ind. Eng. Chem. Res.*, **2002**, *41* (4), 672–679. https://doi.org/10.1021/ie010599r.

[103] Abdirakhimov, M.; Al-Rashed, M. H.; Wójcik, J. Recent Attempts on the Removal of H_2S from Various Gas Mixtures Using Zeolites and Waste-Based Adsorbents. *Energies*, **2022**, *15* (15), 5391. https://doi.org/10.3390/en15155391.

[104] Zhang, X.; Tang, Y.; Qu, S.; Da, J.; Hao, Z. H_2S-Selective Catalytic Oxidation: Catalysts and Processes. *ACS Catal.*, **2015**, *5* (2), 1053–1067. https://doi.org/10.1021/cs501476p.

[105] Guo, J.; Luo, Y.; Lua, A. C.; Chi, R.; Chen, Y.; Bao, X.; Xiang, S. Adsorption of Hydrogen Sulphide (H_2S) by Activated Carbons Derived from Oil-Palm Shell. *Carbon*, **2007**, *45* (2), 330–336. https://doi.org/10.1016/j.carbon.2006.09.016.

[106] Yan, R.; Liang, D. T.; Tsen, L.; Tay, J. H. Kinetics and Mechanisms of H_2S Adsorption by Alkaline Activated Carbon. *Environ. Sci. Technol.*, **2002**, *36* (20), 4460–4466. https://doi.org/10.1021/es0205840.

[107] Micoli, L.; Bagnasco, G.; Turco, M. H_2S Removal from Biogas for Fuelling MCFCs: New Adsorbing Materials. *International Journal of Hydrogen Energy*, **2014**, *39* (4), 1783–1787. https://doi.org/10.1016/j.ijhydene.2013.10.126.

[108] Castrillon, M. C.; Moura, K. O.; Alves, C. A.; Bastos-Neto, M.; Azevedo, D. C. S.; Hofmann, J.; Möllmer, J.; Einicke, W.-D.; Gläser, R. CO_2 and H_2S Removal from CH_4 - Rich Streams by Adsorption on Activated Carbons Modified with K_2CO_3 , NaOH, or Fe_2O_3. *Energy Fuels*, **2016**, *30* (11), 9596–9604. https://doi.org/10.1021/acs.energyfuels.6b01667.

[109] Erto, A.; Deorsola, F. A.; De Falco, G.; Montagnaro, F.; Balsamo, M. Role of H_2O and O_2 during the Reactive Adsorption of H_2S on CuO-ZnO/Activated Carbon at Low Temperature. *Microporous and Mesoporous Materials*, **2020**, *295*, 109949. https://doi.org/10.1016/j.micromeso.2019.109949.

[110] Cepollaro, E. M.; Caputo, D.; Gargiulo, N.; Deorsola, F. A.; Cimino, S.; Lisi, L. H_2S Catalytic Removal at Low Temperature over Cu- and Mg- Activated Carbon Honeycombs. *Catalysis Today*, **2022**, *390–391*, 221–229. https://doi.org/10.1016/j.cattod.2021.11.027.

[111] Yang, C.; Florent, M.; De Falco, G.; Fan, H.; Bandosz, T. J. $ZnFe_2O_4$/Activated Carbon as a Regenerable Adsorbent for Catalytic Removal of H_2S from Air at Room Temperature. *Chemical Engineering Journal*, **2020**, *394*, 124906. https://doi.org/10.1016/j.cej.2020.124906.

[112] Yang, C.; Wang, Y.; Fan, H.; De Falco, G.; Yang, S.; Shangguan, J.; Bandosz, T. J. Bifunctional ZnO-MgO/Activated Carbon Adsorbents Boost H_2S Room Temperature

Adsorption and Catalytic Oxidation. *Applied Catalysis B: Environmental*, **2020**, *266*, 118674. https://doi.org/10.1016/j.apcatb.2020.118674.

[113] Zulkefli, N. N.; Mathuray Veeran, L. S.; Noor Azam, A. M. I.; Masdar, M. S.; Wan Isahak, W. N. R. Effect of Bimetallic-Activated Carbon Impregnation on Adsorption–Desorption Performance for Hydrogen Sulfide (H_2S) Capture. *Materials*, **2022**, *15* (15), 5409. https://doi.org/10.3390/ma15155409.

[114] Siriwardane, I. W.; Udangawa, R.; De Silva, R. M.; Kumarasinghe, A. R.; Acres, R. G.; Hettiarachchi, A.; Amaratunga, G. A. J.; De Silva, K. M. N. Synthesis and Characterization of Nano Magnesium Oxide Impregnated Granular Activated Carbon Composite for H_2S Removal Applications. *Materials & Design*, **2017**, *136*, 127–136. https://doi.org/10.1016/j.matdes.2017.09.034.

[115] Menezes, R. L. C. B.; Moura, K. O.; De Lucena, S. M. P.; Azevedo, D. C. S.; Bastos-Neto, M. Insights on the Mechanisms of H_2S Retention at Low Concentration on Impregnated Carbons. *Ind. Eng. Chem. Res.*, **2018**, *57* (6), 2248–2257. https://doi.org/10.1021/acs.iecr.7b03402.

[116] Bandosz, T. J. On the Adsorption/Oxidation of Hydrogen Sulfide on Activated Carbons at Ambient Temperatures. *Journal of Colloid and Interface Science*, **2002**, *246* (1), 1–20. https://doi.org/10.1006/jcis.2001.7952.

[117] Seredych, M.; Bandosz, T. J. Desulfurization of Digester Gas on Wood-Based Activated Carbons Modified with Nitrogen: Importance of Surface Chemistry. *Energy Fuels*, **2008**, *22* (2), 850–859. https://doi.org/10.1021/ef700523h.

[118] Sisani, E.; Cinti, G.; Discepoli, G.; Penchini, D.; Desideri, U.; Marmottini, F. Adsorptive Removal of H_2S in Biogas Conditions for High Temperature Fuel Cell Systems. *International Journal of Hydrogen Energy*, **2014**, *39* (36), 21753–21766. https://doi.org/10.1016/j.ijhydene.2014.07.173.

[119] Nguyen-Thanh, D.; Bandosz, T. J. Activated Carbons with Metal Containing Bentonite Binders as Adsorbents of Hydrogen Sulfide. *Carbon*, **2005**, *43* (2), 359–367. https://doi.org/10.1016/j.carbon.2004.09.023.

[120] Bagreev, A.; Bashkova, S.; Locke, D. C.; Bandosz, T. J. Sewage Sludge-Derived Materials as Efficient Adsorbents for Removal of Hydrogen Sulfide. *Environ. Sci. Technol.*, **2001**, *35* (7), 1537–1543. https://doi.org/10.1021/es001678h.

[121] Tsai, J.-H.; Jeng, F.-T.; Chiang, H.-L. Removal of H_2S from Exhaust Gas by Use of Alkaline Activated Carbon. *Adsorption*, **2001**, *7*, 357–366. https://doi.org/10.1023/A:1013142405297.

[122] Sitthikhankaew, R.; Chadwick, D.; Assabumrungrat, S.; Laosiripojana, N. Effect of KI and KOH Impregnations over Activated Carbon on H_2S Adsorption Performance at Low and High Temperatures. *Separation Science and Technology*, **2014**, *49* (3), 354–366. https://doi.org/10.1080/01496395.2013.841240.

[123] Frilund, C.; Hiltunen, I.; Simell, P. Activated Carbons for Syngas Desulfurization: Evaluating Approaches for Enhancing Low-Temperature H_2S Oxidation Rate. *ChemEngineering*, **2021**, *5* (2), 23. https://doi.org/10.3390/chemengineering5020023.

[124] Xiao, Y.; Wang, S.; Wu, D.; Yuan, Q. Experimental and Simulation Study of Hydrogen Sulfide Adsorption on Impregnated Activated Carbon under Anaerobic Conditions.

Journal of Hazardous Materials, **2008**, *153* (3), 1193–1200. https://doi.org/10.1016/j.jhazmat.2007.09.081.

[125] Coppola, G.; Papurello, D. Biogas Cleaning: Activated Carbon Regeneration for H_2S Removal. *Clean Technol.*, **2018**, *1* (1), 40–57. https://doi.org/10.3390/cleantechnol1010004.

[126] Su, L.; Chen, M.; Zhuo, G.; Ji, R.; Wang, S.; Zhang, L.; Zhang, M.; Li, H. Comparison of Biochar Materials Derived from Coconut Husks and Various Types of Livestock Manure, and Their Potential for Use in Removal of H_2S from Biogas. *Sustainability*, **2021**, *13* (11), 6262. https://doi.org/10.3390/su13116262.

[127] Bagreev, A.; Rahman, H.; Bandosz, T. J. Study of H_2S Adsorption and Water Regeneration of Spent Coconut-Based Activated Carbon. *Environ. Sci. Technol.*, **2000**, *34* (21), 4587–4592. https://doi.org/10.1021/es001150c.

[128] Adib, F.; Bagreev, A.; Bandosz, T. J. Adsorption/Oxidation of Hydrogen Sulfide on Nitrogen-Containing Activated Carbons. *Langmuir*, **2000**, *16* (4), 1980–1986. https://doi.org/10.1021/la990926o.

[129] Adib, F.; Bagreev, A.; Bandosz, T. J. Effect of PH and Surface Chemistry on the Mechanism of H_2S Removal by Activated Carbons. *Journal of Colloid and Interface Science*, **1999**, *216*, 360–369. https://doi.org/10.1006/jcis.1999.6335.

[130] Ou, H. W.; Fang, M. L.; Chou, M. S.; Chang, H. Y.; Shiao, T. F. Long-Term Evaluation of Activated Carbon as an Adsorbent for Biogas Desulfurization. *Journal of the Air & Waste Management Association*, **2020**, *70* (6), 641–648. https://doi.org/10.1080/10962247.2020.1754305.

[131] Surra, E.; Costa Nogueira, M.; Bernardo, M.; Lapa, N.; Esteves, I.; Fonseca, I. New Adsorbents from Maize Cob Wastes and Anaerobic Digestate for H_2S Removal from Biogas. *Waste Management*, **2019**, *94*, 136–145. https://doi.org/10.1016/j.wasman.2019.05.048.

[132] Tuerhong, T.; Kuerban, Z. Preparation and Characterization of Cattle Manure-Based Activated Carbon for Hydrogen Sulfide Removal at Room Temperature. *Journal of Environmental Chemical Engineering*, **2022**, *10* (2), 107177. https://doi.org/10.1016/j.jece.2022.107177.

[133] Kante, K.; Nieto-Delgado, C.; Rangel-Mendez, J. R.; Bandosz, T. J. Spent Coffee-Based Activated Carbon: Specific Surface Features and Their Importance for H_2S Separation Process. *Journal of Hazardous Materials*, **2012**, *201–202*, 141–147. https://doi.org/10.1016/j.jhazmat.2011.11.053.

[134] Sethupathi, S.; Zhang, M.; Rajapaksha, A.; Lee, S.; Mohamad Nor, N.; Mohamed, A.; Al-Wabel, M.; Lee, S.; Ok, Y. Biochars as Potential Adsorbers of CH_4, CO_2 and H_2S. *Sustainability*, **2017**, *9* (1), 121. https://doi.org/10.3390/su9010121.

[135] Bagreev, A.; Bandosz, T. J. Efficient Hydrogen Sulfide Adsorbents Obtained by Pyrolysis of Sewage Sludge Derived Fertilizer Modified with Spent Mineral Oil. *Environ. Sci. Technol.*, **2004**, *38* (1), 345–351. https://doi.org/10.1021/es0303438.

[136] Gutiérrez Ortiz, F. J.; Aguilera, P. G.; Ollero, P. Biogas Desulfurization by Adsorption on Thermally Treated Sewage-Sludge. *Separation and Purification Technology*, **2014**, *123*, 200–213. https://doi.org/10.1016/j.seppur.2013.12.025.

[137] Yuan, W.; Bandosz, T. J. Removal of Hydrogen Sulfide from Biogas on Sludge-Derived Adsorbents. *Fuel*, **2007**, *86* (17–18), 2736–2746. https://doi.org/10.1016/j.fuel.2007.03.012.

[138] Choudhury, A.; Lansing, S. Adsorption of Hydrogen Sulfide in Biogas Using a Novel Iron-Impregnated Biochar Scrubbing System. *Journal of Environmental Chemical Engineering*, **2021**, *9* (1), 104837. https://doi.org/10.1016/j.jece.2020.104837.

[139] Yuan, Y.; Huang, L.; Zhang, T. C.; Ouyang, L.; Yuan, S. One-Step Synthesis of $ZnFe_2O_4$-Loaded Biochar Derived from Leftover Rice for High-Performance H_2S Removal. *Separation and Purification Technology*, **2021**, *279*, 119686. https://doi.org/10.1016/j.seppur.2021.119686.

[140] Bülow, M.; Lutz, W.; Suckow, M. The Mutual Transformation of Hydrogen Sulphide and Carbonyl Sulphide and Its Role for Gas Desulphurization Processes with Zeolitic Molecular Sieve Sorbents. In *Studies in Surface Science and Catalysis*; Elsevier, 1999; Vol. 120, pp 301–345. https://doi.org/10.1016/S0167-2991(99)80556-4.

[141] Bareschino, P.; Mancusi, E.; Forgione, A.; Pepe, F. Biogas Purification on Na-X Zeolite: Experimental and Numerical Results. *Chemical Engineering Science*, **2020**, *223*, 115744. https://doi.org/10.1016/j.ces.2020.115744.

[142] Barelli, L.; Bidini, G.; Micoli, L.; Sisani, E.; Turco, M. 13X Ex-Cu Zeolite Performance Characterization towards H_2S Removal for Biogas Use in Molten Carbonate Fuel Cells. *Energy*, **2018**, *160*, 44–53. https://doi.org/10.1016/j.energy.2018.05.057.

[143] Wang, S.; Peng, Y. Natural Zeolites as Effective Adsorbents in Water and Wastewater Treatment. *Chemical Engineering Journal*, **2010**, *156* (1), 11–24. https://doi.org/10.1016/j.cej.2009.10.029.

[144] Liu, C.; Zhang, R.; Wei, S.; Wang, J.; Liu, Y.; Li, M.; Liu, R. Selective Removal of H_2S from Biogas Using a Regenerable Hybrid TiO_2 /Zeolite Composite. *Fuel*, **2015**, *157*, 183–190. https://doi.org/10.1016/j.fuel.2015.05.003.

[145] Long, N. Q.; Vuong, H. T.; Ha, H. K. P.; Kuniawan, W.; Hinode, H.; Baba, T. PREPARATION, CHARACTERIZATION AND H2S ADSORPTIVE REMOVAL OF ION-EXCHANGED ZEOLITE X. *ASEAN Engineering Journal*, **2015**, *5* (1), 4–14. https://doi.org/10.11113/aej.v5.15463.

[146] Chen, X.; Shen, B.; Sun, H.; Zhan, G. Ion-Exchange Modified Zeolites X for Selective Adsorption Desulfurization from Claus Tail Gas: Experimental and Computational Investigations. *Microporous and Mesoporous Materials*, **2018**, *261*, 227–236. https://doi.org/10.1016/j.micromeso.2017.11.014.

[147] Yang, J. H. Hydrogen Sulfide Removal Technology: A Focused Review on Adsorption and Catalytic Oxidation. *Korean J. Chem. Eng.*, **2021**, *38* (4), 674–691. https://doi.org/10.1007/s11814-021-0755-y.

[148] Wang, X.; Ma, X.; Xu, X.; Sun, L.; Song, C. Mesoporous-Molecular-Sieve-Supported Polymer Sorbents for Removing H_2S from Hydrogen Gas Streams. *Top Catal*, **2008**, *49* (1–2), 108–117. https://doi.org/10.1007/s11244-008-9072-5.

[149] Xue, Q.; Liu, Y. Removal of Minor Concentration of H_2S on MDEA-Modified SBA-15 for Gas Purification. *Journal of Industrial and Engineering Chemistry*, **2012**, *18* (1), 169–173. https://doi.org/10.1016/j.jiec.2011.11.005.

[150] Wang, X.; Sun, T.; Yang, J.; Zhao, L.; Jia, J. Low-Temperature H_2S Removal from Gas Streams with SBA-15 Supported ZnO Nanoparticles. *Chemical Engineering Journal*, **2008**, *142* (1), 48–55. https://doi.org/10.1016/j.cej.2007.11.013.

[151] Wang, X.; Jia, J.; Zhao, L.; Sun, T. Mesoporous SBA-15 Supported Iron Oxide: A Potent Catalyst for Hydrogen Sulfide Removal. *Water Air Soil Pollut*, **2008**, *193* (1–4), 247–257. https://doi.org/10.1007/s11270-008-9686-z.

[152] Khabazipour, M.; Anbia, M. Removal of Hydrogen Sulfide from Gas Streams Using Porous Materials: A Review. *Ind. Eng. Chem. Res.*, **2019**, *58* (49), 22133–22164. https://doi.org/10.1021/acs.iecr.9b03800.

[153] Liu, D.; Li, B.; Wu, J.; Liu, Y. Sorbents for Hydrogen Sulfide Capture from Biogas at Low Temperature: A Review. *Environ Chem Lett*, **2020**, *18* (1), 113–128. https://doi.org/10.1007/s10311-019-00925-6.

[154] Montes, D.; Tocuyo, E.; González, E.; Rodríguez, D.; Solano, R.; Atencio, R.; Ramos, M. A.; Moronta, A. Reactive H_2S Chemisorption on Mesoporous Silica Molecular Sieve-Supported CuO or ZnO. *Microporous and Mesoporous Materials*, **2013**, *168*, 111–120. https://doi.org/10.1016/j.micromeso.2012.09.018.

[155] Wang, X.; Jia, J.; Zhao, L.; Sun, T. Chemisorption of Hydrogen Sulphide on Zinc Oxide Modified Aluminum-Substituted SBA-15. *Applied Surface Science*, **2008**, *254* (17), 5445–5451. https://doi.org/10.1016/j.apsusc.2008.02.086.

[156] Wang, L.-J.; Fan, H.-L.; Shangguan, J.; Croiset, E.; Chen, Z.; Wang, H.; Mi, J. Design of a Sorbent to Enhance Reactive Adsorption of Hydrogen Sulfide. *ACS Appl. Mater. Interfaces*, **2014**, *6* (23), 21167–21177. https://doi.org/10.1021/am506077j.

[157] Mouchaham, G.; Wang, S.; Serre, C. The Stability of Metal–Organic Frameworks. In *Metal-Organic Frameworks*; García, H., Navalón, S., Eds.; Wiley, 2018; pp 1–28. https://doi.org/10.1002/9783527809097.ch1.

[158] Georgiadis, A. G.; Charisiou, N.; Yentekakis, I. V.; Goula, M. A. Hydrogen Sulfide (H_2S) Removal via MOFs. *Materials*, **2020**, *13* (16), 3640. https://doi.org/10.3390/ma13163640.

[159] Reljic, S.; Broto-Ribas, A.; Cuadrado-Collados, C.; Jardim, E. O.; Maspoch, D.; Imaz, I.; Silvestre-Albero, J. Structural Deterioration of Well-Faceted MOFs upon H_2S Exposure and Its Effect in the Adsorption Performance. *Chemistry A European J*, **2020**, *26* (71), 17110–17119. https://doi.org/10.1002/chem.202002473.

[160] Feng, L.; Wang, K.-Y.; Day, G. S.; Ryder, M. R.; Zhou, H.-C. Destruction of Metal–Organic Frameworks: Positive and Negative Aspects of Stability and Lability. *Chem. Rev.*, **2020**, *120* (23), 13087–13133. https://doi.org/10.1021/acs.chemrev.0c00722.

[161] Jameh, A. A.; Mohammadi, T.; Bakhtiari, O.; Mahdyarfar, M. Synthesis and Modification of Zeolitic Imidazolate Framework (ZIF-8) Nanoparticles as Highly Efficient Adsorbent for H_2S and CO_2 Removal from Natural Gas. *Journal of Environmental Chemical Engineering*, **2019**, *7* (3), 103058. https://doi.org/10.1016/j.jece.2019.103058.

[162] Zhang, H.-Y.; Yang, C.; Geng, Q.; Fan, H.-L.; Wang, B.-J.; Wu, M.-M.; Tian, Z. Adsorption of Hydrogen Sulfide by Amine-Functionalized Metal Organic Framework (MOF-199): An Experimental and Simulation Study. *Applied Surface Science*, **2019**, *497*, 143815. https://doi.org/10.1016/j.apsusc.2019.143815.

[163] Huang, Z.-H.; Liu, G.; Kang, F. Glucose-Promoted Zn-Based Metal–Organic Framework/Graphene Oxide Composites for Hydrogen Sulfide Removal. *ACS Appl. Mater. Interfaces*, **2012**, *4* (9), 4942–4947. https://doi.org/10.1021/am3013104.

[164] Gupta, N. K.; Kim, S.; Bae, J.; Soo Kim, K. Fabrication of Cu(BDC)0.5(BDC-NH_2)0.5 Metal-Organic Framework for Superior H_2S Removal at Room Temperature. *Chemical Engineering Journal*, **2021**, *411*, 128536. https://doi.org/10.1016/j.cej.2021.128536.

[165] Bhoria, N.; Basina, G.; Pokhrel, J.; Kumar Reddy, K. S.; Anastasiou, S.; Balasubramanian, V. V.; AlWahedi, Y. F.; Karanikolos, G. N. Functionalization Effects on HKUST-1 and HKUST-1/Graphene Oxide Hybrid Adsorbents for Hydrogen Sulfide Removal. *Journal of Hazardous Materials*, **2020**, *394*, 122565. https://doi.org/10.1016/j.jhazmat.2020.122565.

[166] Petit, C.; Mendoza, B.; Bandosz, T. J. Hydrogen Sulfide Adsorption on MOFs and MOF/Graphite Oxide Composites. *ChemPhysChem*, **2010**, *11* (17), 3678–3684. https://doi.org/10.1002/cphc.201000689.

[167] Daraee, M.; Ghasemy, E.; Rashidi, A. Synthesis of Novel and Engineered UiO-66/Graphene Oxide Nanocomposite with Enhanced H_2S Adsorption Capacity. *Journal of Environmental Chemical Engineering*, **2020**, *8* (5), 104351. https://doi.org/10.1016/j.jece.2020.104351.

[168] Ebrahim, A. M.; Jagiello, J.; Bandosz, T. J. Enhanced Reactive Adsorption of H_2S on Cu–BTC/ S- and N-Doped GO Composites. *J. Mater. Chem. A*, **2015**, *3* (15), 8194–8204. https://doi.org/10.1039/C5TA01359C.

[169] Shi, R.-H.; Zhang, Z.-R.; Fan, H.-L.; Zhen, T.; Shangguan, J.; Mi, J. Cu-Based Metal–Organic Framework/Activated Carbon Composites for Sulfur Compounds Removal. *Applied Surface Science*, **2017**, *394*, 394–402. https://doi.org/10.1016/j.apsusc.2016.10.071.

[170] Wang, X.-L.; Fan, H.-L.; Tian, Z.; He, E.-Y.; Li, Y.; Shangguan, J. Adsorptive Removal of Sulfur Compounds Using IRMOF-3 at Ambient Temperature. *Applied Surface Science*, **2014**, *289*, 107–113. https://doi.org/10.1016/j.apsusc.2013.10.115.

[171] Paz, L.; Gentil, S.; Fierro, V.; Celzard, A. Assessing the Performance of Adsorbents for CO_2/CH_4 Separation in Pressure Swing Adsorption Units: A Review. *Journal of Environmental Chemical Engineering*, **2024**, *12* (6), 114870. https://doi.org/10.1016/j.jece.2024.114870.

[172] Jiang, D.; Su, L.; Ma, L.; Yao, N.; Xu, X.; Tang, H.; Li, X. Cu–Zn–Al Mixed Metal Oxides Derived from Hydroxycarbonate Precursors for H2S Removal at Low Temperature. *Applied Surface Science*, **2010**, *256* (10), 3216–3223. https://doi.org/10.1016/j.apsusc.2009.12.008.

[173] Raabe, T. Study on Iron-Based Adsorbents for Alternating Removal of H_2S and O_2 from Natural Gas and Biogas. *Chemical Engineering Journal*, **2019**.

[174] Long, N. Q.; Loc, T. X. Experimental and Modeling Study on Room-Temperature Removal of Hydrogen Sulfide Using a Low-Cost Extruded Fe_2O_3-Based Adsorbent. *Adsorption*, **2016**, *22* (3), 397–408. https://doi.org/10.1007/s10450-016-9790-0.

[175] Liu, D.; Chen, S.; Fei, X.; Huang, C.; Zhang, Y. Regenerable CuO-Based Adsorbents for Low Temperature Desulfurization Application. *Ind. Eng. Chem. Res.*, **2015**, *54* (14), 3556–3562. https://doi.org/10.1021/acs.iecr.5b00180.

[176] Wang, J.; Wang, L.; Fan, H.; Wang, H.; Hu, Y.; Wang, Z. Highly Porous Copper Oxide Sorbent for H_2S Capture at Ambient Temperature. *Fuel*, **2017**, *209*, 329–338. https://doi.org/10.1016/j.fuel.2017.08.003.

[177] Huang, G.; He, E.; Wang, Z.; Fan, H.; Shangguan, J.; Croiset, E.; Chen, Z. Synthesis and Characterization of γ-Fe_2O_3 for H_2S Removal at Low Temperature. *Ind. Eng. Chem. Res.*, **2015**, *54* (34), 8469–8478. https://doi.org/10.1021/acs.iecr.5b01398.

[178] Kim, S.; Gupta, N. K.; Bae, J.; Kim, K. S. Fabrication of Coral-like Mn_2O_3/Fe_2O_3 Nanocomposite for Room Temperature Removal of Hydrogen Sulfide. *Journal of Environmental Chemical Engineering*, **2021**, *9* (3), 105216. https://doi.org/10.1016/j.jece.2021.105216.

[179] Feng, Y.; Wang, J.; Hu, Y.; Lu, J.; Zhang, M.; Mi, J. Microwave Heating Motivated Performance Promotion and Kinetic Study of Iron Oxide Sorbent for Coal Gas Desulfurization. *Fuel*, **2020**, *267*, 117215. https://doi.org/10.1016/j.fuel.2020.117215.

[180] Feng, Y.; Hu, T.; Wu, M.; Shangguan, J.; Fan, H.; Mi, J. Effect of Microwave Irradiation on the Preparation of Iron Oxide/Arenaceous Clay Sorbent for Hot Coal Gas Desulfurization. *Fuel Processing Technology*, **2016**, *148*, 35–42. https://doi.org/10.1016/j.fuproc.2016.01.037.

[181] Feng, Y.; Zhang, M.; Sun, Y.; Cao, C.; Wang, J.; Ge, M.; Cai, W.; Mi, J.; Lai, Y. Porous Carbon Nanofibers Supported Zn@MnO Sorbents with High Dispersion and Loading Content for Hot Coal Gas Desulfurization. *Chemical Engineering Journal*, **2023**, *464*, 142590. https://doi.org/10.1016/j.cej.2023.142590.

[182] Feng, W.; Zhang, M.; Zhang, X.; Mi, J.; Yang, C.; Wang, J.; Feng, Y. Carbon Nanofibers Supported Sorbents with Enhanced Performance via Microwave-Assisted in-Situ Structural Modifications for H2S Removal. *Separation and Purification Technology*, **2024**, *350*, 127883. https://doi.org/10.1016/j.seppur.2024.127883.

[183] Zhang, X.; Ru, Z.; Wang, T.; Feng, W.; Zhang, M.; Wang, J.; Mi, J.; Ge, M.; Feng, Y. Insights to the Microwave Effect in Formation and Performance Promotion of Iron-Based Carbon Nanofibrous Composites for H2S Removal. *Composites Communications*, **2023**, *37*, 101468. https://doi.org/10.1016/j.coco.2022.101468.

[184] Ru, Z.; Zhang, X.; Zhang, M.; Mi, J.; Cao, C.; Yan, Z.; Ge, M.; Liu, H.; Wang, J.; Zhang, W.; et al. Bimetallic-MOF-Derived $Zn_x Co_{3-x} O_4$ /Carbon Nanofiber Composited Sorbents for High-Temperature Coal Gas Desulfurization. *Environ. Sci. Technol.*, **2022**, *56* (23), 17288–17297. https://doi.org/10.1021/acs.est.2c04193.

Chapter 2. Evaluation of adsorbents for CO_2 / CH_4 separation and biogas desulfurization

This chapter is divided into two sections. The first one focuses on the separation of CO_2 and CH_4, examining the implementation of pressure swing adsorption units. This approach is commonly applied when removing CO_2 from biogas, where CO_2 separation typically occurs at the final stage, after all other contaminants have been eliminated, leaving a gaseous mixture of CH_4 and CO_2 to separate. The second section addresses the biogas desulfurization process, comparing adsorbents based on their separation capacities when used in fixed-bed adsorption columns.

2.1 CO_2/CH_4 separation by pressure swing adsorption (PSA) systems

The aim of this section is to identify the most effective adsorbent materials and PSA systems for separating CO_2 from CH_4. Unlike previous studies that focused on comparing the physicochemical properties, CO_2 and CH_4 uptake, and CO_2/CH_4 selectivity of various adsorbents using manometric equipment at laboratory scale,[1, 2] this work examines the performance of selected adsorbents tested in PSA conditions. For that purpose, we consider a fundamental operational parameter in PSA systems, adsorption pressure, which is the pressure at which adsorption occurs in the PSA column containing the adsorbent material. Since operating pressure depends on the specific PSA regeneration method, our investigation centers on two distinct adsorption pressures: 5 bar, which is generally the operating pressure for systems undergoing depressurization to atmospheric levels, and 1 bar, representative of the average operating pressure for systems using depressurization to sub-atmospheric levels.

In the present chapter, we use the pure CO_2 and CH_4 adsorption isotherms to conduct simulations and predict their co-adsorption when mixed by employing the IAST (Ideal Adsorbed Solution Theory) method. Then, the estimated amounts of CO_2 and CH_4 adsorbed from the gas mixture are used to calculate the equilibrium selectivity and PSA working capacity ratio for each adsorption operating pressure. While existing review articles have already explored the performance of PSA systems for CO_2/CH_4 separation under various operating conditions,[3–7] our approach transcends the limitations of reported data. We employ full mass balances considering flow rates for the inlet, outlet, purge and vent stages. This approach allows us to calculate the CH_4 productivity and the expected energy consumption of the PSA. These two factors are indeed key performance indicators (KPIs) often overlooked by researchers who concentrate solely on assessing the final purity and recovery from the PSA. In this chapter, we will demonstrate that considering these two KPIs, it is possible to select the most optimal operating mode in PSA units.

2.1.1 Performance indicators of adsorbents in PSA systems

Several types of PSA cycles with distinct advantages and limitations exist, depending on the specific application and gas separation requirements. Given the potential confusion in the nomenclature of different cycles, such as the Vacuum Swing Adsorption process, commonly referred to as VSA or VPSA, we have used the following nomenclature for PSA cycles in the remainder of this chapter:

- *PSA*: pressure swing adsorption (Skarstrom cycle)
- *VSA*: vacuum swing adsorption (PSA cycle with sub-atmospheric depressurization)
- *EPSA*: PSA with pressure equalization
- *EVSA*: PSA with pressure equalization and sub-atmospheric depressurization

Figure 2.1 illustrates the conventional cycles involved in PSA and the corresponding pressure variations. Specifically, **Figure 2.1a** shows the Skarstrom PSA cycle. In the initial phase, bed 2 is pressurized to the adsorption pressure (P_a) with gas feed (CO_2+CH_4), while bed 1 is blowdown to atmospheric pressure. Subsequently, the high-pressure feed then flows through bed 2, where the most strongly adsorbed component is retained in the bed. A gas stream enriched with the least strongly adsorbed component exits as effluent at a pressure slightly below that of the feed. Most of the effluent stream is withdrawn as the product, and a fraction is used to purge bed 1 at low operating pressure. The subsequent two steps follow an identical sequence, but with the interchange of beds. **Figure 2.1b** also presents the pressure equalization cycle, wherein bed 2 is initially pressurized with gas sourced from the outlet region of bed 1. Following pressure equalization, the two beds are disconnected, and bed 2 undergoes pressurization with feed gas, while bed 1 is vented to complete blowdown. The subsequent phases of the Skarstrom cycle proceed normally, with the exception that during the regeneration phase, bed 2 undergoes partial depressurization by connecting to the previously depressurized bed 1. It should be noted that the pressure equalization step interrupts the feed, and if a continuous feed is required, two additional beds are needed.

In order to select the most suitable adsorbent for PSA operation, several factors are considered, including its gas separation properties under both equilibrium and dynamic conditions, ease of regenerability and operating costs. Two key properties, namely adsorbent selectivity and PSA working capacity ratio, are analyzed in detail as they significantly influence adsorbent efficiency in the PSA process.

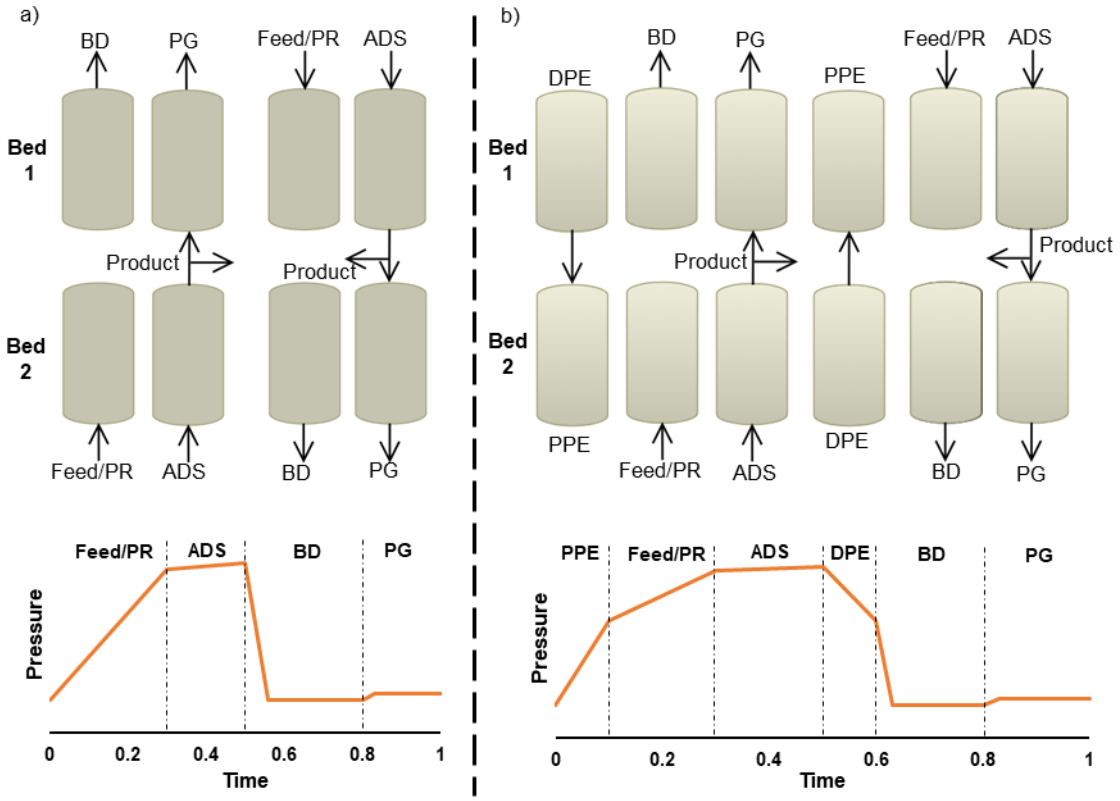

Figure 2.1 Sequence steps for: a) basic Skarstrom PSA cycle; and b) EPSA cycle. *Product/PR*: pressurization with product; *ADS*: adsorption; *BD*: blowdown; *PG*: purge; *Intermediate DP*: intermediate depressurization; *DPE*: Depressurization pressure equalization; *PPE*: pressurization pressure equalization; *IDEL*: standby.

2.1.1.1 Adsorption Selectivity

The adsorption selectivity (*S*) is defined as follows:

$$S = \frac{X_{CO_2}.Y_{CH_4}}{X_{CH_4}.Y_{CO_2}} \tag{2.1}$$

where *X* refers to the molar fraction of a given compound in the adsorbed state, and *Y* is the molar fraction of this compound in the gas phase. The Ideal Adsorption Solution Theory (IAST), introduced by Myers and Prausnitz,[8] is a tool utilized to predict the adsorption behavior of individual components in a gas mixture. IAST relies on three fundamental assumptions that enable a simplified and accurate representation of complex adsorption phenomena:[9] a) thermodynamic inertness of the adsorbent, (b) adsorption of the mixture as an ideal solution under given temperature and pressure conditions, and (c) the equivalence of chemical potential for the adsorbed and gas phases.

For calculations with this model, the system of equations includes the relationships linking the behavior of molecules in the gas state with their behavior when adsorbed. The relationship between the pure component adsorption isotherms and of the so-called reduced spreading pressure is defined as: [10]

$$\frac{\pi A}{RT} = \int_0^{p_i^0} \frac{n_i^0}{p}\, dp \tag{2.2}$$

where π is the spreading pressure, A is the surface area, i represents the molecule under consideration and p_i^0 is the is the saturated vapour pressure exerted by component i in its pure state at the same temperature and spreading pressure of the adsorbed state. [11] The term n_i^0 can be calculated by the appropriate pure component isotherm, in this case the Toth isotherm equation:[8]

$$n_i^0 = n_{i,max}.\frac{b_i.p_i}{[1+(b_i.p)^t]^{\frac{1}{t}}} \tag{2.3}$$

n_i^0 (mol kg^{-1}) and $n_{i,max}$ (mol kg^{-1}) represent the adsorption capacity of the adsorbent at equilibrium pressure and the maximum adsorption capacity when the adsorbent is fully saturated, respectively, and p (Pa) is the equilibrium pressure. The parameters b and t are specific to adsorbate-adsorbent pairs. The Toth model proved its effectiveness in fitting the experimental data within the specified operating range for most of adsorbents. In some cases, the dual-site Langmuir adsorption model was applied for a better fit. Nevertheless, it has been concluded that the IAST predictions are unaffected by the specific equation chosen for fitting the pure gas isotherms. The crucial criterion is a high-quality alignment between the experimental data of single gas and those calculated using the selected model.[12]

The relationship between the mole fractions in the gas phase and in the adsorbed phase is:

$$Y_i.p = X_i.p_i^o \tag{2.4}$$

where Y_i is the mole fraction of component i in the gas phase and X_i is the mole fraction of component i in the adsorbed phase. After solving this system of equations, all the molar fractions within the adsorbed phase are calculated. Using the parameters n_i^0, which are the adsorbed amounts for the pure components for the same pressure range as in the mixture, the total amount adsorbed is determined by:

$$\sum_{i=1}^{k} \frac{X_i}{n_i^0} = \frac{1}{\sum_{i=1}^{k} n_i} \tag{2.5}$$

The system of equations is then solved by Newton's method using 3P Sim software. The IAST multicomponent adsorption approach was applied to analyze experimental data from a range of adsorbents documented in the literature (see **Tables 2.1** and **2.2**).

Table 2.1 Activated carbons for CO_2/CH_4 separation in pressure swing adsorption (PSA) units evaluated at T ≈ 25°C.

Sample / Precursor	**Activation conditions**			**S_{BET} ($m^2 \cdot g^{-1}$)**	**V_{mic} ($cm^3 \cdot g^{-1}$)**	**Amount adsorbed ($mol \cdot kg^{-1}$) for CO_2=35%, CH_4=65%**		**PSA performance parameters for: CO_2=35%, CH_4=65%**		**Ref.**
	Time (min)	T (°C)	Agent			CO_2 - CH_4		CO_2/CH_4 Selectivity – PSA Working capacity ratio		
						P = 5 bar	P = 1 bar	P_{ads} = 5 bar P_{des} = 1 bar	P_{ads} = 1 bar P_{des} = 0.2 bar	
CNS / Coconut shell	73	900	CO_2	1378	0.54	3.0 - 1.7	1.2 - 0.7	3.3 - 1.9	2.9 - 1.6	[13]
W-AC / Coconut shell	120	800	H_3PO_4	-	0.54	-	0.6 - 0.5	-	2.1 - 1.1	[14]
P-AC / Coconut shell	120	600		-	0.68	-	0.7 - 0.0	-	38.5 - 20.6	
PINPEL 20 / Pine wood pellets	300	900	CO_2	-	-	2.0 - 0.8	1.0 - 0.4	4.4 - 2.5	4.2 - 2.3	[15]
CS / Coconut shell	140	900	CO_2	809	0.6	2.8 - 1.4	1.1 - 0.5	3.7 -1.9	4.1 - 2.1	[16]
BC / Babassu coconut				1452	0.32	2.2 - 1.4	0.8 - 0.8	2.9 - 2.4	1.8 - 1.1	
WV1050 / Commercial carbon	-	-	-	1674	0.59	2.6 - 1.0	0.8 - 0.3	4.6 - 2.4	4.6 - 2.4	[17]
CS CO_2 / Cherry stones	120	885	CO_2	1045	0.40	2.5 -	1.1 - 0.5	4.0 - 2.2	3.9 - 2.1	
CS H_2O / Cherry stones		850	H_2O	998	0.38	2.4 - 1.1	1.1 - 0.6	3.6 - 2.1	3.3 - 1.8	
CK-800 / Corncob		800	K_2CO_3	1450	0.62	1.0 - 1.8	0.7 - 0.5	1.1 - 0.7	0.7 - 0.4	[18]
CP-500 / Corncob		500	H_3PO_4	1069	0.10	6.0 - 3.2	0.3 - 0.8	1.5 - 1.3	1.2 - 0.8	

MSS-AC Extrudes / -	-	-	-	1754	0.07	-	1.8 - 0.5	-	6.7 - 1.3	[19]
Organosorb 10-CO / Nut shells	-	-	-	970	0.36	-	1.3 - 0.7	-	2.9 - 1.9	[20]
1S-1 / Wheat straw	-	700	-	882	0.26	1.8 - 0.3	1.1 - 0.2	10.2 - 7.2	8.9 - 5.6	
1S-2 / Wheat straw	-	750	-	760	0.19	1.9 - 0.6	1.1 - 0.4	6.5 - 5.5	5.0 - 3.5	
2S-2 / Wheat straw	-	800	-	998	0.28	2.8 - 0.6	1.5 - 0.4	8.4 - 5.4	7.4 - 4.1	[21]
2S-3 / Wheat straw	-	800	-	957	0.26	5.0 - 0.7	3.5 - 0.8	13.4 -	8.6 - 7.0	
OTS-1-550 / Oil tea shell	-	-	KOH	741	0.25	-	2.8 - 1.1	-	8.5 - 5.4	
OTS-2-650 / Oil tea shell	-	-		1377	0.47	-	4.0 - 1.7	-	4.0 - 2.1	[22]
MCW(PA)3 h / Maize cob waste	180	-	CO_2	820	0.32	2.2 - 1.3	0.9 - 0.6	3.1 - 1.9	2.7 - 1.5	[23]
PS-2-450 / Palm sheath	-	450	NaNH_2	1089	0.42	-	-	-	-	
PS-1-550 / Palm sheath	-	550		892	0.38	-	2.0 - 0.6	-	6.9 - 3.3	[24]
SA-1-700 / Shrimp shell	-	700	KOH	1405	0.60	-	1.8 - 0.7	-	4.6 - 2.5	[25]
WAPC / Waste wool	-	-	KOH	1352	-	-	1.3 - 0.2	-	10.3 - 8.0	
N-WAPC / Waste wool	-	-	KOH and urea	862	-	-	1.4 - 0.4	-	6.4 - 3.6	[26]
J-AC / Cotton pulp, kenaf, and jute as natural cellulose fibers	-	-	KOH and HCl	1731	0.34	4.7 - 3.2	1.7 - 1.6	2.8 - 2.0	2.0 - 1.1	
K-AC / Cotton pulp, kenaf, and jute as natural cellulose fibers	-	-		1978	0.23	4.4 - 3.2	1.5 - 1.6	2.5 - 1.8	1.7 - 1.0	[9]
NAHA 0.5 / -	-	-	Hydro-	747	0.23	4.6 - 0.8	3.0 - 0.6	10.8 - 7.4	9.7 - 4.7	[27]

NAHA 4 / -	-	-	thermal	1538	0.57	5.6 - 1.0	2.8 - 0.6	10.9 - 6.9	9.6 - 4.3	
CBF-1273-CO2-1h / Banana peels	60	1273	Zinc - CO_2	1426	0.56	3.0 - 0.9	6.0 - 3.0	1.4 - 0.4	6.5 - 3.3	[28]
PP-A850C1 / Pomegranate fruit		850	K_2CO_3	1542	0.23	10.2 - 3.8	5.5 - 2.9	5.0 - 5.4	3.5 - 2.0	[29]

2.1.1.2 PSA Working capacity ratio

The PSA working capacity ratio,[35, 42] represents the ratio of the amount of gas that can be adsorbed and desorbed during a single adsorption-desorption cycle under specific adsorption and desorption operating pressures at a given temperature. For the gas analyzed, comprising CO_2 and CH_4 at given contents (e.g., 35% CO_2 and 65 % CH_4), the mixture adsorption isotherms must be known to determine the amounts adsorbed at each operating pressure, as expressed by the following equation:

$$PSA\ working\ capacity\ ratio = \frac{CO_2\ adsorbed\ @\ P_a - CO_2\ adsorbed\ @\ P_d}{CH_4\ adsorbed\ @\ P_a - CH_4\ adsorbed\ @\ P_d} \quad (2.6)$$

where P_a is the adsorption pressure and P_d the desorption pressure of the PSA cycle. The working capacity ratio and selectivity of adsorbents are common criteria that determine the capital and operating costs of the biogas upgrading process. For instance, a high adsorption working capacity ratio can reduce the amount of adsorbent required by the PSA system.[43]

Adsorption pressure depends on the cycle applied during the process. VSA cycles generally operate at P_a between 1 and 2 bar, with regeneration taking place under vacuum. On the other hand, for PSA cycle or any other cycle with regeneration at atmospheric pressure, P_a is generally between 3 and 7 bar. In order to evaluate the cases for regeneration at atmospheric and sub-atmospheric pressure, two hypothetical scenarios were examined: (1) a PSA cycle with P_a = 5 bar and P_d = 1 bar, and (2) a VSA cycle with P_a = 1 bar and P_d = 0.2 bar. For the VSA cycle, pure component isotherms from the literature reporting pressures up to 1 bar were analyzed, while experimental isotherms at higher pressures were studied for both VSA and PSA cycles. Both scenarios were run at an operating temperature of approximately 25 °C. The results are presented in **Figure 2.2**.

Table 2.2 Carbon molecular sieves (CMS), metal organic frameworks (MOFs) and zeolites for CO_2/CH_4 separation in PSA units evaluated at T ≈ 25°C.

Adsorbent	**Sample**	**Amount adsorbed (mol·kg^{-1}) for: CO_2=35%, CH_4=65%** CO_2 - CH_4		**PSA performance parameters for: CO_2=35%, CH_4=65%** CO_2/CH_4 Selectivity – PSA Working capacity ratio		**Ref.**
		P=5 bar	P=1 bar	P_{ads}=5 bar P_{des}=1 bar	P_{ads}=1 bar P_{des}=0.2 bar	
CMS	PKS-carbon-800	-	0.9 - 0.5	-	3.4 - 1.7	[30]
	CMS 3K	1.6 - 0.7	0.8 - 0.3	6.4 - 4.1	5.6 - 2.9	[31]
	CMS KP 407	1.9 - 0.6	1.1 - 0.4	5.9 - 3.4	5.5 - 2.9	[32]
	CMS-FB	1.6 - 0.5	0.8 - 0.3	6.4 - 4.1	5.6 - 2.9	[33]
MOF	Cu-BTC	6.2 - 1.0	2.0 - 0.5	11.8 - 9.0	7.3 - 4.8	[34]
	MOF-5	-	0.3 - 0.1	-	11.6 - 10.5	[35]
	Cu-MOF extrudates	5.5 - 0.9	2.1 - 0.4	10.9 - 5.8	11.1 - 5.9	[36]
	ZIF-L	-	0.6 - 0.0	-	37.7 - 22.4	[37]
	ZrMOF NH_4	2.7 - 0.8	1.0 - 0.3	6.2 - 3.3	6.3 - 3.3	[38]
Zeolite	Zeolite NaX	-	3.2 - 0.1	-	75.9 - 147.2	[39]
	Zeolite CaX	-	2.3 - 0.1	-	45.5 - 109.0	
	Zeolite NaA	-	1.7 - 0.1	-	37.3 - 14.7	
	Zeolite CaA	-	2.3 - 0.0	-	145.8 -	
	Zeolite ZSM-5	-	0.7 - 0.4	-	3.6 - 2.0	
	Zeolite Y	-	0.5 - 0.3	-	3.4 - 1.7	
	Zeolite APGi	-	3.2 - 0.1	-	80.0 - 25.8	[40]
	Zeolite NaUSY	-	2.6 - 0.1	-	50.3 - 30.6	
	Z10-04	4.9 - 0.3	3.9 - 0.1	35.5 - 6.0	81.5 - 21.7	[41]

The adsorption isotherms for the binary gas mixture (e.g. 35% CO_2 and 65 % CH_4) are lower than those for the pure components, indicating a significant impact of the gas mixture on adsorption performance. This is primarily due to the reduction in partial pressures of the individual components upon mixing. The presence of CO_2, which has a high adsorption propensity, leads to a significant decrease in the adsorption of CH_4, which is relatively poorly adsorbed.[12]

Clearly, zeolites perform the best under both atmospheric and sub-atmospheric depressurization conditions. Zeolites with precisely determined micropores[44] are much more selective than carbonaceous adsorbents. Moreover, zeolites generate an electrostatic force that enhances CO_2 capture.[20] Although N-doped ACs provide a considerable improvement over other ACs, such as N-WAPC,[45] which is the second best-performing AC, they are still far from

competitive with zeolites. P-AC[14] is the AC that appears to be highly effective and relatively competitive with zeolites. This AC was derived from coconut shells and subjected to chemical activation by impregnation with a phosphoric acid solution. It was then carbonized at a temperature of 600 °C, resulting in a BET area of 1922 $m^2 \cdot g^{-1}$ and a micropore volume of 0.68 $cm^3 \cdot g^{-1}$, which are exceptional characteristics that make it a promising candidate. Surprisingly, despite its impressive performance, to the best of our knowledge, there are no studies exploring its potential as an innovative adsorbent for CO_2/CH_4 separation.

Zeolites exhibit the highest performance among materials; however, their high heat of adsorption poses a challenge for regeneration, requiring very low sub-atmospheric pressure and increased energy consumption. This drawback of zeolites may create an opportunity for MOFs, which exhibit superior performance compared with ACs and CMSs. The heat of adsorption for CO_2 in MOFs has been reported at -30 $kJ \cdot mol^{-1}$,[34] a value similar to that observed for ACs, of around -28 $kJ \cdot mol^{-1}$,[15] and is significantly lower in absolute values than that observed in zeolites, which can vary between -42 and -63 $kJ \cdot mol^{-1}$.[39] Although CMSs have low selectivity, comparable to that of ACs, their driving force for CO_2/CH_4 separation arises not only from adsorption equilibrium but also from adsorption kinetics. Therefore, their performance in adsorption columns is enhanced and competitive, as will be demonstrated in the next section.

The data also indicate that lower working pressures result in much higher selectivity and working capacity. This is because, at low pressures, the adsorbent material generally has a large number of unoccupied adsorption sites. As the pressure increases, more and more sites become occupied, and the availability of unoccupied sites decreases. This leads to a lower adsorption rate as pressure increases. Consequently, the PSA process would work best at a P_a of around 1 to 2 bar and, due to regeneration requirements, and optimum desorption conditions for this process would require sub-atmospheric pressure.

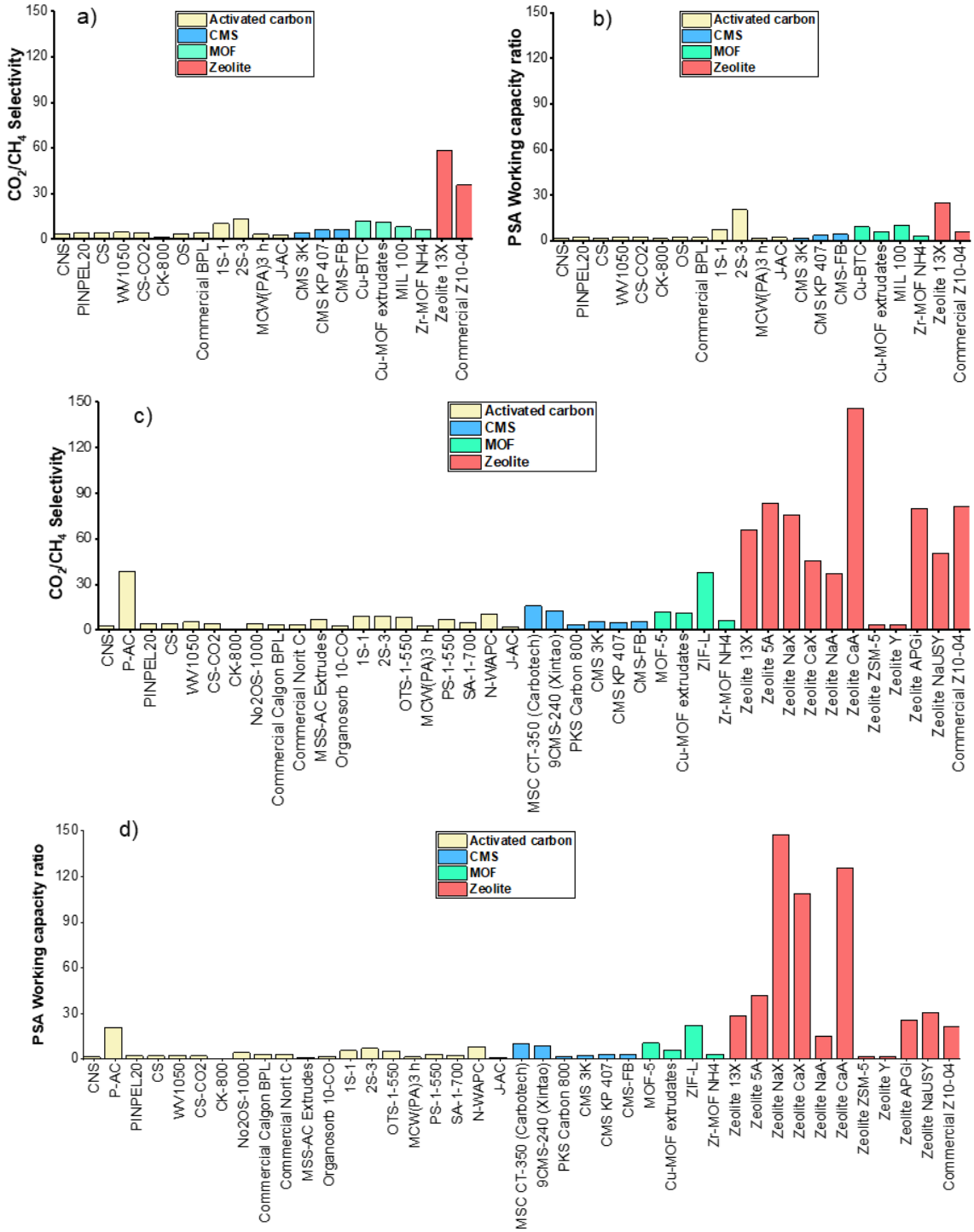

Figure 2.2 Comparison of CO_2/CH_4 equilibrium selectivity and PSA working capacity ratio for various adsorbents at a gas composition of CO_2 = vol. 35% and CH_4 = vol. 65%. a) Selectivity at 5 bar, b) PSA working capacity ratio at: P_a = 5 bar, P_d = 1bar. c) Selectivity at 1 bar, d) PSA working capacity ratio at: P_a =1 bar, P_d = 0.2bar**.**

CNS [13], P-AC [14], PINPEL20 [15], CS [46], Commercial WV1050 [46], CS-CO2 [12], CK-800 [47], OS [48], No2OS-1000 [49], Commercial calgon BPL [49], Commercial Norit C [49], MSS-AC Extrudates [19], Organosorb 10-CO [20], 1S-1 [50], 2S-3 [50], OTS-1-550 [51], MCW(PA)3h [52], PS-1-550 [24], SA-1-700 [25], N-WAPC [45], J-AC [9], MSC CT-350(Carbotech) [20], CMS-240(Xintao) [20], PKS Carbon 800 [30], CMS-3K [31], CMS KP 407 [32], CMS-FB [33], MOF-5 [35], Cu-BTC [34], Cu-MOF extrudates [36], MIL100 [53], ZIF-L [37], Zr-MOF NH4 [38], Zeolite 13X [34], Zeolite 5A [35], Zeolite NaX [39], Zeolite CaX [39], Zeolite NaA [39], Zeolite CaA [39], Commercial Z10-04 [54]. Note that zeolites NaX and 13X are the same, as are zeolites 5A and CaA, but we have left the original names as given in the bibliographical sources, these sources giving slightly different results, as shown in the graphs.

2.1.2 Parameters for PSA performance evaluation

Most studies on PSA units primarily focus on final purity and recovery, while little attention is paid to productivity and energy consumption. While ensuring that the separated gas meets the required purity specifications is essential, it is equally important to consider the overall efficiency of the process. The productivity and energy consumption of a PSA unit can significantly impact its economic feasibility and sustainability. Therefore, to ensure that PSA units are both cost-effective and environmentally friendly, it is crucial to optimize parameters such as productivity and energy consumption, in addition to purity and recovery. To this end, it is useful to examine the purity-recovery-productivity and purity-recovery-energy consumption curves when comparing different process cycles and adsorbents. These parameters can be obtained or calculated using the information provided in each paper from the literature, using the following equations:

Purity: $$CH_4\ Purity\ (\%) = \frac{CH_4\ recovered\ in\ the\ raffinate}{Total\ amount\ of\ the\ produced\ raffinate} \times 100 \quad (2.7)$$

Recovery: $$CH_4\ Recovery\ (\%) = \frac{CH_4\ recovered\ in\ the\ raffinate}{Total\ amount\ of\ gas\ feeding\ the\ system} \times 100 \quad (2.8)$$

Productivity: $$Productivity = \frac{CH_4\ recovered\ in\ the\ raffinate}{Amount\ of\ adsorbent * Cycle\ time} \quad (2.9)$$

Energy consumption: Most energy consumption in PSA separation processes takes place during the compression stage and blowdown, particularly in the blower (compressor) and vacuum pump. The work needed for adiabatic gas compression from suction pressure, P_1, to discharge pressure, P_2, can be calculated using the following equation:[54–56]

$$W_s = \dot{n}.R.T.\left(\frac{k}{k-1}\right).\left(\left(\frac{P_2}{P_1}\right)^{\frac{k-1}{k}} - 1\right).\left(\frac{1}{\eta}\right) \quad (2.10)$$

where $\dot{n}$ is the molar flow rate ($mol \cdot s^{-1}$), R is the universal gas constant ($J \cdot K^{-1} \cdot mol^{-1}$), T is the temperature of the gas (K), k is the heat capacity ratio ($C_p/C_v \approx 1.3$) of the gas mix, and η represents the mechanical efficiency, which is assumed to be 0.8.[55, 57]

2.1.3 Simulation of PSA systems

Effective modelling and simulation of PSA systems is important for optimizing performance and scaling up industrial applications. This involves a dynamic mathematical model that

includes the interaction between fluid flow and mass transfer processes. The simulation repeatedly solves the governing equations using numerical integration to determine the time-dependent behaviour of the variables. The governing equations include: mass balance, energy balance and momentum balance equations, moreover the adsorption onto the adsorbent is described by the adsorption isotherms and kinetics.

Table 2.3 summarizes the mathematical models implemented for the simulation of PSA units for CO_2/CH_4 separation to produce high-purity methane. All of them apply the axially dispersed plug flow (ADPF) model to describe the fluid flow as presented in Eq. 11.[44]

$$-D_L \frac{\partial^2 c_i}{\partial Z^2} + \frac{\partial}{\partial Z}(v c_i) + \frac{\partial c_i}{\partial t} + \frac{1-\varepsilon}{\varepsilon}\frac{\partial \bar{q}_i}{\partial t} = 0 \qquad (2.11)$$

where D_L is the axial dispersion coefficient, c_i is the concentration of the component *i* in the gas phase, *Z* is the axial position along the column, *v* is the gas superficial velocity, *t* is the time, ε is the bed porosity and $\bar{q}_i$ is the average concentration of adsorbed component *i*. The use of the ADPF model accounts for convective flow and axial dispersion, which is more realistic than the plug flow model. Although in small-scale lab systems, the axial dispersion of the flow can be neglected, when numerically solving the system of partial differential equations, it is easier to use the ADPF model as the inclusion of the axial dispersion term eliminates discontinuities in the slope of the concentration profile.[44] The ADPF model does not take radial variations into account, resulting in a 1-dimensional model, which also facilitates its numerical solution.[58]

Table 2.3 Summary of dynamic models for CO_2/CH_4 separation through PSA systems.

System-Adsorbent	Cycle steps	Flow pattern	Isotherm	Mass transfer kinetics	Gas behaviour	Heat effects	Solver	Ref.
2bed - Silicalite	1. Feed/PR - 2. ADS - 3. BD - 4.PG	ADPF	MLM	LDF	Ideal	LTE	PDECOL software using orthogonal collocation on finite elements	[59]
2bed - Zeolite 13X	1. Feed/PR - 2. ADS - 3. DPE - 4. BD - 5. PG - 6. PPE	ADPF	MLM	LDF	Ideal	No LTE	gPROMS software using centered finite difference of second order over a grid of 250 intervals	[55]
4bed - MOF MIL 53	1. Product/PR - 2. ADS - 3. Rinse -	ADPF	MLM	LDF	Ideal	No LTE	gPROMS software using orthogonal collocation on finite elements with second	[60]

	4. BD - 5. PG						order polynomials and 50 intervals	
2bed - Zeolite SAPO 34	1. Feed/PR - 2. ADS - 3. DPE - 4. BD - 5. PG - 6. PPE	ADPF	MLM	LDF	Ideal	LTE	Orthogonal collocation and method of lines	[61]
1bed - Zeolite and CMS	1. Feed/PR - 2. ADS - 3. BD - 4.PG	-	MLM	LDF	-	No LTE	Aspen Adsorption TM version 10	[62]
1bed - Activated carbon	-	ADPF	MLM	LDF	BWR correlation	LTE	gPROMS software using centered finite difference of second order over a grid of 400 intervals	[63]
4bed - Zeolite 13X and CMS 3K	1. Product/PR - 2. Product and production - 3. ADS - 4. ADS - 5. ADS - 6. DPE - 7. BD - 8. PG - 9. PPE	ADPF	MLM	LDF	Ideal	No LTE	gPROMS software using centered finite difference over a grid of 200 intervals	[64]
1bed - Zeolite 13X + CMS 3K	1. Feed/PR - 2. ADS - 3. BD - 4.PG	ADPF	MLM	LDF	-	No LTE	gPROMS software using orthogonal collocation on finite elements	[65]
2bed - Uio66 MOF	1. Feed/PR - 2. ADS - 3. BD - 4.PG	ADPF	MLM	LDF	Ideal	No LTE	Aspen Adsorption using as finite difference method, the upwind differencing scheme with 20 nodes	[66]

In all simulation studies, the multisite Langmuir model (MLM), presented in Eq. 12, which is the simplest model for describing multicomponent adsorption,[8] has been used to predict the mixture isotherm. This model is preferred to the IAST equations as it offers explicit expressions for the adsorbed phase concentrations, thus eliminating the need for iteration during simulation. In contrast, the more accurate IAST equations are implicit and require an iterative subroutine to determine the composition of the adsorbed phase at equilibrium, which increases computation time.

$$\frac{q_i}{q_{si}} = \frac{1 + b_i P_i}{1 + b_i P_i + b_j P_j} \tag{2.12}$$

where q_i is the amount of component i adsorbed per unit mass of adsorbent, q_{si} is the saturation capacity of the adsorbent for component i, b_i is the Langmuir adsorption equilibrium constant and P_i is the partial pressure of the component i in the gas phase. Additionally, if the MLM does not fit well, as can occur at CO_2 concentrations above 39%,[59] the Extended Langmuir-Freundlich equation (see Eq. 13)[67] can be employed as an alternative. This model introduces a power-law expression with an exponent m, making it effective for correlating binary equilibrium data in simulation studies.

$$\frac{q_i}{q_{si}} = \frac{1 + b_i {P_i}^{m_i}}{1 + b_i {P_i}^{m_i} + b_j {P_j}^{m_j}} \tag{2.13}$$

The mass transfer model for adsorption must consider the movement of the gaseous adsorbate through the external gas layer surrounding the solid adsorbent particles and its penetration into the porous structure during adsorption, as well as its displacement in the reverse direction during desorption. In most cases, intraparticle diffusion represents the main resistance to mass transfer.[44] The Linear Driving Force (LDF) model is always used, as it provides a simple and effective means of applying the essential kinetics of adsorption processes (see Eq. 14).

$$\frac{\partial q_i}{\partial t} = k_i({q_i}^* - q_i) \tag{2.14}$$

where k_i is the rate constant for adsorption of component i, ${q_i}^*$ is the amount adsorbed at equilibrium under current conditions and q_i is the amount currently adsorbed. When separation is governed by equilibrium rather than kinetics, mass transfer resistance does not affect the process significantly. The spread of the mass transfer zone along the adsorption column is mainly due to axial dispersion.

The behaviour of bulk gas is modelled using the ideal gas law, except in experiments conducted at pressures as high as 80 bar. In this high-pressure case, the Benedict-Webb-Rubin (BWR) equation was employed to account for deviations from ideal gas behaviour. The assumption of the ideal gas law, where the compressibility factor (z) is equal to 1, can lead to inaccuracies in modelling, particularly at high pressures and low temperatures. To illustrate the impact of operating conditions on CO_2/CH_4 separation, **Figure 2.3** shows the variation in the compressibility factor (z) from the ideal gas assumption. In **Figure 2.3**, 1 - z, is calculated using

the NIST Reference Fluid Thermodynamic and Transport Properties Database (REFPROP-version 10.0).[68]

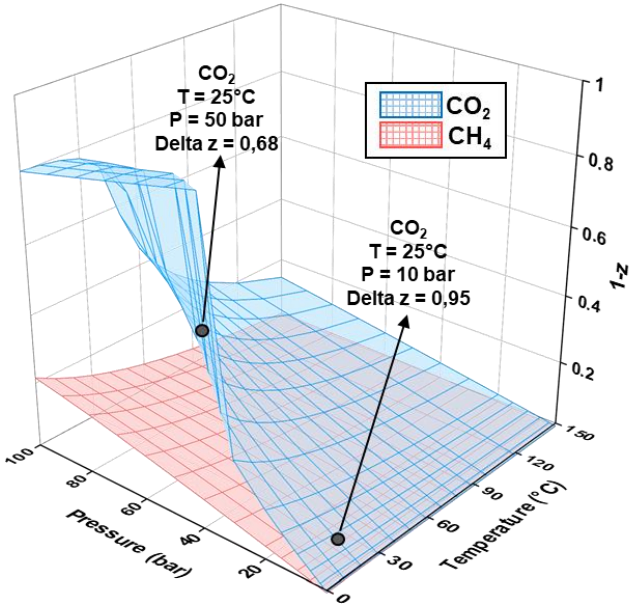

Figure 2.3 1-z (1-Compressibility factor) for CO_2 and CH_4 as a function of temperature and pressure.

At a common operating pressure of 10 bar and a temperature of 25 °C, the compressibility factor for CO_2 is 0.95, resulting in a delta *z* of 0.05. For CH_4, $z = 0.98$, i.e., delta $z = 0.02$. The impact is greater for CO_2 than for CH_4, whose gaseous behaviour is closer to ideal conditions. Even at this moderate pressure (10 bar), neglecting deviations from ideal gas behaviour can lead to inaccuracies in the system model. For example, at 50 bar and 25 °C, the delta *z* for CO_2 is 0.68, indicating that 32% of the value calculated for the bulk gas CO_2 would be incorrect if ideal gas assumptions were used. Due to the exothermic nature of the adsorption process, the temperature can increase by up to 100 °C during the latter part of the adsorption step,[55] but the largest deviations from ideal gas assumptions occur at low temperatures.

The temperature evolution of the PSA system is obtained by applying an energy balance in the packed-bed column. PSA processes involve cyclic adsorption and desorption, which are exothermic and endothermic, respectively. The energy balance is the rate of change in internal energy of a packed bed element and adsorbent particle over time *t*. Thus, when the process is not considered to be isothermal (no local thermal equilibrium), the heat balance of the fluid phase and the heat transfer rate can be expressed respectively as follows: [11]

$$\frac{\partial T_f}{dt} + v\frac{dT_f}{dZ} + \frac{c_s}{c_f}\frac{1-\varepsilon}{\varepsilon}\frac{\partial T_s}{\partial t} + \frac{\Delta H}{c_f}\frac{1-\varepsilon}{\varepsilon}\frac{\partial \overline{q_i}}{\partial t} = 0 \tag{2.15}$$

$$\frac{\partial T_s}{\partial t} = ha\left(T_f - T_s\right) - \frac{\Delta H}{c_s}\frac{\partial \overline{q_i}}{\partial t} \tag{2.16}$$

where T_f is the fluid temperature, v is the gas superficial velocity, Z is the axial position along the column, ε is the bed porosity, T_s is the solid temperature, c_s is the specific heat capacity of the solid, c_f is the specific heat capacity of the fluid, ΔH is the heat of adsorption, $\overline{q_i}$ is the average concentration of adsorbed component i, h is the heat transfer coefficient between fluid and particle and a is specific surface area available for heat transfer.

The main difference between the models is whether local thermal equilibrium (LTE)[59, 61, 63] is assumed or not (No LTE).[55, 60, 62, 64–66] LTE assumes that the gas and the solid adsorbent temperatures are equal at all points and all times. In this case, the energy balance equation is simplified. If LTE is not assumed, gas and adsorbent temperature must be calculated separately. When simulating PSA systems on an industrial scale, the thermal effects generated during the adsorption process are high and must therefore be well modelled in the process.[62]

In addition, the pressure drop $\partial P/\partial Z$ in the column is generally modelled using the hydrodynamics of flow in porous media. This is usually described by the Ergun equation, which accounts for non-linear and turbulent flows: [11]

$$\frac{\partial P}{\partial Z} = 3.5 + 300\left(\frac{1-\varepsilon}{Re}\right)\left(\frac{1-\varepsilon}{\varepsilon^3}\right)\frac{\dot{m}^2}{2d_p\rho} \tag{2.17}$$

where Re is the Reynold number, $\dot{m}$ is the mass flow rate, d_p is particle diameter and ρ is the fluid density.

The resulting mathematical model consists of a set of partial differential equations (PDEs), which exhibit steep fronts and non-linear behaviour,[69] presenting sharp changes in solution values that are difficult to predict accurately in numerical simulation. This complex system of mathematical equations is usually solved by commercial software such as Aspen[62, 66] and gPROMS,[55, 60, 63–65] which incorporate numerical solution techniques for spatial discretization methods such as finite differences[55, 63, 64] or orthogonal collocation.[59, 60, 65] Finite-difference techniques [70] involve discretization of the spatial and time domain to convert PDEs into a set

of linear and nonlinear algebraic equations, which can then be solved by Gaussian elimination for linear algebraic equations and Newton's method for nonlinear algebraic equations. [44] The orthogonal collocation method approximates the solution using a set of basic functions, such as polynomials, evaluated at specific collocation points. This method differs from finite difference methods in that the solution is represented as a continuous or piecewise continuous function.[71] The orthogonal collocation method significantly reduces the number of discretized equations due to the lower number of internal points, resulting in rapid convergence.[61] One of the limitations of these methods is that solving the large set of PDEs does not ensure a real-valued solution, and the Newton solver may fail when confronted with the steep fronts that are typical of PSA separation.[69]

One of the normal shortcomings of the simulation process is the difficulty of achieving cycle steady state (CSS), which depends on the convergence towards consistent values of performance indicators such as CH_4 purity and recovery. Generally speaking, performance indicators should not vary by more than 1% or, in the most stringent cases, 0.1%. PSA cycles involving additional steps such as the inclusion of pressure equalizers or more than one adsorbent layer in the bed may pose more difficulties in achieving CSS, as there are more interactions, non-linear behaviours and more extensive range of system conditions. A basic Skarstrom cycle with a zeolite as adsorbent was reported to reach CSS after only 5 cycles.[59] On the other hand, PSA cycles with pressure equalization reach CSS after 70 cycles for a zeolite.[55, 64] Examples of acceleration schemes for CSS iterations are extrapolators in the quasi-linear convergence region and the recursive projection method of Shroff and Keller.[69]

Achieving CSS is important for correctly evaluating the performance of a PSA process, which is essential for optimizing its operating conditions and design parameters. The optimization process can be based on adjusting or improving parameters such as maximizing CH_4 recovery and purity, or reducing energy consumption for a desired CH_4 purity, for instance. The variables modified are normally cycle design, operating conditions and adsorbent properties. The literature describes some optimization methods for PSA systems.[69, 72–74] In the context of CO_2/CH_4 separation, the Response Surface Methodology (RSM) was investigated to achieve maximum CH_4 purity and recovery with MOF Uio-66 as adsorbent.[66] The results showed that the UiO-66 adsorbent achieved optimized CH_4 purity of 99.99%, recovery of 99.99% and productivity of 8.57 $mol \cdot kg^{-1} \cdot h^{-1}$ by varying the operating temperature and bed length/diameter ratio. In another study, a full factorial design method and analysis of variance

(ANOVA) test were used to investigate the effects of various factors on CH_4 purity and recovery.[42] All factors were shown to significantly influence purity, with purge pressure being the most significant factor, followed by vacuum level. For CH_4 recovery, the ANOVA test revealed that feed pressure and adsorption stage duration were the most significant factors, while purge stage duration and vacuum level had less effect.

An optimization method was proposed to maximize CH_4 recovery while maintaining a specified CH_4 purity of 99% by adjusting the CH_4 composition in the feed gas.[75] The Sequential Quadratic Programming Descent solver was chosen due to its ability to handle discrete changes in boundaries and equations. The conclusion drawn from the analysis of the impact of feed gas composition is that increasing the CH_4 content in the feed gas improves CH_4 recovery. This result is logical, as a higher CH_4 content simplifies the PSA process, reducing the volume of CO_2 that needs to be separated and purged. This efficiency can reduce energy consumption and improve overall process economics.

2.1.4 PSA Performance Evaluation

Tables 2.4, **2.5** and **2.6** provide information on various operating parameters for different PSA units that have been reported in the literature. **Table 2.4** focuses specifically on data from single-column studies. Conversely, **Tables 2.5** and **2.6** present information related to multi-column systems, where **Table 2.5** shows experimental data, and **Table 2.6** presents simulation results.

Concerning the performance of the process, **Figure 2.4** shows purity-recovery-productivity-energy consumption plots for CO_2/CH_4 separation by EVSA and VSA. In general, the literature presents numerous examples of processes demonstrating a trade-off between higher purity and lower recovery, or vice versa. In this work, the data presented from each study were based on the authors' own criteria to select the best result with the aim of achieving the optimum balance between recovery and purity, with an emphasis on purities above 95%

Table 2.4 Single-bed PSA technologies for CO_2/CH_4 separation.

Cycle - time (s)	Cycle steps	Adsorbent	CO_2/CH_4	$P_a - P_d$ (atm)	CH_4 Purity (%) - CH_4 Recovery (%)	Productivity ($mol_{CH4} \cdot kg^{-1} \cdot h^{-1}$) - Energy consumption ($KWh \cdot mol_{CH4}^{-1}$)	Ref.
VSA - 120	1. Feed/PR - 2. ADS -3. BD - 4.PG	CMS Bergbau Forschung	50/50	3.7 - 0.3	95.0 - 58.0	1.7[a] - 0.0050[a]	[76]
		Zeolite 5A		2.0 - 0.3	75.9 - 86.4	0.8[a] - 0.0031[a]	
VSA - 370	1. Feed/PR - 2. ADS - 3. BD - 4. PG	CMS 3K	45/55	3.2 - 0.1	97.1 - 79.4	3.2[a] - 0.0068[a]	[31]
VSA - 425	1. Product/PR - 2. ADS - 3. Intermediate DP - 4. BD - 5. PG	CMS 3K	55/45	7.9 - 0.1	97.3 - 85.6	4.3 - 0.0153[a]	[77]
VSA - 470	1. Feed/PR - 2. ADS - 3. Intermediate DP - 4. BD - 5. PG	Zeolite 13X			97.1 - 60.7	4.4 - 0.0190[a]	
PSA - 1200	1. Feed/PR - 2. ADS - 3. BD - 4.PG	MIL-53	40/60	4.0 - 1.0	94.4 - 35.5	2.5 - 0.0128[a]	[60]
PSA - 1680	1. Feed/PR - 2. ADS - 3. BD, He regeneration - 4. PG	Sawdust Activated Carbon	50/50	4.0 - 1.0	97.0 - 60.0	2.8[a] - 0.0047[a]	[78]

[a] Calculated in this work

The presented operating parameters include cycle type, cycle steps, type of adsorbent used, CO_2/CH_4 feed gas ratio, P_a and P_d, CH_4 purity and recovery percentages, productivity in terms of $mol_{CH4} \cdot kg^{-1} \cdot h^{-1}$, and energy consumption in kWh mol_{CH4}^{-1}. Using mass balances that consider the gas feed to the PSA system, as well as the separation of CO_2 and CH_4 in the production, purge, and blowdown streams, we conducted calculations to assess the productivity and energy consumption of various studies based on the provided data. For the calculation of the biogas compression stage to reach the feed or adsorption pressure in the PSA (Eq. 10), we assumed that the gas would be available at a pressure of 1 bar, as biogas is usually produced at close to atmospheric pressure from a biogas digester. In addition, the blowdown process was assumed to start at atmospheric pressure and proceed down to the desired sub-atmospheric pressure. Furthermore, in cases where precise information regarding the quantity of raffinate used to purge the columns was not available, it was assumed that 10% of the overall production was allocated for this purpose.

Table 2.5 Multi-bed PSA technologies for CO_2/CH_4 separation - experimental studies.

Cycle - time (s)	Cycle steps	Adsorbent	CO_2/CH_4	$P_a - P_d$ (atm)	CH_4 Purity (%) - CH_4 Recovery (%)	Productivity ($mol_{CH4} \cdot kg^{-1} \cdot h^{-1}$) - Energy consumption ($KWh \cdot mol_{CH4}^{-1}$)	Ref.
2bed EPSA - 480	1. Feed/PR - 2. ADS - 3. DPE - 4. BD - 5. PG - 6. PPE	CMS Takeda 3A	50/50	4.0 - 1.0	95.8 - 71.2	5.8 - 0.0056[a]	[79]
2bed EVSA - 362		13X Zeolite Z10-04			90.2 - 92.7	14.1 - 0.0033[a]	
2bed EVSA - 182	1.Feed/PR -2. ADS - 3. DPE - 4. BD - 5. PPE.	Zeolite KZ10-04	42/58	1.5 - 0.1	91.2 - 83.7	11.9 - 0.0039[a]	[54]
2bed EVSA - 336		Zeolite NaUSY			99.3 - 85.9	15.6 - 0.0039[a]	
2bed EVSA - 290		CMS 3K			96.9 - 86.9	11.3 - 0.0038[a]	
2bed VSA - 140	1. Feed/PR - 2. ADS - 3. DPE - 4. BD - 5. PPE	Zeolite NaUSY	50/50	2.0 - 0.1	99.0 - 73.0	12.8[a] - 0.0044[a]	[43]
4bed EVSA - 600	1. Feed/PR - 2. ADS - 3. DPE1 - 4. IDLE - 5. DPE2 - 6. BD - 7. PG - 8. PPE1 - 9. PPE2	Silica gel	45/55	4.0 - 0.3	98.3 - 73.1	2.9[a] - 0.0036	[80]
2bed-1tank EVSA - 1800	1. Feed/PR - 2. ADS - 3. DPE - 4. BD - 5. PG - 6. PPE				97.9 - 91.0	3.8 - 0.0085[a]	
3bed-1tank EVSA - 1560	1. Feed/PR - 2. ADS - 3. Idle - 4. DPE1 and DPE2 - 5. BD - 6. PPE1 and PPE2.	CMS KP 407	40/60	1.5 - 0.1	98.4 - 92.1	2.6 - 0.0084[a]	[81]
2bed EVSA - 336	1. Feed/PR - 2. AD - 3. DPE - 4. DP - 5. BD - 6. PPE	COSMO Zeolite 13X	36/64	4.0 - 0.1	95.5 - 91.3	3.3[a] - 0.0072[a]	[42]

[a] Calculated in this work.

Table 2.6 Multi-bed PSA technologies for CO_2/CH_4 separation - simulation studies.

Cycle - time (s)	Cycle steps	Adsorbent	CO_2/CH_4	P_A - P_D (atm)	CH_4 Purity (%) - CH_4 Recovery (%)	Productivity ($mol_{CH4} \cdot kg^{-1} \cdot h^{-1}$) - Energy consumption ($KWh \cdot mol_{CH4}^{-1}$)	Ref.
2bed VSA - 80	1. Feed/PR - 2. ADS - 3. BD - 4. PG	Silicalite	38/62	1.0 - 0.1	97.8 - 58.5	8.6 -	[59]
2bed VSA - 400	1. Feed/PR - 2. ADS - 3. Intermediate depressurization - 4. BD - 5. PG	2 layers: CMS-3K and Zeolite 13X	45/55	7.9 - 0.1	98.0 - 80.3	7.7 - 0.0069[a]	[57]
2bed EVSA - 850	1. Feed/PR - 2. ADS - 3. DPE - 4. BD - 5. PG - 6. PPE	Zeolite 13 X	33/67	4.0 - 0.3	99.2 - 85.0	5.9 - 0.0086[a]	[55]
4bed VSAm[c] – 1080[b]	1. Product/PR - 2. ADS - 3. Rinse - 4. BD - 5. PG	MIL-53	40/60	4.0 - 0.1	99.4 - 92.8	2.1 - 0.0170	[60]
2bed EVSA – 850[b]	1. Feed/PR - 2. AD - 3. DPE - 4. BD - 5. PG - 6. PPE	COSMO Zeolite 13X	36/64	4.5 - 0.1	97.0 - 95.4	12.8[a] - 0.0076[a]	[42]
2bed PSA -	1. Feed/PR - 2. ADS - 3. BD - 4. PG	Spent coffee	32/68	2.0 - 1.0	97.0 - 95.4	-	[82]
4bed EVSA - 520 (2 systems)[b]	1. Feed/PR - 2. ADS - 3. DPE - 4. BD - 5. PG - 6. PPE (each system)	Zeolite 5A	37/63	6.2-0.2	99.4 - 99.0	8.2[a] – 0.0056	[83]
6bed VSA - 240	1. Feed/PR - 2. ADS - 3. BD - 4. PG	CMS-3K	45/55	6.5-0.3	97.1 – 93.4	8.9 – 0.0058	[84]

[a] Calculated by this work
[b] Industrial scale-up
[c] VSAm: VSA cycle modified.

The results of the studies are representative of real-world scenarios where the CO_2 content in the feed gas stream can vary from around 20 to 50%. At the laboratory scale, the design of PSA units is highly adaptable, allowing the use of single-column configurations,[31, 60, 76–78] as presented in **Table 2.4**. However, the use of a single column in the cycle is not an accurate representation of the actual PSA process, as it cannot be continuously fed and sometimes requires purging with pure CH_4.[55] Although it can still serve as a valuable tool for validating numerical models of the PSA process and provide valuable data for exploring alternative cycles,

on an industrial scale, the PSA unit comprises multiple columns operating in parallel, including configurations with two, three or more columns. Apart from the fact that the gas feed is not continuous, a single column does not allow incorporation of the pressure equalization step, which was the first improvement to the original Skarstrom's cycle introduced by Berlin in 1967.[44, 85] This pressure equalization step can indeed significantly improve CH_4 recovery.

Generally, the most commonly used adsorbent to capture CO_2 in PSA units is either a CMS,[54, 79, 81] for which it is worth recalling that its selectivity is mainly driven by kinetic factors, or a zeolite,[42, 43, 54, 55] whose selectivity is mainly determined by both thermodynamic equilibrium and kinetic aspects. Although ACs and MOFs[60] are potential adsorbents, they are less frequently used due to their lower selectivity and relatively recent stage of development, as well as high production cost, respectively. While MOFs offer promising opportunities for CO_2 capture, exhibiting higher CO_2/CH_4 selectivity and PSA working capacity ratio, further research is necessary to fully explore their potential in this application.

The sub-atmospheric blowdown regeneration method is widely used in most cycles, indicating that adsorbed CO_2 cannot be easily regenerated by simple atmospheric depressurization. However, in the only experimental multi-column example where the columns were regenerated at atmospheric pressure,[79] a low CH_4 recovery of 71 % was achieved, resulting in relatively low productivity. This low recovery can be attributed to a high amount of CH_4 that is part of the raffinate produced and used in the regeneration process as purge. Similarly, the two single-bed studies that used atmospheric pressure depressurization also resulted in very low recoveries and productivities.[60, 78] Although atmospheric depressurization results in low energy consumption due to the absence of a vacuum pump, the normalized energy consumption per amount of CH_4 produced is higher than in many VSA or EVSA studies.

The introduction of pressure equalization (see **Figure 2.4a**) in the VSA cycle (see **Figure 2.4b**) offers significant improvements in recovery, productivity and energy consumption.[33, 68, 87, 112, 113, 120] For instance, in an EVSA cycle, the optimal PSA-adsorbent configuration (see green line in **Figure 2.4a**) achieved a productivity of 15.6 $mol_{CH4}{\cdot}kg^{-1}{\cdot}h^{-1}$ with an energy consumption of 0.0039 $kWh{\cdot}mol_{CH4}^{-1}$.[54] Conversely, in the VSA cycle, the most favorable scenario (see green line in **Figure 2.4b**) achieved a productivity of 12.8 $mol_{CH4}{\cdot}kg^{-1}{\cdot}h^{-1}$ and an energy consumption of 0.0044 $kWh{\cdot}mol_{CH4}^{-1}$.[43]

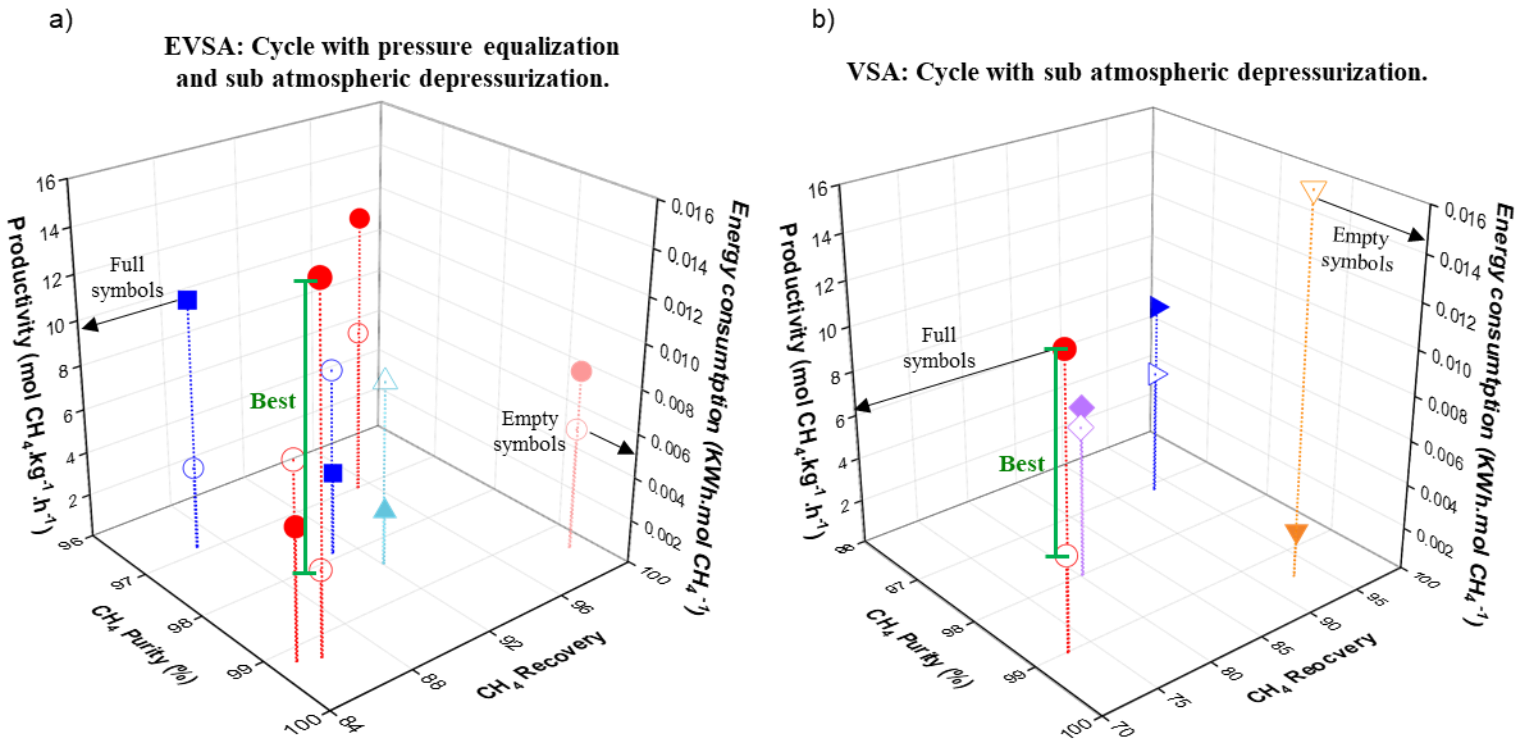

Figure 2.4 Purity, recovery, productivity and energy consumption plots for CO_2/CH_4 separation by EVSA and VSA: a) EVSA cycle, b) VSA cycle – Full symbols represent productivity and empty symbols represent energy consumption - ●: 2-bed Zeolite[42, 43, 54, 55] - ■: 2-bed CMS[54, 79] - ▲: 3-bed + 1tank CMS[81] - ●: 4-bed Zeolite [83] - ◆: 2-bed Zeolite + CMS[57] – ▼: 4-bed MOF + CO_2 production.[60] - ►: 6-bed CMS [84] - ▮ Best PSA-adsorbent configuration.

Recovery is improved by ensuring that the adsorption and desorption phases are carried out evenly across all the adsorbent beds, ensuring full utilization of the beds and maximizing the recovery of the target component. Without pressure equalization, gas flow may be unevenly distributed across the adsorbent beds, leading to preferential adsorption and desorption in certain sections of the beds. Moreover, by equalizing the pressure between the two adsorption columns, the energy derived from the compressed gas in the high-pressure bed is used to partially pressurize the low-pressure bed. Due to the partial depletion of the strongly adsorbed species in this gas, the work of separation is conserved, resulting in energy savings. This process effectively reduces blowdown losses by about 50%, thus enhancing the recovery of the raffinate product.[44] Additionally, maximizing the recovery of CH_4 is of highest importance due to its greenhouse effect, which is even more potent than that of CO_2 and contributes to global warming. It is indeed remarkable that the warming potential of CH_4 is 21 times greater than that of CO_2.[55]

Typically, the duration of a 2-bed adsorption cycle ranges between 150 s to 400 s.[42, 43, 54, 57, 59] However, for scenarios involving more than two beds, additional tanks, or simulations of industrial scale systems,[60, 81] the cycle time can increase significantly, exceeding 1000 s. The duration of the cycle should be sufficient to ensure effective gas adsorption when using adsorbents with high equilibrium adsorption capacity, while fast-adsorbing adsorbents require a shorter cycle time to facilitate fast kinetic adsorption.

Optimum productivity was achieved by maintaining low adsorption pressures, specifically 2 atm or less.[43, 54] Notably, the most effective desorption pressure for regenerating the bed was 0.1 atm. Although such a minimal desorption pressure requires considerable energy consumption on the part of the vacuum pump, this approach demonstrates low energy consumption per mole of CH_4 produced. In other words, despite the high energy requirements, the substantial CH_4 production outweighs the energy consumption, making this operational method advantageous. An effective way to further improve the system and reduce energy consumption is to reduce P_a or increase the sub-atmospheric P_d, which is usually 0.1 atm. Increasing P_d to 0.2 or 0.3 atm could result in significant savings.

Remarkably, different performances can be achieved within the same family of materials, even if the corresponding materials exhibit similar selectivity and PSA working capacity ratio properties. For instance, NaUSY zeolite,[54] which demonstrated the highest productivity and lowest energy consumption (see the green line "best" in **Figure 2.4a**), was used in a purge-free EVSA cycle and exhibited a selectivity and PSA working capacity ratio of 50 and 30, respectively. In contrast, zeolite 13X[55] was employed in an EVSA cycle with purge and exhibited a selectivity and PSA working capacity ratio of 58 and 26, respectively. Both cycles achieved purities in excess of 99%, but the EVSA cycle without purge resulted in more than doubling the productivity and a reduction in energy consumption to less than half. Consequently, it would be advantageous to eliminate purging by regenerating the bed at very low vacuum pressure (0.1 atm).

The performance evaluation of the MOF MIL-53[60] as an adsorbent for CO_2/CH_4 separation differs from other cases because the objective is to produce both CH_4 and CO_2 at high purity. It has been found that achieving these levels of purity and recovery comes at the expense of high energy consumption. This high energy consumption arises from the fact that an additional step is required to pressurize and adsorb the effluent from column regeneration. Moreover, the productivity in terms of CH_4 production was observed to be very low (2.1 $mol_{CH4} \cdot kg^{-1} \cdot h^{-1}$). This

low productivity could be attributed to the adsorbent's low CO_2/CH_4 selectivity of 4 at 4 bar, which is significantly lower than the selectivity of zeolites, typically around 50. Nevertheless, a new process configuration has been proposed, [83] using zeolite 5A with two PSA units, each containing four beds. In this setup, the second unit processes the off-gas from the first unit, which has separated the CO_2 from the residual gas stream. The residual stream is then recycled back to the first unit, improving CH_4 recovery. Final results showed CH_4 purity and recovery of 99.4% and 99.0%, respectively, with modest energy consumption of 0.0056 $kWh \cdot mol_{CH4}^{-1}$ and productivity of 8.2 $mol_{CH4} \cdot kg^{-1} \cdot h^{-1}$. In addition, the system produced CO_2 with a purity of 99.1%. This process represents a promising alternative for achieving high CH_4 recovery and purity, while also producing high-purity CO_2.

CMSs enable faster diffusion of CO_2, reducing adsorption time and increasing productivity. However, CMSs have a significantly lower PSA working capacity ratio than zeolites. Furthermore, the use of CMSs involves the utilization of only a fraction of the overall equilibrium capacity, leading to a reduction in productivity.[77] Zeolites possess steeper isotherms and high CO_2 adsorption enthalpy, necessitating high vacuum conditions for bed regeneration. Conversely, CO_2 isotherms in CMSs are less steep, allowing vacuum desorption at relatively higher pressures.[57] Although column regeneration at atmospheric pressure has been achieved for CMSs,[79] it resulted in lower recovery and productivity. Despite this, CMS regeneration has been carried out at low vacuum pressures of 0.1-0.3 atm.[87, 109, 120] Among these processes, the EVSA process without purge[54] stands out as the most optimal for CMS, offering a productivity of 11.3 $mol_{CH4} \cdot kg^{-1} \cdot h^{-1}$. This value is slightly lower than the productivity of the best zeolite system, which is 15.6 $mol_{CH4} \cdot kg^{-1} \cdot h^{-1}$, indicating that the higher working capacity ratio of PSA in zeolites may be more advantageous than the fast diffusion process of CMSs. Additionally, the energy consumption of the two systems is similar, 0.0038 and 0.0039 $kWh \cdot mol_{CH4}^{-1}$, respectively. Overall, CMSs can offer comparable performance to zeolites. To address the issue of low utilization of equilibrium capacity in kinetic-selective adsorbents, Grande and Rodrigues[57] introduced a mixed layer of CMS and zeolite at the end of the column. By implementing this approach, they were able to achieve a substantial increase in productivity compared with a process relying solely on CMSs as adsorbent. This improvement was mainly attributed to the ability to process a larger amount of feed, as the column retained more CO_2 while retaining the same dimensions.

Most studies do not consider the use of ACs, due to their perceived lack of CO_2/CH_4 selectivity. Nevertheless, these materials offer several potential advantages, including a reduced

environmental impact and uncontrolled waste disposal, lower emissions during their production and the possibility of establishing a circular economy and achieving lower carbon emissions compared with other CO_2 capture methods.[78] Unfortunately, to our knowledge, there are no multi-column experimental studies on ACs. Furthermore, none of the AC producers offers a commercially available AC specifically designed for CO_2/CH_4 gas separation.

2.2 Biogas desulfurization

The literature on H_2S separation from gas streams presents an in-depth comparison of various sorbents under a wide range of test conditions.[86–91] However, the way the results are presented makes it difficult to draw clear conclusions about their relative performance. At lab scale, the initial H_2S concentration at the inlet of the experimental test bench can fluctuate considerably, ranging from 8 ppm[92] to 10000 ppm.[93–95]

Another critical factor to consider is the composition of the gas used in the experiments, with H_2S mixed with N_2 or He (e.g., 10-20000 ppm H_2S in N_2, or 8-100 ppm H_2S in He) often preferred to gas comprising CO_2 (e.g., 1000-10000 ppm H_2S in a mixture of 50-80% CH_4 + 30-60% CO_2). However, the use of CO_2, and even more so real biogas, leads to a decrease in H_2S adsorption capacity. This is due to the presence of other components that also adsorb, therefore reducing the number of sites available for H_2S adsorption. For this reason, studies on H_2S separation using a synthetic gas comprising only N_2 and H_2S, for instance,[96–99] report significantly higher H_2S adsorption capacities, reaching up to 800 $mg \cdot g^{-1}$.[99] This stands in stark contrast to capacities below 70 $mg \cdot g^{-1}$ when considering CO_2 in the feed gas.[100]

In this work, H_2S adsorption capacity is evaluated for various sorbents in the context of biogas upgrading, where biogas is produced from digesters or landfills near ambient conditions (25 °C and 1 atm). Given industrial priorities, the focus is on H_2S adsorption capacity determined at the breakthrough point. In industrial applications, sorbent columns are rarely allowed to reach full saturation before replacement; instead, they are replaced once the exit gas fails to meet the required purity standards, leaving the sorbent partially saturated. The present work therefore prioritizes evaluating adsorption capacity at the breakthrough point rather than assessments of total saturation capacity, to align with industrial practice and avoid redundancy with previous studies on total H_2S separation capacity.[86–91] Moreover, the results are categorized according to the composition of the gas used in the experiment. This approach offers valuable guidance into selecting the most effective sorbents for H_2S separation in biogas

upgrading, with the aim of identifying sorbents with high breakthrough capacity for improved efficiency.

2.2.1 H_2S separation capacity of different adsorbents

Accurate representation of the biogas/H_2S separation process at laboratory scale has been a challenge for the correct interpretation and comparison of sorbents across various studies. The composition of the gas examined, the amount of H_2S in the inlet gas and the type of H_2S separation capacity reported (at a breakthrough point or at full saturation), represent the main restrictions limiting the assessment of adsorption efficiency. In order to mitigate biases due to variations in the initial H_2S input and the breakthrough point at which H_2S separation capacity is reported, it has been proposed to apply a partition coefficient, as presented in **Figure 2.5**.[101] It is calculated using the approach for quantifying the partitioning of target species between aqueous and gaseous phases, similar to the principles of Henry's law.

Partition coefficient equation

$$Partition\ coefficient, \frac{mol}{kg.Pa}\ (\text{at } BTP) = \frac{H_2S\ Separation\ \left(\frac{mol}{kg}\right)}{Outlet\ H_2S\ concentration\ (Pa)}$$

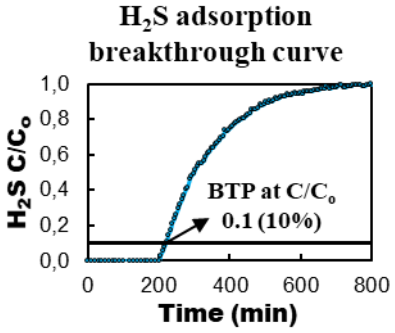

Figure 2.5 Partition coefficient equation and typical breakthrough curve for dynamic H_2S adsorption.

However, due to its intrinsic characteristics, we note that the partition coefficient favors the lowest breakthrough points (see **Figure 2.5**), which is normally set at 10% of the inlet concentration. The partition coefficient should therefore be evaluated at the same breakthrough points for the compared experiments, and it gives better results for the smallest amount of H_2S at the inlet.

The inclusion of all biogas components (CH_4, CO_2, VOCs, H_2O, O_2, siloxanes …) in the synthetic gas used at lab scale presents great difficulties. Nevertheless, a good representation should include CO_2 in the specified proportions (20–50%), as it competes with H_2S for adsorption sites. Achieving high H_2S separation capacities in a gas mixture without CO_2 can lead to misconceptions for biogas applications. Another factor to consider is the presence of

water, which can be beneficial to some extent for H_2S oxidation. To compare accurately the performance of sorbents, they need to be tested under constant humid conditions.

The methodology implemented in this study involves selecting works from the literature dealing with H_2S separation using a sorbent-packed column under dynamic conditions, where H_2S adsorption/separation is reported at a breakthrough point, prior to full sorbent saturation. For a better understanding, the studies are classified according to the composition of the gas being analyzed and the H_2S content at the inlet.

2.2.1.1 Real biogas

Four studies were identified in which real biogas was used for analysis, as shown in **Table 2.7**. Of these, the most efficient sorbent was a granular AC,[102] with an exceptionally high adsorption capacity of 1266.0 $mg \cdot g^{-1}$, which was employed to treat biogas generated from wastewater from a dairy farm. This biogas has a low CO_2 concentration of 24.7%, which is roughly the middle of the CO_2 concentration for the other three cases: 41% for biogas from landfill,[103] 49% for a lab-scale bioreactor[104] and ≈ 50% for a fermenter. Indeed, lower CO_2 concentrations correlate with higher H_2S adsorption due to the increased space available for adsorption in the absence of CO_2. Furthermore, H_2S adsorption was evaluated at a higher breakthrough point, resulting in higher adsorption capacities. Nevertheless, the adsorption capacity exceeded that of AC from maize cob waste with 15.5 $mg \cdot g^{-1}$,[104] zeolite 13X with 76.0 $mg \cdot g^{-1}$,[103] commercial impregnated AC Chemviron with 383.0 $mg \cdot g^{-1}$ by more than three times,[103] and that of α-FeOOH with 49·0 $mg.g^{-1}$.[105] Although zeolite 13X is a commercial material, it is not specifically indicated for commercial use in gas desulfurization.

Although the use of biogas is an interesting approach to adsorption evaluation, lab-scale columns remain the predominant method. Remarkably, Ou et al.[102] used a full-scale PVC column in their study, the only case of a column at actual scale found in this chapter. They used granular AC as sorbent, with biogas collected from an anaerobic digester treating wastewater from a dairy farm with approximately 200 cows. Under these conditions, H_2S content ranged from 932 to 2350 ppm in the feed flow.

The α-FeOOH adsorbent operated at a higher and more favorable temperature (40 °C);[105] however, the gas composition had a significantly lower H_2S concentration (205–350 ppm), leading to reduced adsorption capacities. Additionally, despite the high water content (5%), the

gas contained virtually no oxygen (< 1 ppm), which has a further negative impact on the adsorbent performance.

Table 2.7 H_2S/biogas separation studies.

Sorbent	Biogas origin: composition	BTP C/C_0 (%)	H_2S adsorption ($mg \cdot g^{-1}$)	Ref.
Commercial IAC - Chemviron	Landfill gas: H_2S 4020 ppm; CH_4 42.5%; CO_2 41.1%; O_2 2.2%; H_2O 1.3%	0.03	383.0	[103]
Commercial Zeolite 13X CECA			76.0	
Granular activated carbon (unknown source)	Wastewater from a dairy farm with about 200 cows: H_2S 1500 ppm; CH_4 57.3±2.0%; CO_2 24.7±3.3%; O_2 1.57±0.29%	6.77	1266.0	[102]
Maize cob waste AC	Lab-scale bioreactor: H_2S 1100-1800 ppm; CH_4 51%; CO_2 49%; O_2 <1%; H_2 160ppm; CO 15ppm; NH_3 18ppm	3.50	15.5	[104]
α-FeOOH	Fermenter: H_2S 205-350 ppm; CH_4: Not reported; CO_2 45-55%; H_2O 5%; O_2 <1 ppm	5.00	49.0	[105]

IAC: Impregnated activated carbon
[a] Operating temperature = 40 °C

Working with real biogas at lab scale is challenging for several reasons. Firstly, there are no commercial suppliers available with the exact composition of biogas, which requires sourcing from a biogas production facility, and which can therefore be logistically difficult and costly. Secondly, real biogas contains flammable and hazardous gases, posing safety issues during handling. Finally, the variability and complexity of real biogas make it difficult to calibrate instruments during experimentation. This is why synthetic gases that mimic the most significant aspects of biogas are widely used.

2.2.1.2 Gas composed of CH_4, CO_2 and H_2S

Figure 2.6 shows experiments performed with a synthetic gas containing CH_4, CO_2 and H_2S in proportions very close to the actual biogas composition (CH_4: 59-66%, CO_2: 34-40%, H_2S: 1000-3000 ppm) from any source, including agricultural waste, landfill or industrial waste. This representation focuses on the prevailing contaminant, CO_2, commonly observed in real biogas scenarios, which is the best representation for assessing sorbents in the context of H_2S separation for biogas applications. As presented in **Figure 2.6a**, most research is focused on carbon-based materials, notably biochar and ACs. The effect of activation on biochar by

creating more nanopores leads to a higher adsorption capacity, 64 $mg.g^{-1}$ being the highest adsorption capacity obtained for an AC[106] and 30 $mg.g^{-1}$ for a biochar.[93] Unfortunately, the literature lacks of experiments involving zeolites and MOFs.

The only example different from carbon-based materials is a zeolite 13X modified with Cu ions (13X Ex-Cu),[107] which has an H_2S adsorption capacity of 18.2 $mg.g^{-1}$. The improved performance was attributed to the presence of Cu^{2+} ions in the zeolite, which increases selectivity to H_2S adsorption. This adsorption capacity is comparable to that of biochar materials, but lower than that of most ACs. As presented in **Figure 2.6b**, zeolites are less efficient because ACs have a much larger surface area that provides more sites for H_2S adsorption and storage of H_2S oxidation by-products, especially if the AC is chemically modified.

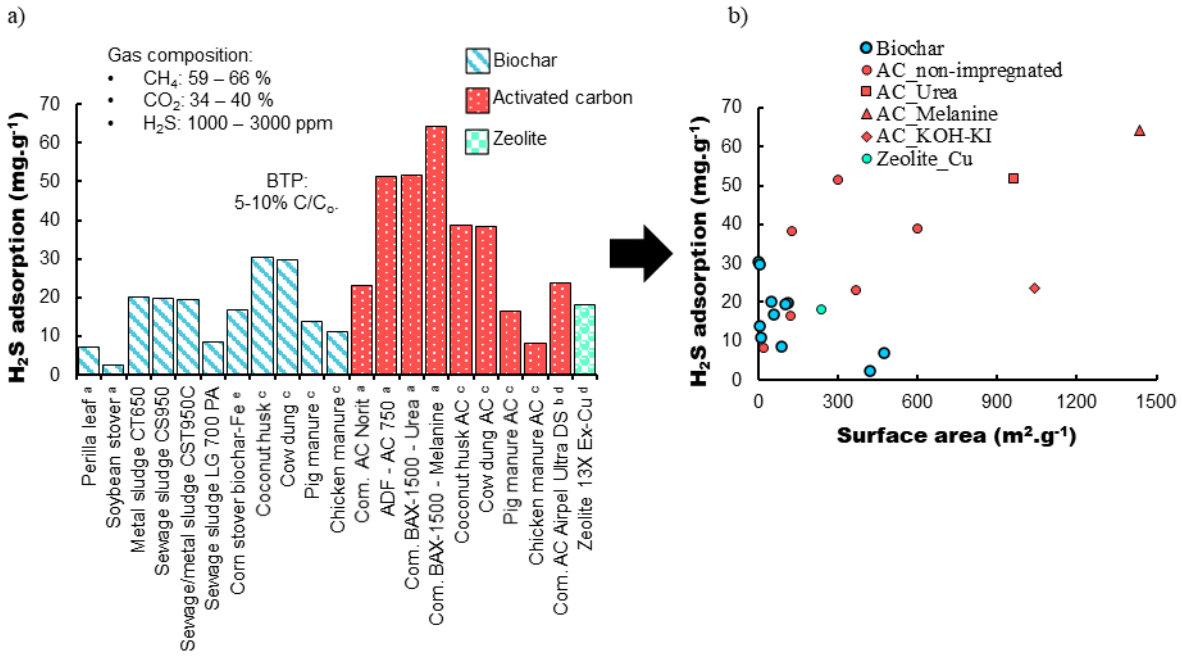

Figure 2.6 Studies on H_2S removal from a gas mixture comprising CH_4, CO_2 and H_2S. a) H_2S adsorption capacity; b) Surface area of the sorbents presented in a). (See **Tables 1.6** to **1.9** for reference).

Perilla leaf [108]; Soybean stover [108]; Metal sludge CT650 [109]; Sewage sludge CS950 [109]; Sewage/metal sludge CST950C [109]; Sewage sludge Corn stover biochar-Fe [110]; Corn stover biochar-Fe [111]; Coconut husk [93]; Pig manure [93]; Chicken manure [93]; Cow dung [93]; Com. AC Norit [100]; ADF-AC 750 [100]; Com. BAX-1500-Urea [106]; Com. BAX-1500-Melanine [106]; Coconut husk AC [93]; Pig manure AC [93]; Chicken manure AC [93]; Cow dung AC [93]; Com. AC Airpel Ultra DS [112]; Zeolite 13X Ex-Cu [107].

Com. AC = Commercial activated carbon
[a] Moisture conditions
[b] Oxygen in the feed gas composition
[c] H_2S inlet: 10000 ppm
[d] H_2S inlet: 100-200 ppm
[e] Breakthrough point was at 50% C/C_o

Biochar surface area is lower, reducing the number of adsorption sites and hence H_2S separation efficiency (< 30 $mg.g^{-1}$). This highlights the importance of activation in creating more accessible pore sites. While biochar has surface areas below 500 $m^2.g^{-1}$, the highest value being that of perilla leaf biochar (473 $m^2.g^{-1}$),[108] ACs have higher values, following a trend where increased surface area corresponds to better adsorption performance. The adsorbent with the highest surface area and the most effective AC is the melamine-modified commercial AC BAX-1500 (MeadWestvaco),[106] with an H_2S separation capacity of 64.1 $mg.g^{-1}$ and a surface area of 1435 $m^2.g^{-1}$. Next comes the same AC but impregnated with urea instead of melamine,[106] with an H_2S separation capacity of 51.6 $mg.g^{-1}$ and a surface area of 963 $m^2.g^{-1}$. Both carbons possess a surface rich in nitrogen-containing basic species. Another top-performing sorbent is the non-modified AC ADF-AC 750,[100] presenting an H_2S separation capacity of 51.2 $mg.g^{-1}$, derived from the pyrolysis and activation of anaerobic digested fibers. Although it is not impregnated, the authors report that it has a high calcium, magnesium and iron content, which enhances the H_2S oxidation process.

One study reported an exceptional H_2S adsorption capacity of 652 $mg.g^{-1}$.[113] The results were obtained with a charcoal from anaerobically digested dairy fiber impregnated with Na_2CO_3. It has a surface area of 142 $m^2.g^{-1}$ when non-impregnated. Nevertheless, the column feed flow rate in the experiment was 5 $mL.min^{-1}$, resulting in a very low linear velocity in the adsorption column of 0.26 $cm.s^{-1}$ and a breakthrough time as long as 38 days. In contrast, typical linear velocities for small lab-scale columns in the literature are in excess of 1 $cm.s^{-1}$. The use of low flow rates allows sufficient time for H_2S dissociation and deposition of reaction byproducts in the porous structure, thus improving separation performance. Although this is possible on a laboratory scale, such conditions pose limitations for industrial application.

2.2.1.3 Gas composed of air and H_2S

Experiments involving air containing 10000 ppm (1%) H_2S conform to the ASTM D6646-03 test, which is a standardized method for determining the H_2S breakthrough capacity of ACs. However, this method does not represent a practical application for biogas desulfurization, as it does not take into account the presence of CO_2, which is the main contaminant of biogas, and the H_2S concentration exceeds the normal levels of H_2S found in biogas (usually < 10000 ppm). For these studies, only commercial ACs were used. The H_2S separation capacity increases considerably compared to synthetic gas containing CO_2, as shown in **Figure 2.7**. In air, AC can

offer a greater number of adsorption sites for H_2S. Among these sorbents (see **Figure 2.7a**), the most effective is the commercial AC Midas,[114] with an H_2S separation capacity of 608 $mg.g^{-1}$, which, although non-impregnated, is characterized by a carbon-metal oxide matrix and well-developed microporosity with a surface area of 1100 $m^2.g^{-1}$. After the commercial AC Midas, the three most effective sorbents were ACs subjected either to metal loading or to chemical impregnation. These are Com. BAX-500-NaOH,[95] Com. G55C-NaOH[95] and Com. AC (Jacobi)-MgO,[115] with H_2S separation capacities of 321.9, 272.2 and 275.0 $mg.g^{-1}$, respectively. Both Com. BAX-500-NaOH and Com. AC (Jacobi)-MgO have high surface areas of 1340 and 1358 $m^2.g^{-1}$, respectively, whereas Com. G55C-NaOH has a lower surface area of 878 $m^2.g^{-1}$. Remarkable performance was also observed for ACs impregnated with NaOH[95] and KOH,[94] achieving H_2S separation capacities of around 200 $mg.g^{-1}$. NaOH and KOH are well-established impregnation agents for use in commercial ACs due to their ability to desulfurize via acid-base reactions. This shows that optimum H_2S removal is achieved by chemisorption, particularly when complemented with either metal loading or basic chemical impregnation, as opposed to the use of unmodified ACs.

Another series of experiments, incorporating air and featuring lower H_2S content in the feeding gas, ranging from 500 to 3000 ppm, is shown in **Figure 2.7b**. ACs again have the highest H_2S separation capacities. Among them, AC-Cu,[116] impregnated with Cu, shows significantly better performance, with an H_2S separation capacity of 496.6 $mg.g^{-1}$. AC-Cu also has the highest surface area among the sorbents (see **Figure 2.7d**). The presence of Cu in the small pores acts as a catalyst for the activation of adsorbed H_2S, facilitating its conversion into more reactive species and leading to H_2S oxidation (according to Equations (1.1) to (1.17) for the oxidation of H_2S and sulfur species). In the same study, when Zn and Fe were used as impregnation agents for the same carbon, the results were poor, with H_2S separation capacities below 40 $mg.g^{-1}$.

MOFs were modified by incorporating AC or N-doped GO during synthesis, which improved their H_2S separation capacity. The best result was obtained with hybrids based on copper-based MOF and GO (HKUST-GO), with an H_2S separation capacity of 199 $mg.g^{-1}$. The addition of GO more than doubled the initial adsorption of the base material, due to the physical H_2O and H_2S adsorption in the pore space formed at the interface between MOF units and GO layers, where dispersive forces are strongest. H_2S also binds to the copper centers of the MOF, progressively reacting to form copper sulfide. Despite this improvement, MOF adsorbents

showed comparable performance to biochar, but a much lower H_2S separation capacity than ACs.

In **Figure 2.7c and 2.7d**, H_2S adsorption capacity is plotted as a function of surface area. The trend shows an increase in H_2S adsorption with a corresponding increase in surface area. In the absence of CO_2, the optimal micropore space (between 0.36 nm to 1.2 nm)[117] is mainly available for H_2S adsorption rather than for CO_2 adsorption, increasing selectivity for the H_2S molecule. Although sorbents with a larger surface area may seem more promising, the efficiency of a sorbent is not solely determined by this factor. As expected, the impact of carbon modification must also be considered. Generally, surface-modified sorbents perform better than unmodified ones.

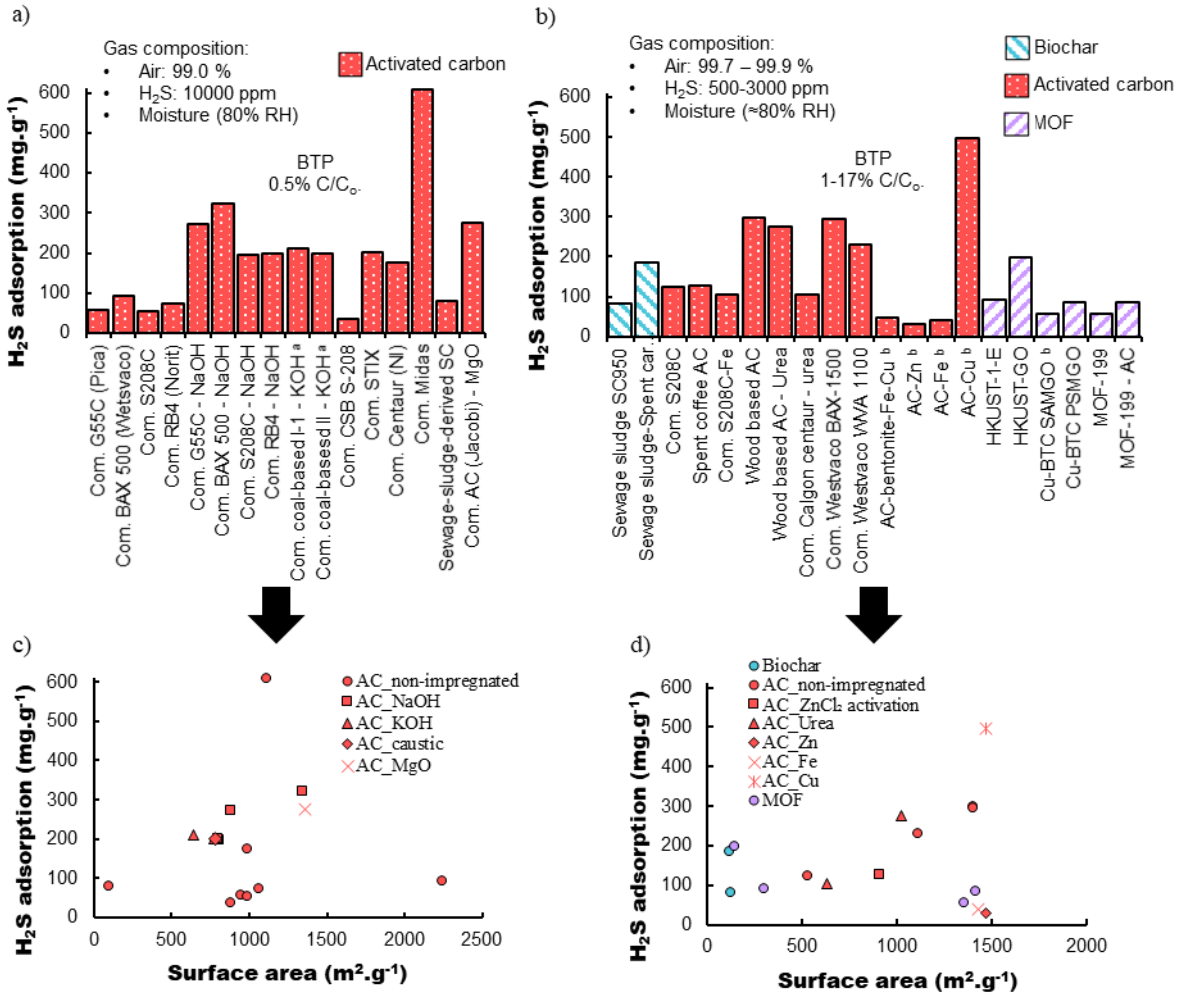

Figure 2.7 Studies on H_2S removal from a gas mixture comprising air, H_2S and moisture. H_2S adsorption capacity for an H_2S inlet concentration of: a) 10000 ppm and a breakthrough point of 0.5% C/C_o, and b) between 500 and 3000 ppm at a breakthrough point of 1-17% C/C_o. H_2S adsorption capacity as a function of surface area for the materials shown: c) in Figure 2.7a, and d) in Figure 2.7b (See Tables 1.6 to 1.10 for reference).

Com. G55C (Pica) [95]; Com. BAX 500 (Wetsvaco) [95]; Com. S208C [95]; Com. RB4 (Norit) [95]; Com. G55C-NaOH [95]; Com. BAX-500-NaOH [95] - Com. S208C-NaOH [95]; Com.RB4-NaOH [95]; Com. Coal based I-1-KOH [94] - Com. Coal based II-OH [94]; Com. CSB S-208 [114]; Com. STIX [114]; Com. Centaur (NI) [114]; Com. Midas [114]; Sewage-sludge derived SC [114]; Com. AC (Jacobi)-MgO [115]; Sewage sludge SC950 [118]; Sewage sludge-Spent car oil [119] - Com. S208C [120]; Spent coffee AC [121]; Com. S208C-Fe [118]; Wood based AC [122]; Wood based AC Urea [122]; Com. Calgon centaur Urea [122]; Com. Wetsvaco BAX-1500 [123]; Com. Westvaco WVA 1100 [123]; AC-bentonite-Fe-Cu [116]; Ac-Zn [116]; AC-Fe [116]; AC-Cu [116] - HKUST-1-E [124]; HKUST-GO [124]; Cu-BTC SAMGO [125]; Cu-BTC PSMGO [125]; MOF-199 [126]; MOF-199-AC [126].

Com. AC = Commercial activated carbon

[a] Gas composition: H_2S 10 000 ppm; Air 74.7%; N_2 24.3%; Moisture 100% RH

[b] Moisture is not included in the feed

The standardized experiments presented in **Figures 2.7a** provide a clearer overview of the sorbents analyzed by different authors, since they all conform to the same experimental conditions. A common trend is observed among non-impregnated ACs, such as Com. G55C (Pica),[95] Com. BAX 500 (Wetsvaco),[95] Com. S208C,[95] Com. RB4 (Norit),[95] Com. CSB S-208,[114] and the Sewage-sludge derived SC,[114] with H_2S separation capacities ranging from 36 $mg.g^{-1}$ to 92 $mg.g^{-1}$. In contrast, a distinct trend is observed among impregnated ACs, including Com. G55C-NaOH,[95] Com. BAX-500-NaOH,[95] Com. S208C-NaOH,[95] Com.RB4-NaOH,[95] Com. Coal based I-1-KOH,[94] Com. Coal based II-OH,[94] Com. STIX,[114] and Com. Centaur (NI).[114] These show significantly higher adsorption capacities, ranging from 180 $mg.g^{-1}$ to 320 $mg.g^{-1}$, due to impregnation with NaOH, KOH or MgO. This confirms that impregnation is a crucial step in the preparation of high-performance ACs.

Whether AC is wood- or coal-based, and despite similar surface areas, H_2S adsorption performance per sorbent mass remains comparable, as reported in the literature. However, in industrial applications, separation capacity per sorbent volume is more critical, as it has a direct impact on the amount of carbon to be packed into a column and, consequently, on operating costs. It is therefore essential to select carbons with a high bulk density, which is a potential problem with some wood-based carbons. To be competitive, bulk density should be at least 400 $kg.m^{-3}$; otherwise, even a carbon with good H_2S separation per mass unit may have a low separation capacity per sorbent volume. The literature often focusses on separation by sorbent mass, with the bulk densities of the carbons involved sometimes not being reported.

2.2.1.4 Gas containing inert gas and H_2S

Studies involving H_2S with N_2 or He have also been carried out. This experimental setup may not exactly represent synthetic biogas conditions, but it serves as an initial screening process to identify effective sorbents for H_2S separation. Several examples of ACs, zeolites and MOFs are presented in **Figure 2.8**. When analyzing H_2S inlet compositions ranging from 100

to 2000 ppm (**see Figure 2.8a**), ACs outperform the other materials; conversely, when considering H_2S inlets of less than 100 ppm (see **Figure 2.8b**), all materials appear to exhibit similar performance. However, it should be noted that a lack of studies may contribute to limiting the possibilities of making clearer comparisons.

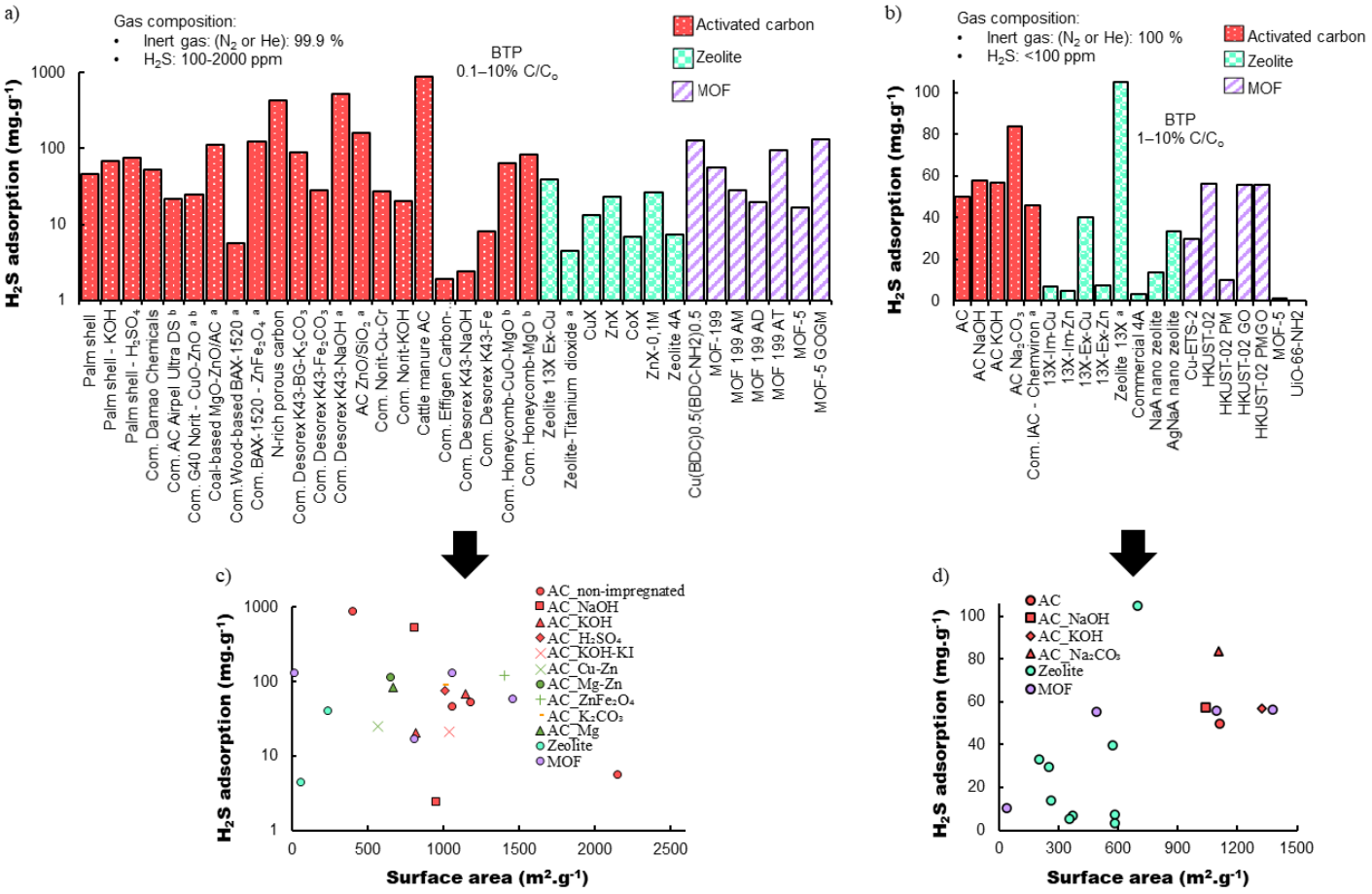

Figure 2.8 Studies on H_2S removal from a gas mixture comprising an inert gas and H_2S. H_2S adsorption capacity at concentrations: a) between 100 to 2000 ppm, and b) of less than 100 ppm; H_2S adsorption capacity as a function of surface area for the materials shown: c) in Figure 2.8a, and d) in Figure 2.8b (See Tables 1.6 to 1.9 for reference).

Palm shell [127]; Palm shell-KOH [127]; Palm shell-H_2SO_4 [127]; Com. Damao chemicals [127]; Com. AC Airpel Ultra DS [112]; Com. Darco G40 Norit Cu-Zn [128]; Coal based MgZn/AC [97]; Com. Wood based BAX-1520 [129]; Com. BAX-1520 $ZnFE_2O_4$ [129]; Com. Desorex K43-BG-K_2CO_3 [96] - Com. Desorex K43-BG-Fe_2CO_3 [96] - Com. Desorex K43-NaOH [96]; AC ZnO/SiO2 [115]; Com. Norit-Cu-Cr [98]; Com. Norit-KOH [98]; Cattle manure AC [99]; Com. Effigen Carbon-ZnAC2/ZnO [130]; Com. Desorex K43-NaOH [131]; Com. Desorex K43-Fe [131] - Com. Honeycumb-Cu-Mg [132] - Com. Honeycumb-Cu- [132] - Zeolite 13X Ex-Cu [107]; Zeolite titanium dioxide [133]; CuX [134]; ZnX [134]; CoX [134]; ZnX-0.1M [134]; Zeolite 4A [135] ; Cu(BDC)0.5(BDC-NH2)0.5 [136]; MOF-199 [137]; MOF199 AM [137] - MOF 199 AD [137]; MOF 199 AT [137]; MOF-5 [138]; MOF-5 GOGM [138] - AC [92]; AC NaOH [92]; AC KOH [92]; AC Na_2CO_3 [92]; Com. IAC Chemvirion [103] ; 13X-Im-Cu [92]; 13X Im-Zn [92]; 13X Ex-Cu [92]; 13X Ex-Zn [92]; Zeolite 13X [103]; Commercial 4A [139]; NaA nano zeolite [139]; AgNaA nano zeolite [139]; Cu-ETS-2 [140]; HKUST-02 [141]; HKUST-02 PM [141]; HKUST-02 GO [141]; HKUST-02 PMGO [141]; MOF-5 [101]; UiO-66 NH_2 [101].

[a] Moisture conditions
[b] Oxygen in the feed gas composition
[c] Breakthrough at 0.02%

AC derived from cattle manure exhibits notable separation performance,[99] well above that of its counterparts, with a separation capacity of over 850 $mg.g^{-1}$. Although it is non-modified and has a surprising low surface of 408 $m^2.g^{-1}$, its high adsorption capacity may be attributed to the presence of minerals such as Ca, Na, K, Mg, P and Fe on its surface, which catalyze the oxidation of H_2S. In addition, the commercial AC Desorex K43-NaOH,[96] impregnated with NaOH and with a surface area of 815 $m^2.g^{-1}$, achieved an H_2S separation capacity of 520.4 $mg.g^{-1}$, tripling the amount adsorbed compared with other materials.

Zeolites generally perform significantly worse than ACs and MOFs for H_2S separation, except when H_2S concentrations are below 100 ppm. This is due to their low surface area (see **Figure 2.8c** and **2.8d**), sub-optimal pore sizes for H_2S molecules (0.36 nm) and a chemical composition and structure less suited to H_2S affinity. Although zeolites may perform better at H_2S concentrations below 100 ppm, such scenarios are uncommon in biogas purification. **Figure 2.8c** and **2.8d** illustrate the relationship between surface area and H_2S adsorption capacity. Once more, surface area alone does not dictate excellent performance, and it is essential to achieve optimum impregnation levels, surface area and microporosity for each material. It is worth noting that impregnation can lead to a reduction in pore space, highlighting the need for careful optimization.

2.2.2 Challenges in biogas desulfurization

Several challenges can be identified in this area:

Unintended interactions: Unintended interactions between contaminants and adsorbent can affect process efficiency primarily through competitive adsorption. In this phenomenon, contaminants such as siloxanes, VOCs and CO_2 compete for the same adsorption sites on the AC surface. Although such competition is an inherent aspect of the process, because pure biogas first passes through the desulfurization stage, ACs remain highly effective in achieving their primary objective: the efficient removal of H_2S. The influence of competing contaminants on removal efficiency varies. For example, zeolites exhibit strong adsorption for CO_2, which is the most important contaminant due to its high concentration, which can reduce their effectiveness for other target molecules. In contrast, ACs are less selective for CO_2, enabling them to be more effective at trapping H_2S, even in gas streams with high CO_2 content.[142] This inherent selectivity is a key factor in the superior performance of ACs in H_2S separation, despite the challenges posed by competing contaminants.

Functionalization of adsorbent: Commercial ACs designed for biogas desulfurization are modified with alkaline impregnates to improve their performance. However, these impregnates can lower the AC's ignition temperature, necessitating special handling precautions to mitigate safety risks. While these modifications improve desulfurization efficiency, they can also pose problems. For example, alkaline substances such as KOH and NaOH can react with water and carbon monoxide, producing bulky carbonates. These carbonates can accumulate in the pores of the AC, causing pore blockages, particle aggregation and increased resistance to air flow in adsorption columns.[143] Impregnation or doping also increases costs due to the addition of materials and processing. Ideally, non-modified ACs would completely eliminate these problems and offer a significantly improved environmental footprint.

Flow pattern in adsorption columns: The adsorption bed can encounter problems such as the channeling effect, where gas flow follows preferential pathways instead of being evenly distributed throughout the entire adsorbent volume. This leads to the formation of "dead zones", which reduce separation efficiency since a substantial part of the bed remains under-utilized. To remedy this problem, specific design recommendations have been proposed. These include ensuring that the bed diameter is at least 10 times greater than the diameter of the adsorbent particles, and that the bed length is at least three times greater than its diameter, particularly in lab-scale test facilities.[144]

Shape of adsorbent: The efficiency of the adsorption process largely depends on the time required for H_2S molecules to break through the adsorption column. Adsorbents in powder form generally demonstrate superior performance to those in pelletized form, as their structure allows H_2S molecules easier access to the micropores. However, powders also create excessive pressure drops, which hinder industrial process optimization by increasing energy consumption due to additional gas compression. Moreover, powders are difficult to handle, as they release fine particles that can contaminate equipment and pose safety risks to personnel. For these reasons, most commercial adsorbents are pelletized. Pelletized adsorbents minimize pressure drop, improve handling safety and increase adsorbent density, thereby optimizing the total adsorbent volume in the column and improving overall process performance.

2.2.3 Assessment of adsorbents

Beyond the efficiency of adsorbents, it is essential to understand their environmental impact, energy consumption and reusability throughout their life cycle, from production and functionalization to regeneration and disposal, in order to choose the most sustainable option.

Specific studies on the life cycle of adsorbents for biogas desulfurization are lacking, as most existing publications focus on improving the separation efficiency of individual adsorbents. The only life cycle assessment dealing with biogas desulfurization is the study by Cano et al.,[145] which compared four technologies for removing H_2S from biogas produced in sewage treatment plants and containing 3000 ppm H_2S. The technologies assessed were biotrickling filtration, anoxic biotrickling filtration, caustic chemical scrubbing, and adsorption on KOH-impregnated AC. The results indicate that biological technologies are more environmentally friendly than adsorption on AC and chemical scrubbing, with chemical scrubbing being the least sustainable option. However, further studies are needed to draw clearer conclusions, as biogas production processes can vary significantly, with flow rate and H_2S concentration strongly influencing the performance and sustainability of each technology.

Table 2.8 provides an overview of the characteristics of adsorbents used in biogas desulfurization processes, highlighting their life-cycle features, including production processes, use, regeneration potential and cost. All adsorbents face a common challenge: the difficulty of regeneration, leading to their disposal by controlled incineration after use. The primary factors differentiating adsorbents are their production costs and performance features. The best-performing adsorbents demonstrate superior H_2S selectivity and high separation capacities, while maintaining cost-effectiveness.

In this context, ACs and metal-based adsorbents, particularly iron-based ones, are both competitive and cost-effective. In fact, they are the only commercially viable option for biogas desulfurization. Additionally, higher separation capacities translate into extended adsorbent usage, reducing the need for frequent replacement.

ACs and metal-based adsorbents are highly competitive in terms of cost, being significantly cheaper than zeolites and MOFs. However, further research is needed to determine which option, taking into account the overall ecological impact, is the best for biogas desulfurization. ACs are generally derived from carbon-rich precursors such as biomass or coal, which undergo activation to enhance porosity, while metal-based adsorbents often require more complex synthesis steps. These differences in production influence not only their cost and availability, but also their environmental impact, which should be taken into account in overall evaluations of their suitability for biogas desulfurization.

Table 2.8 Performance parameters of adsorbents for biogas desulfurization.

	AC 	**Zeolite** 	**MOF** 	**Metal-based adsorbents** 
Production	- Source: Carbon-rich precursors like coal, coconut-shell or wood - Activation: steam at high temperature (800-1000 °C) - Functionalization: with caustic substances - Shaping / densification	- Source: silica and alumina - Zeolite synthesis - Functionalization: ion exchange with metal ions - Shaping / densification	- Source: metal ions/clusters with organic ligands - Synthesis - Functionalization: Incorporation of metals - Shaping / densification	-Source: minerals, clay, biomaterials -Synthesis: precipitation, thermal decomposition - Functionalization: doping with metals or forming composites - Shaping / densification
Use	- Physisorption / chemisorption in adsorption columns at ambient temperature			- Mostly chemisorption in bed reactors at high temperature (> 400 °C), although ambient temperature is also applied, but less effective
H_2S separation under CO_2 and CH_4 ($mg \cdot g^{-1}$)	30 - 60	20	No data	No data
H_2S separation under N_2 ($mg \cdot g^{-1}$)	850	40	130	260
Regeneration	- Thermal regeneration at lab-scale. Some commercial ACs are re-activated and re-functionalized	- Thermal regeneration at lab-scale	- Thermal regeneration and/or re-functionalization at lab-scale	- Oxidative regeneration at lab-scale
Disposal	- Hazardous waste classification - Incineration			
Cost ($USD \cdot kg^{-1}$)	0.8[a]	1.8 – 3.0[a]	10.0 – 70.0 [142]	0.3 – 2.0[a]

[a] Cost on the Chinese market; the cost of zeolites is intended for CO_2/CH_4 separation.
NB: The cost of MOFs is not intended for biogas desulfurization applications.

2.2.4 Simulation of H_2S separation from biogas

Modelling and simulation of a fixed-bed adsorption column is important for performance optimization, scaling-up for industrial applications, breakthrough point prediction and saturation estimation. It consists of a mathematical model that includes the interaction between fluid flow and the mass transfer process. The system is solved by numerical integration to determine the behaviour of the various variables as a function of time.

Simulating sorbents for high-temperature applications, such as metal oxides, is more complex due to the significant role of interactions between H_2S molecules and active metal oxide surfaces. These interactions necessitate the use of 3-dimensional models that incorporate chemical reaction equations and heat transfer dynamics, which are generally omitted in low-temperature (< 40 °C) adsorption simulations. For example, Fe_2O_3-based red clay sorbent was modelled using COMSOL Multiphysics software, enabling desulfurization and regeneration processes to be predicted, by implementing sophisticated mathematical model.[146]

Table 2.9 summarizes the mathematical models used to simulate fixed-bed adsorption columns for biogas desulfurization. The governing equations include mass balance and adsorption onto the adsorbent, which is described by the adsorption isotherms and kinetics. These kinds of models assume a 1-dimensional system, with ideal gas behaviour and no radial variation. The adsorbent particles are spherical and homogeneous in size and density. The linear velocity is constant and the pressure drop across the column is negligible.

Table 2.9 Dynamic models for biogas desulfurization through fixed-bed adsorption columns.

Adsorbent	Gas composition	Flow pattern	Isotherm	Mass transfer kinetics	Solver software	Ref.
Treated sewage-sludge	H_2S 2000 ppm - CH_4 60% - CO_2 40%	PF	Langmuir - Freundlich	LDF	Aspen Adsorption V7.1	[147]
Treated sewage-sludge	H_2S 2000 ppm - CH_4 60% - CO_2 40%	ADPF	Langmuir - Freundlich	LDF	COMSOL Multiphysics 4.3a	[148]
AC-Na_2CO_3	H_2S 1000 ppm - N_2 100%	ADPF	Langmuir	LDF	No data	[149]
Babassu biochar	H_2S 1000 ppm - N_2 100%	ADPF	Langmuir	LDF	Maple	[150]
Commercial AC, AirDep CKC	H_2S 500 ppm - CO_2 40% - CH_4 60% - O_2 0.1%	ADPF	Langmuir	LDF	MATLAB	[151]
Zeolite NaY	H_2S 23500 ppm (2.3%) - He 97.7%	PF	Toth	LDF	Maple	[152]

- Mass balance equation

Most approaches apply the axially dispersed plug flow (ADPF) model to describe fluid flow as presented in Eq. 30 [148–151] (see demonstration in Annex 1).

$$-D_L \frac{\partial^2 c}{\partial Z^2} + \frac{\partial}{\partial Z}(vc) + \frac{\partial c}{\partial t} + \frac{(1-\varepsilon)}{\varepsilon}\frac{\partial q_i}{\partial \mathrm{t}} = 0 \qquad (2.18)$$

where D_L is the axial dispersion coefficient, c is the concentration of H_2S in the gas phase, Z is the axial position along the column, v is the gas superficial velocity, t is the time, ε is the bed porosity and $\bar{q}$ is the average concentration of H_2S adsorbed.

Axial mixing caused by fluid flow through a packed bed reduces separation efficiency, making its minimization a design priority.[144] If mass transfer resistance is significantly greater than axial dispersion, D_L can be ignored and the system of equations can take the form of the ideal plug flow (PF) model:[147, 152]

$$\frac{\partial}{\partial Z}(vc) + \frac{\partial c}{\partial t} + \frac{(1-\varepsilon)}{\varepsilon}\frac{\partial \bar{q}}{\partial \mathrm{t}} = 0 \qquad (2.19)$$

However, the ADPF model is preferred to the PF model for its realistic dispersion, its better prediction of the breakthrough curve, its consideration of non-ideal column packing, its accurate resistance to mass transfer and its suitability for scale-up from laboratory to industry.[142]

- Adsorption

Equilibrium isotherms of adsorption are often generated by performing breakthrough curve experiments at several H_2S concentrations (H_2S partial pressure) and calculating their adsorption capacities at full saturation. Several isotherm models, including Langmuir,[147–151] Toth,[152] and Freundlich,[147, 148] can effectively describe the experimental data. Among these, the Langmuir model is the most commonly used, as represented by equation 32:

$$q^* = \frac{q_s b C}{1 + bC} \qquad (2.20)$$

where q^* is the amount of H_2S adsorbed per unit mass of adsorbent, q_s is the saturation capacity, b is the Langmuir adsorption equilibrium constant and C is the H_2S concentration in the gas phase.[150]

Due to the mass transfer resistance inherent to the adsorption process, instantaneous equilibrium is not achieved. Therefore, a rate expression is employed to determine the amount of H_2S adsorbed ($\bar{q}$). The resistance to adsorption involves interparticle transport (external to the particles) occurring in series with intraparticle transport (within the particles).[153] Consequently, modelling mass flow from a fluid to a solid requires a method for estimating the mass transfer coefficient. The linear driving force (LDF) model is commonly applied, as seen in all the cases presented in **Table 2.9**,[59–62, 66, 154, 155] and presented in Eq. 33:

$$\frac{\partial q_i}{\partial t} = k.(q^* - q_i) \quad (2.21)$$

where k is the rate constant for H_2S adsorption, q^* is the amount of H_2S adsorbed at equilibrium under current conditions and q is the amount of H_2S currently adsorbed. k can be determined by fitting the curve of experimental data and simulation results or by correlations such as the Wilson and Geankoplis correlation.[149] The resulting mathematical model consists of a set of partial differential equations (PDEs), which are usually solved by commercial software such as Aspen,[147] Comsol,[148] Maple[150, 152] and Matlab.[151] Although not yet published for H_2S simulation, the use of ProSim, FAST or gPROMS software is also possible.

- Temperature dependence

During the dynamic process of biogas desulfurization, CO_2 is rapidly adsorbed, saturating the adsorbent in seconds at the lab scale. In contrast, saturation by H_2S occurs much more gradually, taking hours or even days. This rapid CO_2 adsorption at the start of the process can lead to an increase in temperature during this period, as has been observed in pressure swing adsorption processes using columns filled with carbon molecular sieve, where temperature variations of up to 20 °C have been reported.[156] Although the heat of adsorption for H_2S is comparable to that of CO_2,[142] ranging from -27 to -47 kJ·mol^{-1} for AC,[157, 158] -32 to -42 kJ·mol^{-1} for zeolites,[152] and -23 to -41 kJ·mol^{-1} for MOFs,[159] the much slower adsorption of H_2S due to its low concentration, usually in the ppm range, allows the heat generated to dissipate rapidly, stabilized by the surrounding temperature of the adsorption column. Therefore, the isothermal assumption is valid.

- Ideal gas assumption

The behavior of bulk gas is modelled in all cases using the ideal gas law. This assumption, in which the compressibility factor (z) is equal to 1, can lead to modelling inaccuracies, particularly at high pressures and low temperatures. To illustrate the impact of operating conditions on H_2S separation, **Figure 2.9** shows the variation in the compressibility factor (z) from the ideal gas assumption. $1 - z$ (delta z), is calculated using the NIST Reference Fluid Thermodynamic and Transport Properties Database (REFPROP-version 10.0).[68]

At a common operating pressure of 1 bar and a temperature of 25 °C, the compressibility factor for H_2S is 0.9, resulting in a delta z of 0.01, which can be interpreted as ideal gas behavior. However, as pressure increases, deviations become more significant. At a pressure of 15 bar and 25 °C, a condition that could be possible on an industrial scale, the compressibility factor

is 0.88 (1-*z* = 0.12), indicating a deviation of over 10% from ideal gas behavior. Under these conditions, it is advisable to take into account the real gas behavior by using appropriate correlations or property data from databases.

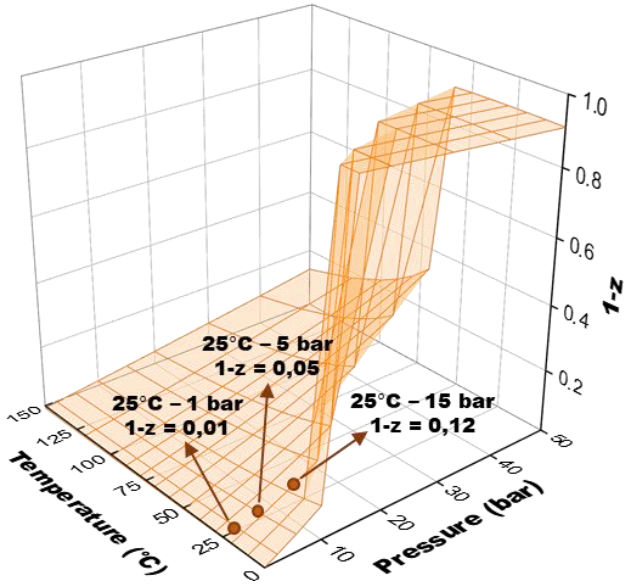

Figure 2.9 1-*z* (*z* being the compressibility factor) for H_2S as a function of temperature and pressure.

- The problem of bed porosity

The literature includes a limited number of examples focusing on the modelling and simulation of H_2S adsorption on various materials, as shown in **Table 2.9**. Among these, some authors have reported high values for bed porosity, such as 0.7 [151] and 0.8,[147, 148] without specifying whether they were determined by calculation or experimental measurement. These values indicate that over 70% or 80% of the adsorption column would be empty, which seems unlikely. In contrast, leading researchers in fixed-bed adsorption simulations routinely use the correlation proposed by Ribeiro et al.[160] to determine bed porosity from bed and particle diameters. Applying this correlation to the aforementioned cases[147, 148, 151] gives a bed porosity of 0.37, a much more realistic value. Bed porosity has a significantly influence on simulation results, as demonstrated by Papurello et al.,[151] who showed that a variation of just 0.1 (10%) could alter the breakthrough time by nearly 50%. Careful consideration of this parameter is therefore recommended for accurate modelling and simulation.

2.2.5 Sorbent regeneration

The industrial applicability of a sorbent relies on its ability to regenerate, a crucial factor in its assessment. Disposal of non-regenerable sorbents presents a hazardous waste risk due to the

presence of sulfuric acid, an oxidation product of the H_2S separation process.[161] When using AC, the substitution with new AC has been proposed as a means of reducing operating costs due to expensive regeneration.[99] Nevertheless, partial regeneration of the sorbent, at least 10 to 14 cycles before recharging the fixed bed with fresh sorbent, results in a saving of 80% compared with using a completely new sorbent after the first adsorption.[162]

Regeneration of sorbents for H_2S separation can pose certain difficulties by reducing their adsorption capacity after each regeneration cycle, as adsorbed H_2S molecules undergo irreversible reactions. It has been observed that during thermal regeneration, the release of SO_2 generates acidic functional groups on carbon, which may prevent efficient H_2S removal.[163]

2.2.5.1 Regeneration methods

- Thermal regeneration

This method involves heating saturated AC to high temperatures (between 100 and 600 °C) under a flow of N_2 or air to desorb H_2S and other contaminants. The heat treatment process involves, first, the removal of H_2O physically adsorbed, with a temperature range up to 100 °C. Then, in a temperature range of 200 °C to 400 °C, the process focuses on extracting the elemental S stored in the adsorbent pores.[129] The effective removal of the majority of sulfur species retained on the sorbent has also been reported, at 600 °C, by means of an inert gas flow.[132] Finally, the temperature range from 500 to 1000 °C corresponds to the decomposition of oxygen-containing groups and the reduction of the impregnating agent.[129] One of the disadvantages of this method is the high energy consumption for heating.

- Water-based regeneration

This involves washing saturated AC with water to remove adsorbed contaminants. This method takes advantage of the solubility of certain substances dissolved in water, enabling them to be removed and restoring some of the AC's adsorption capacity. It is viable when the byproducts of H_2S oxidation are water-soluble acids like sulfuric acid (H_2SO_4), as it is the case with carbons modified by metal loading of high catalytic activity. However, this method is not applicable to caustic carbon, (e.g. NaOH-impregnated AC) where the primary product, sulfur, is found in small pores[120] (see again Eq. (22) and (23)) and is insoluble in water.[123] After the initial adsorption/regeneration cycle, the pH of the sorbents, typically above 9 when fresh, decreases to below 5 due to the formation of acidic byproducts resulting from the acid-base reaction.[120] This represents an additional challenge for maintaining the original adsorption

capacity. To solve this problem, a washing step with distilled water was employed to raise the pH to above 6. [163, 164]

2.2.5.2 Regeneration results for H_2S-saturated sorbents

Table 2.10 shows the different methods used to treat H_2S-saturated sorbents. Separation capacity after each regeneration cycle and total separation degradation are shown in **Figure 2.10.**

None of the sorbents regenerated in the examples included CO_2 in the composition of the gas evaluated, making the process non-representative of biogas scenarios, CO_2 being the principal biogas contaminant.

Micropores are the main sites where most H_2S adsorption or oxidation products accumulate. During thermal regeneration of porous carbon, the reduction in adsorption efficiency compared with fresh sample is probably due to a reaction between the desulfurization product (SO_4^{2-}) and the carbon framework, leading to carbon loss. In addition, the release of significant amounts of SO_2 generates acidic functional groups on the carbon surface, which can hinder H_2S removal.[163]

When regenerating ACs by washing, a significant portion of the initial adsorption capacity is irreversibly lost after the first cycle. This loss is attributed to the permanent depletion of the most active adsorption sites in the micropores, where sulfur forms strong, persistent bonds.[120]

Given the solubility of alkali sulfates and the limited solubility of sulfur (S) in water, a two-step regeneration method was employed for nitrogen-rich hierarchical porous carbons. The process involved water scrubbing to remove sulfates, followed by heating to eliminate sulfur. This approach resulted in an acceptable degradation rate of 13.4% over five regeneration cycles, with adsorption capacity decreasing from 426.2 $mg \cdot g^{-1}$ to 368.9 $mg \cdot g^{-1}$.[163]

Table 2.10 Regeneration methods of H_2S-saturated sorbents.

Sample	Gas composition	Regeneration method	Cycles – Adsorption Degradation (%)	Ref.
Com. BAX-1520 AC	H_2S 1000 ppm; N_2 99.9%; Moisture	N_2 at 150 mL.min^{-1} for 2h with a heating rate of 5 °C.min^{-1} up to 500 °C	3 - 2.2	[129]
$ZnFe_2O_4$-loaded biochar	H_2S 300 ppm; N_2 100%	Calcination in N_2-atmosphere at 500 °C for 2h; Ultra-pure water wash until pH ≈ 7; Vacuum dry at 60 °C	5 - 8.3	[164]
AgNaA Zeolite	H_2S 15 ppm; N_2 100 %	Air flow at 350 °C for 2h at 200 mL.min^{-1}	4 - 13.0	[139]
Composite UiO66-Graphene oxide ZMGO-3	H_2S 4500 ppm; N_2 100%	N_2 flow at 200 °C	3 - 13.0	[161]
N-rich hierarchical porous carbons	H_2S 1000 ppm; O_2 1%; N_2 99%; Moisture	Ultrasonic scrubbing with distilled water at 80 °C until pH=6.5; Calcination in N_2-atmosphere at 400 °C for 1 h with a heating rate of 5 °C.min-1	5 – 13.4	[163]
N_2-doped carbon	H_2S 1000 ppm; N_2 99.9%	N_2 flow at 120 °C	4 - 27.2	[165]
Desorex K43 AC Desorex K43-Fe AC Desorex K43-Na AC	H_2S 100 ppm; He 100%	He at 15 mL.min^{-1} at 150 °C during 12h	3 - 33.3 3 - 80.0 3 - 78.9	[131]
Zeolite ZnX	H_2S 100 ppm; N_2 100%	Vacuum condition at 200 °C for 2h	1 - 41.5	[134]
AC-$ZnAc_2$-ZnO-KOH	H_2S 5000 ppm; N_2 99.5%	Air flow at 50 °C Air flow at 100 °C Air flow at 150 °C	3 - 63.0 3 - 58.9 3 - 51.0	[130]
Composite AC-Mesoporous silica Zno/SiO_2	H_2S 800 ppm; N_2 100%; Moisture	100 mL.min^{-1} of 20% O_2 and 80% N_2 for 5h at 500 °C	3 - 56.2	[166]
Zeolite 4A	H_2S 860 ppm; N_2 100%	N_2 at 350 °C for 2h at 200 mL.min^{-1}	4 - 64.8	[135]
CuBDC MOF	H_2S 500 ppm; unknown gas	200 mg of MOF were stirred in 10 mL of methanol for 24 h at 300 rpm; Separation of MOF by centrifugation and drying at 70 °C for 24 h – MOF irradiation in a 1.0 L Pyrex tube fitted in an acryl reactor with 4 UV lamps (19 W. UV-C. I_{max} 254 nm) for 4h in N_2 environment	1 - 70.4	[167]
Com. S208c AC SW AC	H_2S 3000 ppm; Air 99.7%; Moisture	5 washing cycles with 150 mL of cold water for 30 min for 18g of carbon in a beaker 5 washing cycles with 200 mL of hot water each cycle. for 18g of carbon in a Soxhlet apparatus	3 - 79.2 3 - 70.4	[120]
Zeolite 20Zn/ZA	H_2S 200 ppm; N_2 100 %	Heating at 100 °C Heating at 200 °C Heating at 300 °C	2 - 80.8 2 - 86.7 2 - 90.9	[168]
$Cu(BDC)_{0.5}(BDC\text{-}NH_2)_{0.5}$	H_2S 500 ppm; N_2 100%	1 g of MOF was stirred in 50 mL of methanol for 24 h at 600 rpm – Separation of MOF by centrifugation and drying at 70 °C for 48 h – MOF irradiation in a 1.0 L Pyrex tube fitted in an acryl reactor with 4 UV lamps (20 W each. UV-C. I_{max} ~254 nm) in a N_2/O_2 environment	2 - 86.4 2 - 92.3	[136]

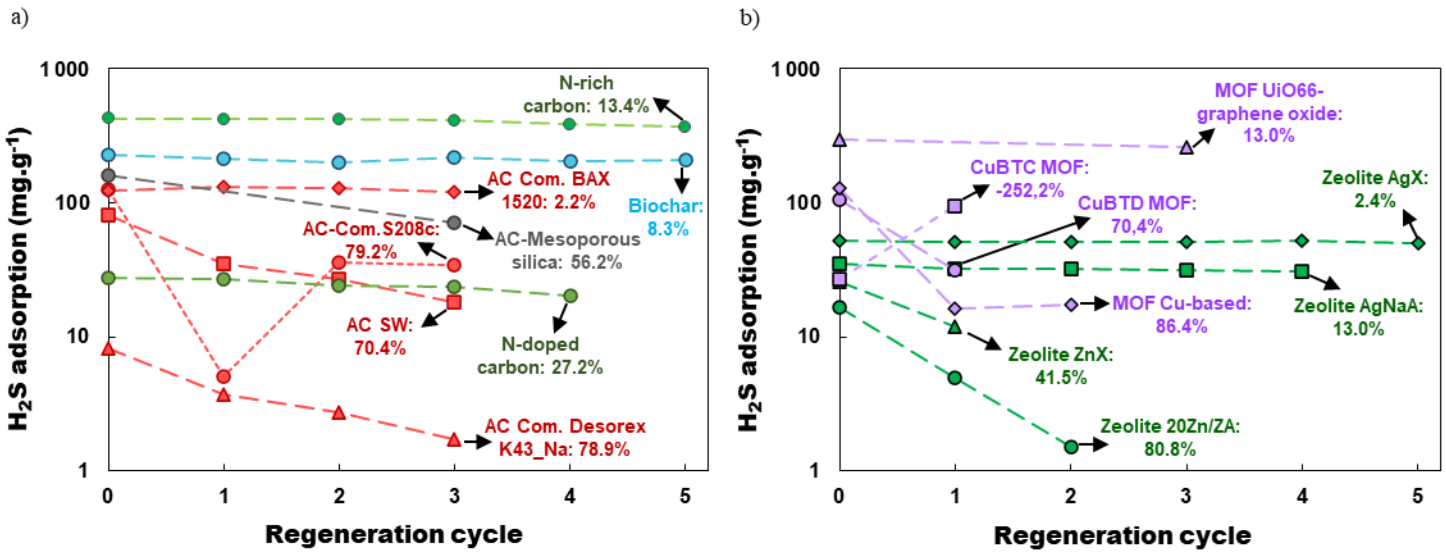

Figure 2.10 H_2S separation capacity after each regeneration cycle and corresponding degradation of the separation capacity: a) Carbon-based materials; b) Zeolites and MOFs.

$ZnFe_2O_4$-biochar [164]; Com. S208C AC [120]; SW AC [120]; Com. BAX-1520 AC [129]; Desorex K43-Na AC [131]; N_2-doped Carbon [165]; AC-Mesoporous silica [166]; N-rich porous carbon [163]; Zeolite 20Zn/ZA [168]; AgNaA Zeolite [139]; Zeolite AgX [169]; Zeolite ZnX [134]; CuBDC MOF [167]; CuBTC MOF [167]; Cu-based MOF [136]; ZMGO-3 [161]

Two zeolites, AgNaA [139] and ZnX,[134] retained their structural integrity after regeneration with airflow at 350 °C and heating at 200 °C under vacuum, as confirmed by XRD and SEM analyses. However, their adsorption performance was negatively affected. AgNaA zeolite exhibited a slight reduction in adsorption capacity of 13% after four regeneration cycles, from 35.3 mg·g^{-1} to 30.7 mg·g^{-1}. In contrast, ZnX zeolite experienced a significantly higher degradation rate of 41.5%, with its adsorption capacity falling from 26.0 mg·g^{-1} to 15.2 mg·g^{-1}.

Thermal regeneration at low temperatures, such as 150 °C, is insufficient to fully regenerate the sorbent. This limitation arises from the strong chemical bonds formed between H_2S molecules and the impregnates, as well as pore blockage caused by sulfur deposition. For example, the commercial AC Desorex K43-Na showed a significant 78.9% degradation in adsorption capacity after four regeneration cycles using helium flow at 150 °C.[131]

The best case of successful regeneration was observed with a commercial wood-based AC modified with a $ZnFe_2O_4$ loading (Com. BAX-1520).[129] The fresh carbon adsorbed 122.5 mg·g^{-1} of H_2S. After three cycles of regeneration with N_2 flow at 500 °C, the adsorbent retained an adsorption capacity of 119.8 mg·g^{-1} of H_2S, showing only a 2.2% degradation. According to

the authors, temperatures below 500 °C led to the decomposition of surface reaction products. At 500 °C, the $ZnFe_2O_4$ loading remains intact in the carbon structure, as it degrades at temperatures above 500 °C. This result is somewhat surprising because, although $ZnFe_2O_4$ is unaffected at 500 °C, it is expected to react completely and form sulfide products, which would imply that it should not be available for subsequent cycles after regeneration.

AgX zeolite showed comparable performance, with a very low degradation rate of 2.4% after exposure to airflow at 350 °C for 2 hours. Its initial adsorption capacity of 52.2 $mg \cdot g^{-1}$ decreased only slightly to 51.0 $mg \cdot g^{-1}$ after four regeneration cycles.[169]

A biochar synthesized by mixing leftover rice with $ZnCl_2$ and $FeCl_3$, followed by heat-treatment at 500 °C under N_2 flow,[164] also achieved good degradation of just 8.3% after the 5th regeneration cycle. The sample was heat-treated in N_2 atmosphere at 500 °C for 2h, the recycled carbon material was washed with ultra-pure water until the pH of filtrate reached around 7, then dried under vacuum at 60 °C. An acceptable degradation of 13% was also obtained after 4 regeneration cycles for a Zr-MOF (UiO-66) - GO nanocomposite:[161] initially, it separated 296.6 $mg.g^{-1}$ of H_2S and then, after 4 regeneration cycles, the separation was 258.1 $mg \cdot g^{-1}$ of H_2S. The regeneration method was carried out under N_2 flow at 200 °C.

An airflow at 350 °C was found to be optimal for the zeolite AgNaA, leading to only a 13% reduction in adsorption capacity after four regeneration cycles (decreasing from 35.3 $mg \cdot g^{-1}$ to 30.7 $mg \cdot g^{-1}$). The sorbent preserved its structural integrity, with XRD and SEM analyses revealing no significant changes in its morphology or crystal phase.

Air and nitrogen flow have been used at high temperature for various zeolites and carbon-based adsorbents,[130, 135, 139, 161, 164–166] but after a few cycles, the percentage of degradation can increase from 13 to 90%. Helium at 150 °C for 12h was also tried for AC,[131] but the degradation rate after 3 cycles was 33.3% for the non-impregnated AC and almost 80% for impregnated ACs.

Unfortunately, the three best cases of successful regeneration, with degradation rates lower than 13% after three regeneration cycles, have not studied in deep the structural changes of the materials after regeneration.

MOFs were subjected to complex regeneration methods involving stirring in methanol and irradiation. This regeneration process showed limited success, with adsorption degradations above 70%.[136, 167] For instance, fresh CuBDC MOF initially adsorbed 105.6 $mg.g^{-1}$ of H_2S.[167]

However after undergoing a regeneration process (stirring in methanol for 24h, centrifugation, drying at 70 °C for 24h and irradiation with 4 UV lamps for 4h under N_2), the H_2S separation capacity decreased drastically to 31.3 $mg.g^{-1}$, presenting a degradation rate of 70.4% after just a single regeneration cycle. In a similar case, Cu-based MOF subjected to a similar regeneration process decreased H_2S separation from 128.4 $mg \cdot g^{-1}$ to 17.4 $mg \cdot g^{-1}$, [98] presenting a degradation rate of 86.4%. Due to its low performance and high energy consumption and cost, this type or regeneration is impractical for both lab-scale and industrial-scale applications.

However, this regeneration method proved highly effective when applied to the CuBTC MOF. It exhibited an exceptionally high adsorption capacity of 95.6 $mg \cdot g^{-1}$ during the first regeneration cycle, representing a significant increase over its initial capacity of 27.1 $mg \cdot g^{-1}$.[167] This improvement was attributed to the reactivation of Cu sites and the enhancement of surface area and porosity.

After the desulfurization process, the stability of the MOF was partially compromised. However, the spent CuBTC was successfully regenerated, as suggested by XRD and XPS analysis, which indicate that Cu-MOF sorbent, after chemisorbing H_2S, can be restored by the combined effects of methanol treatment and UV-C irradiation.[167] After H_2S adsorption, CuBTC surface area and pore volume decreased by 65% and 49%, respectively, due to the cleavage of Cu–carboxylate bonds caused by interactions between H_2S and Cu active sites. Remarkably, the regenerated CuBTC exhibited a surface area of 410.8 $m^2 \cdot g^{-1}$, exceeding the initial value of the fresh MOF (317.0 $m^2 \cdot g^{-1}$). Additionally, the pore volume improved significantly, increasing from 0.152 $cm^3 \cdot g^{-1}$ to 0.278 $cm^3 \cdot g^{-1}$ after regeneration.

Water washing would be a better solution than thermal regeneration, as it avoids consuming much energy. For a non-impregnated adsorbent, washing with water would remove all S products from the micropores, leaving a carbon with characteristics similar to those of fresh carbon. However, the results are limited and unsatisfactory. In one case, unmodified coconut-shell based AC was exposed to hot and cold water washing, with significant degradation of its adsorption capacity (70 to 80 %).[120] With cold water, the initial H_2S adsorption capacity of 125.0 $mg \cdot g^{-1}$ dropped to 26.0 $mg \cdot g^{-1}$ after the 3rd regeneration cycle.

2.3 Conclusions

In this chapter, various adsorbents were compared based on their selectivity for CO_2/CH_4 adsorption and their working capacity ratio in pressure swing adsorption (PSA) for biogas

upgrading. Zeolites exhibit significantly higher equilibrium selectivity, making them favorable for PSA units. While metal-organic frameworks (MOFs) may be an alternative, further research is needed for practical PSA application. Carbon molecular sieves (CMSs), despite lacking high equilibrium selectivity, are excellent PSA candidates due to exceptional kinetic selectivity, comparable to zeolites. Activated carbons (ACs), with lower selectivity, offer sustainability and cost-effectiveness. Despite extensive research, integrating results into real multi-column PSA systems is lacking. To foster global research efforts, the development of highly selective materials for CO_2 over CH_4 is crucial for global PSA process optimization.

The simulation of PSA systems was examined by comparing dynamic modeling from literature. All the studies utilize the axially dispersed plug flow model for describing fluid flow and they use the Multicomponent Langmuir isotherm and the Linear Driving Force model for equilibrium and mass transfer kinetics. Ideal gas behavior is assumed, although deviations at high pressures are accounted with equations of state. Achieving cycle steady state is essential for evaluating PSA performance, with optimization methods often focusing on maximizing CH_4 recovery and purity or reducing energy consumption.

A comparative analysis of PSA unit operations was conducted, integrating various performance parameters such as purity, recovery, productivity, and energy consumption. Our study revealed that, while obtaining high-purity CH_4 was relatively straightforward using various adsorbents or cycles, it is crucial to consider productivity and energy consumption, as these factors have a direct impact on the competitiveness and sustainability of the process. According to these results, we can assert that the most optimal approach for achieving high purity and productivity with low energy consumption is the cycle involving pressure equalization and sub-atmospheric regeneration with either zeolites or CMSs.

A bibliographical review on biogas desulfurization using adsorbent materials with H_2S separation capacities reported at breakthrough point has also been carried out. The literature generally focuses little on raw biogas and often excludes CO_2 in synthetic gas studies for all adsorbents except biochar and AC. Since CO_2 is the main contaminant in biogas and is present in high proportions, its exclusion limits the proper evaluation of the performance of adsorbents such as zeolites and MOFs for biogas upgrading purposes.

The application of MOFs to H_2S adsorption is a relatively new endeavor, but much remains to be explored. At present, MOFs and zeolites are not competitive with ACs. ACs are the most

optimal materials, and although they have to be functionalized by impregnation or metal loading, which implies a higher cost, improved separation makes them very competitive for industrial use.

Comparison of experiments carried out by different authors is difficult due to the significant influence of experimental conditions on the results. For biogas applications, a standardized method that includes the presence of CO_2 should be implemented. When analyzing the results of various experiments, it is important to take into account the effects of water and oxygen, both of which can have a positive impact on H_2S separation to some extent.

Finally, it should be pointed out that there are shortcomings in terms of regenerability. This limitation stems mainly from the irreversible reaction between H_2S molecules and surface functionalities. Although non-impregnated carbons are believed to be easily regenerable, the existing literature lacks sufficient studies to support this claim. While H_2S separation capacity may decrease after each regeneration cycle, at least some regeneration cycles still offer cost savings and environmental benefits, but future research should focus on the development of cost-effective, environmentally-friendly sorbents.

While the literature provides valuable insights, it often neglects the complexity of raw biogas by excluding CO_2 in synthetic gas studies, except when examining biochar and activated carbon (AC). Since CO_2 is a major biogas contaminant, its omission limits the comprehensive evaluation of adsorbents like zeolites and MOFs for biogas upgrading applications. Incorporating in standardized methods not only CO_2 but also water and oxygen, which can positively affect H_2S separation, would allow for more accurate assessments of adsorbent performance. MOFs, although relatively new H_2S sorbents, still show promise but are not yet competitive with ACs or zeolites. ACs remain the most effective materials, combining high separation efficiency with adaptability for industrial use, despite the need for costly functionalization via impregnation or metal loading.

Simulations of biogas desulfurization are still limited, and only a few examples were discussed in the present work. These examples often rely on similar mathematical models, many of which can be solved using commercially available software. However, challenges arise due to incomplete presentation of the data needed for accurate modeling. For instance, there are significant discrepancies in bed porosity values reported under identical conditions for adsorbents sieved in small-scale laboratory adsorption columns. These discrepancies are not supported by any calculation or justification. To solve this problem, it is recommended that

mathematical models be presented in greater detail, with clear explanations of how the parameters and characteristics of the adsorbent-column configuration are derived.

Regenerability is another critical limitation. Irreversible reactions between H_2S molecules and adsorbent surface functionalities often hinder reuse. While non-impregnated ACs are believed to be regenerable, there is a lack of consistent evidence to substantiate this claim. Although H_2S separation capacity may decline after regeneration cycles, even partial regenerability can yield cost savings and environmental benefits. Future research should prioritize the development of cost-effective, environmentally-friendly sorbents that balance high performance with ease of regeneration, enabling a more sustainable approach to biogas desulfurization.

2.4 References

[1] Abd, A. A.; Naji, S. Z.; Hashim, A. S.; Othman, M. R. Carbon Dioxide Removal through Physical Adsorption Using Carbonaceous and Non-Carbonaceous Adsorbents: A Review. *Journal of Environmental Chemical Engineering*, **2020**, *8* (5), 104142. https://doi.org/10.1016/j.jece.2020.104142.

[2] Aghel, B.; Behaein, S.; Alobaid, F. CO2 Capture from Biogas by Biomass-Based Adsorbents: A Review. *Fuel*, **2022**, *328*, 125276. https://doi.org/10.1016/j.fuel.2022.125276.

[3] Bahrun, M. H. V.; Bono, A.; Othman, N.; Zaini, M. A. A. Carbon Dioxide Removal from Biogas through Pressure Swing Adsorption – A Review. *Chemical Engineering Research and Design*, **2022**, *183*, 285–306. https://doi.org/10.1016/j.cherd.2022.05.012.

[4] Abd, A. A.; Othman, M. R.; Naji, S. Z.; Hashim, A. S. Methane Enrichment in Biogas Mixture Using Pressure Swing Adsorption: Process Fundamental and Design Parameters. *Materials Today Sustainability*, **2021**, *11–12*, 100063. https://doi.org/10.1016/j.mtsust.2021.100063.

[5] Shah, G.; Ahmad, E.; Pant, K. K.; Vijay, V. K. Comprehending the Contemporary State of Art in Biogas Enrichment and CO2 Capture Technologies via Swing Adsorption. *International Journal of Hydrogen Energy*, **2021**, *46* (9), 6588–6612. https://doi.org/10.1016/j.ijhydene.2020.11.116.

[6] Grande, C. A. Biogas Upgrading by Pressure Swing Adsorption. In *Biofuel's Engineering Process Technology*; 2011.

[7] Hosseini, S. S.; Denayer, J. F. M. Biogas Upgrading by Adsorption Processes: Mathematical Modeling, Simulation and Optimization Approach – A Review. *Journal of Environmental Chemical Engineering*, **2022**, *10* (3), 107483. https://doi.org/10.1016/j.jece.2022.107483.

[8] Do, D. D. *Adsorption Analysis: Equilibria and Kinetics*; Imperial College Press: Queensland, Australia, 1998.

[9] Ahmadi, R.; Ardjmand, M.; Rashidi, A.; Rafizadeh, M. High Performance Novel Nanoadsorbents Derived - Natural Cellulose Fibers for Superior CO2 Adsorption and CO2 / CH4 Separation. *Energy Sources, Part A: Recovery, Utilization, and Environmental Effects*, **2020**, *0* (0), 1–19. https://doi.org/10.1080/15567036.2020.1845878.

[10] Ruthven, D. M. *Principles of Adsorption and Adsorption Processes*, A Wiley-Interscience publication.; JOHN WILEY & SONS: United States, 1984.

[11] Crittenden, Ba.; Thomas, J. *Adsorption Technology and Design*; Butterworth and Heinemann: Great Britain, 1998.

[12] Álvarez-Gutiérrez, N.; Gil, M. V.; Rubiera, F.; Pevida, C. Adsorption Performance Indicators for the CO2/CH4 Separation: Application to Biomass-Based Activated Carbons. *Fuel Processing Technology*, **2016**, *142*, 361–369. https://doi.org/10.1016/j.fuproc.2015.10.038.

[13] Abdeljaoued, A.; Querejeta, N.; Durán, I.; Álvarez-Gutiérrez, N.; Pevida, C.; Chahbani, M. Preparation and Evaluation of a Coconut Shell-Based Activated Carbon for CO2/CH4 Separation. *Energies*, **2018**, *11* (7), 1748. https://doi.org/10.3390/en11071748.

[14] Yang, H.; Gong, M.; Chen, Y. Preparation of Activated Carbons and Their Adsorption Properties for Greenhouse Gases: CH4 and CO2. *Journal of Natural Gas Chemistry*, **2011**, *20* (5), 460–464. https://doi.org/10.1016/S1003-9953(10)60232-0.

[15] Vivo-Vilches, J. F.; Pérez-Cadenas, A. F.; Maldonado-Hódar, F. J.; Carrasco-Marín, F.; Faria, R. P. V.; Ribeiro, A. M.; Ferreira, A. F. P.; Rodrigues, A. E. Biogas Upgrading by Selective Adsorption onto CO2 Activated Carbon from Wood Pellets. *Journal of Environmental Chemical Engineering*, **2017**, *5* (2), 1386–1393. https://doi.org/10.1016/j.jece.2017.02.015.

[16] Vilella, P. C.; Lira, J. A.; Azevedo, D. C. S.; Bastos-Neto, M.; Stefanutti, R. Preparation of Biomass-Based Activated Carbons and Their Evaluation for Biogas Upgrading Purposes. *Industrial Crops and Products*, **2017**, *109*, 134–140. https://doi.org/10.1016/j.indcrop.2017.08.017.

[17] Álvarez-Gutiérrez, N. Adsorption Performance Indicators for the CO2/CH4 Separation: Application to Biomass-Based Activated Carbons. *Fuel Processing Technology*, **2016**.

[18] Sun, Y.; Webley, P. A. Preparation of Activated Carbons with Large Specific Surface Areas from Biomass Corncob and Their Adsorption Equilibrium for Methane, Carbon Dioxide, Nitrogen, and Hydrogen. *Ind. Eng. Chem. Res.*, **2011**.

[19] Munusamy, K.; Somani, R. S.; Bajaj, H. C. Breakthrough Adsorption Studies of Mixed Gases on Mango (Mangifera IndicaL.) Seed Shell Derived Activated Carbon Extrudes. *Journal of Environmental Chemical Engineering*, **2015**, *3* (4), 2750–2759. https://doi.org/10.1016/j.jece.2015.05.010.

[20] Rainone, F.; D'Agostino, O.; Erto, A.; Balsamo, M.; Lancia, A. Biogas Upgrading by Adsorption onto Activated Carbon and Carbon Molecular Sieves: Experimental and Modelling Study in Binary CO2/CH4 Mixture. *Journal of Environmental Chemical Engineering*, **2021**, *9* (5), 106256. https://doi.org/10.1016/j.jece.2021.106256.

[21] Greco, G.; Canevesi, R. L. S.; Di Stasi, C.; Celzard, A.; Fierro, V.; Manyà, J. J. Biomass-Derived Carbons Physically Activated in One or Two Steps for CH4/CO2 Separation. *Renewable Energy*, **2022**, *191*, 122–133. https://doi.org/10.1016/j.renene.2022.04.035.

[22] Zhang, Y.; Zhang, P.; Yu, W.; Wang, J.; Deng, Q.; Yang, J.; Zeng, Z.; Xu, M.; Deng, S. Facile and Controllable Preparation of Ultramicroporous Biomass-Derived Carbons and Application on Selective Adsorption of Gas-Mixtures. *Industrial & Engineering Chemistry Research*, **2018**. https://doi.org/10.1021/acs.iecr.8b02139.

[23] Surra, E.; Ribeiro, R. P. P. L.; Santos, T.; Bernardo, M.; Mota, J. P. B.; Lapa, N.; Esteves, I. A. A. C. Evaluation of Activated Carbons Produced from Maize Cob Waste for Adsorption-Based CO2 Separation and Biogas Upgrading. *Journal of Environmental Chemical Engineering*, **2022**, *10* (1), 107065. https://doi.org/10.1016/j.jece.2021.107065.

[24] Liu, F.; Zhang, Y.; Zhang, P.; Xu, M.; Tan, T.; Wang, J.; Deng, Q.; Zhang, L.; Wan, Y.; Deng, S. Facile Preparation of N and O-Rich Porous Carbon from Palm Sheath for Highly Selective Separation of CO2/CH4/N2 Gas-Mixture. *Chemical Engineering Journal*, **2020**, *399*, 125812. https://doi.org/10.1016/j.cej.2020.125812.

[25] Yang, F.; Wang, J.; Liu, L.; Zhang, P.; Yu, W.; Deng, Q.; Zeng, Z.; Deng, S. Synthesis of Porous Carbons with High N Content from Shrimp Shells for Efficient CO2 Capture and Gas Separation.

[26] Li, Y.; Xu, R.; Wang, B.; Wei, J.; Wang, L.; Shen, M.; Yang, J. Enhanced N-Doped Porous Carbon Derived from KOH-Activated Waste Wool: A Promising Material for Selective Adsorption of CO2/CH4 and CH4/N2. *Nanomaterials (Basel)*, **2019**, *9* (2), 266. https://doi.org/10.3390/nano9020266.

[27] Yuan, B.; Wang, J.; Chen, Y.; Wu, X.; Luo, H.; Deng, S. Unprecedented Performance of N-Doped Activated Hydrothermal Carbon towards C2H6/CH4, CO2/CH4, and CO2/H2 Separation. *J. Mater. Chem. A*, **2016**, *4* (6), 2263–2276. https://doi.org/10.1039/C5TA08436A.

[28] Arami-Niya, A.; Rufford, T. E.; Zhu, Z. Nitrogen-Doped Carbon Foams Synthesized from Banana Peel and Zinc Complex Template for Adsorption of CO_2, CH_4, and N_2. *Energy Fuels*, **2016**, *30* (9), 7298–7309. https://doi.org/10.1021/acs.energyfuels.6b00971.

[29] Saadi, W.; Rodríguez-Sánchez, S.; Ruiz, B.; Najar-Souissi, S.; Ouederni, A.; Fuente, E. From Pomegranate Peels Waste to One-Step Alkaline Carbonate Activated Carbons. Prospect as Sustainable Adsorbent for the Renewable Energy Production. *Journal of Environmental Chemical Engineering*, **2022**, *10* (1), 107010. https://doi.org/10.1016/j.jece.2021.107010.

[30] Prasetyo, I.; Mukti, N. I. F.; Cahyono, R. B.; Prasetya, A.; Ariyanto, T. Nanoporous Carbon Prepared from Palm Kernel Shell for CO2/CH4 Separation. *Waste Biomass Valor*, **2020**, *11* (10), 5599–5606. https://doi.org/10.1007/s12649-020-01006-4.

[31] Cavenati, S.; Grande, C. A.; Rodrigues, A. E. Upgrade of Methane from Landfill Gas by Pressure Swing Adsorption. *Energy Fuels*, **2005**, *19* (6), 2545–2555. https://doi.org/10.1021/ef050072h.

[32] Rocha, L. A. M.; Andreassen, K. A.; Grande, C. A. Separation of CO 2 /CH 4 Using Carbon Molecular Sieve (CMS) at Low and High Pressure. *Chemical Engineering Science*, **2017**, *164*, 148–157. https://doi.org/10.1016/j.ces.2017.01.071.

[33] Kim, Y. J.; Nam, Y. S.; Kang, Y. T. Study on a Numerical Model and PSA (Pressure Swing Adsorption) Process Experiment for CH4/CO2 Separation from Biogas. *Energy*, **2015**, *91*, 732–741. https://doi.org/10.1016/j.energy.2015.08.086.

[34] Liang, Z.; Marshall, M.; Chaffee, A. L. CO_2 Adsorption-Based Separation by Metal Organic Framework (Cu-BTC) versus Zeolite (13X). *Energy Fuels*, **2009**, *23* (5), 2785–2789. https://doi.org/10.1021/ef800938e.

[35] Saha, D.; Bao, Z.; Jia, F.; Deng, S. Adsorption of CO_2 , CH_4 , N_2O, and N_2 on MOF-5, MOF-177, and Zeolite 5A. *Environ. Sci. Technol.*, **2010**, *44* (5), 1820–1826. https://doi.org/10.1021/es9032309.

[36] Cavenati, S.; Grande, C. A.; Rodrigues, A. E.; Kiener, C.; Müller, U. Metal Organic Framework Adsorbent for Biogas Upgrading. *Ind. Eng. Chem. Res.*, **2008**, *47* (16), 6333–6335. https://doi.org/10.1021/ie8005269.

[37] Chen, R.; Yao, J.; Gu, Q.; Smeets, S.; Baerlocher, C.; Gu, H.; Zhu, D.; Morris, W.; Yaghi, O. M.; Wang, H. A Two-Dimensional Zeolitic Imidazolate Framework with a Cushion-Shaped Cavity for CO2 Adsorption. *Chem. Commun.*, **2013**, *49* (82), 9500. https://doi.org/10.1039/c3cc44342f.

[38] Abid, H. R.; Pham, G. H.; Ang, H.-M.; Tade, M. O.; Wang, S. Adsorption of CH4 and CO2 on Zr-Metal Organic Frameworks. *Journal of Colloid and Interface Science*, **2012**, *366* (1), 120–124. https://doi.org/10.1016/j.jcis.2011.09.060.

[39] Li, Y.; Yi, H.; Tang, X.; Li, F.; Yuan, Q. Adsorption Separation of CO2/CH4 Gas Mixture on the Commercial Zeolites at Atmospheric Pressure. *Chemical Engineering Journal*, **2013**, *229*, 50–56. https://doi.org/10.1016/j.cej.2013.05.101.

[40] Jiang, Y.; Ling, J.; Xiao, P.; He, Y.; Zhao, Q.; Chu, Z.; Liu, Y.; Li, Z.; Webley, P. A. Simultaneous Biogas Purification and CO2 Capture by Vacuum Swing Adsorption Using Zeolite NaUSY. *Chemical Engineering Journal*, **2018**, *334*, 2593–2602. https://doi.org/10.1016/j.cej.2017.11.090.

[41] Arya, A.; Divekar, S.; Rawat, R.; Gupta, P.; Garg, M. O.; Dasgupta, S.; Nanoti, A.; Singh, R.; Xiao, P.; Webley, P. A. Upgrading Biogas at Low Pressure by Vacuum Swing Adsorption. *Ind. Eng. Chem. Res.*, **2015**, *54* (1), 404–413. https://doi.org/10.1021/ie503243f.

[42] Chen, Y.-F.; Lin, P.-W.; Chen, W.-H.; Yen, F.-Y.; Yang, H.-S.; Chou, C.-T. Biogas Upgrading by Pressure Swing Adsorption with Design of Experiments. *Processes*, **2021**, *9* (8), 1325. https://doi.org/10.3390/pr9081325.

[43] Jiang, Y.; Ling, J.; Xiao, P.; He, Y.; Zhao, Q.; Chu, Z.; Liu, Y.; Li, Z.; Webley, P. A. Simultaneous Biogas Purification and CO2 Capture by Vacuum Swing Adsorption Using Zeolite NaUSY. *Chemical Engineering Journal*, **2018**, *334*, 2593–2602. https://doi.org/10.1016/j.cej.2017.11.090.

[44] Ruthven, Douglas M; Farooq, Shamsuzzaman; Knaebel, Kent S. *Pressure Swing Adsorption*; VCH Publishers, Inc, 1994.

[45] Li, Y.; Xu, R.; Wang, B.; Wei, J.; Wang, L.; Shen, M.; Yang, J. Enhanced N-Doped Porous Carbon Derived from KOH-Activated Waste Wool: A Promising Material for Selective Adsorption of CO2/CH4 and CH4/N2. *Nanomaterials*, **2019**, *9* (2), 266. https://doi.org/10.3390/nano9020266.

[46] Vilella, P. C.; Lira, J. A.; Azevedo, D. C. S.; Bastos-Neto, M.; Stefanutti, R. Preparation of Biomass-Based Activated Carbons and Their Evaluation for Biogas Upgrading Purposes. *Industrial Crops and Products*, **2017**, *109*, 134–140. https://doi.org/10.1016/j.indcrop.2017.08.017.

[47] Sun, Y.; Webley, P. A. Preparation of Activated Carbons with Large Specific Surface Areas from Biomass Corncob and Their Adsorption Equilibrium for Methane, Carbon Dioxide, Nitrogen, and Hydrogen. *Ind. Eng. Chem. Res.*, **2011**.

[48] Álvarez-Gutiérrez, N. Towards Bio-Upgrading of Biogas: Biomass Waste-Based Adsorbents. *Energy Procedia*, **2014**, No. 63, 6527–6533. https://doi.org/10.1016/j.egypro.2014.11.688.

[49] Gil, M. V.; Álvarez-Gutiérrez, N.; Martínez, M.; Rubiera, F.; Pevida, C.; Morán, A. Carbon Adsorbents for CO2 Capture from Bio-Hydrogen and Biogas Streams: Breakthrough Adsorption Study. *Chemical Engineering Journal*, **2015**, *269*, 148–158. https://doi.org/10.1016/j.cej.2015.01.100.

[50] Greco, G.; Canevesi, R. L. S.; Di Stasi, C.; Celzard, A.; Fierro, V.; Manyà, J. J. Biomass-Derived Carbons Physically Activated in One or Two Steps for CH4/CO2 Separation. *Renewable Energy*, **2022**, *191*, 122–133. https://doi.org/10.1016/j.renene.2022.04.035.

[51] Zhang, Y.; Zhang, P.; Yu, W.; Wang, J.; Deng, Q.; Yang, J.; Zeng, Z.; Xu, M.; Deng, S. Facile and Controllable Preparation of Ultramicroporous Biomass-Derived Carbons and Application on Selective Adsorption of Gas-Mixtures. *Ind. Eng. Chem. Res.*, **2018**, *57* (42), 14191–14201. https://doi.org/10.1021/acs.iecr.8b02139.

[52] Surra, E.; Ribeiro, R. P. P. L.; Santos, T.; Bernardo, M.; Mota, J. P. B.; Lapa, N.; Esteves, I. A. A. C. Evaluation of Activated Carbons Produced from Maize Cob Waste for Adsorption-Based CO2 Separation and Biogas Upgrading. *Journal of Environmental Chemical Engineering*, **2022**, *10* (1), 107065. https://doi.org/10.1016/j.jece.2021.107065.

[53] Hamon, L.; Heymans, N.; Llewellyn, P. L.; Guillerm, V.; Ghoufi, A.; Vaesen, S.; Maurin, G.; Serre, C.; De Weireld, G.; Pirngruber, G. D. Separation of CO2–CH4 Mixtures in the Mesoporous MIL-100(Cr) MOF: Experimental and Modelling Approaches. *Dalton Trans.*, **2012**, *41* (14), 4052. https://doi.org/10.1039/c2dt12102f.

[54] Arya, A.; Divekar, S.; Rawat, R.; Gupta, P.; Garg, M. O.; Dasgupta, S.; Nanoti, A.; Singh, R.; Xiao, P.; Webley, P. A. Upgrading Biogas at Low Pressure by Vacuum Swing Adsorption. *Ind. Eng. Chem. Res.*, **2015**, *54* (1), 404–413. https://doi.org/10.1021/ie503243f.

[55] Santos, M. P. S.; Grande, C. A.; Rodrigues, A. E. Pressure Swing Adsorption for Biogas Upgrading. Effect of Recycling Streams in Pressure Swing Adsorption Design. *Ind. Eng. Chem. Res.*, **2011**, *50* (2), 974–985. https://doi.org/10.1021/ie100757u.

[56] Park, J.-H.; Beum, H.-T.; Kim, J.-N.; Cho, S.-H. Numerical Analysis on the Power Consumption of the PSA Process for Recovering CO $_2$ from Flue Gas. *Ind. Eng. Chem. Res.*, **2002**, *41* (16), 4122–4131. https://doi.org/10.1021/ie010716i.

[57] Grande, C. A.; Rodrigues, A. E. Layered Vacuum Pressure-Swing Adsorption for Biogas Upgrading. *Ind. Eng. Chem. Res.*, **2007**, *46* (23), 7844–7848. https://doi.org/10.1021/ie070942d.

[58] Paz, L.; Grekov, D. I.; Pré, P. Dynamics of Hydrogen Storage through Adsorption: Process Simulation and Energy Analysis. *Processes*, **2023**, *11* (10), 2940. https://doi.org/10.3390/pr11102940.

[59] Delgado, J. A.; Uguina, M. A.; Sotelo, J. L.; Ruíz, B.; Gómez, J. M. Fixed-Bed Adsorption of Carbon Dioxide/Methane Mixtures on Silicalite Pellets. *Adsorption*, **2006**, *12* (1), 5–18. https://doi.org/10.1007/s10450-006-0134-3.

[60] Ferreira, A. F. P.; Ribeiro, A. M.; Kulaç, S.; Rodrigues, A. E. Methane Purification by Adsorptive Processes on MIL-53(Al). *Chemical Engineering Science*, **2015**, *124*, 79–95. https://doi.org/10.1016/j.ces.2014.06.014.

[61] Fakhroleslam, M.; Fatemi, S. Comparative Simulation Study of PSA, VSA, and TSA Processes for Purification of Methane from CO 2 via SAPO-34 Core-Shell Adsorbent. *Separation Science and Technology*, **2016**, *51* (14), 2326–2338. https://doi.org/10.1080/01496395.2016.1210640.

[62] Ali Abd, A.; Roslee Othman, M. Biogas Upgrading to Fuel Grade Methane Using Pressure Swing Adsorption: Parametric Sensitivity Analysis on an Industrial Scale. *Fuel*, **2022**, *308*, 121986. https://doi.org/10.1016/j.fuel.2021.121986.

[63] Grande, C. A.; Blom, R.; Möller, A.; Möllmer, J. High-Pressure Separation of CH4/CO2 Using Activated Carbon. *Chemical Engineering Science*, **2013**, *89*, 10–20. https://doi.org/10.1016/j.ces.2012.11.024.

[64] Santos, M. S.; Grande, C. A.; Rodrigues, A. E. New Cycle Configuration to Enhance Performance of Kinetic PSA Processes. *Chemical Engineering Science*, **2011**, *66* (8), 1590–1599. https://doi.org/10.1016/j.ces.2010.12.032.

[65] Cavenati, S.; Grande, C. A.; Rodrigues, A. E. Separation of CH 4 / CO 2 / N 2 Mixtures by Layered Pressure Swing Adsorption for Upgrade of Natural Gas. *Chemical Engineering Science*, **2006**, *61* (12), 3893–3906. https://doi.org/10.1016/j.ces.2006.01.023.

[66] Abd, A. A.; Othman, M. R.; Shamsudin, I. K.; Helwani, Z.; Idris, I. Biogas Upgrading to Natural Gas Pipeline Quality Using Pressure Swing Adsorption for CO_2 Separation over UiO-66: Experimental and Dynamic Modelling Assessment. *Chemical Engineering Journal*, **2023**, *453*, 139774. https://doi.org/10.1016/j.cej.2022.139774.

[67] Ruthven, D. M. *Principles of Adsorption and Adsorption Processes*; A Wiley-Interscience Publication: United States of America, 1984.

[68] Lemmon, E. W.; Huber, M. L.; McLinden, M. O. NIST Standard Reference Database 23: Reference Fluid Thermodynamic and Transport Properties-REFPROP, 2018.

[69] Biegler, L. T.; Jiang, L.; Fox, V. G. Recent Advances in Simulation and Optimal Design of Pressure Swing Adsorption Systems. *Separation & Purification Reviews*, **2005**, *33* (1), 1–39. https://doi.org/10.1081/SPM-120039562.

[70] Liu, Y.; Delgado, J.; Ritter, J. A. Comparison of Finite Difference Techniques for Simulating Pressure Swing Adsorption. **1998**.

[71] Young, L. C. Orthogonal Collocation Revisited. *Computer Methods in Applied Mechanics and Engineering*, **2019**, *345*, 1033–1076. https://doi.org/10.1016/j.cma.2018.10.019.

[72] Khajuria, H.; Pistikopoulos, E. N. Dynamic Modeling and Explicit/Multi-Parametric MPC Control of Pressure Swing Adsorption Systems. *Journal of Process Control*, **2011**, *21* (1), 151–163. https://doi.org/10.1016/j.jprocont.2010.10.021.

[73] Zhang, R.; Shen, Y.; Tang, Z.; Li, W.; Zhang, D. A Review of Numerical Research on the Pressure Swing Adsorption Process. *Processes*, **2022**, *10* (5), 812. https://doi.org/10.3390/pr10050812.

[74] Kadam, R. S.; Yadav, G. D. Pressure Swing Distillation: Heat Integration and Economics. *Separation & Purification Reviews*, **2024**, 1–27. https://doi.org/10.1080/15422119.2024.2306595.

[75] Kim S.; Ko D.; Moon I. Dynamic Optimization of Ch4/Co2 Separating Operation Using Pressure Swing Adsorption Process with Feed Composition Varies. *Chemical Engineering Transactions*, **2015**, *45*, 853–858. https://doi.org/10.3303/CET1545143.

[76] Kapoor, A.; Yang, R. T. Kinetic Separation of Methane—Carbon Dioxide Mixture by Adsorption on Molecular Sieve Carbon. *Chemical Engineering Science*, **1989**, *44* (8), 1723–1733. https://doi.org/10.1016/0009-2509(89)80014-4.

[77] Grande, C. A.; Rodrigues, A. E. Biogas to Fuel by Vacuum Pressure Swing Adsorption I. Behavior of Equilibrium and Kinetic-Based Adsorbents. *Ind. Eng. Chem. Res.*, **2007**, *46* (13), 4595–4605. https://doi.org/10.1021/ie061341+.

[78] Durán, I.; Rubiera, F.; Pevida, C. Modeling a Biogas Upgrading PSA Unit with a Sustainable Activated Carbon Derived from Pine Sawdust. Sensitivity Analysis on the Adsorption of CO2 and CH4 Mixtures. *Chemical Engineering Journal*, **2022**, *428*, 132564. https://doi.org/10.1016/j.cej.2021.132564.

[79] Kim, M.-B.; Bae, Y.-S.; Choi, D.-K.; Lee, C.-H. Kinetic Separation of Landfill Gas by a Two-Bed Pressure Swing Adsorption Process Packed with Carbon Molecular Sieve: Nonisothermal Operation. *Ind. Eng. Chem. Res.*, **2006**, *45* (14), 5050–5058. https://doi.org/10.1021/ie0511074.

[80] Shen, Y.; Shi, W.; Zhang, D.; Na, P.; Fu, B. The Removal and Capture of CO2 from Biogas by Vacuum Pressure Swing Process Using Silica Gel. *Journal of CO2 Utilization*, **2018**, *27*, 259–271. https://doi.org/10.1016/j.jcou.2018.08.001.

[81] Canevesi, R. L. S.; Andreassen, K. A.; Silva, E. A.; Borba, C. E.; Grande, C. A. Evaluation of Simplified Pressure Swing Adsorption Cycles for Bio-Methane Production. *Adsorption*, **2019**, *25* (4), 783–793. https://doi.org/10.1007/s10450-019-00049-x.

[82] Abd, A. A.; Othman, M. R.; Shabbani, H. J. K.; Helwani, Z. Biomethane Upgrading to Transportation Fuel Quality Using Spent Coffee for Carbon Dioxide Capture in Pressure Swing Adsorption. *Journal of Environmental Chemical Engineering*, **2022**, *10* (2), 107169. https://doi.org/10.1016/j.jece.2022.107169.

[83] Augelletti, R.; Conti, M.; Annesini, M. C. Pressure Swing Adsorption for Biogas Upgrading. A New Process Configuration for the Separation of Biomethane and Carbon Dioxide. *Journal of Cleaner Production*, **2017**, *140*, 1390–1398. https://doi.org/10.1016/j.jclepro.2016.10.013.

[84] Vilardi, G.; Bassano, C.; Deiana, P.; Verdone, N. Exergy and Energy Analysis of Biogas Upgrading by Pressure Swing Adsorption: Dynamic Analysis of the Process. *Energy Conversion and Management*, **2020**, *226*, 113482. https://doi.org/10.1016/j.enconman.2020.113482.

[85] Berlin, N. H. Vacuum Cycle Adsorption. 3,313,091, April 11, 1967.

[86] Becker, C. M.; Marder, M.; Junges, E.; Konrad, O. Technologies for Biogas Desulfurization - An Overview of Recent Studies. *Renewable and Sustainable Energy Reviews*, **2022**, *159*, 112205. https://doi.org/10.1016/j.rser.2022.112205.

[87] Peluso, A.; Gargiulo, N.; Aprea, P.; Pepe, F.; Caputo, D. Nanoporous Materials as H_2S Adsorbents for Biogas Purification: A Review. *Separation & Purification Reviews*, **2019**, *48* (1), 78–89. https://doi.org/10.1080/15422119.2018.1476978.

[88] Georgiadis, A.; Charisiou, N.; Goula, M. Removal of Hydrogen Sulfide From Various Industrial Gases: A Review of The Most Promising Adsorbing Materials. *Catalysts*, **2020**, *10* (5), 521. https://doi.org/10.3390/catal10050521.

[89] Pudi, A.; Rezaei, M.; Signorini, V.; Andersson, M. P.; Baschetti, M. G.; Mansouri, S. S. Hydrogen Sulfide Capture and Removal Technologies: A Comprehensive Review of Recent Developments and Emerging Trends. *Separation and Purification Technology*, **2022**, *298*, 121448. https://doi.org/10.1016/j.seppur.2022.121448.

[90] Khabazipour, M.; Anbia, M. Removal of Hydrogen Sulfide from Gas Streams Using Porous Materials: A Review. *Ind. Eng. Chem. Res.*, **2019**, *58* (49), 22133–22164. https://doi.org/10.1021/acs.iecr.9b03800.

[91] Liu, D.; Li, B.; Wu, J.; Liu, Y. Sorbents for Hydrogen Sulfide Capture from Biogas at Low Temperature: A Review. *Environ Chem Lett*, **2020**, *18* (1), 113–128. https://doi.org/10.1007/s10311-019-00925-6.

[92] Micoli, L.; Bagnasco, G.; Turco, M. H_2S Removal from Biogas for Fuelling MCFCs: New Adsorbing Materials. *International Journal of Hydrogen Energy*, **2014**, *39* (4), 1783–1787. https://doi.org/10.1016/j.ijhydene.2013.10.126.

[93] Su, L.; Chen, M.; Zhuo, G.; Ji, R.; Wang, S.; Zhang, L.; Zhang, M.; Li, H. Comparison of Biochar Materials Derived from Coconut Husks and Various Types of Livestock Manure, and Their Potential for Use in Removal of H_2S from Biogas. *Sustainability*, **2021**, *13* (11), 6262. https://doi.org/10.3390/su13116262.

[94] Yan, R.; Liang, D. T.; Tsen, L.; Tay, J. H. Kinetics and Mechanisms of H_2S Adsorption by Alkaline Activated Carbon. *Environ. Sci. Technol.*, **2002**, *36* (20), 4460–4466. https://doi.org/10.1021/es0205840.

[95] Bagreev, A.; Bandosz, T. J. A Role of Sodium Hydroxide in the Process of Hydrogen Sulfide Adsorption/Oxidation on Caustic-Impregnated Activated Carbons. *Ind. Eng. Chem. Res.*, **2002**, *41* (4), 672–679. https://doi.org/10.1021/ie010599r.

[96] Castrillon, M. C.; Moura, K. O.; Alves, C. A.; Bastos-Neto, M.; Azevedo, D. C. S.; Hofmann, J.; Möllmer, J.; Einicke, W.-D.; Gläser, R. CO_2 and H_2S Removal from CH_4 -Rich Streams by Adsorption on Activated Carbons Modified with K_2CO_3 , NaOH, or Fe_2O_3. *Energy Fuels*, **2016**, *30* (11), 9596–9604. https://doi.org/10.1021/acs.energyfuels.6b01667.

[97] Yang, C.; Wang, Y.; Fan, H.; De Falco, G.; Yang, S.; Shangguan, J.; Bandosz, T. J. Bifunctional ZnO-MgO/Activated Carbon Adsorbents Boost H_2S Room Temperature Adsorption and Catalytic Oxidation. *Applied Catalysis B: Environmental*, **2020**, *266*, 118674. https://doi.org/10.1016/j.apcatb.2020.118674.

[98] Sisani, E.; Cinti, G.; Discepoli, G.; Penchini, D.; Desideri, U.; Marmottini, F. Adsorptive Removal of H_2S in Biogas Conditions for High Temperature Fuel Cell Systems. *International Journal of Hydrogen Energy*, **2014**, *39* (36), 21753–21766. https://doi.org/10.1016/j.ijhydene.2014.07.173.

[99] Tuerhong, T.; Kuerban, Z. Preparation and Characterization of Cattle Manure-Based Activated Carbon for Hydrogen Sulfide Removal at Room Temperature. *Journal of*

Environmental Chemical Engineering, **2022**, *10* (2), 107177. https://doi.org/10.1016/j.jece.2022.107177.

[100] Ayiania, M.; Carbajal-Gamarra, F. M.; Garcia-Perez, T.; Frear, C.; Suliman, W.; Garcia-Perez, M. Production and Characterization of H_2S and PO_4^{3-} Carbonaceous Adsorbents from Anaerobic Digested Fibers. *Biomass and Bioenergy*, **2019**, *120*, 339–349. https://doi.org/10.1016/j.biombioe.2018.11.028.

[101] Lee, M.-H.; Vikrant, K.; Younis, S. A.; Szulejko, J. E.; Kim, K.-H. Chemisorption of Hydrogen Sulfide by Metal-Organic Frameworks and Covalent-Organic Polymers Based on Experimental/Theoretical Evaluation. *Journal of Cleaner Production*, **2020**, *250*, 119486. https://doi.org/10.1016/j.jclepro.2019.119486.

[102] Ou, H. W.; Fang, M. L.; Chou, M. S.; Chang, H. Y.; Shiao, T. F. Long-Term Evaluation of Activated Carbon as an Adsorbent for Biogas Desulfurization. *Journal of the Air & Waste Management Association*, **2020**, *70* (6), 641–648. https://doi.org/10.1080/10962247.2020.1754305.

[103] Sigot, L.; Fontseré Obis, M.; Benbelkacem, H.; Germain, P.; Ducom, G. Comparing the Performance of a 13X Zeolite and an Impregnated Activated Carbon for H_2S Removal from Biogas to Fuel an SOFC: Influence of Water. *International Journal of Hydrogen Energy*, **2016**, *41* (41), 18533–18541. https://doi.org/10.1016/j.ijhydene.2016.08.100.

[104] Surra, E.; Costa Nogueira, M.; Bernardo, M.; Lapa, N.; Esteves, I.; Fonseca, I. New Adsorbents from Maize Cob Wastes and Anaerobic Digestate for H_2S Removal from Biogas. *Waste Management*, **2019**, *94*, 136–145. https://doi.org/10.1016/j.wasman.2019.05.048.

[105] Raabe, T. Study on Iron-Based Adsorbents for Alternating Removal of H_2S and O_2 from Natural Gas and Biogas. *Chemical Engineering Journal*, **2019**.

[106] Seredych, M.; Bandosz, T. J. Desulfurization of Digester Gas on Wood-Based Activated Carbons Modified with Nitrogen: Importance of Surface Chemistry. *Energy Fuels*, **2008**, *22* (2), 850–859. https://doi.org/10.1021/ef700523h.

[107] Barelli, L.; Bidini, G.; Micoli, L.; Sisani, E.; Turco, M. 13X Ex-Cu Zeolite Performance Characterization towards H_2S Removal for Biogas Use in Molten Carbonate Fuel Cells. *Energy*, **2018**, *160*, 44–53. https://doi.org/10.1016/j.energy.2018.05.057.

[108] Sethupathi, S.; Zhang, M.; Rajapaksha, A.; Lee, S.; Mohamad Nor, N.; Mohamed, A.; Al-Wabel, M.; Lee, S.; Ok, Y. Biochars as Potential Adsorbers of CH_4, CO_2 and H_2S. *Sustainability*, **2017**, *9* (1), 121. https://doi.org/10.3390/su9010121.

[109] Yuan, W.; Bandosz, T. J. Removal of Hydrogen Sulfide from Biogas on Sludge-Derived Adsorbents. *Fuel*, **2007**, *86* (17–18), 2736–2746. https://doi.org/10.1016/j.fuel.2007.03.012.

[110] Gutiérrez Ortiz, F. J.; Aguilera, P. G.; Ollero, P. Biogas Desulfurization by Adsorption on Thermally Treated Sewage-Sludge. *Separation and Purification Technology*, **2014**, *123*, 200–213. https://doi.org/10.1016/j.seppur.2013.12.025.

[111] Choudhury, A.; Lansing, S. Adsorption of Hydrogen Sulfide in Biogas Using a Novel Iron-Impregnated Biochar Scrubbing System. *Journal of Environmental Chemical Engineering*, **2021**, *9* (1), 104837. https://doi.org/10.1016/j.jece.2020.104837.

[112] Barelli, L.; Bidini, G.; De Arespacochaga, N.; Pérez, L.; Sisani, E. Biogas Use in High Temperature Fuel Cells: Enhancement of KOH-KI Activated Carbon Performance toward

H_2S Removal. *International Journal of Hydrogen Energy*, **2017**, *42* (15), 10341–10353. https://doi.org/10.1016/j.ijhydene.2017.02.021.

[113] Pelaez-Samaniego, M. R.; Smith, M. W.; Zhao, Q.; Garcia-Perez, T.; Frear, C.; Garcia-Perez, M. Charcoal from Anaerobically Digested Dairy Fiber for Removal of Hydrogen Sulfide within Biogas. *Waste Management*, **2018**, *76*, 374–382. https://doi.org/10.1016/j.wasman.2018.03.011.

[114] Bagreev, A.; Bandosz, T. J. On the Mechanism of Hydrogen Sulfide Removal from Moist Air on Catalytic Carbonaceous Adsorbents. *Ind. Eng. Chem. Res.*, **2005**, *44* (3), 530–538. https://doi.org/10.1021/ie049277o.

[115] Siriwardane, I. W.; Udangawa, R.; De Silva, R. M.; Kumarasinghe, A. R.; Acres, R. G.; Hettiarachchi, A.; Amaratunga, G. A. J.; De Silva, K. M. N. Synthesis and Characterization of Nano Magnesium Oxide Impregnated Granular Activated Carbon Composite for H_2S Removal Applications. *Materials & Design*, **2017**, *136*, 127–136. https://doi.org/10.1016/j.matdes.2017.09.034.

[116] Nguyen-Thanh, D.; Bandosz, T. J. Activated Carbons with Metal Containing Bentonite Binders as Adsorbents of Hydrogen Sulfide. *Carbon*, **2005**, *43* (2), 359–367. https://doi.org/10.1016/j.carbon.2004.09.023.

[117] Zhang, X.; Tang, Y.; Qu, S.; Da, J.; Hao, Z. H_2S-Selective Catalytic Oxidation: Catalysts and Processes. *ACS Catal.*, **2015**, *5* (2), 1053–1067. https://doi.org/10.1021/cs501476p.

[118] Bagreev, A.; Bashkova, S.; Locke, D. C.; Bandosz, T. J. Sewage Sludge-Derived Materials as Efficient Adsorbents for Removal of Hydrogen Sulfide. *Environ. Sci. Technol.*, **2001**, *35* (7), 1537–1543. https://doi.org/10.1021/es001678h.

[119] Bagreev, A.; Bandosz, T. J. Efficient Hydrogen Sulfide Adsorbents Obtained by Pyrolysis of Sewage Sludge Derived Fertilizer Modified with Spent Mineral Oil. *Environ. Sci. Technol.*, **2004**, *38* (1), 345–351. https://doi.org/10.1021/es0303438.

[120] Bagreev, A.; Rahman, H.; Bandosz, T. J. Study of H_2S Adsorption and Water Regeneration of Spent Coconut-Based Activated Carbon. *Environ. Sci. Technol.*, **2000**, *34* (21), 4587–4592. https://doi.org/10.1021/es001150c.

[121] Kante, K.; Nieto-Delgado, C.; Rangel-Mendez, J. R.; Bandosz, T. J. Spent Coffee-Based Activated Carbon: Specific Surface Features and Their Importance for H_2S Separation Process. *Journal of Hazardous Materials*, **2012**, *201–202*, 141–147. https://doi.org/10.1016/j.jhazmat.2011.11.053.

[122] Adib, F.; Bagreev, A.; Bandosz, T. J. Adsorption/Oxidation of Hydrogen Sulfide on Nitrogen-Containing Activated Carbons. *Langmuir*, **2000**, *16* (4), 1980–1986. https://doi.org/10.1021/la990926o.

[123] Adib, F.; Bagreev, A.; Bandosz, T. J. Effect of PH and Surface Chemistry on the Mechanism of H_2S Removal by Activated Carbons. *Journal of Colloid and Interface Science*, **1999**, *216*, 360–369. https://doi.org/10.1006/jcis.1999.6335.

[124] Petit, C.; Mendoza, B.; Bandosz, T. J. Hydrogen Sulfide Adsorption on MOFs and MOF/Graphite Oxide Composites. *ChemPhysChem*, **2010**, *11* (17), 3678–3684. https://doi.org/10.1002/cphc.201000689.

[125] Ebrahim, A. M.; Jagiello, J.; Bandosz, T. J. Enhanced Reactive Adsorption of H_2S on Cu–BTC/ S- and N-Doped GO Composites. *J. Mater. Chem. A*, **2015**, *3* (15), 8194–8204. https://doi.org/10.1039/C5TA01359C.

[126] Shi, R.-H.; Zhang, Z.-R.; Fan, H.-L.; Zhen, T.; Shangguan, J.; Mi, J. Cu-Based Metal–Organic Framework/Activated Carbon Composites for Sulfur Compounds Removal. *Applied Surface Science*, **2017**, *394*, 394–402. https://doi.org/10.1016/j.apsusc.2016.10.071.

[127] Guo, J.; Luo, Y.; Lua, A. C.; Chi, R.; Chen, Y.; Bao, X.; Xiang, S. Adsorption of Hydrogen Sulphide (H_2S) by Activated Carbons Derived from Oil-Palm Shell. *Carbon*, **2007**, *45* (2), 330–336. https://doi.org/10.1016/j.carbon.2006.09.016.

[128] Erto, A.; Deorsola, F. A.; De Falco, G.; Montagnaro, F.; Balsamo, M. Role of H_2O and O_2 during the Reactive Adsorption of H_2S on CuO-ZnO/Activated Carbon at Low Temperature. *Microporous and Mesoporous Materials*, **2020**, *295*, 109949. https://doi.org/10.1016/j.micromeso.2019.109949.

[129] Yang, C.; Florent, M.; De Falco, G.; Fan, H.; Bandosz, T. J. $ZnFe_2O_4$/Activated Carbon as a Regenerable Adsorbent for Catalytic Removal of H_2S from Air at Room Temperature. *Chemical Engineering Journal*, **2020**, *394*, 124906. https://doi.org/10.1016/j.cej.2020.124906.

[130] Zulkefli, N. N.; Mathuray Veeran, L. S.; Noor Azam, A. M. I.; Masdar, M. S.; Wan Isahak, W. N. R. Effect of Bimetallic-Activated Carbon Impregnation on Adsorption–Desorption Performance for Hydrogen Sulfide (H_2S) Capture. *Materials*, **2022**, *15* (15), 5409. https://doi.org/10.3390/ma15155409.

[131] Menezes, R. L. C. B.; Moura, K. O.; De Lucena, S. M. P.; Azevedo, D. C. S.; Bastos-Neto, M. Insights on the Mechanisms of H_2S Retention at Low Concentration on Impregnated Carbons. *Ind. Eng. Chem. Res.*, **2018**, *57* (6), 2248–2257. https://doi.org/10.1021/acs.iecr.7b03402.

[132] Cepollaro, E. M.; Caputo, D.; Gargiulo, N.; Deorsola, F. A.; Cimino, S.; Lisi, L. H_2S Catalytic Removal at Low Temperature over Cu- and Mg- Activated Carbon Honeycombs. *Catalysis Today*, **2022**, *390–391*, 221–229. https://doi.org/10.1016/j.cattod.2021.11.027.

[133] Liu, C.; Zhang, R.; Wei, S.; Wang, J.; Liu, Y.; Li, M.; Liu, R. Selective Removal of H_2S from Biogas Using a Regenerable Hybrid TiO_2 /Zeolite Composite. *Fuel*, **2015**, *157*, 183–190. https://doi.org/10.1016/j.fuel.2015.05.003.

[134] Long, N. Q.; Vuong, H. T.; Ha, H. K. P.; Kuniawan, W.; Hinode, H.; Baba, T. PREPARATION, CHARACTERIZATION AND H2S ADSORPTIVE REMOVAL OF ION-EXCHANGED ZEOLITE X. *ASEAN Engineering Journal*, **2015**, *5* (1), 4–14. https://doi.org/10.11113/aej.v5.15463.

[135] Liu, X.; Wang, R. Effective Removal of Hydrogen Sulfide Using 4A Molecular Sieve Zeolite Synthesized from Attapulgite. *Journal of Hazardous Materials*, **2017**, *326*, 157–164. https://doi.org/10.1016/j.jhazmat.2016.12.030.

[136] Gupta, N. K.; Kim, S.; Bae, J.; Soo Kim, K. Fabrication of Cu(BDC)0.5(BDC-NH_2)0.5 Metal-Organic Framework for Superior H_2S Removal at Room Temperature. *Chemical Engineering Journal*, **2021**, *411*, 128536. https://doi.org/10.1016/j.cej.2021.128536.

[137] Zhang, H.-Y.; Yang, C.; Geng, Q.; Fan, H.-L.; Wang, B.-J.; Wu, M.-M.; Tian, Z. Adsorption of Hydrogen Sulfide by Amine-Functionalized Metal Organic Framework (MOF-199): An Experimental and Simulation Study. *Applied Surface Science*, **2019**, *497*, 143815. https://doi.org/10.1016/j.apsusc.2019.143815.

[138] Huang, Z.-H.; Liu, G.; Kang, F. Glucose-Promoted Zn-Based Metal–Organic Framework/Graphene Oxide Composites for Hydrogen Sulfide Removal. *ACS Appl. Mater. Interfaces*, **2012**, *4* (9), 4942–4947. https://doi.org/10.1021/am3013104.

[139] Bahraminia, S.; Anbia, M.; Koohsaryan, E. Hydrogen Sulfide Removal from Biogas Using Ion-Exchanged Nanostructured NaA Zeolite for Fueling Solid Oxide Fuel Cells. *International Journal of Hydrogen Energy*, **2020**, *45* (55), 31027–31040. https://doi.org/10.1016/j.ijhydene.2020.08.091.

[140] Rezaei, S.; Jarligo, M. O. D.; Wu, L.; Kuznicki, S. M. Breakthrough Performances of Metal-Exchanged Nanotitanate ETS-2 Adsorbents for Room Temperature Desulfurization. *Chemical Engineering Science*, **2015**, *123*, 444–449. https://doi.org/10.1016/j.ces.2014.11.041.

[141] Bhoria, N.; Basina, G.; Pokhrel, J.; Kumar Reddy, K. S.; Anastasiou, S.; Balasubramanian, V. V.; AlWahedi, Y. F.; Karanikolos, G. N. Functionalization Effects on HKUST-1 and HKUST-1/Graphene Oxide Hybrid Adsorbents for Hydrogen Sulfide Removal. *Journal of Hazardous Materials*, **2020**, *394*, 122565. https://doi.org/10.1016/j.jhazmat.2020.122565.

[142] Paz, L.; Gentil, S.; Fierro, V.; Celzard, A. Assessing the Performance of Adsorbents for CO_2/CH_4 Separation in Pressure Swing Adsorption Units: A Review. *Journal of Environmental Chemical Engineering*, **2024**, *12* (6), 114870. https://doi.org/10.1016/j.jece.2024.114870.

[143] Bandosz, T. J. On the Adsorption/Oxidation of Hydrogen Sulfide on Activated Carbons at Ambient Temperatures. *Journal of Colloid and Interface Science*, **2002**, *246* (1), 1–20. https://doi.org/10.1006/jcis.2001.7952.

[144] Wilkins, N. S.; Rajendran, A.; Farooq, S. Dynamic Column Breakthrough Experiments for Measurement of Adsorption Equilibrium and Kinetics. *Adsorption*, **2021**, *27* (3), 397–422. https://doi.org/10.1007/s10450-020-00269-6.

[145] Cano, P. I.; Colón, J.; Ramírez, M.; Lafuente, J.; Gabriel, D.; Cantero, D. Life Cycle Assessment of Different Physical-Chemical and Biological Technologies for Biogas Desulfurization in Sewage Treatment Plants. *Journal of Cleaner Production*, **2018**, *181*, 663–674. https://doi.org/10.1016/j.jclepro.2018.02.018.

[146] Feng, Y.; Wen, J.; Hu, Y.; Wu, B.; Wu, M.; Mi, J. Evaluation of the Cycling Performance of a Sorbent for H2S Removal and Simulation of Desulfurization-Regeneration Processes. *Chemical Engineering Journal*, **2017**, *326*, 1255–1265. https://doi.org/10.1016/j.cej.2017.05.098.

[147] Gutiérrez Ortiz, F. J.; Aguilera, P. G.; Ollero, P. Modeling and Simulation of the Adsorption of Biogas Hydrogen Sulfide on Treated Sewage–Sludge. *Chemical Engineering Journal*, **2014**, *253*, 305–315. https://doi.org/10.1016/j.cej.2014.04.114.

[148] Aguilera, P. G.; Gutiérrez Ortiz, F. J. Prediction of Fixed-Bed Breakthrough Curves for H_2S Adsorption from Biogas: Importance of Axial Dispersion for Design. *Chemical Engineering Journal*, **2016**, *289*, 93–98. https://doi.org/10.1016/j.cej.2015.12.075.

[149] Xiao, Y.; Wang, S.; Wu, D.; Yuan, Q. Experimental and Simulation Study of Hydrogen Sulfide Adsorption on Impregnated Activated Carbon under Anaerobic Conditions. *Journal of Hazardous Materials*, **2008**, *153* (3), 1193–1200. https://doi.org/10.1016/j.jhazmat.2007.09.081.

[150] Scheufele, F. B.; Da Silva, E. S.; Cazula, B. B.; Marins, D. S.; Sequinel, R.; Borba, C. E.; Patuzzo, G. S.; Lopez, T. F. M.; Alves, H. J. Mathematical Modeling of Low-Pressure H_2S Adsorption by Babassu Biochar in Fixed Bed Column. *Journal of Environmental Chemical Engineering*, **2021**, *9* (1), 105042. https://doi.org/10.1016/j.jece.2021.105042.

[151] Papurello, D.; Gandiglio, M.; Lanzini, A. Experimental Analysis and Model Validation on the Performance of Impregnated Activated Carbons for the Removal of Hydrogen Sulfide (H2S) from Sewage Biogas. *Processes*, **2019**, *7* (9), 548. https://doi.org/10.3390/pr7090548.

[152] De Oliveira, L. H.; Meneguin, J. G.; Pereira, M. V.; Da Silva, E. A.; Grava, W. M.; Do Nascimento, J. F.; Arroyo, P. A. H_2S Adsorption on NaY Zeolite. *Microporous and Mesoporous Materials*, **2019**, *284*, 247–257. https://doi.org/10.1016/j.micromeso.2019.04.014.

[153] Thomas, W. J.; Crittenden, B. D. *Adsorption Technology and Design*; Butterworth-Heinemann: Oxford ; Boston, 1998.

[154] De Witte, N.; Denayer, J. F. M.; Van Assche, T. R. C. Effect of Adsorption Duration and Purge Flowrate on Pressure Swing Adsorption Performance. *Ind. Eng. Chem. Res.*, **2021**, *60* (37), 13684–13691. https://doi.org/10.1021/acs.iecr.1c02291.

[155] Chouikhi, N.; Brandani, F.; Pullumbi, P.; Perre, P.; Puel, F. Biomethane Production by Adsorption Technology: New Cycle Development, Adsorbent Selection and Process Optimization. *Adsorption*, **2020**, *26* (8), 1275–1289. https://doi.org/10.1007/s10450-020-00250-3.

[156] Cavenati, S.; Grande, C. A.; Rodrigues, A. E. Upgrade of Methane from Landfill Gas by Pressure Swing Adsorption. *Energy Fuels*, **2005**, *19* (6), 2545–2555. https://doi.org/10.1021/ef050072h.

[157] De Oliveira, L. H.; Meneguin, J. G.; Pereira, M. V.; Do Nascimento, J. F.; Arroyo, P. A. Adsorption of Hydrogen Sulfide, Carbon Dioxide, Methane, and Their Mixtures on Activated Carbon. *Chemical Engineering Communications*, **2019**, *206* (11), 1533–1553. https://doi.org/10.1080/00986445.2019.1601627.

[158] Bagreev, A.; Adib, F.; Bandosz, T. J. Initial Heats of H2S Adsorption on Activated Carbons: Effect of Surface Features. *Journal of Colloid and Interface Science*, **1999**, *219* (2), 327–332. https://doi.org/10.1006/jcis.1999.6485.

[159] Yang, Y.; Liu, X.; Yang, C.; Wang, Y.; Wang, H.; Fan, H. Study on the Essential Features for MOFs to Reversible Adsorption of H_2S at Room Temperature. *Colloids and Surfaces A: Physicochemical and Engineering Aspects*, **2023**, *674*, 131914. https://doi.org/10.1016/j.colsurfa.2023.131914.

[160] Ribeiro, A. M.; Neto, P.; Pinho, C. Mean Porosity and Pressure Drop Measurements in Packed Beds of Monosized Spheres: Side Wall Effects. **2010**, *2* (1).

[161] Daraee, M.; Ghasemy, E.; Rashidi, A. Synthesis of Novel and Engineered UiO-66/Graphene Oxide Nanocomposite with Enhanced H_2S Adsorption Capacity. *Journal of Environmental Chemical Engineering*, **2020**, *8* (5), 104351. https://doi.org/10.1016/j.jece.2020.104351.

[162] Aguilera, P. G.; Gutiérrez Ortiz, F. J. High Performance Regenerative Adsorption of Hydrogen Sulfide from Biogas on Thermally-Treated Sewage-Sludge. *Fuel Processing Technology*, **2016**, *145*, 148–156. https://doi.org/10.1016/j.fuproc.2016.01.036.

[163] Chen, L.; Yuan, J.; Li, T.; Jiang, X.; Ma, S.; Cen, W.; Jiang, W. A Regenerable N-Rich Hierarchical Porous Carbon Synthesized from Waste Biomass for H_2S Removal at Room Temperature. *Science of The Total Environment*, **2021**, *768*, 144452. https://doi.org/10.1016/j.scitotenv.2020.144452.

[164] Yuan, Y.; Huang, L.; Zhang, T. C.; Ouyang, L.; Yuan, S. One-Step Synthesis of $ZnFe_2O_4$-Loaded Biochar Derived from Leftover Rice for High-Performance H_2S Removal. *Separation and Purification Technology*, **2021**, *279*, 119686. https://doi.org/10.1016/j.seppur.2021.119686.

[165] Yu, Z.; Wang, X.; Song, X.; Liu, Y.; Qiu, J. Molten Salt Synthesis of Nitrogen-Doped Porous Carbons for Hydrogen Sulfide Adsorptive Removal. *Carbon*, **2015**, *95*, 852–860. https://doi.org/10.1016/j.carbon.2015.08.105.

[166] Yang, C.; Wang, J.; Fan, H.; Hu, Y.; Shen, J.; Shangguan, J.; Wang, B. Activated Carbon-Assisted Fabrication of Cost-Efficient ZnO/SiO_2 Desulfurizer with Characteristic of High Loadings and High Dispersion. *Energy Fuels*, **2018**, *32* (5), 6064–6072. https://doi.org/10.1021/acs.energyfuels.8b00532.

[167] Gupta, N. K.; Kim, S.; Bae, J.; Kim, K. S. Chemisorption of Hydrogen Sulfide over Copper-Based Metal–Organic Frameworks: Methanol and UV-Assisted Regeneration. *RSC Adv.*, **2021**, *11* (9), 4890–4900. https://doi.org/10.1039/D0RA09017D.

[168] Abdullah, A. H.; Mat, R.; Somderam, S.; Abd Aziz, A. S.; Mohamed, A. Hydrogen Sulfide Adsorption by Zinc Oxide-Impregnated Zeolite (Synthesized from Malaysian Kaolin) for Biogas Desulfurization. *Journal of Industrial and Engineering Chemistry*, **2018**, *65*, 334–342. https://doi.org/10.1016/j.jiec.2018.05.003.

[169] Chen, X.; Shen, B.; Sun, H.; Zhan, G. Ion-Exchange Modified Zeolites X for Selective Adsorption Desulfurization from Claus Tail Gas: Experimental and Computational Investigations. *Microporous and Mesoporous Materials*, **2018**, *261*, 227–236. https://doi.org/10.1016/j.micromeso.2017.11.014.

Chapter 3. Tailoring wood-based activated carbons and assessing the role of impregnation and O_2 for efficient H_2S removal from biogas

3.1 Introduction

The growing demand for sustainable energy sources has increased interest in biogas as a renewable alternative to fossil fuels. Biogas is mainly derived from the anaerobic digestion of organic waste, such as food, sludge, agricultural, livestock and industrial waste.[1] It is a clean energy source with a wide range of applications, including integration into natural gas grids, serving as a fuel for electricity generation through engines and gas turbines, and functioning as a sustainable biofuel, among other uses.[2, 3] It mainly comprises methane (CH_4) and carbon dioxide (CO_2), as well as traces of impurities such as hydrogen sulfide (H_2S).[4] The presence of H_2S in biogas poses several challenges, including corrosion of handling equipment, environmental pollution and adverse effects on human health.[5, 6] In industrial applications, the maximum permissible concentration of H_2S in the final product is generally set at 4 ppm for biomethane production. For fuel cells, the tolerance range is between 0.1 and 10 ppm.[7]

H_2S removal is therefore mandatory to ensure the protection and longevity of these infrastructures. Among the conventional techniques employed for H_2S removal (absorption, adsorption and biofiltration), adsorption stands out as a preferred choice due to its cost-effectiveness, ease of implementation and ability to operate at ambient temperature, unlike metal oxides, which require high temperatures (100 °C to 300 °C) to operate efficiently.[8] Additionally, at ambient temperature, activated carbons (ACs) outperform other sorbents such as zeolites and metal organic frameworks (MOFs), mainly studied at laboratory scale.[7]

Currently, the best-performing ACs are those that have been modified by chemical impregnation,[9–11] achieving more than twice the separation capacity of their non-modified counterparts.[12] These materials display a series of beneficial characteristics for the H_2S sorption process, including high surface area, high microporosity and the presence of impregnating compounds that improve the selectivity for H_2S separation.

H_2S separation is usually evaluated by dynamic adsorption of a synthetic gas, which, according to the literature, can be composed of H_2S mixed with only N_2,[13–15] He,[9, 16] or air,[12, 17–20] often neglecting CO_2. However, CO_2 (20–50% in biogas) is highly adsorbable due to its molecular size (0.33 nm) similar to that of H_2S (0.36 nm),[21] which puts it in competition for adsorption sites and affects separation efficiency. Therefore, and although its presence reduces adsorption capacities,[7] it is strongly recommended to incorporate CO_2 in the gas meant to mimic the case of a real biogas, as it more closely reflects its actual composition.

The objective of this work is to develop an AC whose H_2S separation capabilities are competitive with commercial alternatives. To this end, we studied the production of AC at different activation times and temperatures. The best ACs were impregnated with three different impregnating agents (KI, KOH and K_2CO_3) and at different impregnation percentages for each agent. The best impregnated AC was then selected to carry out desulphurization tests under different conditions. The H_2S separation performance was evaluated by dynamic adsorption tests using H_2S at concentrations of 400 and 4000 ppm in a mixture of N_2 and CO_2, which are levels typically found in real biogas situations. The effect of AC humidification and the presence of O_2 in the feed gas were also addressed. A one-dimensional mathematical model was developed to simulate the H_2S adsorption process, incorporating kinetic diffusion and equilibrium isotherms. The model was validated using our experimental data, ensuring its accuracy and reliability.

A comparison of H_2S separation results was also carried out with nine commercial ACs designed for biogas purification. Having our own commercial references is indeed crucial for accurate evaluation under consistent conditions, avoiding variations in performance due to changes in feed gas, H_2S levels, flow rates, particle size, and the presence of humidity or oxygen.

3.2 Experimental

3.2.1 Materials

The activated carbon (AC) precursor was a hardwood-based charcoal supplied by the French company Groupe Bordet as part of the "CarBioLab" joint laboratory (LabCom ANR). The charcoal produced from oak and beech sawdust by Groupe Bordet's own slow, continuous pyrolysis process gives it a very high degree of purity (> 90%). The impregnating agents used for the chemical modification of ACs were KOH, KI and K_2CO_3, all of analytical grade (purity ≥ 99%), and their solutions were prepared using bi-distilled water.

To compare our materials with references in biogas treatment, nine commercial ACs (CACs) specifically used for biogas desulfurization were also analyzed. Their sources and modification types are presented in **Table 3.1**. Most of these commercial carbons originate from mineral coal, with the exception of CAC 1 and CAC 2, which are derived from wood and coconut shell, respectively. All CACs undergo chemical impregnation during preparation; however, while

some suppliers provide details of the type and rate of impregnation, others do not to disclose this information (**Table 3.1**).

Table 3.1 Commercial activated carbons (CACs) for biogas desulfurization.

Sample name	Origin	Impregnation	Form
CAC 1	Wood	Unknown	Pellet (Ø = 4 mm – L = 4 - 7 mm)
CAC 2	Coconut-shell	KOH 5 wt.%	Granular (2.4 - 5 mm)
CAC 3	Coal	KOH 5 wt.%	Pellet (Ø = 4 mm – L = 4 - 12 mm)
CAC 4	Coal	$KMnO_4$	Pellet (Ø = 4 mm – L = 4 - 12 mm)
CAC 5	Coal	KI and alkali	Pellet (Ø = 4 mm – L = 4 - 12 mm)
CAC 6	Coal	Unknown	Granular (2.4 - 8 mm)
CAC 7	Coal	NaOH 10 wt.%	Pellet (Ø = 4 mm- L = 4 - 12 mm)
CAC 8	Coal	Unknown	Pellet (Ø = 3 mm – L = 4 - 10 mm)
CAC 9	Coal	Unknown 7 wt.%	Pellet (Ø = 4 mm – L = 4 - 9 mm)

A series of wood-derived ACs were selected for this study. Briefly, these ACs were prepared as follows. Groupe Bordet's charcoal, with particle sizes ranging from 3 to 8 mm, was physically activated with steam using a horizontal rotary tube furnace (Carbolite TSO 11/800). The activation process was conducted with a heating rate of 5 °C·min^{-1} at activation temperatures (T) between 850 °C and 900 °C and activation times (t) ranging from 1 to 3 hours under a continuous N_2 flow of 300 mL·min^{-1}. Steam, 6 mL·min^{-1}, was injected during the isothermal phase. The reactor remained in rotation throughout this period. ACs were labeled AC_T_t, where "T" and "t" represent activation temperature (°C) and time (h), respectively. For example, AC_900°C_3h represents the charcoal activated with steam at 900 °C for 3 h.

3.2.2 Impregnation process

Three ACs of interest were selected for the impregnation tests, using the incipient wetness method.[22] First, the ACs were dried at 105 °C for 24 hours. Next, the dry ACs were mixed with an impregnation solution, the volume of which was exactly that of the pore space of the AC grains calculated using Eq. (3.1):

$$Pore\ space = \left(\frac{1}{Grain\ density} - \frac{1}{Skeletal\ density}\right) \times Mass\ of\ AC \qquad \textbf{(3.1)}$$

where grain density and skeletal density respectively include and do not include the porosity of the AC grain, and were determined as explained in the following subsection. The impregnation solution contained the necessary amount of KOH, KI or K_2CO_3 to achieve the desired impregnation rate (wt.%) in the AC. Various impregnation rates were tested, ranging from 5 to 30 wt.%. Finally, the impregnated ACs were dried under vacuum at 80 °C overnight.

One example of how to determine the concentration of the KOH solution to obtain an AC impregnated at 10 wt.% KOH is presented in annex 2. Non-impregnated and impregnated ACs at different impregnation rates were selected for biogas desulfurization tests.

3.2.3 AC Characterization

All the carbon materials were characterized to determine their physicochemical properties. Because they are supplied in impregnated form, the CACs were first washed with hydrochloric acid to remove the impregnating agents, enabling the porosity of the substrate material to be analyzed. They were then rinsed with distilled water and dried for 24 h at 105 °C before being subjected to N_2 adsorption isotherm measurements. Textural characteristics were determined by N_2 adsorption-desorption isotherms at -196 °C using an ASAP 2020 instrument (Micromeritics). The samples were first degassed under vacuum at 110 °C for 24 h. The isotherms were used to determine the BET area (A_{BET}) by applying the BET (Brunauer-Emmett-Teller) model.[23] In addition, the NLDFT surface area (S_{NLDFT}) was obtained using the SAIEUS® software based on the non-local density functional theory (NLDFT) method.[24]

Total pore volume (V_{tot}), mesopore volume (V_{mes}, pore size $2 < w < 50$ nm), ultramicropore volume ($V_{ultra\text{-}mic}$, $0.7 < w < 2$ nm), micropore volume (V_{mic}, $w < 2$ nm) and pore size distribution (PSD) were also determined by applying the NLDFT approach. Furthermore, the micropore volume was also calculated using the Dubinin–Radushkevich method (V_{DR}) for comparison. The total pore volume at a relative pressure of 0.97 ($V_{0.97}$), derived from N_2 adsorption isotherms, was also calculated to estimate the total accessible pore volume. The burn-off of the ACs was determined by comparing the weight loss before and after activation relative to the precursor material.

To determine their pH, 1g of each AC was placed in 100 mL distilled water under agitation during 24 h. The contents of the flasks were then filtered and the pH measured on the solution obtained.

The skeletal density of ACs was measured using a Micromeritics AccuPyc II 1340 gas pycnometer. Helium gas was used as the probe molecule to ensure accurate volume measurements by penetrating the narrowest pores. Prior to analysis, samples were degassed to remove any adsorbed moisture or gases. The skeletal density was calculated based on the displaced volume, and represents the real density of the solid material, i.e., excluding pores.

The grain density was determined using a Micromeritics GeoPyc 1360 pycnometer, using a dry powder deemed incompressible. Samples were carefully compacted using a calibrated DryFlow® medium to ensure consistent packing. The grain density was then calculated based on the volume displaced, reflecting the overall density of the material grains, i.e., including internal pores but not inter-grain spaces.

3.2.4 H_2S dynamic adsorption

Dynamic adsorption experiments were conducted using the test bench shown in **Figure 3.1a**. All tested samples were ground and sieved to obtain homogeneous particles of sizes between 0.5 and 1.0 mm. The volume of sorbent tested was kept constant to ensure complete filling of a stainless-steel adsorption column with an inner diameter of 0.77 cm and a length of 10 cm. The column temperature was maintained at 25 °C using a water bath, while the system was operated at atmospheric pressure. As humidity can positively influence their performance, uniform conditions were ensured by humidifying the ACs for 24 hours in a controlled environment at 50% relative humidity (RH) and 25 °C before filling the column.

The gas entering the column for dynamic adsorption tests was synthetic biogas composed of 400 or 4000 ppm H_2S, 60% N_2, with the balance made up of CO_2. Oxygen at 1.1 % was also used in some experiments. Gas analysis at the outlet of the adsorption column was performed using a micro-GC gas chromatograph (Micro GC Fusion, Inficon). The gas flow rate was maintained constant at 80 $mL \cdot min^{-1}$ using mass flow controllers, resulting in a linear velocity of 2.9 $cm \cdot s^{-1}$.

In industrial desulfurization, ACs are not fully saturated prior to replacement; instead, they are partially saturated once the breakthrough point (BTP) is reached or the H_2S outlet concentration exceeds acceptable limits. On the other hand, ASTM D6646 for H_2S removal using ACs recommends a BTP of 50 ppm when the H_2S concentration at the inlet is 10000 ppm. Herein, adsorption capacity was determined at an outlet H_2S concentration of 40 ppm, corresponding to a BTP of 10% for experiments with an inlet H_2S concentration of 400 ppm,

and a BTP of 1% for experiments with 4000 ppm H_2S. The threshold of 40 ppm was chosen to ensure a BTP close to 4 ppm, which corresponds to an acceptable concentration of H_2S to use biogas as a substitute for natural gas.[25]

The H_2S adsorption capacity (or uptake, or separation capacity), q_{H_2S} (mg), was calculated using Eq. (3.2) (see **Figure A2.1** for demonstration):

$$q_{H_2S} = Q\ C_0 \int_{t_0}^{t_m} \left(1 - \frac{C_m}{C_0}\right) dt \qquad \textbf{(3.2)}$$

where Q (mL·min^{-1}) is the inlet flow rate, t_0 (min) is the time at the start of the experiment, t_m (min) is the time at which the separation capacity is measured, which can be at BTP or at full saturation, C_0 (mg·mL^{-1}) is the concentration of H_2S at the inlet and C_m (mg·mL^{-1}) is the concentration of H_2S at the outlet at t_m.

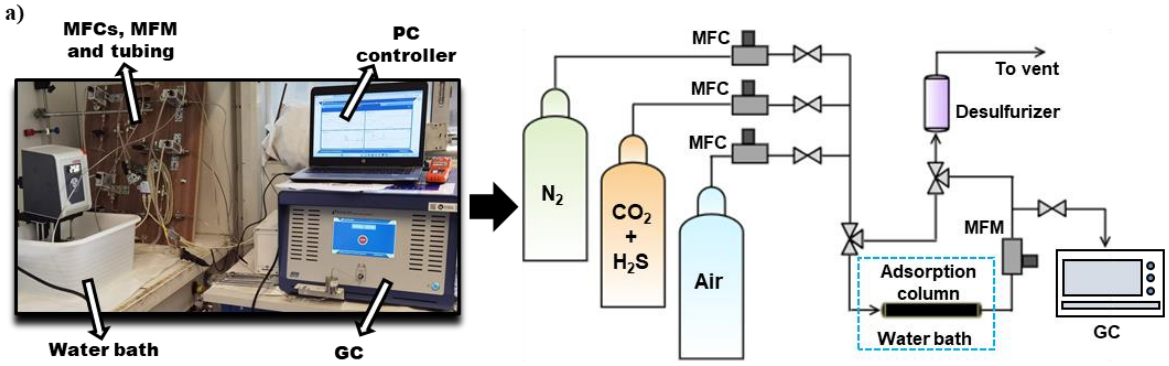

b)

Charcoal and activated charcoal

Sample	BET area ($m^2.g^{-1}$)	Bulk density ($kg.m^{-3}$)
Charcoal	400	387
AC_850°C_1h	655	340
AC_850°C_2h	840	295
AC_850°C_3h	1085	268
AC_900°C_2h	1120	263
AC_900°C_3h	1445	229

CACs for biogas desulfurization

Sample	BET area ($m^2.g^{-1}$)	Bulk density ($kg.m^{-3}$)
CAC 1	1025	518
CAC 2	1145	687
CAC 3	925	559
CAC 4	940	584
CAC 5	920	600
CAC 6	830	753
CAC 7	920	764
CAC 8	885	704
CAC 9	900	714

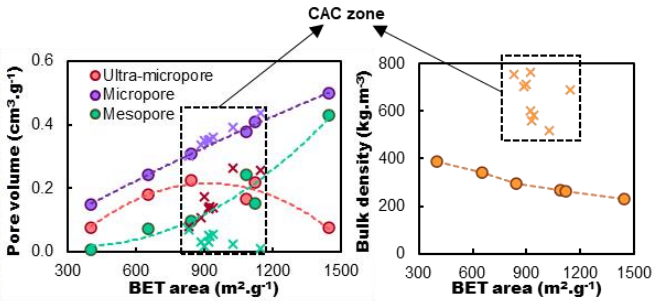

Figure 3.1 a) Experimental test bench for dynamic H_2S adsorption. MFC: mass flow controller; MFM: mass flow meter; GC: gas chromatograph. B) BET area and bulk density of lab-made wood-derived ACs and commercial ACs (CACs) for biogas desulfurization investigated here (tables), as well as pore volume and bulk density vs BET area of ACs (solid discs) and CACs (crosses).

The separation capacity is expressed normalized by adsorbent mass (g) or adsorbent volume (cm^3) as presented in Eq. (3.3) and Eq. (3.4), respectively.

$$q^{m}_{H_2S} = \frac{q_{H_2S}}{AC\ mass} \quad \textbf{(3.3)}$$

$$q^{v}_{H_2S} = \frac{q_{H_2S}}{AC\ volume} \quad \textbf{(3.4)}$$

The separation of H_2S on ACs was investigated, along with the effects of H_2O and O_2. Additionally, a comparison of the performance of the most efficient AC developed here with CACs was made by evaluating its efficiency at both low (400 ppm) and high (4000 ppm) H_2S concentrations, as well as in the presence of O_2 in the gas feed.

3.2.5 Mathematical model

The adsorption dynamics are analysed using the axially dispersed plug flow model with mass transfer described by the linear driving force (LDF) approach and equilibrium governed by the Langmuir isotherm. The model assumes isothermal conditions, negligible radial dispersion, constant fluid velocity and adsorbent particles uniform in size and density, with a constant void fraction in the bed. Thus, the mass balance equation, as demonstrated elsewhere,[7] becomes:

$$-D_L \frac{\partial^2 c_g}{\partial Z^2} + \frac{\partial}{\partial Z}\left(v c_g\right) + \frac{\partial c_g}{\partial t} + \frac{(1-\varepsilon)}{\varepsilon}\rho \frac{\partial q_i}{\partial \mathrm{t}} = 0 \quad (3.5)$$

where D_L ($m^2 \cdot s^{-1}$) is the axial dispersion coefficient, c_g ($mol \cdot m^{-3}$) is the concentration of bulk H_2S not adsorbed in the column, Z (m) is the axial position along the column, v ($m \cdot s^{-1}$) is the surface velocity of the gas, t (s) is time, ε (dimensionless) is the void fraction of the adsorbent bed, ρ is the AC bulk density ($kg \cdot m^{-3}$) and q_i ($mol \cdot kg^{-1}$) is the average concentration of H_2S adsorbed. D_L is calculated from the correlation of Chung and Wen:[26]

$$D_L = \frac{2\ R_p\ v\ \varepsilon}{0.2 + 0.011\ \ Re^{0.48}} \quad (3.6)$$

where R_p (m) is the particle diameter and Re is the Reynolds number.

The LDF model describes the mass transfer rate involving interparticle and intraparticle transport of the adsorbate from the fluid phase to the inner surface of the solid:

$$\frac{\partial q_i}{\partial t} = k\ (q^* - q_i) \quad (3.7)$$

where k (s^{-1}) is the rate constant for H_2S adsorption determined by fitting experimental data and simulation results, and q^* ($mol \cdot kg^{-1}$) is the amount of H_2S adsorbed at equilibrium under present conditions.

The equilibrium isotherm parameters were determined by fitting the experimental H_2S adsorption data to the Langmuir isotherm model:

$$q^* = \frac{q_s\, b\, C_o}{1 + bC_o} \tag{3.8}$$

where q_s ($mol \cdot kg^{-1}$) is the maximum adsorbed capacity, b ($m^3 \cdot mol^{-1}$) is the Langmuir affinity constant, and C_0 ($mol \cdot m^{-3}$) is the inlet H_2S concentration.

The system of equations is solved using an in-house MATLAB code, which employs the finite-difference approximation for discretization and uses the ode15s solver. The initial conditions are $C = 0$ and $q = 0$ for $0 \leq Z \leq L$, where L is the column length. The boundary conditions are $C = C_0$ at $Z = 0$ and $\frac{\partial c}{\partial Z} = 0$ at $Z = L$. **Table 3.2** presents the input data required to simulate dynamic H_2S adsorption, including bed characteristics and AC and gas properties.

Table 3.2 Parameters used for simulation of dynamic H_2S adsorption.

Gas properties		Bed properties	
Feed gas flow rate ($m^3 \cdot s^{-1}$)	1.33×10^{-6}	Length (m)	0.1
Gas density ($kg \cdot m^{-3}$)	1.41	Diameter (m)	7.7×10^{-3}
Gas viscosity (Pa.s)	1.66×10^{-5}	Bed void fraction	0.23
Reynolds number	7.7	Activated carbon properties	
Peclet number	132.9	Particle diameter (m)	7.5×10^{-4}
D_L ($m^2 \cdot s^{-1}$)	9.13×10^{-5}	Bulk density ($kg \cdot m^{-3}$)	Mass of adsorbent / Bed volume

The bed void fraction was estimated from the adsorbent mass and calculating the volume it occupies based on its envelope density. The void space was then determined by subtracting this volume from the total bed volume. Bulk density was determined by dividing the mass of adsorbent filling the bed by the total bed volume. Gas density and viscosity were calculated at 25 °C and 1 bar for the gas composition tested (N_2 60% - CO_2 40%), using the NIST Reference Fluid Thermodynamic and Transport Properties Database (REFPROP-version 10.0).[27]

3.3 Results and discussion

3.3.1 Characteristics of synthesized and commercial ACs

Textural parameters (A_{BET}, $V_{ultra\text{-}mic}$, V_{mic} and V_{mes}) and bulk densities of wood-derived ACs on the one hand, and of CACs on the other hand, are presented in **Figure 3.1b**, along with N_2 adsorption-desorption isotherms and tabulated values in **Figure A2.2** and **Table A2.1**, respectively.

For wood-derived ACs, the micropore volume increases linearly with A_{BET}. At the highest BET area (1445 $m^2 \cdot g^{-1}$), the micropore volume reaches 0.5 $cm^3 \cdot g^{-1}$, highlighting a strong microporosity development. The mesopore volume also correlates positively with A_{BET}, with significant development evident above 840 $m^2 \cdot g^{-1}$, corresponding to AC_850°C_2h. The ultra-micropore volume follows a parabolic trend, increasing up to a maximum of 840 $m^2 \cdot g^{-1}$, and then decreasing as A_{BET} continues to grow. This decline indicates that ultra-micropores are converted into larger micropores and mesopores with further activation, due to pore widening.

For CACs, BET areas range from 830 to 1145 $m^2 \cdot g^{-1}$. Micropores represent the largest fraction of total pore volume, with CAC 1 and CAC 2 having the highest ultra-micropore volumes (0.39 $cm^3 \cdot g^{-1}$ and 0.44 $cm^3 \cdot g^{-1}$, respectively). Overall, ACs with $A_{BET} \geq 840$ $m^2 \cdot g^{-1}$ are competitive with the CACs in terms of ultra- and microporosity, while also exhibiting a remarkably higher mesoporosity.

In terms of bulk density, CAC 1, a wood-based carbon, has the lowest density among commercial samples (518 $kg \cdot m^{-3}$). In contrast, our wood-based ACs present lower bulk densities, between 340 and 229 $kg.m^{-3}$, depending on the degree of activation. The highest bulk density is observed for CAC 7 (764 $kg \cdot m^{-3}$), a coal-based carbon, highlighting a key advantage of mineral ACs: their inherently higher densities. Although CAC 1 has the same woody origin as our ACs, it is pelletized, like all commercial ACs, which enhances its density and structural integrity. Similarly, CAC 2, derived from coconut shell, presents a high density of 687 $kg \cdot m^{-3}$. Densification plays a crucial role in increasing compactness, allowing more carbon to be packed into the same volume, thereby improving volumetric adsorption performance and mechanical stability.

3.3.2 H_2S adsorption on wood-derived ACs

3.3.2.1 Effect of H_2S initial concentration

The experimental breakthrough curves are presented in **Figure 3.2a** for the 400 ppm H_2S scenario and in **Figure 3.2b** for the 4000 ppm case. Separation capacities at BTP are normalized by mass (**Figure 3.2c**) and volume (**Figure 3.2d**) of AC, and also shown as a function of micropore, again per unit mass (**Figure 3.2e**) and per unit volume (**Figure 3.2f**) of AC. The corresponding values are presented in **Table A2.2**.

Increasing the H_2S concentration from 400 to 4000 ppm leads to an increase in separation capacity at both BTP and saturation at 4000 ppm, due to the increased exposure to H_2S. For both H_2S concentrations, the results follow the same trend. The pristine charcoal exhibits the shortest breakthrough time and, consequently, the poorest performance. AC_850°C_1h, the least activated sample, shows the lowest adsorption values among the ACs, with 1.46 $mg \cdot g^{-1}$ H_2S and 2.37 $mg \cdot g^{-1}$ H_2S separated at BTP at 400 and 4000 ppm, respectively.

The highest adsorption capacities at 4000 ppm were achieved by AC_850°C_3h and AC_900°C_2h, with adsorption values of 5.55 $mg \cdot g^{-1}$ and 5.26 $mg \cdot g^{-1}$ at BTP and corresponding microporosity values of 0.38 $cm^3 \cdot g^{-1}$ and 0.41 $cm^3 \cdot g^{-1}$, respectively. In contrast, the carbon with the highest A_{BET} and microporosity (AC_900°C_3h: 1445 $m^2 \cdot g^{-1}$ and 0.50 $cm^3 \cdot g^{-1}$, respectively) did not achieve the expected high performance, as initially suggested by the N_2 adsorption isotherms (see **Figure A2.2a** and **Table A2.1**). Although it demonstrated competitive performance in terms of separation per unit mass, achieving 5.23 $mg \cdot g^{-1}$ of H_2S at BTP at 4000 ppm (see **Figures 3.2c** and **3.2e**), its separation per unit volume was notably lower: 1.06 $mg \cdot cm^{-3}$ (see **Figures 3.2d** and **3.2f**). This is significantly less than the 1.36 $mg \cdot cm^{-3}$ and 1.34 $mg \cdot cm^{-3}$ achieved by AC_850°C_3h and AC_900°C_2h, respectively. Thus, the highest H_2S separation was achieved by ACs that maintain the best balance between ultra-microporosity and microporosity (see **Figure 3.1b**), which, for this charcoal, is achieved at a microporosity of ≈ 0.4 $cm^3 \cdot g^{-1}$. At higher values, the conversion of part of the supermicropores into mesopores reduces H_2S adsorption capacity. In fact, pores smaller than 0.7 nm are more effective, as their size closely matches the molecular diameter of H_2S, which is 0.33 nm.[7] Furthermore, it has been suggested that elemental sulfur formed during the oxidation of H_2S preferentially adsorbs in pores smaller than 1.2 nm.[7] While mesopores play a role in facilitating

mass transfer kinetics, the dominant factor influencing adsorption performance is the availability of appropriately sized micropores.

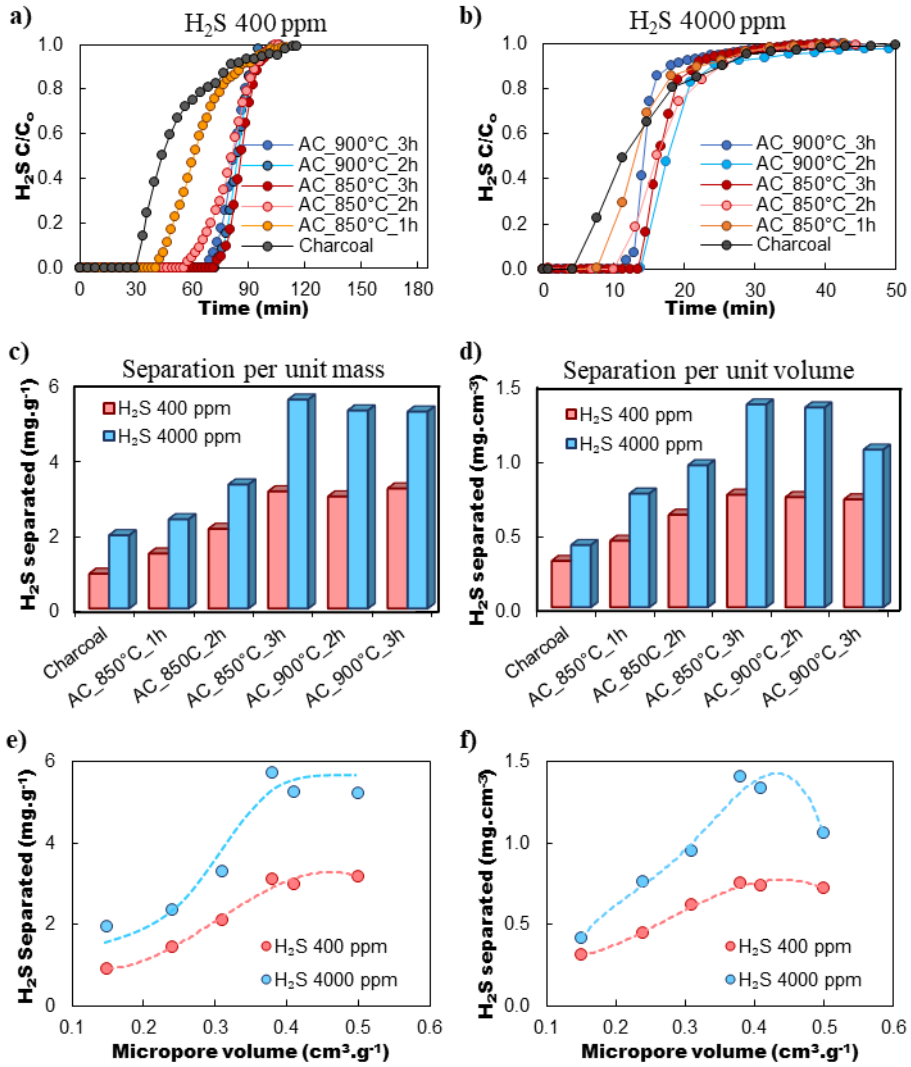

Figure 3.2 Breakthrough curves for dynamic H_2S adsorption in wood charcoal and non-impregnated wood-derived ACs at H_2S concentrations of a) 400 ppm and b) 4000 ppm. H_2S separation capacities at BTP expressed per c) unit mass and d) unit volume of AC, and as a function of micropore volume per e) unit mass and f) unit volume of AC.

3.3.2.2 Effect of AC impregnation

Three wood-derived ACs were selected for impregnation: AC_850°C_2h (A_{BET} = 840 $m^2 \cdot g^{-1}$) for its high ultra-microporosity, AC_850°C_3h (A_{BET} = 1085 $m^2 \cdot g^{-1}$) for its balanced micro- and mesoporosity, and AC_900°C_3h (A_{BET} = 1445 $m^2 \cdot g^{-1}$) for its high meso- and microporosity despite the absence of ultra-microporosity. AC_900°C_2h (A_{BET} = 1120 $m^2 \cdot g^{-1}$)

was discarded due to its textural properties similar to AC_850°C_3h (**Figure 3.1b**). Impregnations were performed with KOH, KI and K_2CO_3 at loadings of 5–30 wt.%.

Figure 3.3a, 3.3b and 3.3c show breakthrough curves for AC_850°C_3h impregnated with KOH, KI and K_2CO_3, respectively, using 400 ppm H_2S in a mixture of 60% N_2 and ~40% CO_2. The corresponding separation capacities at BTP are presented by unit mass and unit volume in **Figures 3.3d** and **3.3e**, with detailed values in **Tables A2.3–A2.5**. Additional curves for AC_850°C_2h and AC_900°C_3h are presented in **Figure A2.3**.

Chemical impregnation always extends adsorption time, which underlines its effectiveness. Whether the carbon has greater mesoporosity (AC_900°C_3h) or greater ultra-microporosity (AC_850°C_2h), impregnation remains most effective in the sample with the best balance between ultra-microporosity and microporosity (AC_850°C_3h), which was previously identified as the optimum carbon without impregnation (see again **Figure 3.2**).

KOH impregnation resulted in the longest breakthrough times, reaching 226 minutes with AC_850°C_3h at 20 wt.%. In comparison, KI and K_2CO_3 reached 196 minutes (at 30 wt.%) and 175 minutes (at 20 wt.%), respectively. The efficacy of KOH is well documented,[10, 11, 28] and it is indeed widely used in CACs for biogas desulfurization (e.g., CAC 2 and CAC 3; see **Table 3.1**).

Breakthrough time increased remarkably from 5 to 10 wt.% impregnation. Above 10 wt.%, improvements were minimal or even disappeared, as seen with AC_900°C_3h at 30 wt.% KOH. Higher loadings also increase costs and risk blocking pores, reducing efficiency. Thus, 10 wt.% is the optimum impregnation rate for all samples, whatever the impregnating agent.

AC_850°C_3h with 10 wt.% KOH shows the best performance, reaching 6.82 $mg \cdot g^{-1}$ and 2.22 $mg \cdot cm^{-3}$ at BTP. Although AC_900°C_3h with KOH achieved a similar mass-based separation (6.70 $mg \cdot g^{-1}$), its volumetric capacity is lower (1.80 $mg \cdot cm^{-3}$), confirming that AC_850°C_3h KOH is optimal. KI proved slightly competitive with respect to K_2CO_3, with 1.60 vs. 1.71 $mg \cdot cm^{-3}$ at 10 wt.% on AC_850°C_3h.

An impregnation level of 10 wt.% is widely recognized as optimal for maximizing H_2S removal, both in the literature and in commercial ACs.[7] For instance, Bagreev and Bandosz reported an increase from 56.3 to 272.2 $mg \cdot g^{-1}$ for the commercial AC called G55C (formerly produced by PICA, now Jacobi), when impregnated with 10 wt.% NaOH.[12] Similarly, Yang et al. found that impregnating the commercial AC called BAX-1520 with 10 wt.% $ZnFe_2O_4$ was

optimal, increasing removal from 5.6 to 122.5 mg·g^{-1}.[14] CACs also typically use 2–10 wt.% (see **Table 3.1**), which is in line with our results.

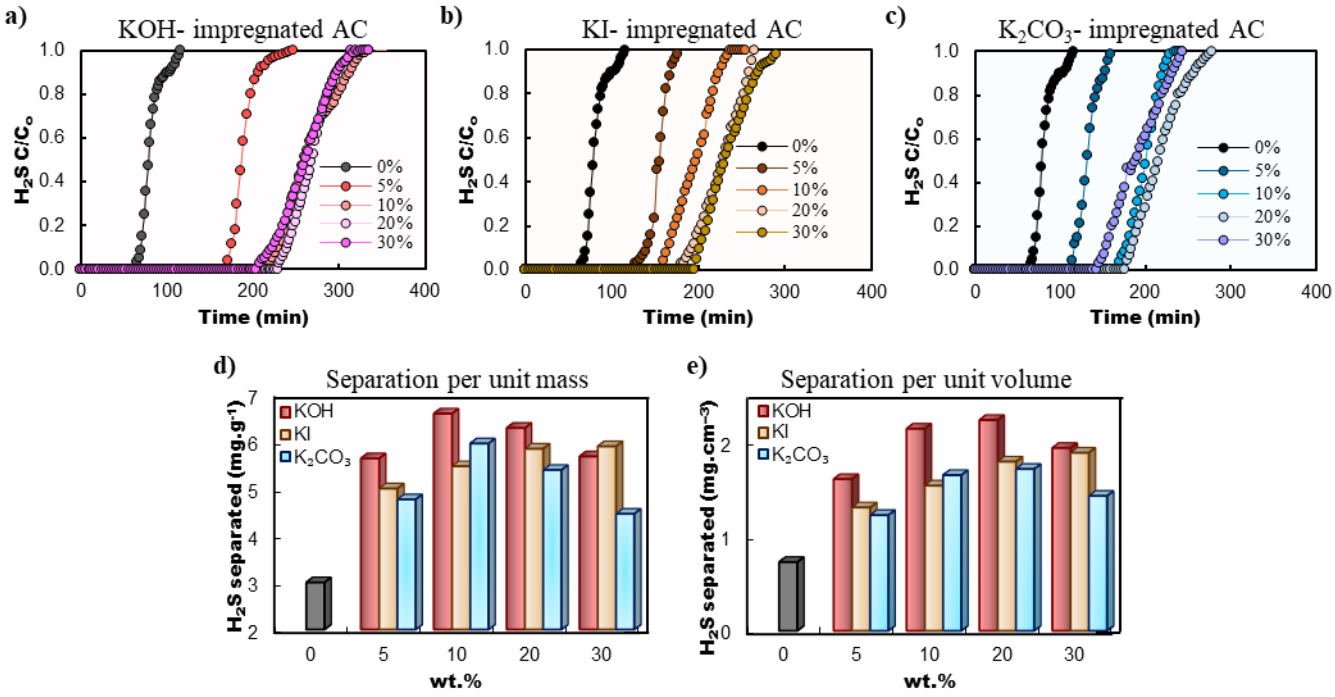

Figure 3.3 Effect of impregnating agent and impregnation ratio on H_2S (400 ppm) adsorption by AC_850C_3h impregnated with: a) KOH b) KI and c) K_2CO_3, and separation capacities at BTP expressed per d) unit mass and e) unit volume.

ACs impregnated with strong bases always exhibit higher H_2S adsorption capacities than unmodified ACs. In alkaline environments, such as those created by KOH or K_2CO_3, H_2S indeed undergoes acid-base reactions that promote its removal. Although the exact mechanisms involving KI are less well understood, it has been suggested that at elevated temperatures (around 550 °C), KI also facilitates H_2S removal through similar reactions. Additionally, potassium compounds not only contribute to the formation of intermediates such as KHS, but also promote the selective oxidation of H_2S, particularly in the presence of water and oxygen. Detailed H_2S removal mechanisms using impregnated ACs have been listed elsewhere.[7]

3.3.2.3 Effect of humidity on H_2S separation

To assess the impact of humidity on H_2S separation, three ACs (AC_900°C_3h, AC_900°C_2h and AC_850°C_3h) were tested after drying (24 h at 104 °C) on the one hand, and after moisture sorption (24 h at 50% RH, 25 °C) on the other hand, using a gas mixture consisting of 60% N_2, 400 ppm H_2S, and ~ 40% CO_2. As shown in **Figure 3.4a**, humidified

samples showed three times longer breakthrough times, indicating enhanced H_2S adsorption. **Figures 3.4b and 3.4c**, respectively showing separation capacity at BTP per unit mass and per unit volume, confirm this, with humidified ACs achieving higher capacities. For example, AC_850°C_3h adsorbed 3.11 $mg \cdot g^{-1}$ when humidified, compared with just 1.26 $mg \cdot g^{-1}$ when dry, thus more than doubling its performance in the presence of moisture.

AC_850°C_3h with 10 wt.% KOH was pre-humidified at different RH levels for 24 h before H_2S adsorption. Breakthrough curves and corresponding separation capacities at BTP are shown in **Figures 3.4d–f**, with values in **Table A2.6**. Lower RH (10%) led to earlier breakthrough and reduced adsorption, while higher RH prolonged breakthrough times. The highest capacity was achieved at 90% RH: 7.07 $mg \cdot g^{-1}$ and 2.58 $mg \cdot cm^{-3}$, i.e. 9 times more than the same carbon without impregnation and under dry conditions of separation per unit volume.

In the dry state, H_2S is mainly removed by physical adsorption. In the presence of humidity, a film of water forms on the carbon surface, which promotes H_2S dissociation and its interaction with the basic sites of the AC. Thus, H_2S first adsorbs onto the surface, and then dissolves into the water layer as a liquid-like phase, where it dissociates into HS^- and H^+ ions.[7]

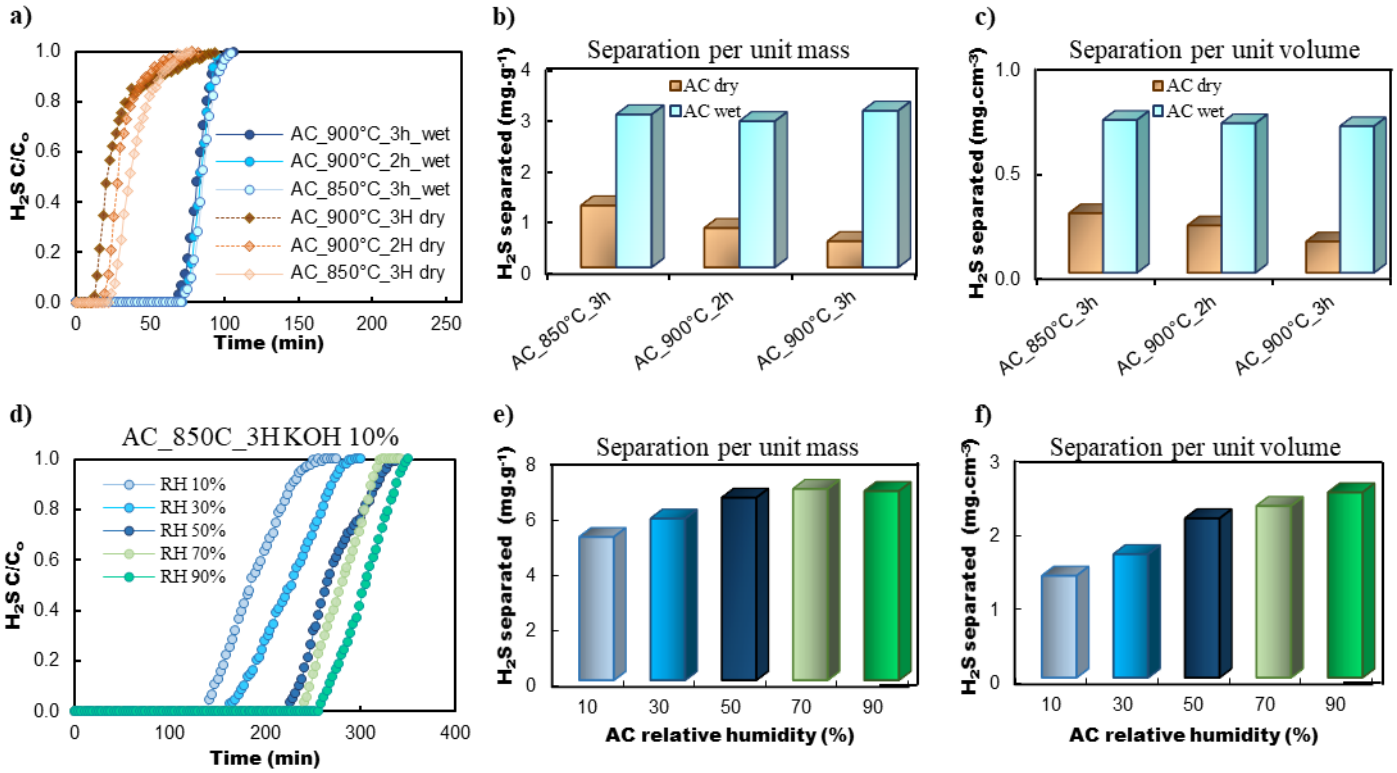

Figure 3.4 Humidified and dried ACs for H_2S (400 ppm) separation: a) breakthrough curves, and separation capacity per b) unit mass and c) unit volume. Effect of humidity on H_2S (400 ppm) separation of AC_850°C_3h impregnated with 10 wt.% KOH: d) breakthrough curves, and separation capacity per e) unit mass and f) unit volume.

The literature has also focused on investigating the effect of the presence of water by humidifying the gas feed. For instance, in the work of Barelli et al., an H_2S separation test was carried out on the commercial AC Desotec Ultra DS in dry gas and humidified to 90 % RH, showing an increase from 15.71 $mg \cdot g^{-1}$ H_2S adsorbed under dry gas conditions to 34.87 $mg \cdot cm^{-3}$ H_2S at 90 % RH.[29] The higher separation capacities reported in their study for the dried AC test are due to two main conditions: their feed gas contained only H_2S and N_2, leaving more micropore space for H_2S adsorption due to the absence of CO_2, and they used impregnated carbon, which was not the case with ours.

Other studies have reached the same kind of conclusion. For example, Cimino et al. compared dry gas to humidified gas, obtaining better performance for ACs when 50% RH was present in the feed gas.[30] Castrillon et al. also compared the performance of commercial Desorex AC impregnated with NaOH in dry gas and humidified gas at 70% RH, and found better performance under wet conditions.[13]

During biogas purification, water is usually retained during the H_2S removal stage to facilitate this process, and is removed thereafter to ensure optimum separation for downstream applications.[7] Moreover, CAC suppliers suggest maintaining a RH of 40% to 80% in the gas for optimum efficiency.[31]

3.3.2.4 Effect of O_2 on H_2S separation

Oxygen, typically present in biogas at concentrations ranging from 0.5 to 2%, was introduced into the feed gas at 1.1%, with 4000 ppm H_2S, 60% N_2, and the remainder (~39%) CO_2. **Figure 3.5a** presents the H_2S breakthrough curve for the wood-derived ACs as well as their separation capacities at BTP, compared with the same test but without O_2. Detailed values are listed in **Table A2.7**. Longer breakthrough times indicate increased separation capacity compared with H_2S adsorption without oxygen (**Figure 3.2b**). It can be seen that O_2 enhanced H_2S removal for all tested ACs. AC_850°C_3h and AC_900°C_2h remained the best performers, with mass-based capacities of 47.22 and 46.70 $mg \cdot g^{-1}$, and volumetric capacities of 12.74 and 12.53 $mg \cdot cm^{-3}$, respectively. Oxygen thus increased separation efficiency by up to eight times, highlighting its positive effect under oxidizing conditions.

The effect of O_2 was also evaluated for AC_850°C_3h impregnated with 10 wt.% KI, 10 wt.% K_2CO_3 and 10 wt.% KOH, and compared with the non-impregnated sample (**Figures 3.5b**). KOH showed the highest performance with a breakthrough capacity of 121.2 $mg \cdot g^{-1}$, followed by K_2CO_3 (97.2 $mg \cdot g^{-1}$) and KI (82.9 $mg \cdot g^{-1}$). The same trend was observed for the separation of H_2S per unit volume, with 10 wt.% KOH giving the highest separation capacity (38.2 $mg \cdot cm^{-3}$), followed by K_2CO_3 (27.7 $mg \cdot cm^{-3}$) and KI (29.1 $mg \cdot cm^{-3}$).

The presence of oxygen (either in the gas phase or adsorbed) plays a key role in the oxidation of H_2S on AC, leading to the decomposition of H_2S and the formation of various sulfur-containing compounds, including elemental sulfur (S or S_8), sulfur dioxide (SO_2), and water. Solid sulfur deposited on the carbon surface can undergo further oxidation, contributing to the production of SO_2. Additionally, sulfur species such as elemental sulfur or polysulfides adsorbed on carbon may act as active sites, facilitating the oxidation of H_2S. These sites can form reactive intermediates, including sulfur radicals and oxidized sulfur species, which promote a catalytic cycle of sulfur transformation and H_2S removal.[7]

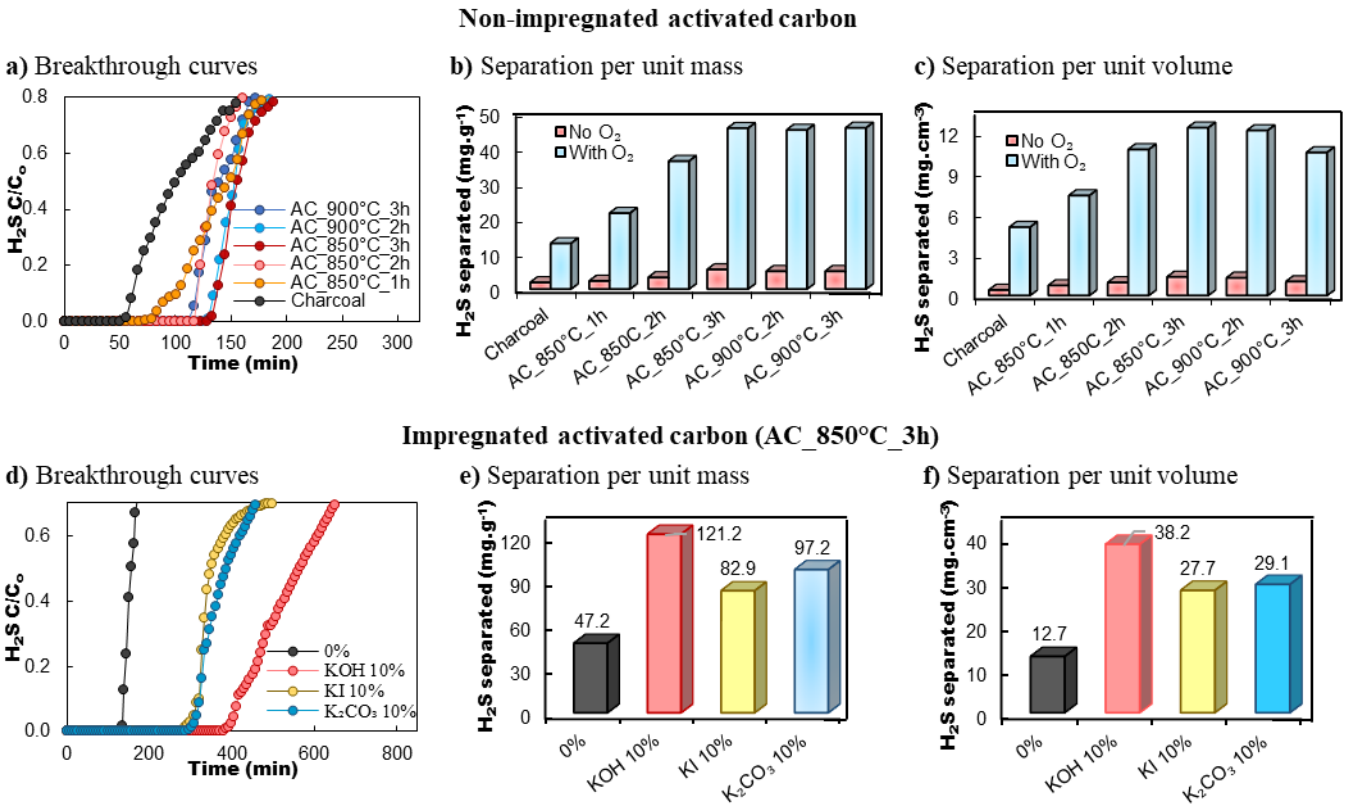

Figure 3.5 Effect of O_2 on H_2S (4000 ppm) separation performance of wood-derived (non-impregnated) ACs: a) breakthrough curves, and separation capacities per b)unit mass and c) unit volume. Effect of O_2 on H_2S (4000 ppm) separation of AC_850°C_3g impregnated at 10 wt.%: d) breakthrough curves, , and separation capacities per e) unit mass and f) unit volume.

3.4 Performance comparison with commercial activated carbons

Figure 3.6 compares the H_2S adsorption behavior and separation capacities at BTP of the KOH-impregnated AC, AC_850°C_3h_KOH10, with CACs in three different cases: H_2S concentration of 400 ppm (**Figure 3.6a**), 4000 ppm (**Figure 3.6b**), and 4000 ppm in the presence of O_2 at 1.1% (**Figure 3.6c**), again in a mixture of 60% N_2 balanced with CO_2. Separation capacities at saturation are presented in **Tables A2.8** and **A2.9**.

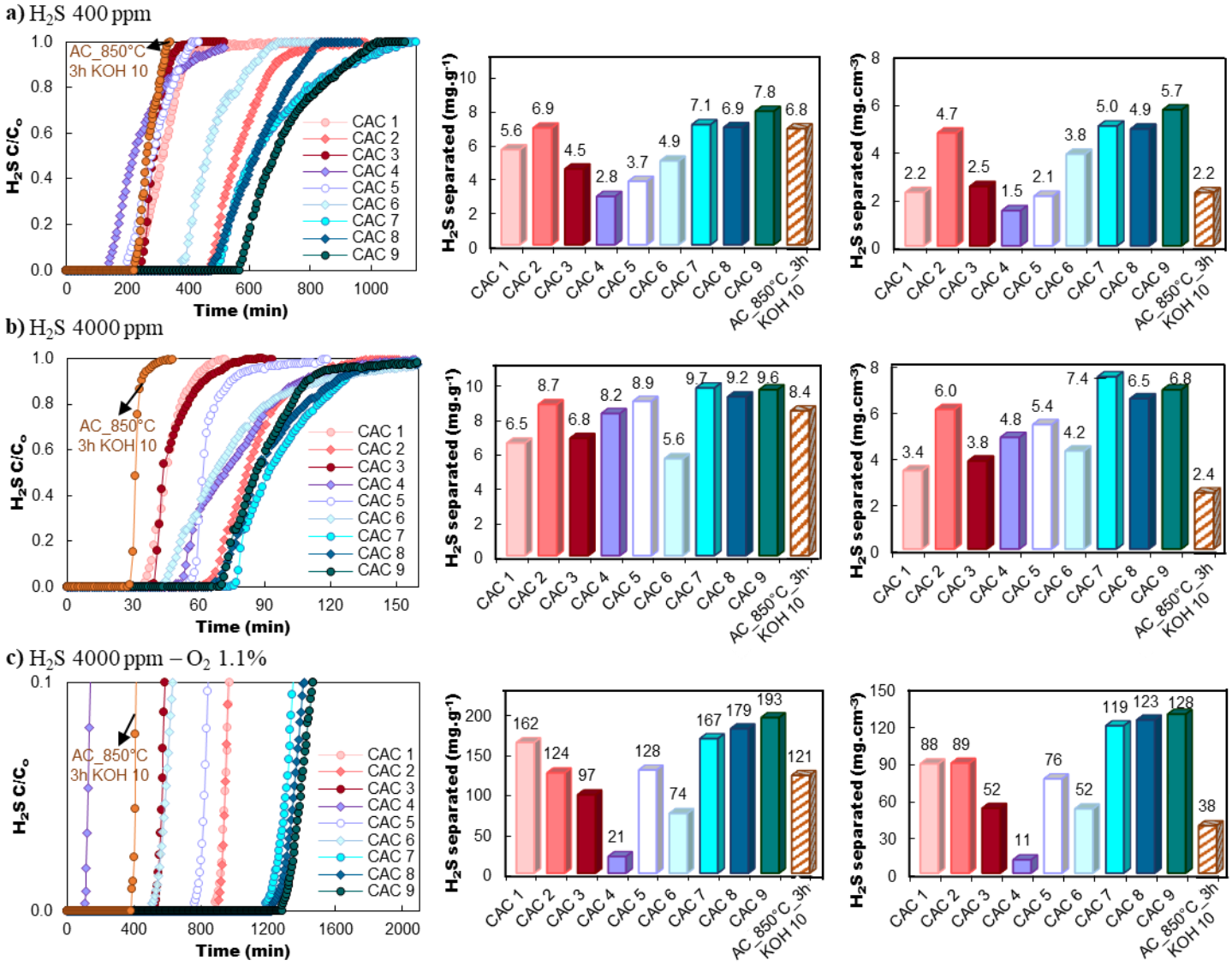

Figure 3.6 H_2S breakthrough curves and separation capacities of commercial ACs and wood-derived AC_850°C_3h_KOH 10, using: a) 400 ppm H_2S, b) 4000 ppm H_2S, and c) 4000 ppm H_2S in the presence of O_2.

3.4.1 Effect of H_2S initial concentration

At 400 ppm H_2S, CAC 9 exhibited the longest breakthrough time and highest separation capacities (7.8 mg·g^{-1} and 5.7 mg·cm^{-3}), attributed to its high bulk density (714 kg·m^{-3}), highest ultra-microporosity (0.17 cm^3·g^{-1}) among mineral coal-based CACs, and substantial microporosity (0.35 cm^3·g^{-1}). Although the nature of its impregnating agent is undisclosed, the loading (7 wt.%) is close to the optimal 10 wt.% identified in this study. CAC 2, a coconut-shell-based carbon, also performed well, ranking just behind CAC 9, with separation capacities

of 6.9 $mg \cdot g^{-1}$ and 4.7 $mg \cdot cm^{-3}$, supported by high ultra-microporosity (0.26 $cm^3 \cdot g^{-1}$), microporosity (0.44 $cm^3 \cdot g^{-1}$) and bulk density (687 $kg \cdot m^{-3}$). Despite CAC 1 having the highest porosity overall (ultra-microporosity: 0.26 $cm^3 \cdot g^{-1}$; microporosity: 0.39 $cm^3 \cdot g^{-1}$), its low bulk density (518 $kg \cdot m^{-3}$) limited its volumetric capacity (2.2 $mg \cdot cm^{-3}$), although its mass-based performance remained significant (5.6 $mg \cdot g^{-1}$), surpassing CACs 3, 4, 5, and 6. CAC 4, impregnated with $KmnO_4$ and designed for use without O_2, showed the shortest breakthrough time and poorest performance (2.8 $mg \cdot g^{-1}$, 1.5 $mg \cdot cm^{-3}$), likely due to the absence of H_2O in the feed gas, essential for $KmnO_4$ activation, which involves dissolution and reduction to MnO_2 and other active manganese species[32]. Our optimized material, AC_850°C_3h_KOH 10, achieved high mass-based performance (6.8 $mg \cdot g^{-1}$) and outperformed CACs 1, 4, and 5 in breakthrough time (2.2 $mg \cdot cm^{-3}$), benefiting from a well-developed pore structure (0.17 and 0.38 $cm^3 \cdot g^{-1}$ for ultra-microporosity and microporosity, respectively) and optimal KOH impregnation. However, its low bulk density (268 $kg \cdot m^{-3}$) remained a limiting factor for volumetric performance.

At 4000 ppm H_2S without O_2, breakthrough times decreased for all samples due to faster saturation, but higher H_2S concentration led to increased separation capacities. The performance trend remained, with CACs 7, 8, and 9 showing the best volumetric performance; CAC 7 stood out with 9.7 $mg \cdot g^{-1}$ and 7.4 $mg \cdot cm^{-3}$, aided by its well-balanced porosity (micropores: 0.35 $cm^3 \cdot g^{-1}$; mesopores: 0.03 $cm^3 \cdot g^{-1}$) and 10 wt.% NaOH impregnation, known to promote H_2S decomposition[12]. CAC 1 and AC_850°C_3h_KOH 10 showed lower volumetric performance (3.4 and 2.4 $mg \cdot cm^{-3}$, respectively) due to low bulk density, but the latter AC remained competitive with a strong mass-based capacity of 8.4 $mg \cdot g^{-1}$, confirming its potential despite volumetric limitations.

3.4.2 Effect of O_2 in the gas feed

In the presence of O_2, CAC 1 showed a marked improvement in H_2S separation capacity (88 $mg \cdot cm^{-3}$), outperforming the denser CAC 6 (764 vs. 518 $kg \cdot m^{-3}$ for CAC 1), likely due to its well-developed porosity and an effective, though undisclosed, impregnating agent active under oxidizing conditions. CAC 2, previously among the top performers in the absence of O_2, exhibited diminished performance, now comparable to CAC 1 and CAC 5. This decline may be attributed to its low KOH impregnation level (5 wt.%), suggesting that increasing it to 10 wt.% could enhance separation. CAC 3 also showed reduced performance (97 $mg \cdot g^{-1}$,

52 mg·cm^{-3}) despite comparable porosity, possibly due to its lower-than-expected bulk density (559 kg·m^{-3}) and limited 5 wt.% KOH loading. Similarly, CAC 4, the least effective sorbent (21 mg·g^{-1}, 11 mg·cm^{-3}), showed minimal improvement with O_2, likely because it was designed for operation without O_2 and is impregnated with $KmnO_4$, which requires moisture for activation. CAC 5 displayed modest performance (128 mg·g^{-1}, 76 mg·cm^{-3}), possibly limited by its KI-based impregnation, which our results suggest is suboptimal under oxidizing conditions. By comparison, AC_850°C_3h_KOH 10 achieved competitive mass-based separation (121 mg·g^{-1}), similar to mid-range CACs such as CAC 2, 3, 4, and 6. Its enhanced performance under O_2 is attributed to improved oxidation and available pore volume. However, in terms of volumetric capacity, it only outperformed CAC 3, indicating that densification is necessary to improve its overall performance.

3.5 Modeling of breakthrough curves

To validate the mathematical model against experimental data in realistic conditions, AC_850°C_3h was again studied with and without 10 wt.% KOH impregnation. In addition, the KOH-impregnated AC was also evaluated for separation in the presence of 1.1% O_2. To determine their H_2S adsorption isotherms, various H_2S concentrations were tested and the total saturation capacity was calculated for each concentration, as shown by the breakthrough curves in **Figure 3.7a**. **Figure 3.7b** presents the fit of the Langmuir isotherm to the experimental isotherm data (See **Table A2.10** for values).

The Langmuir isotherm equilibrium constants were calculated by fitting the experimental adsorption capacity results (solid discs in **Figure 3.7b**) by Eq. (3.8), and are presented in **Table A2.11**. The Langmuir model provides a reasonable estimate of the maximum adsorption capacity, as the calculated q_s values slightly exceed the experimentally determined adsorbed amounts at the highest H_2S concentration tested of 4000 ppm. For instance, for AC_850°C_3h, q_s is 8.52 mg·g^{-1}, slightly above the experimental value of 7.05 mg·g^{-1} at 4000 ppm. This overestimation may due to the inherent limitations of the Langmuir model, which assumes ideal conditions such as monolayer adsorption, uniform surface and identical adsorption sites,[33] assumptions from which real systems deviate. As a result, although the model may accurately capture the overall shape of the isotherm, it can misrepresent the true maximum adsorption capacity.

The mass transfer coefficient, *k*, or LDF coefficient (see **Table 3.3**), was determined by fitting the simulation (dashed lines) to the experimental data presented in **Figure 3.7a**, demonstrating good agreement.

K tends to stabilize as the concentration exceeds 400 ppm, meaning that mass transfer resistance becomes similar. This is confirmed by the comparable slopes observed in the adsorption curves above 400 ppm H_2S. However, when AC_850°C_3h_KOH 10 wt.% was evaluated in the presence of O_2, *k* decreased further from 3.0×10^{-4} s^{-1} at 1000 ppm H_2S to 1.5×10^{-4} s^{-1} at 4000 ppm H_2S.

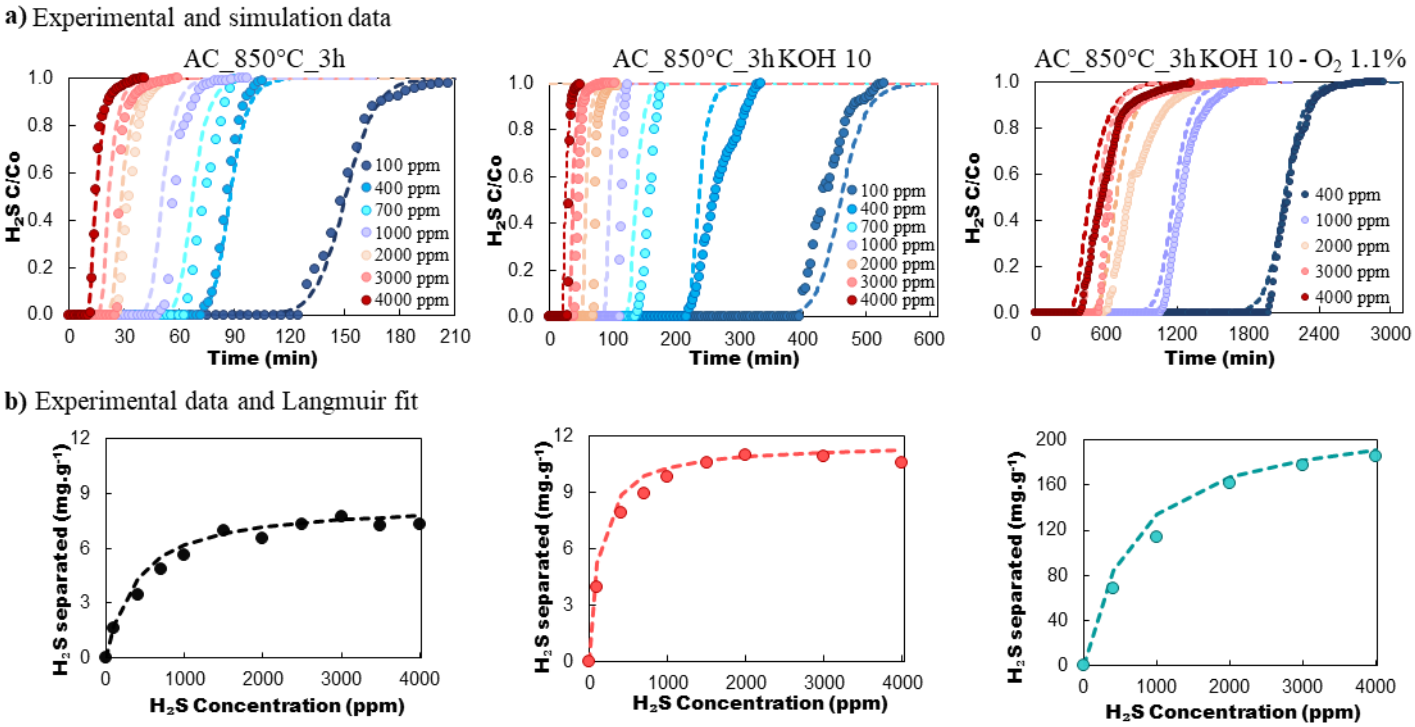

Figure 3.7 a) Experimental (solid discs) and simulated (dashed lines) breakthrough curves at different H_2S concentrations for AC_850°C_3h, AC_850°C_3h_KOH 10 and AC_850°C_3h_KOH 10 under the presence of O_2. **B)** H_2S equilibrium adsorption isotherms at 25 °C from experimental breakthrough curves: discs correspond to experimental data and dashed lines correspond to Langmuir fits. (Gas composition: 60% N_2, balanced with CO_2, and 1.1% O_2 when present).

Table 3.3 Mass transfer coefficients k (s^{-1}) estimated by fitting experimental and simulation data at different H_2S feed concentrations.

H_2S concentration (ppm)	100	400	700	1000	2000	3000	4000
AC_850°C_3h	1.5×10^{-2}	6.0×10^{-3}	4.5×10^{-3}	4.5×10^{-3}	4.5×10^{-3}	4.5×10^{-3}	4.5×10^{-3}
AC_850°C_3h_KOH 10	4.0×10^{-3}	2.0×10^{-3}	3.0×10^{-3}	3.0×10^{-3}	3.0×10^{-3}	3.0×10^{-3}	3.0×10^{-3}
AC_850°C_3h_KOH 10 – O_2 1.1%	-	8.0×10^{-4}	-	3.0×10^{-4}	2.0×10^{-4}	2.0×10^{-4}	1.5×10^{-4}

The coefficient k is inversely related to breakthrough time and, consequently, to the H_2S separation capacity: the longer the breakthrough time, the lower the k value. The KOH-impregnated sample, AC_850°C_3h_KOH 10, has a lower k (3.0×10^{-3} s^{-1} at 4000 ppm H_2S) than its non-impregnated counterpart (4.5×10^{-3} s^{-1} at 4000 ppm). Additionally, AC_850°C_3h_KOH 10, when tested in the presence of O_2, gives a much lower k value of 1.5×10^{-4} s^{-1}. The improvement in H_2S separation observed with KOH impregnation and in the presence of O_2 is effectively captured in the model by the mass transfer coefficient, k. A reduced k indicates a slower apparent mass transfer rate, consistent with the prolonged breakthrough time and higher separation capacity observed experimentally.

Thus, the combined effects of surface modification and reaction conditions are expressed by kinetic and equilibrium terms in the dynamic adsorption model. In addition to k, which represents adsorption kinetics, the Langmuir isotherm parameters (q_s and b) are also affected by changes in the adsorbent's surface chemistry. These effects are reflected quantitatively in the Langmuir fit, as the parameters correlate directly with the amount of H_2S adsorbed.

As far as we know, our study is the first to produce H_2S adsorption isotherms in the presence of O_2. Previous studies that have produced H_2S adsorption isotherms without O_2 reported k values similar to those obtained in our O_2-free tests. For example, Aguilera and Ortiz reported a k value of 8.0×10^{-3} s^{-1} with a maximum Langmuir adsorption capacity (q_s) of 11.9 $mg \cdot g^{-1}$.[34] Gutierrez et al. reported 1.9×10^{-3} s^{-1} for a q_s of 15.0 $mg \cdot g^{-1}$,[35] and Papurello et al. obtained 0.128 s^{-1} for a q_s of 5.9 $mg \cdot g^{-1}$.[36] Similarly, our tests without O_2 gave k values of 4.5×10^{-3} s^{-1} and 2.0×10^{-3} s^{-1} for q_s values of 8.5 $mg \cdot g^{-1}$ and 11.6 $mg \cdot g^{-1}$ (see again **Table A2.11**), respectively. In the presence of O_2, on the other hand, k was significantly lower; for instance, at 4000 ppm H_2S, with a q_s of 221.5 $mg \cdot g^{-1}$, the k value dropped to 1.5×10^{-4} s^{-1}.

Distributions of H_2S concentration along the adsorbent bed as a function of time are presented for the three ACs studied, at 400 ppm H_2S (**Figure 3.8a**) and at 4000 ppm (**Figure 3.8b**). At 400 ppm H_2S without O_2, AC_850°C_3h showed faster movement of the mass transfer zone (MTZ), meaning that the bed became saturated earlier than the KOH-impregnated sample. AC_850°C_3h KOH 10 exhibited a slower progression of the MTZ, indicating a more gradual saturation process.

At 4000 ppm, the MTZ progresses much faster through the adsorbent bed compared to 400 ppm because the driving force for mass transfer is greater at higher concentrations, increasing the adsorption rate. Moreover, there is a broader MTZ represented by the intermediate color between black and yellow. The KOH-impregnated AC shows a slower movement of the adsorption front than the non-impregnated sample, but still saturates ~ 30-40 minutes earlier than in the 400 ppm case.

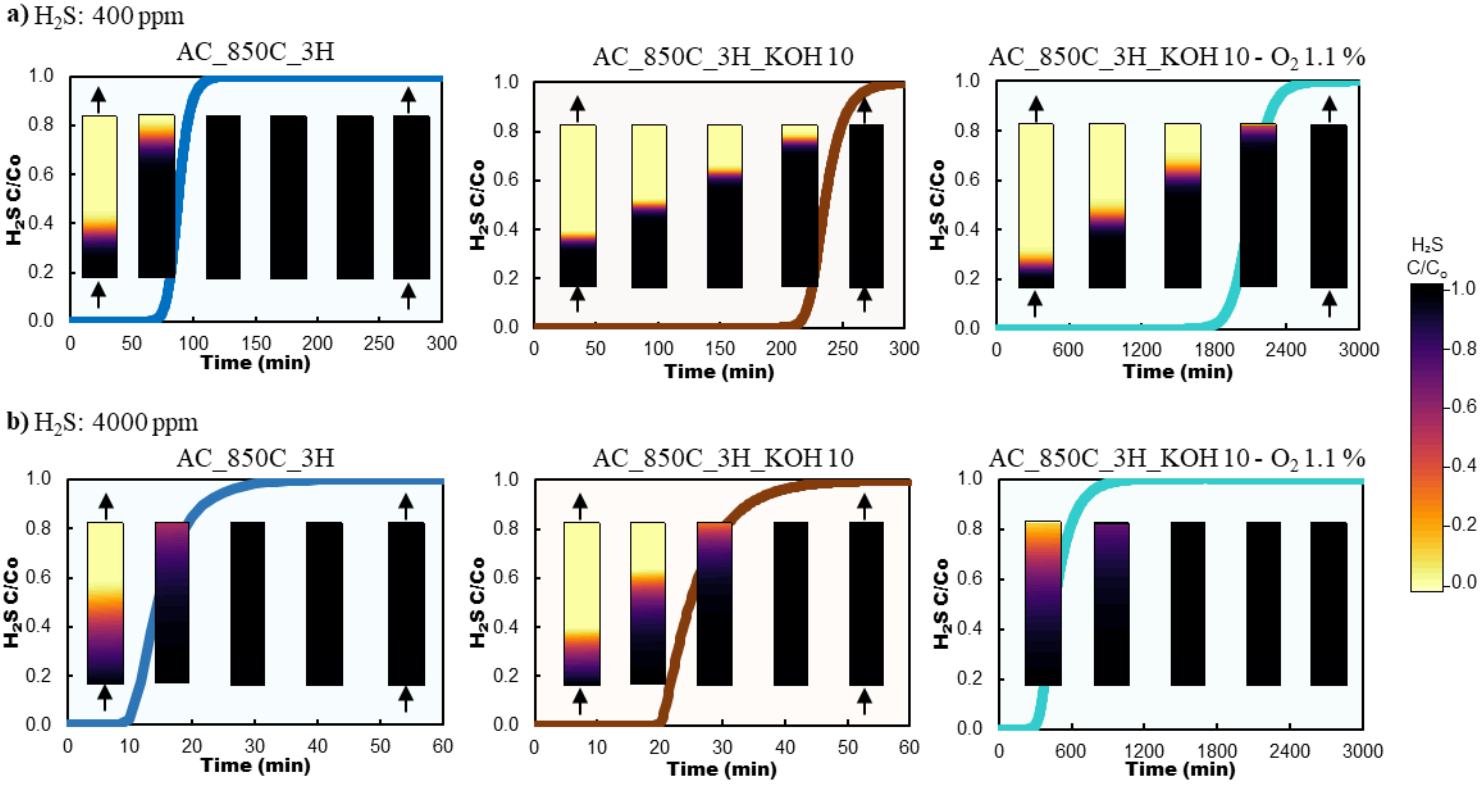

Figure 3.8 Breakthrough curves and H_2S concentration profiles from simulations at H_2S concentrations of: a) 400 ppm, and b) 4000 ppm.

In the presence of O_2, different concentrations of H_2S at the inlet show similar trends compared to adsorption without O_2; however, breakthrough times are up to 10 times longer,

which is attributed to the enhanced H_2S removal facilitated by oxidation reactions. This highlights the critical importance of conducting adsorption studies under oxidative conditions, which remain underexplored in the existing literature.

3.6 Conclusions

Activated carbons (ACs) were successfully synthesized from wood-based charcoal for efficient biogas desulfurization. Steam-activated charcoals at 850°C for 3 h and 900°C for 2 h yielded sorbents with the most effective H_2S removal performance, attributed to an optimal balance between ultramicroporosity and microporosity, thus highlighting the critical role of narrow micropores in H_2S adsorption, compared to mesoporosity. Among chemical impregnations evaluated, potassium hydroxide (KOH) was the most effective agent. An impregnation rate of 10 wt.% was identified as optimal, aligning with practices used for commercial ACs (CACs). The presence of H_2O positively influences the separation of H_2S, with humidified ACs showing separation capacities up to three times greater than their dried counterparts. Furthermore, the addition of only 1.1% O_2 to the feed gas resulted in an eightfold increase in separation efficiency, underscoring its catalytic role in promoting H_2S removal through oxidation pathways.

Comparative testing with nine CACs under identical conditions demonstrated that the AC prepared at 850°C for 3 hours (AC_850°C_3h), when impregnated with 10 wt.% KOH, exhibited superior mass-based separation performance due to its high micropore volume. However, its low bulk density resulted in reduced volumetric adsorption capacity. Therefore, further densification strategies are recommended to enhance performance on a volumetric basis. Additionally, a one-dimensional mathematical model was developed, validated against experimental data, and used to extract mass transfer coefficients under various feed gas conditions. The model reliably captured the adsorption behaviour and is a robust tool for process optimization and scale-up. Notably, the beneficial introduction of 1% O_2 into the feed resulted in a significant reduction in mass transfer coefficients, among the lowest reported for comparable systems, and extended breakthrough times by a factor of up to ten.

3.7 References

[1] Mishra, A.; Kumar, M.; Bolan, N. S.; Kapley, A.; Kumar, R.; Singh, L. Multidimensional Approaches of Biogas Production and Up-Gradation: Opportunities

and Challenges. *Bioresource Technology*, **2021**, *338*, 125514. https://doi.org/10.1016/j.biortech.2021.125514.

[2] Kapoor, R.; Ghosh, P.; Tyagi, B.; Vijay, V. K.; Vijay, V.; Thakur, I. S.; Kamyab, H.; Nguyen, D. D.; Kumar, A. Advances in Biogas Valorization and Utilization Systems: A Comprehensive Review. *Journal of Cleaner Production*, **2020**, *273*, 123052. https://doi.org/10.1016/j.jclepro.2020.123052.

[3] Ahmed, S. F.; Mofijur, M.; Tarannum, K.; Chowdhury, A. T.; Rafa, N.; Nuzhat, S.; Kumar, P. S.; Vo, D.-V. N.; Lichtfouse, E.; Mahlia, T. M. I. Biogas Upgrading, Economy and Utilization: A Review. *Environ Chem Lett*, **2021**, *19* (6), 4137–4164. https://doi.org/10.1007/s10311-021-01292-x.

[4] Paz, L.; Gentil, S.; Fierro, V.; Celzard, A. Assessing the Performance of Adsorbents for CO_2/CH_4 Separation in Pressure Swing Adsorption Units: A Review. *Journal of Environmental Chemical Engineering*, **2024**, *12* (6), 114870. https://doi.org/10.1016/j.jece.2024.114870.

[5] Becker, C. M.; Marder, M.; Junges, E.; Konrad, O. Technologies for Biogas Desulfurization - An Overview of Recent Studies. *Renewable and Sustainable Energy Reviews*, **2022**, *159*, 112205. https://doi.org/10.1016/j.rser.2022.112205.

[6] Peluso, A.; Gargiulo, N.; Aprea, P.; Pepe, F.; Caputo, D. Nanoporous Materials as H_2S Adsorbents for Biogas Purification: A Review. *Separation & Purification Reviews*, **2019**, *48* (1), 78–89. https://doi.org/10.1080/15422119.2018.1476978.

[7] Paz, L.; Gentil, S.; Fierro, V.; Celzard, A. Activated Carbons Outperform Other Sorbents for Biogas Desulfurization. *Chemical Engineering Journal*, **2025**, *506*, 160304. https://doi.org/10.1016/j.cej.2025.160304.

[8] Yang, J. H. Hydrogen Sulfide Removal Technology: A Focused Review on Adsorption and Catalytic Oxidation. *Korean J. Chem. Eng.*, **2021**, *38* (4), 674–691. https://doi.org/10.1007/s11814-021-0755-y.

[9] Guo, J.; Luo, Y.; Lua, A. C.; Chi, R.; Chen, Y.; Bao, X.; Xiang, S. Adsorption of Hydrogen Sulphide (H_2S) by Activated Carbons Derived from Oil-Palm Shell. *Carbon*, **2007**, *45* (2), 330–336. https://doi.org/10.1016/j.carbon.2006.09.016.

[10] Yan, R.; Liang, D. T.; Tsen, L.; Tay, J. H. Kinetics and Mechanisms of H_2S Adsorption by Alkaline Activated Carbon. *Environ. Sci. Technol.*, **2002**, *36* (20), 4460–4466. https://doi.org/10.1021/es0205840.

[11] Micoli, L.; Bagnasco, G.; Turco, M. H_2S Removal from Biogas for Fuelling MCFCs: New Adsorbing Materials. *International Journal of Hydrogen Energy*, **2014**, *39* (4), 1783–1787. https://doi.org/10.1016/j.ijhydene.2013.10.126.

[12] Bagreev, A.; Bandosz, T. J. A Role of Sodium Hydroxide in the Process of Hydrogen Sulfide Adsorption/Oxidation on Caustic-Impregnated Activated Carbons. *Ind. Eng. Chem. Res.*, **2002**, *41* (4), 672–679. https://doi.org/10.1021/ie010599r.

[13] Castrillon, M. C.; Moura, K. O.; Alves, C. A.; Bastos-Neto, M.; Azevedo, D. C. S.; Hofmann, J.; Möllmer, J.; Einicke, W.-D.; Gläser, R. CO_2 and H_2S Removal from CH_4 - Rich Streams by Adsorption on Activated Carbons Modified with K_2CO_3 , NaOH, or Fe_2O_3. *Energy Fuels*, **2016**, *30* (11), 9596–9604. https://doi.org/10.1021/acs.energyfuels.6b01667.

[14] Yang, C.; Florent, M.; De Falco, G.; Fan, H.; Bandosz, T. J. $ZnFe_2O_4$/Activated Carbon as a Regenerable Adsorbent for Catalytic Removal of H_2S from Air at Room Temperature. *Chemical Engineering Journal*, **2020**, *394*, 124906. https://doi.org/10.1016/j.cej.2020.124906.

[15] Zulkefli, N. N.; Mathuray Veeran, L. S.; Noor Azam, A. M. I.; Masdar, M. S.; Wan Isahak, W. N. R. Effect of Bimetallic-Activated Carbon Impregnation on Adsorption–Desorption Performance for Hydrogen Sulfide (H_2S) Capture. *Materials*, **2022**, *15* (15), 5409. https://doi.org/10.3390/ma15155409.

[16] Menezes, R. L. C. B.; Moura, K. O.; De Lucena, S. M. P.; Azevedo, D. C. S.; Bastos-Neto, M. Insights on the Mechanisms of H_2S Retention at Low Concentration on Impregnated Carbons. *Ind. Eng. Chem. Res.*, **2018**, *57* (6), 2248–2257. https://doi.org/10.1021/acs.iecr.7b03402.

[17] Bagreev, A.; Bandosz, T. J. On the Mechanism of Hydrogen Sulfide Removal from Moist Air on Catalytic Carbonaceous Adsorbents. *Ind. Eng. Chem. Res.*, **2005**, *44* (3), 530–538. https://doi.org/10.1021/ie049277o.

[18] Siriwardane, I. W.; Udangawa, R.; De Silva, R. M.; Kumarasinghe, A. R.; Acres, R. G.; Hettiarachchi, A.; Amaratunga, G. A. J.; De Silva, K. M. N. Synthesis and Characterization of Nano Magnesium Oxide Impregnated Granular Activated Carbon Composite for H_2S Removal Applications. *Materials & Design*, **2017**, *136*, 127–136. https://doi.org/10.1016/j.matdes.2017.09.034.

[19] Bagreev, A.; Bashkova, S.; Locke, D. C.; Bandosz, T. J. Sewage Sludge-Derived Materials as Efficient Adsorbents for Removal of Hydrogen Sulfide. *Environ. Sci. Technol.*, **2001**, *35* (7), 1537–1543. https://doi.org/10.1021/es001678h.

[20] Bagreev, A.; Rahman, H.; Bandosz, T. J. Study of H_2S Adsorption and Water Regeneration of Spent Coconut-Based Activated Carbon. *Environ. Sci. Technol.*, **2000**, *34* (21), 4587–4592. https://doi.org/10.1021/es001150c.

[21] Abdirakhimov, M.; Al-Rashed, M. H.; Wójcik, J. Recent Attempts on the Removal of H_2S from Various Gas Mixtures Using Zeolites and Waste-Based Adsorbents. *Energies*, **2022**, *15* (15), 5391. https://doi.org/10.3390/en15155391.

[22] Celzard, A.; Marêché, J. F.; Furdin, G.; Fierro, V.; Sayag, C.; Pielaszek, J. Preparation and Catalytic Activity of Active Carbon-Supported Mo2C Nanoparticles. *Green Chem.*, **2005**, *7* (11), 784. https://doi.org/10.1039/b507971c.

[23] Brunauer, S.; Emmett, P. H.; Teller, E. Adsorption of Gases in Multimolecular Layers. *J. Am. Chem. Soc.*, **1938**, *60* (2), 309–319. https://doi.org/10.1021/ja01269a023.

[24] Jagiello, J.; Olivier, J. P. 2D-NLDFT Adsorption Models for Carbon Slit-Shaped Pores with Surface Energetical Heterogeneity and Geometrical Corrugation. *Carbon*, **2013**, *55*, 70–80. https://doi.org/10.1016/j.carbon.2012.12.011.

[25] Vu, H. P.; Nguyen, L. N.; Wang, Q.; Ngo, H. H.; Liu, Q.; Zhang, X.; Nghiem, L. D. Hydrogen Sulphide Management in Anaerobic Digestion: A Critical Review on Input Control, Process Regulation, and Post-Treatment. *Bioresource Technology*, **2022**, *346*, 126634. https://doi.org/10.1016/j.biortech.2021.126634.

[26] Rastegar, S. O.; Gu, T. Empirical Correlations for Axial Dispersion Coefficient and Peclet Number in Fixed-Bed Columns. *Journal of Chromatography A*, **2017**, *1490*, 133–137. https://doi.org/10.1016/j.chroma.2017.02.026.

[27] Lemmon, E. W.; Huber, M. L.; McLinden, M. O. NIST Standard Reference Database 23: Reference Fluid Thermodynamic and Transport Properties-REFPROP, 2018.

[28] Sisani, E.; Cinti, G.; Discepoli, G.; Penchini, D.; Desideri, U.; Marmottini, F. Adsorptive Removal of H_2S in Biogas Conditions for High Temperature Fuel Cell Systems. *International Journal of Hydrogen Energy*, **2014**, *39* (36), 21753–21766. https://doi.org/10.1016/j.ijhydene.2014.07.173.

[29] Barelli, L.; Bidini, G.; De Arespacochaga, N.; Pérez, L.; Sisani, E. Biogas Use in High Temperature Fuel Cells: Enhancement of KOH-KI Activated Carbon Performance toward H_2S Removal. *International Journal of Hydrogen Energy*, **2017**, *42* (15), 10341–10353. https://doi.org/10.1016/j.ijhydene.2017.02.021.

[30] Erto, A.; Deorsola, F. A.; De Falco, G.; Montagnaro, F.; Balsamo, M. Role of H_2O and O_2 during the Reactive Adsorption of H_2S on CuO-ZnO/Activated Carbon at Low Temperature. *Microporous and Mesoporous Materials*, **2020**, *295*, 109949. https://doi.org/10.1016/j.micromeso.2019.109949.

[31] Sigot, L.; Fontseré Obis, M.; Benbelkacem, H.; Germain, P.; Ducom, G. Comparing the Performance of a 13X Zeolite and an Impregnated Activated Carbon for H_2S Removal from Biogas to Fuel an SOFC: Influence of Water. *International Journal of Hydrogen Energy*, **2016**, *41* (41), 18533–18541. https://doi.org/10.1016/j.ijhydene.2016.08.100.

[32] Fu, Q.; Xu, Q.; Liu, Z.; Wang, D.; Liu, X.; He, D.; He, Y.; Li, Y.; Yang, J.; Duan, A. Insights into Potassium Permanganate Reducing H_2S Generation from Anaerobic Fermentation of Sludge. *Chemical Engineering Journal*, **2022**, *430*, 133150. https://doi.org/10.1016/j.cej.2021.133150.

[33] Do, D. D. *Adsorption Analysis: Equilibria and Kinetics*; Imperial College Press: Queensland, Australia, 1998.

[34] Aguilera, P. G.; Gutiérrez Ortiz, F. J. Prediction of Fixed-Bed Breakthrough Curves for H_2S Adsorption from Biogas: Importance of Axial Dispersion for Design. *Chemical Engineering Journal*, **2016**, *289*, 93–98. https://doi.org/10.1016/j.cej.2015.12.075.

[35] Gutiérrez Ortiz, F. J.; Aguilera, P. G.; Ollero, P. Modeling and Simulation of the Adsorption of Biogas Hydrogen Sulfide on Treated Sewage–Sludge. *Chemical Engineering Journal*, **2014**, *253*, 305–315. https://doi.org/10.1016/j.cej.2014.04.114.

[36] Papurello, D.; Gandiglio, M.; Lanzini, A. Experimental Analysis and Model Validation on the Performance of Impregnated Activated Carbons for the Removal of Hydrogen Sulfide (H_2S) from Sewage Biogas. *Processes*, **2019**, *7* (9), 548. https://doi.org/10.3390/pr7090548.

Chapter 4. Densification and impregnation of wood-based activated charcoal for industrial biogas desulfurization

4.1 Introduction

Biogas, produced mainly from the anaerobic digestion of organic waste, is a clean, methane-rich energy source and an important sustainable alternative to fossil fuels. However, its composition often includes hydrogen sulfide (H_2S), a corrosive and toxic impurity that must be removed to avoid damaging equipment and ensure the safety of the atmosphere. Among the various desulfurization techniques, adsorption on activated carbon (AC) is known as a widely used industrial method due to its efficiency and cost-effectiveness. [1]

However, pure adsorption may not be sufficient, and this is why impregnation of ACs is a widely used technique to enhance their performance for biogas desulfurization. By introducing chemical agents such as metal oxides (e.g. iron, zinc or copper) [2–4] or alkaline compounds (e.g. KOH or K_2CO_3), [5–7] the surface reactivity of AC is indeed significantly improved, allowing more efficient H_2S removal.

Extensive research has focused on the impregnation of ACs to improve their adsorption performance for biogas desulfurization, with results mainly reported per unit weight, such as milligram of H_2S per gram of AC, as illustrated in literature reviews. [1, 8–10] However, on a commercial scale, H_2S removal relies on densified sorbents, which offer higher separation efficiency per unit volume, a metric preferred in industrial applications due to space constraints and the need to replace sorbents as less frequently as possible.

To our knowledge, no published research has evaluated the effect of AC densification on biogas desulfurization, despite its performance-enhancing potential. Additionally, impregnation of the densified AC is essential to further improve H_2S separation efficiency. Commercial activated carbons (CAC) used for industrial-scale biogas purification already incorporate both optimization processes. [1]

Furthermore, densified ACs are mandatory for industrial adsorption columns. Thus, ACs are generally pelletized to optimize particle size and structural integrity. Fine or low-density carbons can indeed lead to significant pressure drops, increasing process energy consumption.[11] Pelletization increases particle size and uniformity, which improves bed packing, provides greater mechanical stability and facilitates gas flow with minimal pressure drop, which also extends the operational life of adsorption bed systems.

In this work, we investigated the densification of wood-based activated charcoal by compaction with binders. Three kinds of binders were considered: sugar cane molasses, beet

molasses, and polyphenols of plant origin (not disclosed for reasons of industrial secrecy). Moreover, the densified ACs were impregnated with alkaline substances, including KI, K_2CO_3, NaOH and KOH, to improve their desulfurization performance. The study aimed to determine the optimal amounts of impregnating agents and binders, as well as the most effective modification sequence to maximize H_2S adsorption efficiency. Finally, the best-performing adsorbent developed was compared with CACs under identical evaluation conditions, enabling assessment of its potential for industrial application in biogas desulfurization.

H_2S separation was evaluated by a dynamic adsorption process using a gas mixture containing N_2, CO_2 and O_2. The presence of CO_2 is important, as it can compete with H_2S for adsorption sites and influence overall desulfurization performance. Moreover, the inclusion of O_2 allowed oxidation reactions that enhance sulfur retention on the AC surface. Thus, this study ensured that the developed adsorbents were tested under relevant and practical operational parameters. A mathematical model for dynamic adsorption simulation of H_2S was also applied for mass transfer characterization of the adsorbent. In addition, thermal regeneration was tested on the optimum sorbents developed, revealing the challenges associated with their regeneration.

4.2 Experimental

4.2.1 Materials

Wood-based activated charcoal (particle size 3–8 mm) was supplied by the French company Groupe Bordet as part of a joint (LabCom “CarBioLab”) laboratory. The charcoal was produced from oak and beech sawdust using Groupe Bordet’s slow, continuous pyrolysis process, giving it high purity with a carbon content of over 90%. It was steam-activated at 900 °C for 2 hours with a heating rate of 5 °C·min^{-1} in a rotary reactor. These conditions were selected based on our previous work. [12] The resulting activated carbon, called Bordet AC, had a granular form and a bulk density of 263 kg·m^{-3}, measured by sieving the sorbent to retain particles between 0.5 and 1 mm, then filling a known volume and determining the mass it contained.

For AC pelletization, four eco-friendly binders were considered: two sugar cane molasses, one beet molasses and polyphenols of plant origin, the exact name of which will not be revealed here. The sugar cane molasses had a viscosity of 1000 to 6000 cP at 20 °C, while that of the beet molasses was 500 to 1500 cP at the same temperature. Plant-based polyphenols were in

the shape of a solid powder. Pelletization was carried out using an Atlas 15T manual hydraulic press.

For chemical modification, activated charcoal was impregnated with analytical-grade potassium iodide (KI), potassium carbonate (K_2CO_3), sodium hydroxide (NaOH) or potassium hydroxide (KOH) (purity ≥ 99%), using solutions prepared with distilled water.

To compare our materials, nine commercial activated carbons (CACs) used in industrial biogas desulfurization were analysed. **Figure 4.1a** shows their bulk densities (ρb), origins, chemical modifications and shapes. Most are coal-based, with the exception of CAC 1 and CAC 2, derived from wood and from coconut shell, respectively. All are chemically impregnated, although some suppliers do not specify impregnation details.

4.2.2 Densification process

The densification procedures are illustrated in **Figure 4.1b** as Method 1 (top route) and Method 2 (bottom route). In Method 1, Bordet AC was first mixed with a binder, either molasses or polyphenols, then sieved to a particle size of less than 1 mm. In the case of molasses, 3 wt.% water (relative to the total mass of AC) was added to improve malleability. Similarly, 5 wt.% water was added in the case of polyphenols. The mixture was then compacted into pellets under 87 Mpa for 1 minute. These pellets were dried overnight at 105 °C before being carbonized at 700 °C for 2 hours under nitrogen flow (80 $mL \cdot min^{-1}$). The carbonization ramp included a heating rate of 2 $°C \cdot min^{-1}$ up to 400 °C, followed by 5 $°C \cdot min^{-1}$ up to 700 °C. In the final stage, chemical impregnation of the carbonized pellets was performed to obtain the densified and impregnated AC product. Impregnation will be described in detail in the next subsection 2.3.

In contrast, Method 2 began with an initial chemical impregnation of Bordet AC prior to pelletization. The impregnated AC was then mixed with a binder and compacted under the same conditions (87 Mpa, 1 min), then dried and carbonized according to the same thermal profile as in Method 1.

The densified ACs were labelled as binder_%, where the type of binder is followed by its weight percentage. The suffix “nc” indicates that the densified AC was prepared without undergoing carbonization.

In addition, pellets were also prepared by first sieving the Bordet AC to obtain very fine particles between 20 and 40 µm, followed by the same procedure as described above. These samples were labelled "20 µm" to distinguish this preparation method.

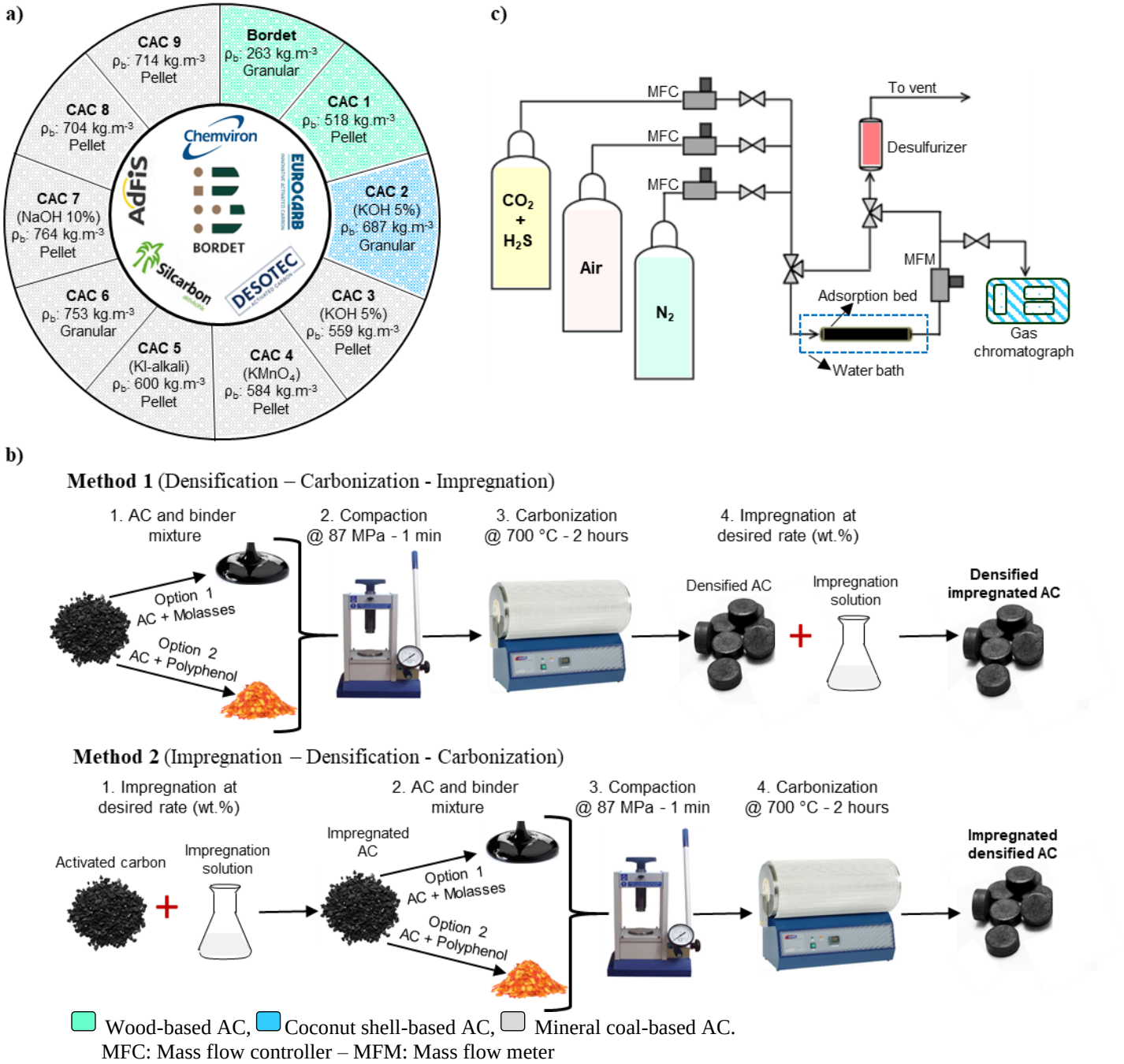

Figure 4.1 a) Bulk density, source, modification and shape of Bordet and commercial ACs for biogas desulfurization. B) Experimental test bench for dynamic H_2S adsorption. C) Synthesis of lab-made densified-impregnated activated carbon.

4.2.3 Impregnation process

Figure 4.1b also describes the impregnation procedures used in both methods. In Method 1, impregnation was carried out after the densification and carbonization steps. Conversely, in Method 2, impregnation was performed prior to densification and carbonization. In both cases, impregnation was carried out using the incipient wetness method. [13] Prior to impregnation, the AC materials were dried at 105 °C for 24 hours. The impregnation volume corresponded to the total pore volume of the ACs, estimated according to Eq. (3.1), using the skeletal density and grain density defined in the next subsection 2.4. The impregnation solutions contained specific amounts of KI, K_2CO_3, NaOH or KOH, selected to achieve a target impregnation ratio (wt.%). After impregnation, the samples were vacuum-dried overnight at 80 °C.

4.2.4 Characterization

The binders used for densification were characterized in terms of ash content, and were also studied by thermogravimetric analysis (TGA), elemental analysis and, for the ashes obtained, by X-ray diffraction (XRD). To determine ash content, samples were heated in ceramic crucibles at a rate of 5 °C·min^{-1} up to 650 °C and held for 4 hours to ensure complete combustion of the organic matter. After cooling, the residual ash was weighed. Each sample was tested in triplicate, and the average ash content was reported. The collected ash was subsequently analysed by XRD to assess its crystalline composition.

Thermal decomposition was analysed using a Netzsch STA 449 F3 Jupiter thermogravimetric (TGA) analyser. Binders were heated from room temperature to 900 °C at 5 °C·min^{-1} under argon flowing at 50 mL·min-1. TGA data revealed mass loss, volatile matter and fixed carbon contents. This information allowed us to choose the right temperature for carbonizing the pellets.

The bulk elemental composition (C, H, O, N and S) was analyzed using a Vario EL Cube (Elementar). Dried binder sample (≈ 2 mg) were burnt in a helium-driven O_2 stream, and the resulting gases were separated using trap columns and quantified using a thermal conductivity detector. The textural properties of the sorbent materials (pristine Bordet AC and densified (non-impregnated) ACs) were analyzed by N_2 adsorption–desorption isotherms at -196 °C using an ASAP 2020 apparatus (Micromeritics). Prior to analysis, the samples were degassed under vacuum at 110 °C for 24 h. The BET area (A_{BET}) was calculated using the Brunauer–Emmett–Teller (BET) model, [14] while the NLDFT specific surface area (S_{NLDFT}) and pore size

distribution were obtained with SAIEUS® software based on the non-local density functional theory (NLDFT). [15] Pore volumes, including total (V_{tot}), mesopore (V_{mes}, pore width $2 < w < 50$ nm), micropore (V_{mic}, $w < 2$ nm), and ultramicropore ($V_{ultra-mic}$, $0.7 < w < 2$ nm) volumes were also obtained using the NLDFT. For comparison, the micropore volume was also calculated using the Dubinin–Radushkevich method (V_{DR}). The total accessible pore volume was estimated from the N_2 adsorbed volume at -196 °C and a relative pressure of 0.97 ($V_{0.97}$).

The skeletal density was measured using a Micromeritics AccuPyc II 1340 gas pycnometer with helium as the probe molecule to ensure accurate volume measurements by penetrating the narrowest pores. Samples were degassed beforehand to remove moisture and adsorbed gases. The skeletal density, calculated from the volume of He displaced, reflects the true density of the solid material excluding pore spaces.

The grain density was measured with a Micromeritics GeoPyc 1360 pycnometer using an incompressible DryFlow® medium. AC grains were embedded in this medium, whose grains are fine enough to fill all intergranular spaces, but not fine enough to penetrate intragranular porosity. The grain density was then calculated from the volume of DryFlow® displaced, accounting for internal pores but excluding interparticle voids.

4.2.5 H_2S dynamic adsorption

Dynamic adsorption experiments were carried out using the fixed-bed setup shown in **Figure 4.1b**. The AC pellets were ground and sieved to 0.5–1.0 mm particles, and a fixed volume was used to completely fill a stainless-steel column (0.77 cm internal diameter, 10 cm length). The column was maintained at 25 °C using a thermostated water bath and operated at atmospheric pressure. To standardize moisture content, the ACs were pre-humidified for 24 h at 50% relative humidity (RH) and 25 °C before testing.

Dynamic adsorption tests used synthetic biogas containing either 400 or 4000 ppm H_2S, 60% N_2, and the balance CO_2; 1% O_2 was also included in some experiments to simulate oxidative conditions, even more representative of a real biogas. Outlet gas composition was analysed with a Micro GC Fusion (Inficon). A constant flow rate of 80 $mL \cdot min^{-1}$ was maintained by mass flow controllers, and corresponded to a linear velocity of 2.9 $cm \cdot s^{-1}$.

In industrial desulfurization, ACs are replaced at partial saturation once the breakthrough point (BTP) is reached or H_2S content at the column outlet exceeds acceptable levels. ASTM D6646 [16] recommends a BTP of 50 ppm for an inlet of 10,000 ppm H_2S. In this study,

adsorption capacity was measured at an outlet H_2S concentration of 40 ppm, equivalent to a 10% BTP for 400 ppm inlet concentration and 1% BTP for 4000 ppm. This threshold was chosen to approximate a BTP of 4 ppm, the limit for using biogas as a substitute for natural gas. [17]

The H_2S separation capacity, q_{H_2S} (mg), was calculated using Eq. (3.2). The separation capacity was then normalized by either adsorbent mass (g) or volume (cm^3) using Eq. (3.3) and Eq. (3.4), respectively, as already explained in Chapter 3.

4.3 Results and discussion

4.3.1 Binder characteristics

The results of binder characterization by thermogravimetric analysis, ash content measurement determination and XRD analysis of these ashes are presented in **Figure 4.2a**, **2b** and **4.2c**. The TGA profiles (**Figure 4.2a**) show the thermal decomposition behavior of the four binders from room temperature to 900 °C. All binders exhibited significant weight loss between 100 °C and 300 °C, attributed to moisture evaporation and release of volatile organic compounds. Cane molasses 1 and cane molasses 2 displayed comparable thermal profiles, whereas the polyphenol-based binder showed lower weight loss over the whole temperature range (up to 900 °C), indicating better thermal stability.

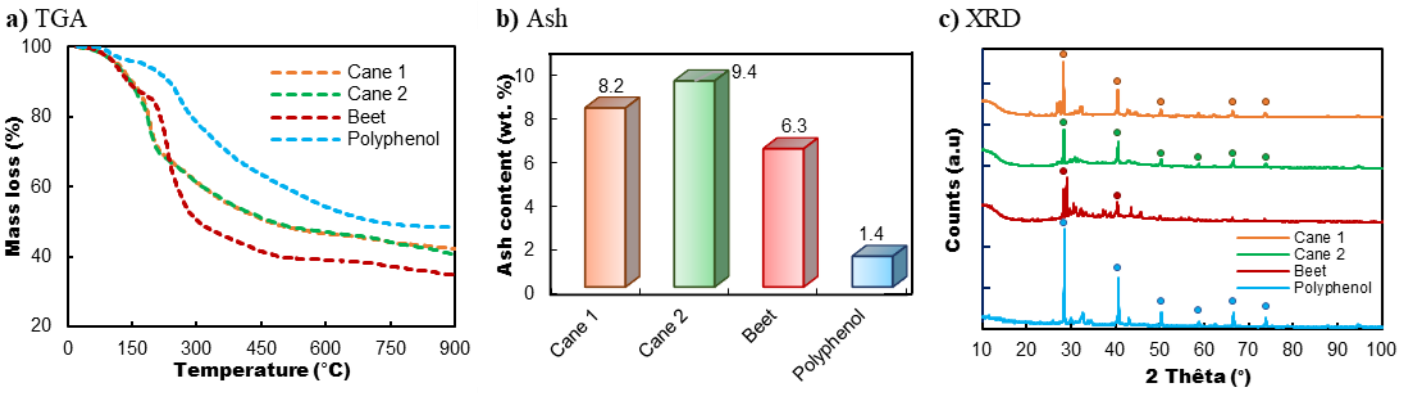

Figure 4.2 Characterization of molasses: a) TGA curve, b) Ash content and c) XRD.

The amount of water (mass loss up to 200 °C) in the binders is much higher for the cane molasses, presenting around 25 wt.%, followed by beet molasses at 15.6 wt.% and polyphenols with only 6.4 wt.%. This is why more water is required for the preparation of the AC pellet

when polyphenols are used. Above 200 °C, continued degradation of heavier organic substances is observed. The total mass losses follow the order: beet molasses (49.8%) > polyphenols (45.3%) > cane 1 molasses (33.9%) > cane 2 molasses (31.5%) (see **Table A3.1** in annex 3).

This behavior reflects differences in volatile matter content and suggests that cane molasses and polyphenol-based binders produce a higher yield of fixed carbon during pyrolysis, an essential factor in maintaining structural integrity during pelletization. In particular, the fixed carbon content on a dry basis is higher in cane 1 (57.9%) and cane 2 (59.1%) molasses, and in polyphenols (53.3%), than in beet molasses (43.9%).

Furthermore, ash content influences the final purity of the densified AC, with a higher ash content introducing more residual inorganic matter, affecting the quality and performance of the final densified AC product. Among the samples, cane 2 molasses has the highest ash content (9.4%), followed by cane 1 molasses (8.2%) and beet molasses (6.3%). Polyphenols, on the other hand, have the minimum ash content (1.4%).

The XRD pattern compares the crystalline phases present in the ashes of the binder. The dots mark the diffraction peaks that could correspond to potassium chloride (KCl), present in all samples. The ashes of molasses and polyphenols contain inorganic components such as Ca, K, Mg, and Na, which remain in the densified AC after the carbonization process. [18, 19] These residual elements are known to positively influence the separation of H_2S, as they play a catalytic role in promoting H_2S oxidation. [1]

4.3.2 AC Characteristics

Bordet AC was densified as explained in section 4.2.2. Pellets were produced when the cane molasses content reached at least 30 wt.% relative to the amount of AC, but a higher content of 40 wt.% produced pellets with improved mechanical properties, such as greater hardness and reduced generation of fine particles during handling. An even higher proportion of 50 wt.% was also tested and identified as the most effective in producing high-quality pellets, based on our evaluation criteria, which include the release of fragments and fine particles during handling and after dropping the pellets from a height of 1 meter onto the ground.

In contrast, the formation of pellets using beet molasses failed, even with a binder content of 50 wt.%, as the resulting pellets were brittle and broke easily after carbonization. This poor

performance is attributed to the lower thermal stability and reduced fixed carbon content of beet molasses (see **Figure 4.2a**), which compromises the mechanical integrity of the pellets. Nonetheless, the material, even in its brittle state, was used for measurements of bulk density and H_2S adsorption performance. For the plant-based polyphenol binder, a lower binder content was sufficient, with just 10 wt.% to achieve optimum pellet quality. In addition, a 20 wt.% content was also evaluated, as it further enhanced pellet quality.

The bulk density of ACs densified with different binders is presented in **Figure 4.3a**. To assess the impact of carbonization, the non-carbonized (nc) forms of ACs with cane molasses 2 and polyphenols were also considered. All densified samples show higher bulk densities than the non-densified Bordet AC, confirming the effectiveness of pelletization. In the carbonized form, density remained relatively constant for the same type of binder, whatever the binder content (30–50% for molasses and 10–20% for polyphenols). Non-carbonized samples presented higher densities; for example, Can2_50% reached 437 $kg \cdot m^{-3}$, while its non-carbonized form was at 591 $kg \cdot m^{-3}$.

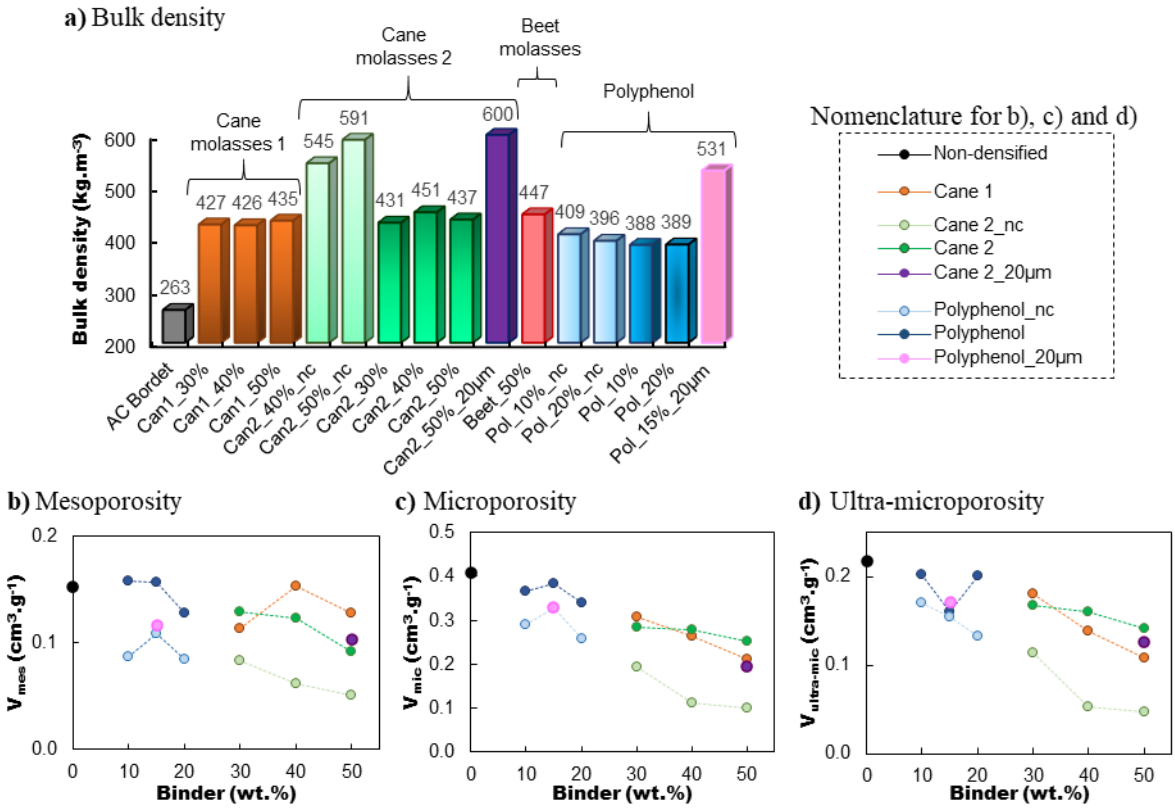

Figure 4.3 Bulk density (a) and pore volume variation by binder type and content for mesoporosity (b), microporosity (c) and ultra-microporosity (d) on densified ACs.

When the particle size was reduced to very fine particles ranging from 20 to 40 µm, the resulting sorbent became denser, as observed with cane molasses 2 (can2_50%_20um) and polyphenol (pol_15%_20um) binders, which exhibit densities of 600 and 531 $kg \cdot m^{-3}$, respectively. This is because the finer particles pack more efficiently, reducing the voids between them and leading to a more compact structure.

Can2_50%_nc also showed high density (591 $kg \cdot m^{-3}$) but, as it was not carbonized, its high content of binder-derived volatiles might have a negative effect on H_2S separation. When carbonized, AC with cane molasses 1 reached a density of around 430 $kg \cdot m^{-3}$, similar to AC with cane molasses 2 at 440 $kg \cdot m^{-3}$, both slightly higher than AC with polyphenols, which gave 402 $kg \cdot m^{-3}$ when not carbonized and 389 $kg \cdot m^{-3}$ when carbonized.

The impact of binder type and content on porosity was assessed by N_2 physisorption analysis, with adsorption isotherms at 77 K presented in **Figure A3.1**. **Figures 4.3b**, **4.3c** and **4.3d** show the evolution of mesopore (V_{mes}), micropore (V_{mic}), and ultramicropore ($V_{ultra\text{-}mic}$) volumes, respectively, as a function of binder loading. The non-densified material exhibited the highest textural properties: BET area of 1120 $m^2 \cdot g^{-1}$, total pore volume of 0.56 $cm^3 \cdot g^{-1}$, and V_{mic} of 0.44 $cm^3 \cdot g^{-1}$. As expected, increasing binder content in densified samples systematically reduced all porosity parameters (see **Table A3.2**), as shown in **Figures 4.3b** to **4.3d**. This decrease is due to partial obstruction or collapse of pores during densification and carbonization.

Among the densified materials, polyphenol-based ACs retained the highest porosity at comparable binder levels, with Pol_10% reaching a BET area of 1012 $m^2 \cdot g^{-1}$ and V_{mic} of 0.40 $cm^3 \cdot g^{-1}$, close to the non-densified reference. In contrast, samples densified with 50 wt.% cane molasses (e.g. Can1_50%) exhibited significantly reduced porosity (BET area of 595 $m^2 \cdot g^{-1}$ and V_{mic} of 0.24 $cm^3 \cdot g^{-1}$).

Carbonization proved essential for recovering microporosity. Non-carbonized samples (Pol_nc and Can2_nc) indeed showed drastically lower V_{mic} and $V_{ultra\text{-}mic}$ values. For instance, Can2_50%_nc has V_{mic} and $V_{ultra\text{-}mic}$ values of just 0.11 $cm^3 \cdot g^{-1}$ and 0.05 $cm^3 \cdot g^{-1}$, respectively, compared with 0.28 $cm^3 \cdot g^{-1}$ and 0.14 $cm^3 \cdot g^{-1}$ for the carbonized Can2_50% sample.

ACs sieved to 20–40 µm exhibited higher packing densities, which also led to a more pronounced reduction in pore volume. Pol_15%_20µm showed a BET area of 910 $m^2 \cdot g^{-1}$, compared with 1075 $m^2 \cdot g^{-1}$ for the sample sieved to a broader particle size range (pol_15%). A similar trend was observed for the cane molasses 2 binder, where cane2_50%_20µm reached

550 $m^2 \cdot g^{-1}$, while cane2_50% retained 700 $m^2 \cdot g^{-1}$. The greater loss in porosity with finer particles can be attributed to tighter packing, increased binder penetration, and possible pore blockage or collapse during densification.

Overall, these results highlight the importance of binder selection and carbonization in preserving microporosity and maximizing H_2S removal efficiency. Polyphenol-based binders offer the best compromise between structural integrity and porosity retention at lower binder dosages.

4.3.3 Effect of binder on H_2S separation

To evaluate binder effect of densified ACs for H_2S separation, dynamic adsorption tests were run with 400 ppm H_2S in a gas of 60% N_2 and CO_2 balance. Breakthrough curves are shown in **Figure 4.4a** (cane 1 and beet-based AC), **4.4b** (cane 2-based AC), and **4.4c** (polyphenol-based AC). Separation capacities, normalized by AC mass and volume, appear in **Figures 4.4d** and **4.4e** respectively, with tabulated values in **Table A3.3**.

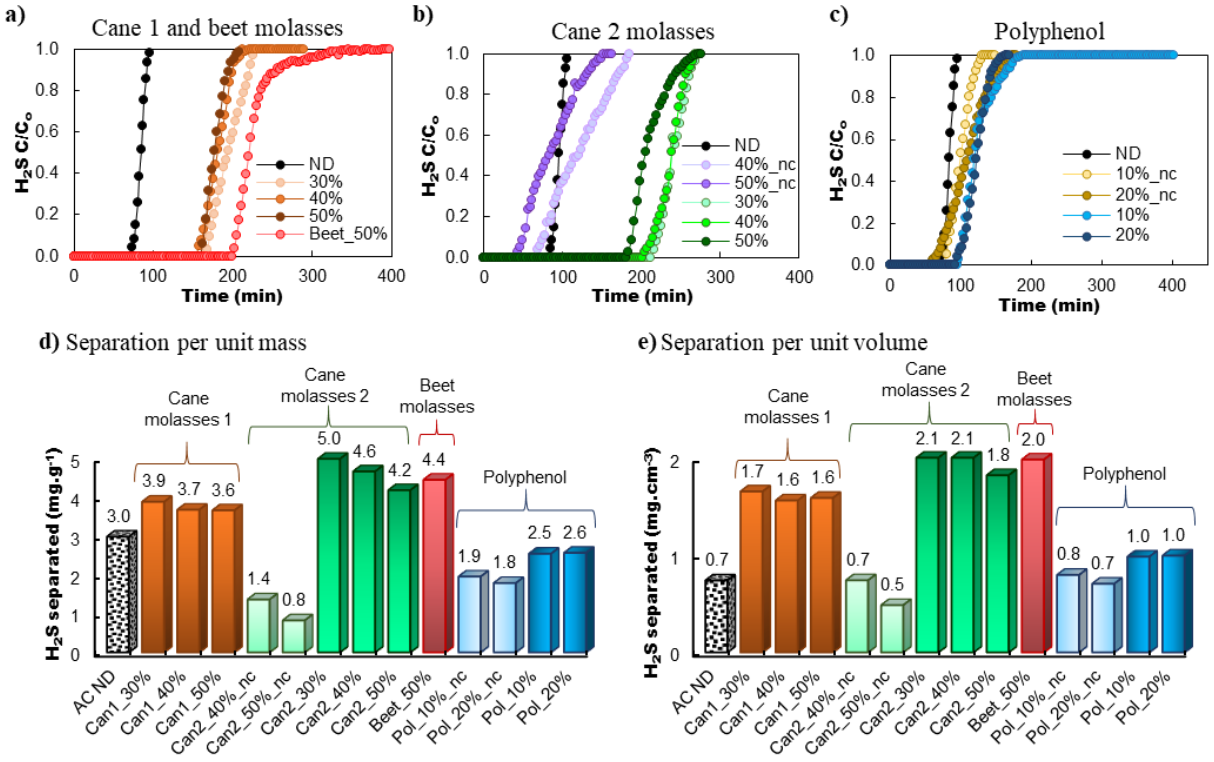

Figure 4.4 Breakthrough curve of densified activated carbons by binder type for H_2S (400 ppm) separation: a) Cane 1 and beet molasses, b) Cane molasses 2 and c) Polyphenol – Separation capacities at BTP per mass unit e) and per volume unit f).

ACs densified with cane molasses 2 and beet molasses undergoing carbonization showed the longest durations (≈ 200 min). On the contrary, despite the higher densities of non-carbonized samples based on cane molasses (Can2_40%_nc, Can2_50%_nc), separation breakthrough times were reduced (< 50 min).

Cane 1-based AC presents breakthrough times (≈ 159 min) shorter than cane 2-based AC, which may be due to difference in their compositions; for instance, cane molasses 2 contains a higher ash content (see **Figure 4.2b**), indicating a greater presence of mineral compounds that contribute to enhanced H_2S adsorption.

Although polyphenol-based densified ACs retained higher porosity levels than molasses-based densified ACs (see **Figures 4.3b**, **4.3c** and **4.3d**), they showed shorter breakthrough times (≈ 93 min) than carbonized molasses-based ACs and only better than non-densified AC (ND). This is due to the fact that, in molasses-based carbons, the material remaining after carbonization at 700 °C has been enriched in ashes, thus in metal compounds that act as catalysts, promoting H_2S separation by oxidation reactions and thus improving H_2S adsorption performance. [1]

Non-carbonized, polyphenol-based ACs demonstrated comparable performance to their carbonized counterparts. For instance, the non-carbonized sample Pol_10%_nc achieved an H_2S separation capacity of 1.9 $mg \cdot g^{-1}$ at breakthrough, while the carbonized form (Pol_10%) reached 2.5 $mg \cdot g^{-1}$. Since the binder content of polyphenol-based ACs is lower (10-20 wt.%) compared to cane-based ACs (50 wt.%), the reduction in separation performance in the non-carbonized form is more favorable.

Overall, densification increased breakthrough times and therefore improved separation efficiency per unit volume, but it increased sample mass and could thus reduce separation capacity per unit mass. For example, the polyphenol-based AC (pol_10%) adsorbed 2.4 $mg \cdot g^{-1}$ of H_2S, which is less than the 2.9 $mg \cdot g^{-1}$ of non-densified AC (AC ND). Despite this, pol_10% achieved a higher volumetric separation capacity, 0.9 $mg \cdot cm^{-3}$ versus 0.7 $mg \cdot cm^{-3}$ for AC ND. In contrast, molasses-based ACs showed better performance, both per unit mass and volume, due to the binder-induced surface functionalization that improves H_2S separation.

The highest H_2S separation capacity was observed for can2_30%**,** with 5.0 $mg \cdot g^{-1}$ and 2.1 $mg \cdot cm^{-3}$ of H_2S removed. However, can2_50%**,** with a slightly lower performance (4.2 $mg \cdot g^{-1}$ and 2.1 $mg \cdot cm^{-3}$), is considered more suitable due to its higher hardness, making it more

relevant for industrial applications. In contrast, although polyphenol-based ACs showed lower initial performance, their greater microporous volume makes them promising candidates for functionalization by impregnation.

4.3.4 Selection of best impregnating agent under O_2 presence

The effect of four impregnating agents (KI, K_2CO_3, NaOH and KOH) was tested at 5 and 10 wt.%. These compounds either directly react with H_2S or function as catalysts to promote its oxidation. [1] Tests used a gas mixture containing 1.1% O_2, 4000 ppm H_2S, 60% N_2, and the rest CO_2. The positive influence of O_2 on enhancing H_2S adsorption capacity is well documented, [1] and its effect was also observed and evaluated here. Non-carbonized polyphenol-based AC (Pol_15%_nc) on the one hand, and cane 2-based AC on the other hand (Can_50%), were used for this test, all synthetized by Method 2 with the density values reported in **Table A3.4**. **Figure 4.5a** shows the H_2S breakthrough curves for non-carbonized polyphenol-based ACs, and **Figure 4.5b** for cane-2-based ACs. **Figures 4.5c** and 4.**5d** show the separation capacities normalized by mass and volume, respectively; the corresponding values are presented in **Table A3.5**. Higher impregnation rates further extended the breakthrough curves. KOH gave the best results, with an optimum loading of 10 wt.%. The polyphenol-based AC reached breakthrough time at 550 minutes, while cane-2-based AC did so at 640 minutes. NaOH performed best among the other agents at 10 wt.% loading, with a 400-minute breakthrough time for polyphenol-based AC, higher than KI (240 min) and K_2CO_3 (230 min), but still lower than KOH. For cane-2-based AC, all agents (NaOH, K_2CO_3, KI) gave similar breakthrough times of around 480 minutes for 10 wt.% impregnation.

KOH at 10 wt.% showed the highest H_2S separation capacity, confirming its superior performance. In non-carbonized, polyphenol-based AC, it achieved 111 $mg \cdot g^{-1}$ and 54 $mg \cdot cm^{-3}$, outperforming NaOH (76 $mg \cdot g^{-1}$, 37 $mg \cdot cm^{-3}$). With cane-2-based AC, it allowed reaching 146 $mg \cdot g^{-1}$ and 62 $mg \cdot cm^{-3}$, well above NaOH (105 $mg \cdot g^{-1}$ and 44 $mg \cdot cm^{-3}$).

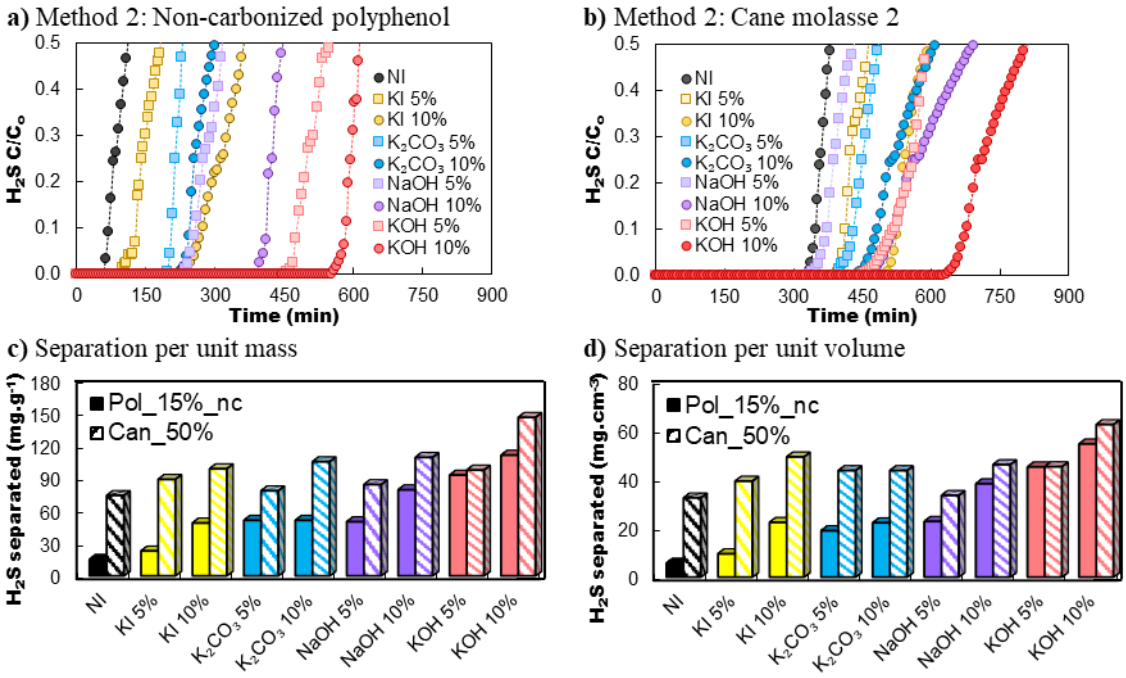

Figure 4.5 Breakthrough curves for the separation of H_2S (4000 ppm), in the presence of O2, of densified ACs with (a) non-carbonized polyphenol binder and (b) cane molasses 2 binder, all prepared by Method 2. Corresponding separation capacities: (c) per unit mass, and (d) per unit volume. NI means non-impregnated, still densified.

Cane 2 binder performed better than the non-carbonized polyphenols. However, the non-carbonization aspect is attractive, as it could lead to substantial energy savings in industrial applications. Therefore, in the next test (see subsection 4.3.5.2), the non-carbonized polyphenol binder will be reconsidered to compare its performance with that of the carbonized version.

4.3.5 Selection of best impregnation method with KOH

4.3.5.1 In the absence of O_2

Two binders were chosen for AC impregnation: can2_50% for its high separation capacity without impregnation, and pol_15% (carbonized and non-carbonized) for its microporosity offering potential performance after impregnation with KOH. Impregnation levels of 5, 10, and 15 wt.% were tested. H_2S separation was evaluated at 4000 ppm in a gas mixture of 60% N_2 and the rest CO_2.

The two methods of impregnation explained in subsections 4.2.2 and 4.2.3, and summarized in **Figure 4.1b**, were applied. It is useful to recall here that these methods differ in whether

KOH was added before or after densification. Adding KOH prior to carbonization at 700 °C can cause chemical activation of the carbon matrix, forming potassium-based compounds (e.g. K, K_2O, K_2CO_3). [20] Without washing after carbonization, these residues (or the products of their oxidation and reaction with moisture) remain on the carbon surface and improve H_2S removal, which is in line with the intended purpose.

Figure 4.6 shows the breakthrough curves obtained by the two methods for non-carbonized polyphenol-based AC (**4.6a**), carbonized polyphenol-based AC (**4.6b**) and cane 2-based AC (**4.6c**). The separation capacities are presented per unit mass and unit volume in **Figures 4.6d** and **4.6e**, respectively. Tabulated values of separation capacities at saturation are presented in **Table A3.6**.

Cane-based ACs showed the longest breakthrough time (45 min), followed by carbonized polyphenol-based AC (41 min). Breakthrough time improved until impregnation reached 10 wt.%, but dropped at 15 wt.% due to excessive pore blocking.

Method 1 performed slightly better than Method 2: for instance, at 10 wt.% KOH on the cane-based AC, it achieved 8.75 $mg \cdot g^{-1}$ and 4.30 $mg \cdot cm^{-3}$ against 8.62 $mg \cdot g^{-1}$ and 4.11 $mg \cdot cm^{-3}$ with Method 2. This trend is found in all comparisons carried out with identical impregnation levels and the same binder.

Impregnated, polyphenol-based AC performed similarly to impregnated, cane-based AC. At 10 wt.% KOH (method 1), the former removed 8.74 $mg \cdot g^{-1}$ and 4.10 $mg \cdot cm^{-3}$ of H_2S versus 8.75 $mg \cdot g^{-1}$ and 4.30 $mg \cdot cm^{-3}$ for the latter. This small difference contrasts with the larger discrepancy observed in non-impregnated samples, and highlights the high microporosity of the polyphenol-based AC for functionalization by impregnation. Overall, the two methods gave similar results, with method 1 being slightly superior. The same comparison is made in the next subsection 4.3.5.2 under O_2, which improves separation and allows for more definite conclusions.

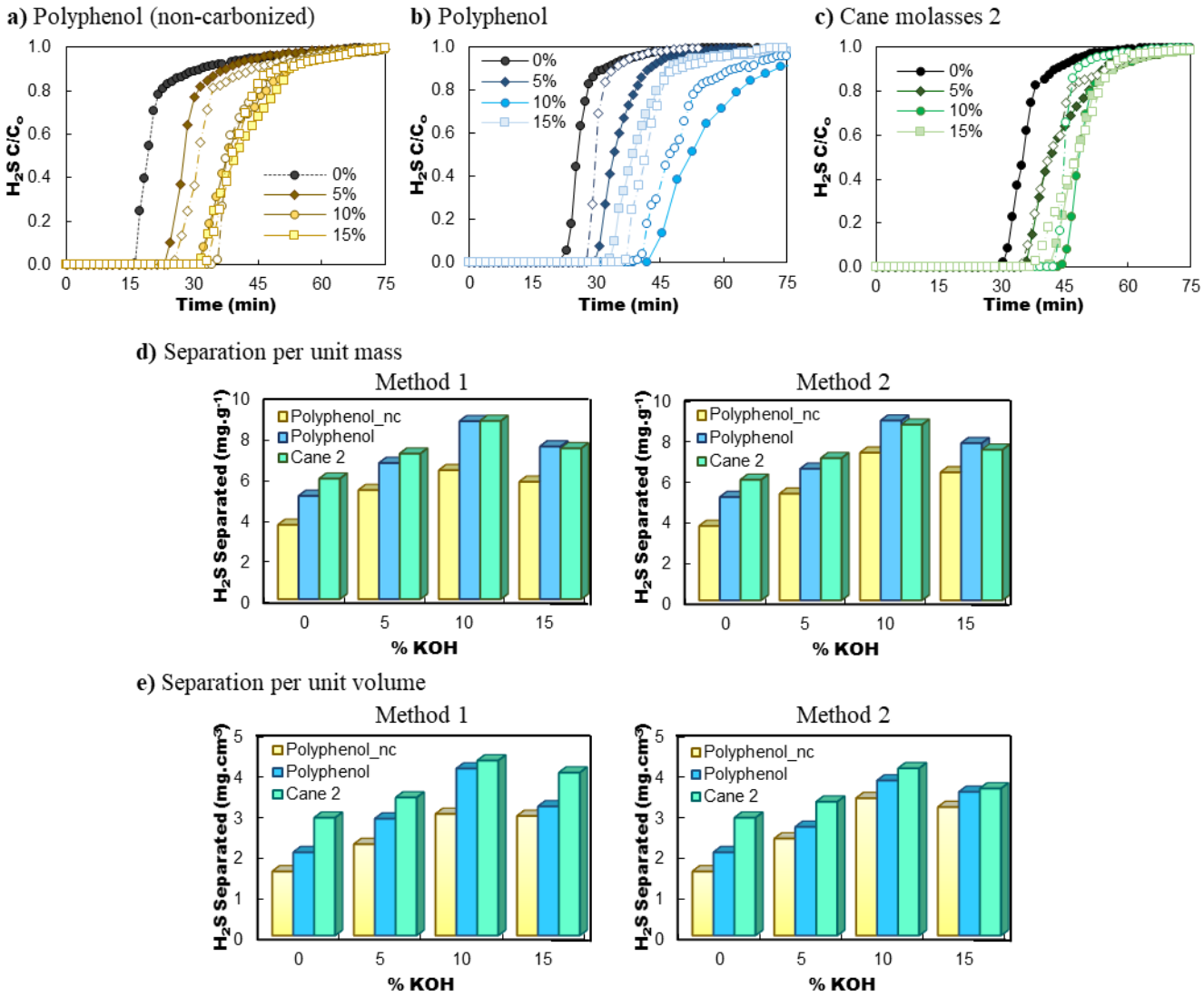

Figure 4.6 Breakthrough curves for the separation of H_2S (4000 ppm), without O2, of densified ACs with binders: (a) non-carbonized polyphenols, (b) carbonized polyphenols, and (c) cane molasses 2, prepared by Method 1 (full symbols) or Method 2 (empty symbols). Corresponding separation capacities: (d) per unit mass, and (e) per unit volume.

4.3.5.2 In the presence of O_2

KOH at 10 wt.%, identified as the most effective impregnating agent, was used to select the best method and type of binder for the fabrication of AC pellets, in a gas mixture containing O_2 (1.1% O_2, 4000 ppm H_2S, 60% N_2 and the rest balanced with CO_2). A higher impregnation level of 15 wt.% was also tested to determine whether oxygen content could further improve performance. **Figure 4.7** shows the H_2S breakthrough curves for Method 1 (**4.7a**) and Method

2 (**4.7b**). **Figures 4.7c** and **4.7d** present H_2S separation capacities per unit mass and unit volume, respectively.

Among polyphenol and cane 2 binders, fabricated in the same way (by sieving the granular AC to a particle size of less than 1 mm), the longest breakthrough time occurs for the cane-2-based sample with 10 wt.% KOH using Method 1 (880 minutes), followed by the carbonized polyphenol-based sample with the same method (820 minutes). Increasing KOH up to 15 wt.% reduced performance, confirming that 10 wt.% is optimal. For example, cane-2-based AC reduced breakthrough time to 500 minutes using Method 1, while polyphenol-based ACs also showed a decrease (from 820 to 670 minutes by Method 1). Non-carbonized polyphenols remained less competitive with a breakthrough time of 580 min using Method 1.

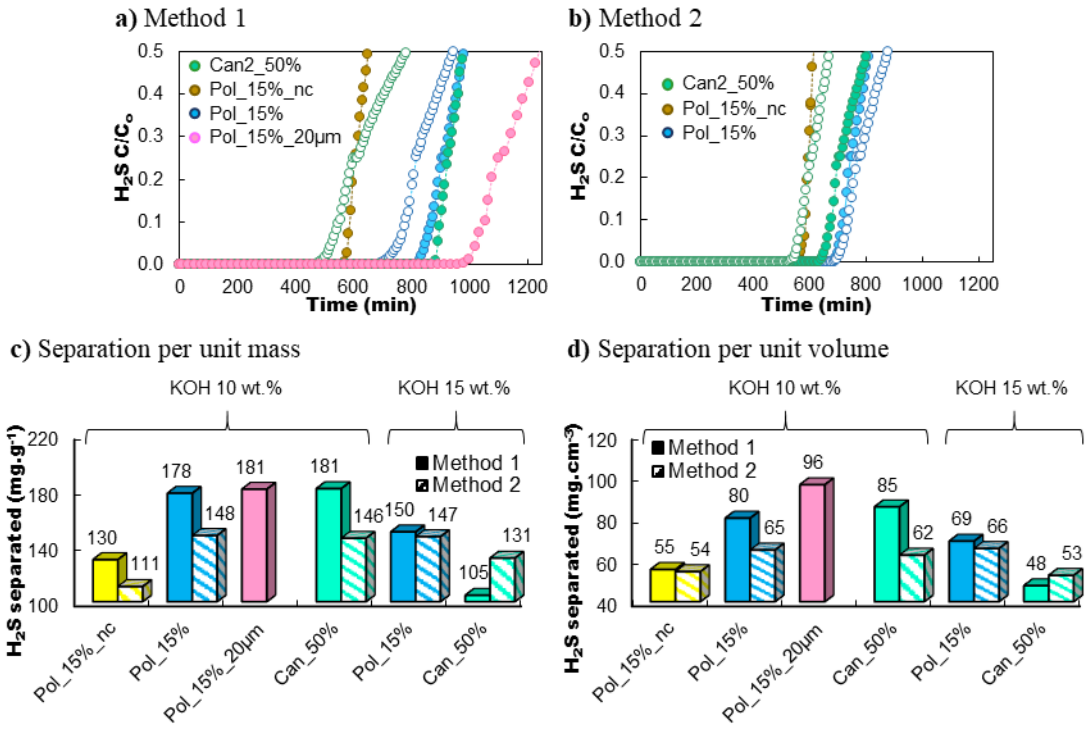

Figure 4.7 Breakthrough curves for the separation of H_2S (4000 ppm), in the presence of O2, of densified ACs impregnated with KOH at 10 wt.% (full symbols) and 15 wt.% (empty symbols), synthetized by (a) Method 1 and (b) Method 2. Corresponding separation capacities normalized by (c) unit mass and (d) unit volume of adsorbent.

Under these optimum preparation conditions (Method 1), the separation capacity per unit mass was nearly identical for the polyphenol-based AC (178 $mg \cdot g^{-1}$) and the cane molasses 2-based AC (181 $mg \cdot g^{-1}$). This is due to the higher density of cane molasses-based AC, which reduces separation capacity when normalized per unit mass. However, when considering H_2S

separation capacity per unit volume, the cane molasses 2-based AC demonstrated slightly higher performance (85 mg·cm^{-3}) compared to the polyphenol-based AC (80 mg·cm^{-3}).

KOH impregnation at 10 wt.% using Method 1, identified as the most optimal, was applied to pellets made from AC sieved to a particle size of 20–40 µm, resulting in denser sorbents. However, the dynamic adsorption test could only be performed on pol_15%_*20µm*. For can2_50%_*20µm*, the test was not possible due to excessive pressure drop. This was caused by high flow resistance due to the high packing density of the bed, primarily due to the high binder content (50%), which reduced porosity and limited gas flow. Pol_15%_20µm showed the longest breakthrough curve, lasting 1000 minutes. Its capacity per unit mass, 181 mg·g^{-1}, was nearly the same as that of the version synthesized with AC < 1 mm, 178 mg·g^{-1}. However, the volumetric capacity increased significantly from 80 mg·cm^{-3} to 96 mg·cm^{-3}. This confirms that the polyphenol binder performs better than cane molasses 2.

Experiments conducted in the presence of O_2 resulted in greater H_2S separation capacities, more than 20 times higher than those observed under O_2-free conditions (see **Figure 4.6**). Although Methods 1 and 2 showed comparable performance in the absence of O_2, the substantial increase in H_2S uptake under oxidative conditions makes the differences between the two methods more obvious.

It is useful to recall here that, in Method 1, the AC is first pelletized and carbonized before being impregnated, thus allowing the structural integrity of the pellets to be preserved during high-temperature treatment. Method 2, on the other hand, involves impregnation of the AC prior to pelletization and carbonization, which presents certain disadvantages. During compaction, the impregnating agent may indeed not effectively penetrate the microporous structure, resulting in uneven distribution throughout the material and compromising the uniformity of surface functionality. Additionally, subjecting the impregnated AC to carbonization at 700 °C may degrade or volatilize some of the chemical agents, reducing impregnation efficiency and altering surface properties. By isolating the impregnation step after heat treatment, Method 1 maintains both chemical functionality and structural stability, leading to greater separation efficiency.

Method 1 is in line with industrial practice, as it avoids introducing reactive chemicals into high-temperature furnaces, an approach preferred for safety, operational and environmental reasons. Chemicals such as KOH are highly corrosive and reactive, especially at 700 °C,

presenting risks to equipment and personnel. In addition, the management of waste and effluents, such as potassium vapors, is a major concern.

4.3.6 Comparison with commercial activated carbons for biogas desulfurization

As we have seen, bulk density significantly affects H_2S separation efficiency: higher density provides more adsorbent per unit volume, which increases H_2S uptake. While low-density AC can give good results per gram due to its intrinsic properties, it offers lower volumetric efficiency due to limited packing. As shown in **Figure 4.8a**, our best-performing sorbent (Pol_15%_20µm_KOH 10%) has an acceptable bulk density (531 $kg \cdot m^{-3}$), comparable to CAC 1, the only wood-based CAC (518 $kg \cdot m^{-3}$), highlighting the disadvantage of wood-based ACs compared with mineral-coal based ACs. CAC 6 and CAC 7 have the highest densities at 753 $kg \cdot m^{-3}$ and 764 $kg \cdot m^{-3}$, respectively, while CAC 2, CAC 8 and CAC are around 700 $kg \cdot m^{-3}$.

Figure 4.8b shows the relationships between pore volumes (ultra, micro and mesopores), which were determined in a previous study, considering only the substrate material without impregnation. [12] Non-coal-based CACs (CAC 1 and CAC 2) have the highest BET areas (1125–1145 $m^2 \cdot g^{-1}$), while coal-based CACs range from 830 to 940 $m^2 \cdot g^{-1}$ with similar microporosity (~ 0.35 $cm^3 \cdot g^{-1}$) and ultramicroporosity (0.08–0.17 $cm^3 \cdot g^{-1}$). Our AC made with polyphenol binder show average textural properties, with a BET area of 910 $m^2 \cdot g^{-1}$, a micropore volume of 0.33 $cm^3 \cdot g^{-1}$, and an ultra-micropore volume of 0.17 $cm^3 \cdot g^{-1}$. Remarkably, it features a high mesopore volume of 0.12 $cm^3 \cdot g^{-1}$, greater than that of CACs (max 0.07 $cm^3 \cdot g^{-1}$, CAC 6).

The CACs were evaluated under the same conditions as in subsection 3.5.2 (1.1% O_2, 4000 ppm H_2S, 60% N_2, the rest CO_2) and the resulting breakthrough curves are presented in **Figure 4.8c**, along with the calculated H_2S separation capacities shown in **Figure 4.8d** (per unit mass) and **Figure 4.8e** (per unit volume). [12]

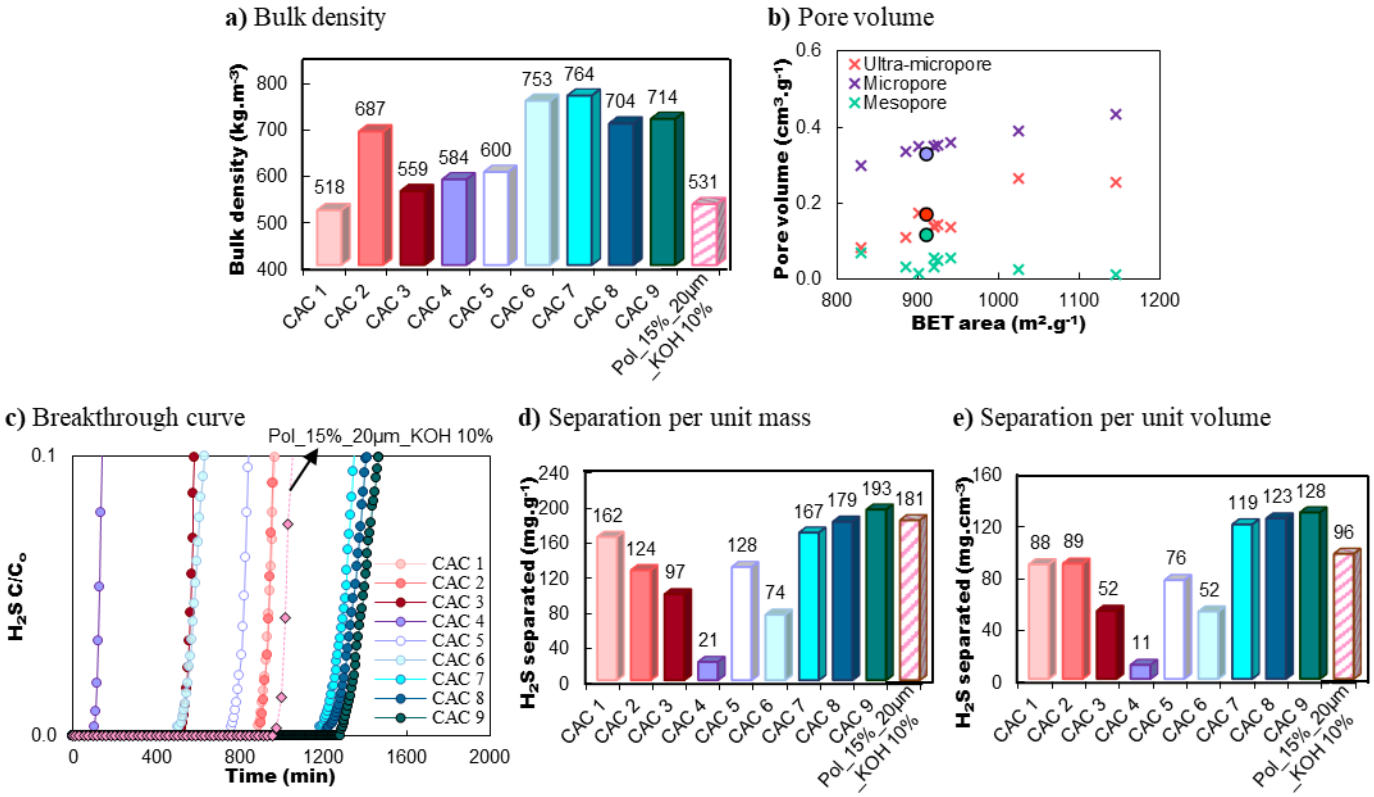

Figure 4.8 (a) Bulk density of Pol_15%_20µm_KOH 10% and CACs for biogas desulfurization investigated here. (b) Pore volume vs BET area of Pol_15%_20µm (circles) and CACs (crosses). (c) H_2S breakthrough curves and separation capacities of CACs and Pol_15%_20µm_KOH 10% per (d) unit mass and (e) unit volume of sorbent.

CAC 7, CAC 8 and CAC 9 have the longest breakthrough times (1180–1280 min), outperforming all other sorbents. With bulk densities above 650 kg·m^{-3} and probably optimal surface functionalization, confirmed for CAC 7 (10 wt.% NaOH), they combine the three key factors for high performance: high microporosity, effective functionalization and high bulk density. Other dense CACs such as CAC 6 (753 kg·m^{-3}) and CAC 2 (687 kg·m^{-3}) perform less effectively, likely due to less efficient functionalization. CAC 2, for instance, uses only 5 wt.% KOH. CAC 1, CAC 2 and CAC 5, form a second group of high-performance adsorbents, with breakthrough times of between 770 and 870 minutes. The sorbent developed here (Pol_15%_20µm_KOH 10%) outperforms them, achieving a breakthrough time of 1000 minutes.

Despite the lower bulk density of our developed AC, it is competitive with 6 of the 9 CACs in terms of separation efficiency per unit volume (96 mg·cm^{-3}). In fact, when normalized by mass, our ACs rank among the best (181 mg·g^{-1}), surpassed only by CAC 9 (193 mg·g^{-1}). Such high performance from our relatively low-density AC offers the advantage of easier handling

and transport, which is especially beneficial for mobile systems or small-scale digesters in rural or off-grid facilities.

4.4 Mathematical model

The mathematical model used to simulate dynamic H_2S adsorption and its constitutive equations are detailed in section 3.2.5 in chapter 3. To implement it, the data in **Table 4.1** were used. Adsorption isotherms were obtained by testing different H_2S concentrations and calculating the total saturation capacity from the corresponding breakthrough curves shown in **Figure 4.9a**. The sample used was Pol_15%_KOH10. Langmuir equilibrium constants were determined by fitting the experimental results for adsorption capacity (circles in **Figure 4.9b**) by Eq. (3.8). The calculated equilibrium constants were q_s = 7.1 mol·kg^{-1} (245.4 mg·g^{-1}) and b = 38.1 m^3·mol^{-1} with a coefficient of determination (R^2) of 0.94.

Table 4.1 Parameters used for H_2S dynamic adsorption simulation.

Gas properties		Bed properties	
Feed gas flow rate (m^3·s^{-1})	1.33E-06	Length (m)	0.1
Gas density (kg·m^{-3})	1.41	Diameter (m)	7.7E-03
Gas viscosity (kg·m^{-3})	1.66E-05	Bed voidage	0.21
Reynolds number	8.5	Activated carbon properties	
Peclet number	146.4	Particle diameter (m)	7.5E-04
D_L (m^2·s^{-1})	9.08E-05	Bulk density (kg.m^{-3})	m_{ads}/V_{bed}

m_{ads}: Mass of adsorbent
V_{bed}: Bed volume

The Langmuir model fitted the experimental data well but overestimated adsorption, predicting a q_s of 245.4 mg·g^{-1} against an experimental value of 203.1 mg·g^{-1} at 4000 ppm. This discrepancy stems from the model's idealized assumptions, which do not fully reflect the complexities of the real system. Thus, while useful for isotherm shape, it may not accurately predict the maximum capacity.

The simulation (dashed lines) presented in **Figure 4.9a** closely follows the experimental data (dots), showing good agreement. A slight deviation is observed at the 4000 ppm concentration; however, the predicted value still follows the general trend. The mass transfer coefficient k or LDF coefficient (see **Table 4.2**), was determined by fitting the experimental data to the simulation results shown in **Figures 4.9a**. k tends to stabilize (0.0002 s^{-1}) as soon as the

concentration exceeds 400 ppm, meaning that the resistance to mass transfer becomes similar. This is confirmed by the comparable slopes observed in the adsorption curves above 1000 ppm H_2S. To fit the experimental data with the simulation at 400 ppm, a higher *k* was required (0.0004 s^{-1}).

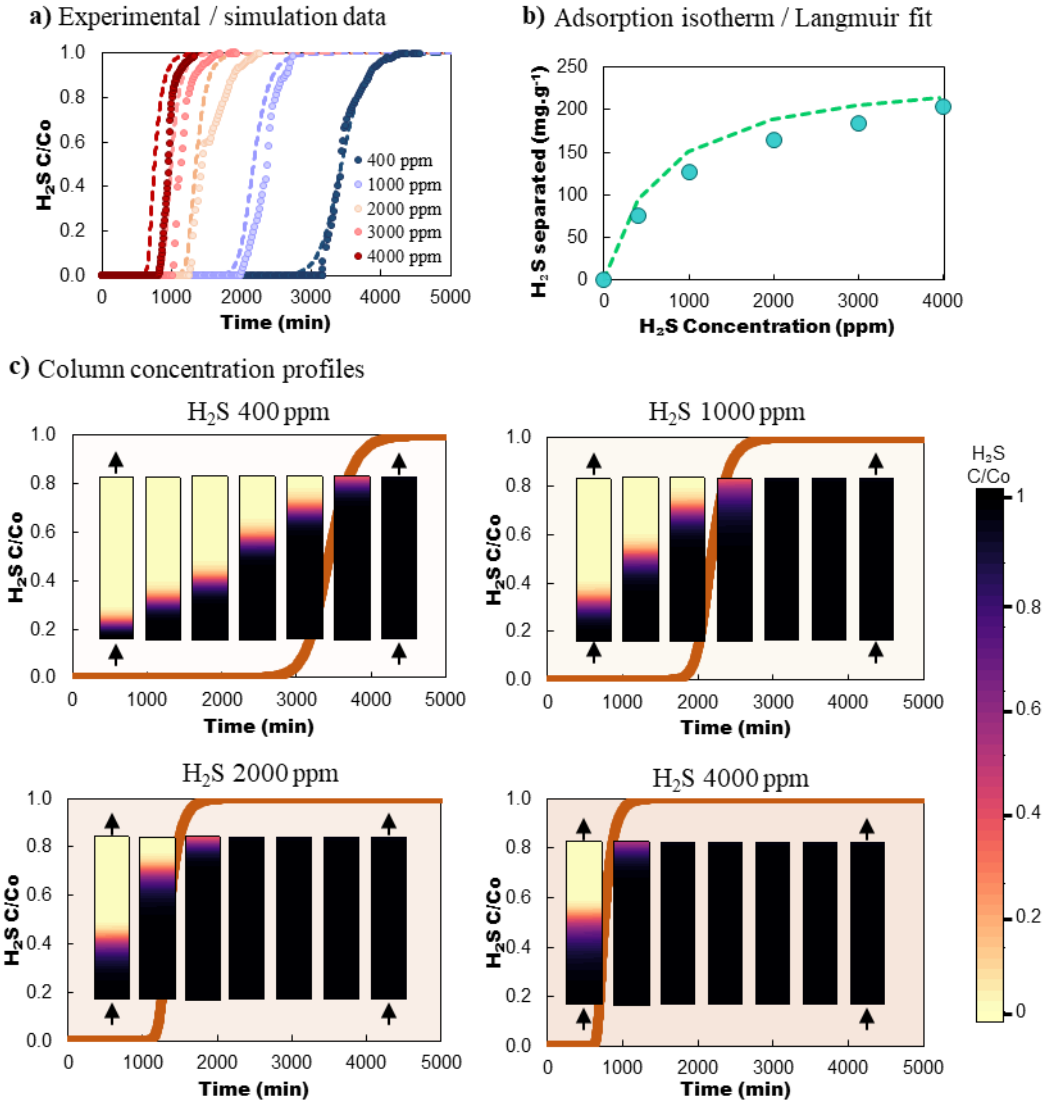

Figure 4.9 (a) Experimental (dots) and simulated (dashed lines) breakthrough curves at different H_2S concentrations. (b) H_2S equilibrium adsorption isotherms at 25 °C based on experimental breakthrough curves (circles), along with Langmuir fit (dashed lines). (c) Breakthrough curves and H_2S concentration profiles from simulations.

Table 4.2 Mass transfer coefficients estimate by fitting experimental and simulation data at different H_2S feed concentrations.

H_2S concentration (ppm)	400	1000	2000	3000	4000
Mass transfer coefficient (s^{-1})	0.0004	0.0002	0.0002	0.0002	0.0002

The coefficient *k* is inversely related to breakthrough time, with a longer breakthrough time corresponding to a lower *k* value. In this experiment, including densified AC and O_2 in the feed gas, high separation capacities were obtained, with a q_s (Langmuir coefficient) of 245.4 $mg \cdot g^{-1}$ and a *k* of 0.0002 s^{-1}. On the other hand, other studies on H_2S adsorption simulation reported lower capacities and higher *k* values: q_s = 11.9 $mg \cdot g^{-1}$ (k = 0.008 s^{-1}), [21] q_s = 15.0 $mg \cdot g^{-1}$ (k = 0.0019 s^{-1}), [22] and q_s = 5.9 $mg \cdot g^{-1}$ (k = 0.128 s^{-1}). [23] These results demonstrate the importance of simulating realistic biogas conditions.

The H_2S concentration distribution in the adsorption column at different H_2S inlet concentration is shown in **Figure 4.9c**. At the lowest concentration (400 ppm), the adsorption front moves slower through the bed due to the lower driving force for mass transfer. In contrast, at higher concentrations, particularly at 2000 and 4000 ppm, the front advances more rapidly and breakthrough occurs sooner. In addition, the mass transfer zone (MTZ) becomes broader at higher H_2S concentrations. Ideally, a lower inlet H_2S concentration would enhance the efficiency of the separation process by extending the lifetime of the adsorbent. However, the actual H_2S concentration is dictated by the composition of the biogas, which depends on its production conditions.

4.5 Conclusions

Wood-based activated charcoal was effectively densified with eco-friendly binders and chemically impregnated for competitive H_2S removal in biogas purification. Although densification reduced the sorbent's microporosity, its performance improved due to the increase in bulk density. The material's density rose from 263 to 531 $kg \cdot m^{-3}$.

Among the impregnating agents evaluated, KOH proved to be the most effective, with an impregnation ratio of 10 wt.% giving the best results. Among the binders tested, cane molasses and polyphenols performed similarly when impregnated with AC grains of less than 1 mm.

However, sieving AC to 20–40 μm produced denser and more efficient sorbents, although only the polyphenol-based AC could be tested under these conditions.

The presence of O_2 during H_2S adsorption increased separation capacity by more than tenfold, enabling clearer conclusions to be drawn compared with adsorption without O_2.

The optimum sequence for material preparation was identified as densification followed by carbonization and chemical impregnation, resulting in improved structural and adsorption properties. The AC developed here thus demonstrated high efficiency per unit mass compared with commercial activated carbons for biogas desulfurization, and is competitive with most of them. It is a sustainable alternative, as most CACs are derived from mineral coal.

Furthermore, a mathematical model was applied to describe the mass transfer dynamics in the adsorption column using densified AC in the presence of O_2 in the feed gas. These conditions led to significantly higher separation capacities than those reported in the literature, resulting in much lower mass transfer coefficients and longer breakthrough times.

4.6 References

[1] Paz, L.; Gentil, S.; Fierro, V.; Celzard, A. Activated Carbons Outperform Other Sorbents for Biogas Desulfurization. *Chemical Engineering Journal*, **2025**, *506*, 160304. https://doi.org/10.1016/j.cej.2025.160304.

[2] Erto, A.; Deorsola, F. A.; De Falco, G.; Montagnaro, F.; Balsamo, M. Role of H_2O and O_2 during the Reactive Adsorption of H_2S on CuO-ZnO/Activated Carbon at Low Temperature. *Microporous and Mesoporous Materials*, **2020**, *295*, 109949. https://doi.org/10.1016/j.micromeso.2019.109949.

[3] Yang, C.; Wang, Y.; Fan, H.; De Falco, G.; Yang, S.; Shangguan, J.; Bandosz, T. J. Bifunctional ZnO-MgO/Activated Carbon Adsorbents Boost H_2S Room Temperature Adsorption and Catalytic Oxidation. *Applied Catalysis B: Environmental*, **2020**, *266*, 118674. https://doi.org/10.1016/j.apcatb.2020.118674.

[4] Cepollaro, E. M.; Caputo, D.; Gargiulo, N.; Deorsola, F. A.; Cimino, S.; Lisi, L. H_2S Catalytic Removal at Low Temperature over Cu- and Mg- Activated Carbon Honeycombs. *Catalysis Today*, **2022**, *390–391*, 221–229. https://doi.org/10.1016/j.cattod.2021.11.027.

[5] Yan, R.; Liang, D. T.; Tsen, L.; Tay, J. H. Kinetics and Mechanisms of H_2S Adsorption by Alkaline Activated Carbon. *Environ. Sci. Technol.*, **2002**, *36* (20), 4460–4466. https://doi.org/10.1021/es0205840.

[6] Sisani, E.; Cinti, G.; Discepoli, G.; Penchini, D.; Desideri, U.; Marmottini, F. Adsorptive Removal of H_2S in Biogas Conditions for High Temperature Fuel Cell Systems. *International Journal of Hydrogen Energy*, **2014**, *39* (36), 21753–21766. https://doi.org/10.1016/j.ijhydene.2014.07.173.

[7] Castrillon, M. C.; Moura, K. O.; Alves, C. A.; Bastos-Neto, M.; Azevedo, D. C. S.; Hofmann, J.; Möllmer, J.; Einicke, W.-D.; Gläser, R. CO_2 and H_2S Removal from CH_4 - Rich Streams by Adsorption on Activated Carbons Modified with K_2CO_3 , NaOH, or Fe_2O_3. *Energy Fuels*, **2016**, *30* (11), 9596–9604. https://doi.org/10.1021/acs.energyfuels.6b01667.

[8] Liu, D.; Li, B.; Wu, J.; Liu, Y. Sorbents for Hydrogen Sulfide Capture from Biogas at Low Temperature: A Review. *Environ Chem Lett*, **2020**, *18* (1), 113–128. https://doi.org/10.1007/s10311-019-00925-6.

[9] Khabazipour, M.; Anbia, M. Removal of Hydrogen Sulfide from Gas Streams Using Porous Materials: A Review. *Ind. Eng. Chem. Res.*, **2019**, *58* (49), 22133–22164. https://doi.org/10.1021/acs.iecr.9b03800.

[10] Ozekmekci, M.; Salkic, G.; Fellah, M. F. Use of Zeolites for the Removal of H_2S: A Mini-Review. *Fuel Processing Technology*, **2015**, *139*, 49–60. https://doi.org/10.1016/j.fuproc.2015.08.015.

[11] Norouzi, A. M.; Siavashi, M.; Soheili, A. R.; Khaliji Oskouei, M. Experimental Investigation of Effects of Grain Size, Inlet Pressure and Flow Rate of Air and Argon on Pressure Drop through a Packed Bed of Granular Activated Carbon. *International Communications in Heat and Mass Transfer*, **2018**, *96*, 20–26. https://doi.org/10.1016/j.icheatmasstransfer.2018.05.019.

[12] Paz, L.; Selmi, T.; Fierro, V.; Celzard, A. Tailoring Wood-Based Activated Carbons and Assessing the Role of Impregnation and O_2 for Efficient H_2S Removal from Biogas. *Separation and Purification Technology*, **2025**.

[13] Celzard, A.; Marêché, J. F.; Furdin, G.; Fierro, V.; Sayag, C.; Pielaszek, J. Preparation and Catalytic Activity of Active Carbon-Supported Mo2C Nanoparticles. *Green Chem.*, **2005**, *7* (11), 784. https://doi.org/10.1039/b507971c.

[14] Brunauer, S.; Emmett, P. H.; Teller, E. Adsorption of Gases in Multimolecular Layers. *J. Am. Chem. Soc.*, **1938**, *60* (2), 309–319. https://doi.org/10.1021/ja01269a023.

[15] Jagiello, J.; Olivier, J. P. 2D-NLDFT Adsorption Models for Carbon Slit-Shaped Pores with Surface Energetical Heterogeneity and Geometrical Corrugation. *Carbon*, **2013**, *55*, 70–80. https://doi.org/10.1016/j.carbon.2012.12.011.

[16] Standard Test Method for Determination of the Accelerated Hydrogen Sulfide Breakthrough Capacity of Granular and Pelletized Activated Carbon, 2023.

[17] Vu, H. P.; Nguyen, L. N.; Wang, Q.; Ngo, H. H.; Liu, Q.; Zhang, X.; Nghiem, L. D. Hydrogen Sulphide Management in Anaerobic Digestion: A Critical Review on Input Control, Process Regulation, and Post-Treatment. *Bioresource Technology*, **2022**, *346*, 126634. https://doi.org/10.1016/j.biortech.2021.126634.

[18] Palmonari, A.; Cavallini, D.; Sniffen, C. J.; Fernandes, L.; Holder, P.; Fagioli, L.; Fusaro, I.; Biagi, G.; Formigoni, A.; Mammi, L. Short Communication: Characterization of Molasses Chemical Composition. *Journal of Dairy Science*, **2020**, *103* (7), 6244–6249. https://doi.org/10.3168/jds.2019-17644.

[19] Kader, D. A. E.; Molina, E.; Colina, G.; Montero, L.; de Pinto, G. L. Cationic Composition and the Tannin Content of FIve Gums from Venezuelan Mimosaceae Species. *Food Hydrocolloids*, **2003**.

[20] Oginni, O.; Singh, K.; Oporto, G.; Dawson-Andoh, B.; McDonald, L.; Sabolsky, E. Influence of One-Step and Two-Step KOH Activation on Activated Carbon Characteristics. *Bioresource Technology Reports*, **2019**, *7*, 100266. https://doi.org/10.1016/j.biteb.2019.100266.

[21] Aguilera, P. G.; Gutiérrez Ortiz, F. J. Prediction of Fixed-Bed Breakthrough Curves for H_2S Adsorption from Biogas: Importance of Axial Dispersion for Design. *Chemical Engineering Journal*, **2016**, *289*, 93–98. https://doi.org/10.1016/j.cej.2015.12.075.

[22] Gutiérrez Ortiz, F. J.; Aguilera, P. G.; Ollero, P. Modeling and Simulation of the Adsorption of Biogas Hydrogen Sulfide on Treated Sewage–Sludge. *Chemical Engineering Journal*, **2014**, *253*, 305–315. https://doi.org/10.1016/j.cej.2014.04.114.

[23] Papurello, D.; Gandiglio, M.; Lanzini, A. Experimental Analysis and Model Validation on the Performance of Impregnated Activated Carbons for the Removal of Hydrogen Sulfide (H_2S) from Sewage Biogas. *Processes*, **2019**, *7* (9), 548. https://doi.org/10.3390/pr7090548.

[24] Daraee, M.; Ghasemy, E.; Rashidi, A. Synthesis of Novel and Engineered UiO-66/Graphene Oxide Nanocomposite with Enhanced H_2S Adsorption Capacity. *Journal of Environmental Chemical Engineering*, **2020**, *8* (5), 104351. https://doi.org/10.1016/j.jece.2020.104351.

[25] Yu, Z.; Wang, X.; Song, X.; Liu, Y.; Qiu, J. Molten Salt Synthesis of Nitrogen-Doped Porous Carbons for Hydrogen Sulfide Adsorptive Removal. *Carbon*, **2015**, *95*, 852–860. https://doi.org/10.1016/j.carbon.2015.08.105.

Chapter 5. Biogas purification at pilot scale and regeneration of H_2S-saturated sorbents

5.1 Introduction

An essential aspect of this thesis has been the establishment of an industrial partnership aimed at exchanging knowledge and aligning research objectives with practical, real-world needs. This collaboration has enabled us to tailor our project to a clearly defined goal: the development of a steam-activated wood-based carbon material with the potential to move to industrial applications. Thanks to this partnership, it has been possible to conduct pilot-scale adsorption experiments using real biogas streams, in particular for the removal of H_2S and volatile organic compounds (VOCs), using pilot-scale adsorption columns. Despite the valuable insights obtained, these experiments could not be completed due to the intrinsic operational challenges associated with maintaining stable biogas purification facilities. Nevertheless, the procedures developed for adsorbent production, surpassing typical lab-scale quantities, and the knowledge acquired demonstrate a significant step towards practical scalability. These are detailed in the following sections.

We also conducted regeneration tests on densified, KOH-impregnated activated carbons that had been saturated with H_2S during biogas desulfurization processes. To evaluate the potential for reuse and performance recovery, different regeneration methods were applied, including washing and heat treatments in air and nitrogen atmospheres. The effectiveness of each approach was assessed in terms of sorbent adsorption efficiency. The results of these regeneration trials are presented and discussed below.

5.2 H_2S and VOCs removal on a pilot scale

5.2.1 Sorbent preparation

The charcoal supplied by Groupe Bordet for this set of experiments had a different particle size compared to the material used in Chapters 3 and 4, which ranged from 3-8 mm. In this case, the charcoal had a particle size of 1-3 mm. From now on, this material will be referred to as charcoal 2, and its activated form will be denoted as AC 2. Due to the difference in particle size, a new activation campaign was conducted in accordance with the activation procedure described in section 2.1 of Chapter 2. Furthermore, it was compared with three commercial activated carbons used for VOC removal from biogas (CAC_VOC), presented in **Table 5.1**. The characteristics of the CACs used for VOC removal are similar to those used for H_2S

removal (see **Table 3.1**), being densified ACs reaching bulk densities above 600 $kg \cdot m^{-3}$. The main remark concerning CAC_VOC is that they are not impregnating, suggesting an adsorption mechanism based predominantly on physisorption.

Table 5.1 Commercial activated carbons (CACs) for VOCs removal.

Sample name	Origin	Bulk density ($kg.m^{-3}$)	Impregnation	Form
CAC 1_VOC	Coal	622	Non impregnated	Granular (2.4 - 5 mm)
CAC 2_VOC	Coal	709	Non impregnated	Pellet (Ø = 4 mm – L = 4 - 12 mm)
CAC 3_VOC	Coal	652	Non impregnated	Pellet (Ø = 4 mm – L = 4 - 12 mm)

Figure 5.1a presents the N_2 adsorption-desorption isotherms of activated charcoal 2 (AC 2) at different activation conditions and of the optimum activated charcoal developed in Chapter 3 for H_2S adsorption (AC_900°C_2h), which is the reference for textural properties. Their pore size distributions are presented in **Figure 5.1b** and the corresponding cumulative pore volumes are presented in **Figure 5.1c**. The same curves are presented for commercial CAC_VOC in **Figures 5.1d**, **5.1e** and **5.1f**, respectively. The corresponding textural parameters are presented in **Table 5.2**.

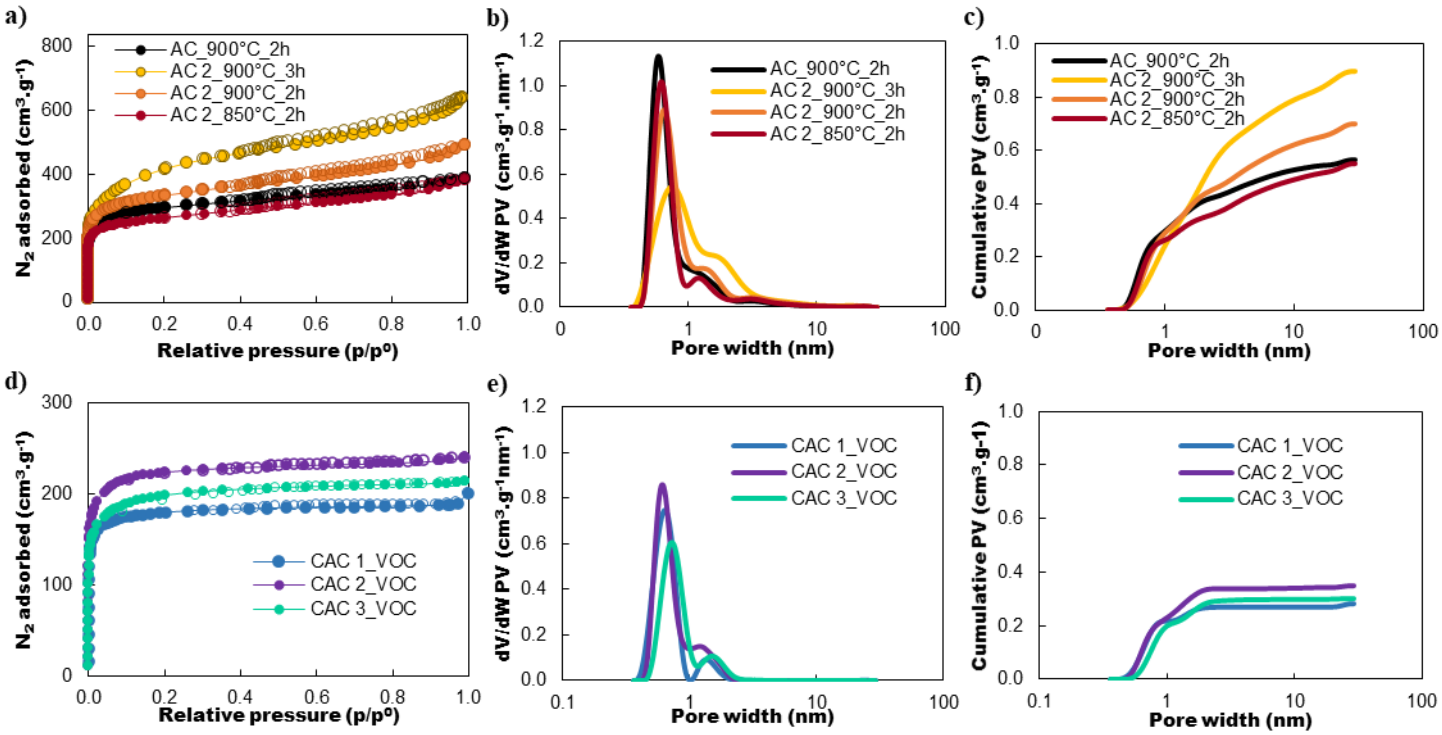

Figure 5.1 Nitrogen adsorption (solid symbols)-desorption (empty symbols) isotherms of a) AC_900°C_2h reference and activated charcoal 2 at different activation conditions, and d) commercial ACs for VOC removal (CAC_VOC), and their corresponding pore size distributions (b and e) and cumulative pore volumes (c and f).

Activated charcoal 2 (grain size 1-3 mm) has a higher BET area compared to the 3–8 mm grain size charcoal activated under identical conditions (see **Table 3.1 again**). The higher BET area and increased burn-off obtained for activated charcoal 2 are attributed to the smaller particle size, which allows steam to penetrate the carbon structure more effectively and develop the desired microporosity.

This activation campaign enabled us to select AC 2_850°_2h as the most suitable candidate for the H_2S and VOC removal pilot experiments. It retains a similar level of N_2 adsorption and pore size distribution than the reference AC_900°C_2h, for which the objective is a strong presence of ultramicroporosity.

Although we did not have the means to study and select an optimum AC specifically for VOC removal, observations showed that CACs used for this purpose have very low mesoporosity, with well-developed ultra microporosity, similar to the findings in Chapter 3 for H_2S removal. The lower ultramicroporosity in CAC_VOC compared with AC 2 is attributed to their densification, which reduces porosity but results in a higher bulk density. They are therefore more efficient than highly porous materials with low bulk density.

Due to limited production capacity, it was not possible to produce densified activated carbon on a pilot scale, as daily lab-scale production remains low, in the order a few grams. However, for the activation and impregnation processes, it is possible to produce more than 100 g of sorbent per day. As a result, 1000 g of activated charcoal 2 (AC 2_850 °C_2h) were prepared. Of this total, 400 g were impregnated with 10 wt.% KOH for the biogas desulfurization test, previously identified as the optimum impregnation condition (see Chapters 3 and 4), while the remaining non-impregnated charcoal was reserved for VOC removal experiments.

Table 5.2 also presents the results of nine different charcoal activation at 850 °C for 2 hours. The results are consistent, with BET areas ranging from 940 to 1030 $m^2 \cdot g^{-1}$. Each activation started with approximately 250 g of raw charcoal. With an average burn-off of 54.0%, this yielded about 115 g of activated charcoal per batch activated.

Table 5.2 Textural parameters of charcoal-derived ACs (as a function of activation time and temperature) and their burn-offs, and those of commercial ACs for VOC removal.

Sample	BET, DR and V_{tot}			NLDFT					Burn-off (%)
	A_{BET} ($m^2 \cdot g^{-1}$)	V_{DR} ($cm^3 \cdot g^{-1}$)	$V_{0.97}$ ($cm^3 \cdot g^{-1}$)	S_{NLDFT} ($m^2 \cdot g^{-1}$)	$V_{ultra-mic}$ ($cm^3 \cdot g^{-1}$)	$V_{<2nm}$ ($cm^3 \cdot g^{-1}$)	V_{mes} ($cm^3 \cdot g^{-1}$)	V_{tot} ($cm^3 \cdot g^{-1}$)	
Reference activated charcoal from chapter 3									
AC_900°C_2h	1120	0.44	0.60	1166	0.22	0.41	0.15	0.56	52.3
Activated charcoal 2 from grain size 1-3 mm									
AC 2_900°C_3h	1465	0.56	0.99	1225	0.10	0.50	0.40	0.90	82.9
AC 2_900°C_2h	1250	0.49	0.76	1167	0.16	0.44	0.26	0.70	65.3
AC 2_850°C_2h	995	0.39	0.59	1025	0.19	0.35	0.20	0.55	54.0
Commercial activated carbons for VOC removal									
CAC_VOC_1	710	0.28	0.29	765	0.16	0.27	0.02	0.28	-
CAC_VOC_2	865	0.343	0.371	865	0.16	0.33	0.01	0.35	-
CAC_VOC_3	755	0.297	0.331	680	0.08	0.28	0.02	0.30	-
Activated charcoal 2 at 850°C and 2h									
AC 2_850°C_2h _1	970	0.38	0.59	1043	0.20	0.34	0.22	0.56	53.7
AC 2_850°C_2h _2	1025	0.40	0.63	1090	0.20	0.36	0.23	0.60	54.6
AC 2_850°C_2h _3	960	0.38	0.59	1022	0.20	0.34	0.22	0.56	56.1
AC 2_850°C_2h _4	1030	0.40	0.70	1075	0.17	0.35	0.30	0.65	57.2
AC 2_850°C_2h _5	930	0.37	0.54	1042	0.20	0.33	0.18	0.51	53.5
AC 2_850°C_2h _6	940	0.37	0.58	1050	0.20	0.33	0.22	0.55	52.6
AC 2_850°C_2h _7	955	0.38	0.64	995	0.19	0.33	0.21	0.54	53.2
AC 2_850°C_2h _8	965	0.38	0.57	1047	0.21	0.34	0.19	0.53	53.2
AC 2_850°C_2h _9	985	0.39	0.61	1072	0.21	0.35	0.23	0.58	51.5

A_{BET}: BET area
V_{DR}: Dubinin–Radushkevich micropore volume
$V_{0.97}$: Pore volume at relative pressure $P/P_o = 0.97$
S_{NLDFT}: Surface area from non-local density functional theory
$V_{ultra-mic}$: Ultramicropore volume (pore size < 0.7 nm)
$V_{<2nm}$: Micropore volume (pore size < 2 nm)
V_{mes}: Mesopore volume (2 < pore size < 50 nm)
V_{tot}: Total pore volume

The impregnation of the sorbent was carried out as described in section 3.2.2 of Chapter 3. However, due to the large quantity of material, an additional step was introduced, as shown in **Figure 5.2** (step 3). This step involved an initial extraction of water using a steam extraction oven at 100 °C for 8 hours. This pre-drying step was necessary to support the final drying process in the lab-scale vacuum oven, which was not sufficient on its own to remove all the moisture. Without this step, the vacuum oven would have been saturated, leaving the activated charcoal still humid.

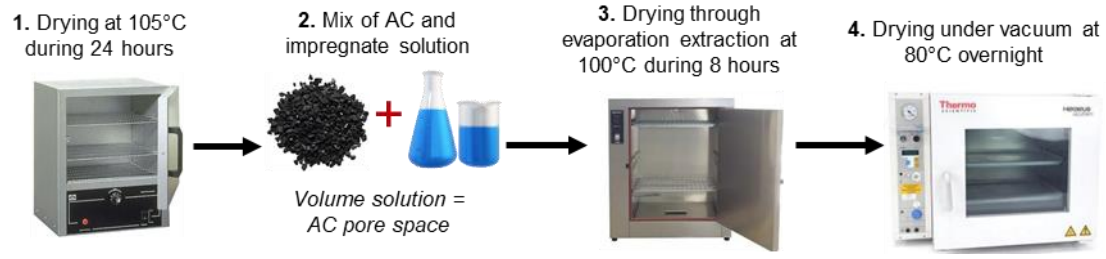

Figure 5.2 Activated carbon impregnation procedure for pilot experiments.

5.2.1 H_2S adsorption test

Landfill gas with the following composition (vol. %): 43.79 % CH_4, 40.09 % CO_2, 1.49 % O_2, 1.01 % H_2O, and 0.7 % H_2S (7000 ppm), was directed (see **Figure 5.3a**) into a pilot-scale adsorption column (**Figure 5.3b**). The column was partially filled with 93 g of AC 2_850 °C_3h activated charcoal, impregnated with 10 wt.% KOH. The column was 30 cm long with an internal diameter of 5.3 cm. A flow rate of 1000 $mL \cdot min^{-1}$ was applied, corresponding to a linear velocity of 0.76 $cm \cdot s^{-1}$, and was regulated using a rotameter. The gas composition at the outlet of the column was monitored continuously by infrared spectroscopy.

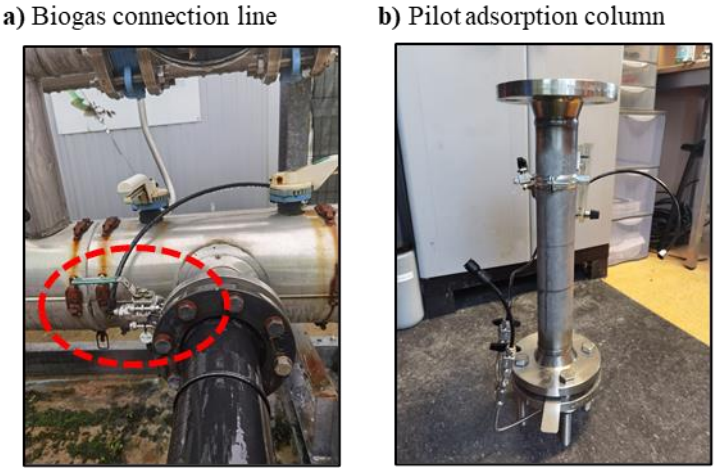

Figure 5.3 H_2S removal from landfill gas. a) Biogas connection line and b) pilot adsorption column.

The test was conducted over a period of 6 hours, and it had to be stopped for operational concerns. During this time, no H_2S breakthrough was observed, indicating complete adsorption of the contaminant. The amount of H_2S removed was determined to be 38.06 $mg \cdot g^{-1}$, as detailed in the following calculation:

$$1000\ \frac{cm^3}{min} \times \frac{0.7}{100} \times \frac{60\ min}{1\ h} \times 6\ h \times \frac{1\ L}{1000\ cm^3} \times 1.4045\ \frac{g\ H_2S}{1\ L\ H_2S} = 3.539\ g\ H_2S$$

$$3.539\ g\ H_2S \times\ \frac{1000\ mg}{1\ g} \times \frac{1}{93\ g\ AC} = \mathbf{38.06\ \frac{mg\ H_2S}{g\ AC}}$$

Although complete saturation of the adsorbent was not achieved, this experiment demonstrated significantly higher H_2S separation capacities than those previously obtained in our laboratory (< 10 mg·g^{-1}) conducted without O_2 in the feed gas. Initially, our lab experiments were conducted using a gas mixture consisting solely of N_2 and CO_2. However, when O_2 was introduced into the feed gas, the adsorption capacity increased more than tenfold, as presented in Chapters 3 and 4. This presence of O_2 is also responsible for the high separation capacities observed under real biogas conditions. An additional experiment is planned to complete the breakthrough curve with this landfill gas and compare it with the commercial activated carbon used in this facility for H_2S removal.

5.2.2 VOCs adsorption test

Landfill gas, from a facility different to the pilot test of H_2S, had the following composition (vol.%): 39.89% CH_4, 34.89% CO_2, 2.65% O_2, 0.7% H_2O, with unknown concentrations of H_2S and VOCs. As in the H_2S pilot test, the gas was directed to the pilot adsorption column (see **Figure 5.4a**). The adsorption column used was the same as that shown in **Figure 5.3b** and was fully packed with 157 g of non-impregnated AC 2_850 °C_2h. The flow rate was maintained at 1000 mL·min^{-1} and regulated using a rotameter.

As the biogas facility is not equipped to measure VOC content, xylene concentrations were assessed using Dräger detection tubes. These tubes, capable of detecting up to 400 ppm of xylene, were filled with samples of raw landfill gas and gas exiting the pilot adsorption column. As presented in **Figure 5.4b**, the detection tube exposed to the raw biogas turned entirely black, indicating a xylene concentration of at least 400 ppm. In contrast, tubes used to sample the treated gas exiting the column retained their original colour throughout the entire 28-hour test, indicating that all the xylene had been effectively adsorbed by the activated charcoal. As the total concentration of contaminants in the biogas is unknown, it is not possible to estimate the amount adsorbed during the test period.

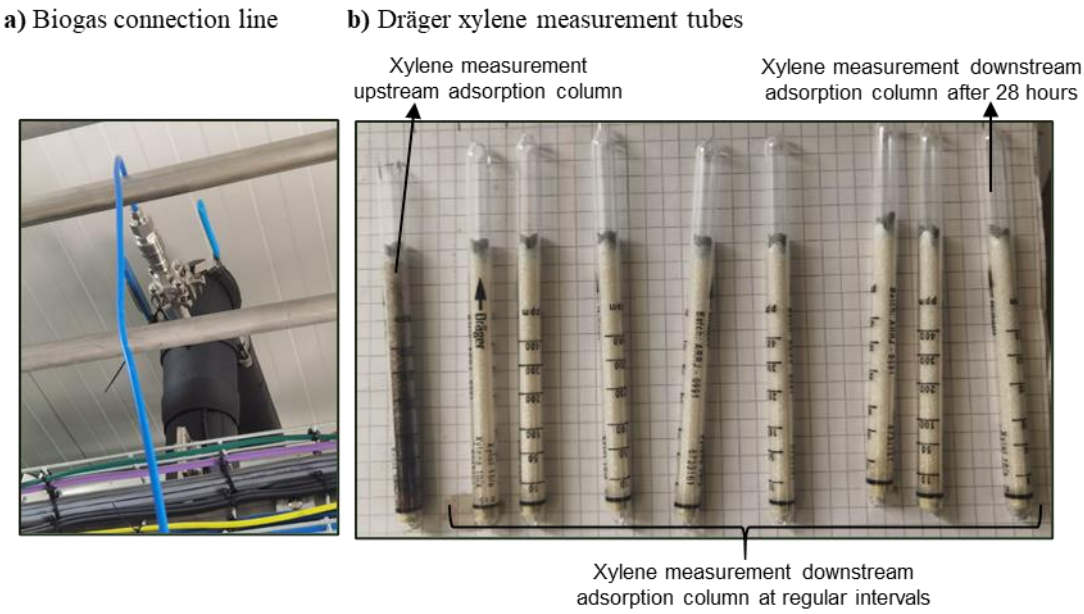

Figure 5.4 VOCs removal from landfill gas. a) Biogas connection line and b) xylene measurement using Dräger tubes calibrated to 400 ppm of xylene.

Measuring VOCs in biogas is challenging due to their complex and variable composition, [1] as they often comprise a wide range of chemical species present in low concentrations. For this reason, studies typically focus on a few representative or abundant compounds, such as xylene in our case, in order to simplify analysis. For pilot-scale experiments, it becomes essential to implement reliable analytical techniques capable of accurately monitoring VOC concentrations. Methods such as gas chromatography (GC) and infrared (IR) spectroscopy are commonly employed for this purpose, as they enable continuous or periodic measurement of specific VOCs in both the inlet and outlet streams. This data is critical for constructing breakthrough curves, which in turn allow the determination of separation capacities and adsorption dynamics.

5.3 Regeneration of H_2S saturated activated carbon

Table 5.3 summarizes the regeneration methods investigated, after using a gas mixture of 1.1% O_2, 4000 ppm H_2S, 60% N_2, and ~39% CO_2 for saturating the sorbents. The spent sorbents evaluated were densified impregnated ACs: Pol_15%_KOH 10 and Can_50%_KOH 10. Unlike previous studies that ignore CO_2, [1] this work includes CO_2 levels typical of real biogas, requiring its desorption during regeneration and adding complexity compared to systems with only H_2S and inert gases. [1] **Figure 5.5a-c** shows the breakthrough curves and separation capacities of the regenerated sorbents.

Table 5.3. Regeneration methods and H_2S separation capacities of densified, impregnated ACs: Pol_15%_KOH 10 and Can_50%_KOH 10.

Sample	Regeneration method	Cycle	H_2S separated at BTP C/C_0 1% ($mg \cdot g^{-1}$)
Pol_15%_KOH 10	Fresh	-	178
	Soxhlet washing during 24 h	1	≈ 0
	Air flow (100 $mL \cdot min^{-1}$) at 150 °C during 2 h, ramp temperature 5°C·min^{-1}	1	≈ 0
	N_2 flow (100 $mL \cdot min^{-1}$) at 300 °C during 2 h, ramp temperature 5°C·min^{-1}	1	≈ 0
	N_2 flow (100 $mL \cdot min^{-1}$) at 500 °C during 2 h, ramp temperature 5°C·min^{-1}	1	13
		2	31
	N_2 flow (100 $mL \cdot min^{-1}$) at 500 °C during 2 h, ramp temperature 5°C·min^{-1}, followed by impregnation with KOH 10 wt.% – Cycle 1	1	71
		2	79
Can_50%_KOH 10	Fresh	-	181
	N_2 flow (100 $mL \cdot min^{-1}$) at 500 °C during 2 h, ramp temperature 5°C·min^{-1} – Cycle 1	1	62
		2	58
	N_2 flow (100 $mL \cdot min^{-1}$) at 500 °C during 2 h, ramp temperature 5°C·min^{-1}, followed by impregnation with KOH 10 wt.% – Cycle 1	1	104
		2	75

Soxhlet washing, air at 150 °C and N_2 at 300 °C failed to regenerate Pol_15%_KOH 10, as its adsorption capacity lost, indicating that the sorbent remained saturated (**Figure 5.4a**). Some studies report successful regeneration with N_2 at 120–200 °C using simplified gas streams (H_2S in N_2). For example, a UiO-66/graphene oxide composite retained 87% of its capacity after three cycles, [2] and a N-doped porous carbon maintained 20.1 $mg \cdot g^{-1}$ of its initial capacity of 27.6 $mg \cdot g^{-1}$ after four regeneration cycles. [3] In contrast, our sorbent operates under real biogas conditions and achieves >175 $mg \cdot g^{-1}$, demonstrating greater complexity.

Thermal regeneration at 500 °C with N_2 improved the results. **Figures 5.4b–e** show breakthrough curves and separation capacities for Pol_15%_KOH 10 and Can_50%_KOH 10. The impregnating agent probably lost its catalytic activity by reacting into pore-blocking compounds, such as potassium sulfate, with local accumulation. Additionally, H_2S removal on KOH-impregnated ACs in the presence of O_2 generates strongly bound sulfur species (e.g., S_8, SO_2, HS_2^-, polysulfides), which are difficult to desorb or even decompose, further complicating regeneration. To investigate whether the loss of performance was due to KOH depletion or

degradation during the 1st adsorption test, a second impregnation step with 10% KOH was applied after heat treatment at 500 °C (500°C_KOH 10). The amount of KOH was calculated based on the AC mass after regeneration, without confirming how much active KOH remained. As a result, the actual KOH content may have exceeded 10 wt.%.

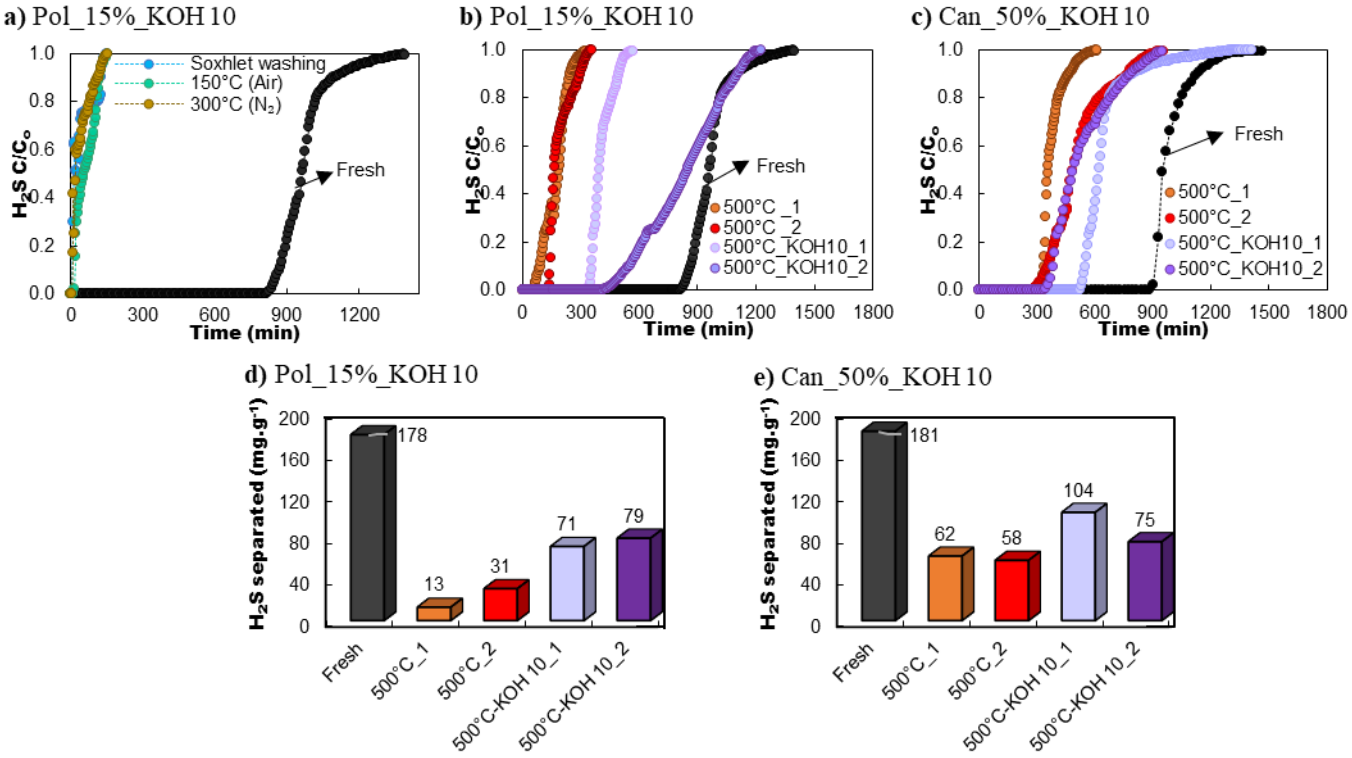

Figure 5.5 (a) Breakthrough curves of sample Pol_15%_ KOH 10 before (fresh) and after regeneration by Soxhlet washing or thermal regeneration with either air (150 °C) and or N_2 (300 °C). Breakthrough curves of sample (b) Pol_15%_ KOH 10 and (c) Can_50%_KOH 10 after thermal regeneration with N_2 at 500 °C and thermal regeneration with impregnation with KOH 10 wt.%. Separation capacities at BTP C/Co 1% corresponding to the regeneration methods of (d) Figure 5.4b, and (e) Figure 5.4c.

Figures 5.5b and 5.5c show breakthrough curves for Pol_15%_KOH 10 and Can_50%_KOH 10, respectively, after regeneration at 500 °C for the first (500C_1) and second cycle (500C_2), as well as after regeneration followed by re-impregnation with 10 wt.% KOH for the first (500C_KOH10_1) and second cycle (500C_KOH10_2). For both samples, re-impregnation improved performance, but it remained difficult to achieve the same adsorption capacity as the fresh, pristine sample.

Iodine number tests (ASTM D4607-94) were conducted on fresh and thermally regenerated samples at 500 °C. The iodine number of Pol_15%_KOH 10 decreased from 1138 to

1022 $mg \cdot g^{-1}$, and Cane_50%_KOH 10 from 1020 to 964 $mg \cdot g^{-1}$. Although partial H_2S adsorption capacity was recovered after re-impregnation, the initial iodine number was not fully restored. Since the iodine number reflects micropore volume, this decline suggests irreversible pore blockage or structural changes.

Despite the challenges associated with regenerating impregnated ACs, they are the preferred choice for industrial applications due to their high performance comparted with non-impregnated ACs. In industry, saturated AC columns are replaced by fresh ones rather than being regenerated in situ.

5.4 Conclusions

Preliminary experiments on the removal of H_2S and VOCs from real biogas provided valuable insights despite being interrupted due to limited access to purification facilities. The results indicated that the presence of oxygen in real biogas enhanced the separation capacity for H_2S, which made modify our lab-test bench for including it. In contrast, the assessment of VOC removal proved more challenging due to the lack of appropriate monitoring systems at the facility. Xylene levels were estimated using detection tubes, but this method offers only limited accuracy. Although the experiments could not be completed, they underscored key operational considerations and measurement limitations that will inform future trials. Both experiments are planned to be repeated under more controlled conditions to confirm these initial findings and to better quantify the removal performance.

The regeneration of H_2S-saturated, densified KOH-impregnated activated carbons was systematically investigated using various methods, including Soxhlet washing and thermal treatments under different conditions. Soxhlet extraction proved ineffective in restoring the sorbent's performance, thermal regeneration at 150 °C in air and 300 °C in nitrogen also failed to recover the adsorption capacity. On the other side, thermal regeneration at 500 °C under nitrogen atmosphere resulted in partial restoration of the sorbent's performance. Further improvement was achieved by re-impregnating the thermally regenerated carbon with KOH, reintroducing active sites for chemisorption and catalytic oxidation. However, even after re-impregnation, the regenerated sorbent did not reach the original performance level of the fresh material, losing 60% of its initial adsorption capacity for the polyphenol-based densified AC and 43% for the cane 2-based densified AC.

5.5 References

[1] Paz, L.; Gentil, S.; Fierro, V.; Celzard, A. Activated Carbons Outperform Other Sorbents for Biogas Desulfurization. *Chemical Engineering Journal*, **2025**, *506*, 160304. https://doi.org/10.1016/j.cej.2025.160304.

[2] Daraee, M.; Ghasemy, E.; Rashidi, A. Synthesis of Novel and Engineered UiO-66/Graphene Oxide Nanocomposite with Enhanced H_2S Adsorption Capacity. *Journal of Environmental Chemical Engineering*, **2020**, *8* (5), 104351. https://doi.org/10.1016/j.jece.2020.104351.

[3] Yu, Z.; Wang, X.; Song, X.; Liu, Y.; Qiu, J. Molten Salt Synthesis of Nitrogen-Doped Porous Carbons for Hydrogen Sulfide Adsorptive Removal. *Carbon*, **2015**, *95*, 852–860. https://doi.org/10.1016/j.carbon.2015.08.105.

Conclusions and perspectives

This thesis presents an in-depth study of the use of activated carbons (ACs) for biogas purification, focusing particularly on CO_2/CH_4 separation and H_2S removal, through a literature review and experimental work. The research contributes to the understanding of adsorbent selection, material preparation, process optimization and modeling strategies for dynamic adsorption.

From a literature perspective, a comparative review of adsorbents for CO_2/CH_4 separation in pressure swing adsorption (PSA) systems identified zeolites and carbon molecular sieves (CMSs) as the best sorbents due to their high equilibrium and kinetic selectivity, respectively. ACs, although less selective, offer advantages in terms of cost, sustainability and ease of functionalization. However, their integration into multi-column PSA systems remains limited, no examples having been found, indicating the need to translate laboratory results into scalable technologies. On the other hand, for biogas desulfurization, ACs emerged as the most industrially viable option, outperforming MOFs and zeolites when appropriately functionalized. However, the review highlighted current gaps in the literature, including the inadequate consideration of CO_2 in synthetic gas studies, as well as high-impact components like H_2O and O_2.

Experimental work focused on the synthesis and optimization of wood-based activated charcoal for H_2S removal. The main results demonstrate that steam activation and KOH impregnation significantly improve the separation performance of the charcoal-based precursor, with the development of ultra-microporosity playing a vital role in relation to mesoporosity. Remarkably, the presence of oxygen significantly enhances H_2S separation capacity via catalytic oxidation mechanisms, a factor often neglected in literature studies. Densification of ACs, while reducing microporosity, improved volumetric performance due to increased bulk density. The combination of densification with either cane molasses or plant-based polyphenol as binder, carbonization and chemical impregnation with KOH at 10 wt.% was identified as the optimum preparation sequence. Compared with commercial ACs, the sorbents thus prepared offered comparable or superior performance per unit mass, while being derived from more sustainable precursors.

Furthermore, mathematical modeling was employed to describe adsorption dynamics and evaluate mass transfer characteristics under various gas compositions. The models were validated experimentally and proved effective for system optimization and scaling-up.

However, regeneration studies revealed that full recovery of spent sorbents performance remains a challenge. Although partial restoration was possible thanks to high-temperature heat treatment at 500 °C under N_2 flow, followed by re-impregnation with KOH, the regenerated sorbents always performed worse than fresh materials, highlighting the inherent limitations of current regeneration approaches.

Despite the substantial progress made in this thesis, several avenues for future research remain open and critical:

1. Inclusion of water in the gas feed: a key aspect that must be addressed in future studies is the inclusion of water vapor in the feed gas during adsorption experiments. Water is inherently present in raw biogas and has been shown to influence H_2S separation performance significantly. Our experimental results showed that humidified activated carbons exhibited separation capacities up to three times higher than those of their dried counterparts, highlighting the catalytic or synergistic role of water in enhancing adsorption efficiency. Therefore, incorporating controlled humidity into test conditions is critical for accurately assessing adsorbent behavior and developing robust, efficient materials and processes in realistic biogas compositions.

2. Evaluation of densified activated carbon in pellet form: another important direction for future research is the evaluation of densified ACs in their actual pelletized form, without sieving them into powder fractions. While previous experiments used sieved materials to ensure uniformity and control in the adsorption column, real industrial applications rely on shaped adsorbents, such as pellets or extrudates, which directly influence packing density, pressure drop and mass transfer dynamics. Testing ACs in their final shape will enable a more accurate assessment of their adsorption performance and mechanical stability. To take account of these larger pellets, future experiments should use a wider adsorption column respecting the minimum height and diameter according to particle size, higher gas flow rates and larger diameter tubes to reproduce realistic operating conditions more effectively. This approach will also lead to a better understanding of the optimum adsorbent geometry and configuration for practical biogas purification systems.

3. Advanced regeneration techniques: the limited recovery of adsorption capacity observed in current regeneration methods highlights the need for more advanced and effective

regeneration strategies. Future work should investigate the use of higher-temperature thermal treatments, possibly above 500 °C, to better desorb strongly bound H_2S species and restore surface functionality. Additionally, the combination of thermal regeneration and chemical washing, using basic solutions, due to their ability to dissolve sulfur species, may help remove residual sulfur compounds and improve reusability. Another promising approach is the reactivation of spent sorbents with steam at 900 °C, enabling these often incineration-prone materials to be reused in industrial purification.

4. VOCs and siloxanes removal research: while this work has primarily focused on CO_2 and H_2S separation, future research should extend to the study of volatile organic compounds and siloxanes, which are also critical contaminants in biogas. ACs are widely employed on an industrial scale for the removal of these compounds, but further studies should aim to quantify the removal efficiency of different AC formulations, considering the influence of co-contaminants such as moisture, CO_2 and O_2. Modification of the current test bench used for dynamic H_2S adsorption could be used to include VOCs and siloxanes. Broadening the scope of investigation to include these trace contaminants will improve the applicability of biogas purification systems and contribute to a more integrated and effective upgrading process.

Annex 1. Complementary data for chapter 2

Axially dispersed plug flow equation:

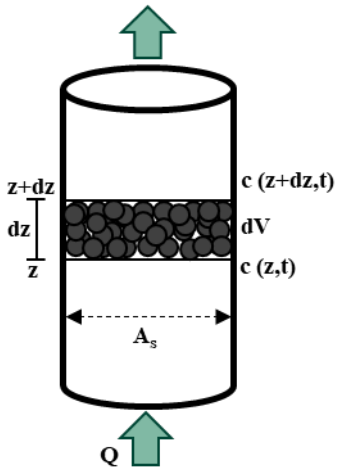

Figure A1.1 Control volume for axially dispersed plug flow model in adsorption columns.

Assumptions

1. Isothermal process
2. Constant physical properties of the gases
3. Constant interstitial velocity
4. Negligible radial and angular dispersion

Nomenclature

z: Column abscissa
V: Column volume (m^3)
c: Fluid phase concentration ($mol \cdot m^{-3}$)
q: Quantity adsorbed ($mol \cdot m^{-3}$)
t: Time (s)
A_s: Cross-sectional area (m^2)
ε: Bed porosity
$\dot{M}_{in}$: Mass inflow ($mol \cdot m^{-2} \cdot s^{-1}$)
$\dot{M}_{out}$: Mass outflow ($mol \cdot m^{-2} \cdot s^{-1}$)
Q: Flow rate ($m^3 \cdot s^{-1}$)
v: Interstitial velocity ($m \cdot s^{-1}$) = $Q \cdot \varepsilon / A_s$
M_{in}: Mass inlet (mol)
M_{out}: Mass outlet (mol)
M_a: Mass accumulation (mol)
D_L: Axial dispersion coefficient ($m^2 \cdot s^{-1}$)

Taylor expansion derivative

$$(z + dz, t) = c(z, t) + \frac{\partial c(z, t)}{\partial z} . dz$$

$$\frac{\partial c(z+dz,t)}{\partial z} = \frac{\partial c(z,t)}{\partial z} + \frac{\partial^2 c(z,t)}{\partial z^2}.dz$$

Mass balance in the adsorption column

- *Mass inflow:*

$$\dot{M_{in}} = \frac{Q}{A_s}.c(z,t) - \mathcal{E}.D_L.\frac{\partial c(z,t)}{\partial z}$$

$$\dot{M_{in}} = \mathcal{E}.v.c(z,t) - \mathcal{E}.D_L.\frac{\partial c(z,t)}{\partial z}$$

- *Mass inlet:*

$$M_{in} = \dot{M_{in}}.A_s.dt = \left(\mathcal{E}.v.c(z,t) - \mathcal{E}.D_L.\frac{\partial c(z,t)}{\partial z}\right).A_s.dt$$

- *Mass outflow:*

$$\dot{M_{out}} = \frac{Q}{A_s}.c(z+dz,t) - \mathcal{E}.D_L.\frac{\partial c(z+dz,t)}{\partial z}$$

$$\dot{M_{out}} = \mathcal{E}.v.\left(c(z,t) + \frac{\partial c(z,t)}{\partial z}.dz\right) - \mathcal{E}.D_L.\left(\frac{\partial c(z,t)}{\partial z} + \frac{\partial^2 c(z,t)}{\partial z^2}.dz\right)$$

- *Mass outlet:*

$$M_{out} = \dot{M_{out}}.A_s.dt$$

$$M_{out} = \mathcal{E}.v.A_s.dt.\left(c(z,t) + \frac{\partial c(z,t)}{\partial z}.dz\right) - \mathcal{E}.D_L.\left(\frac{\partial c(z,t)}{\partial z} + \frac{\partial^2 c(z,t)}{\partial z^2}.dz\right).A_s.dt$$

Accumulation in *dv*, between *z* and *z+dz*:

- *Mass accumulation:*

$$M_a = dV\left(\mathcal{E}.\frac{\partial c(z,t)}{\partial t} + (1-\mathcal{E}).\frac{\partial q(z,t)}{\partial t}\right).dt$$

$$M_a = A_s.dz.\left(\mathcal{E}.\frac{\partial c(z,t)}{\partial t} + (1-\mathcal{E}).\frac{\partial q(z,t)}{\partial t}\right).dt$$

- *Mass inlet – Mass outlet = Mass accumulation:*

$$\mathcal{E}.v.A_s.dt.\frac{\partial c(z,t)}{\partial z}.dz - \mathcal{E}.D_L.\frac{\partial^2 c(z,t)}{\partial z^2}.dz.A_s.dt$$

$$= A_s.dz.\left(\mathcal{E}.\frac{\partial c(z,t)}{\partial z} + (1-\mathcal{E}).\frac{\partial q(z,t)}{\partial z}\right).dt$$

$$\mathcal{E}.v.\frac{\partial c(z,t)}{\partial z} - \mathcal{E}.D_L.\frac{\partial^2 c(z,t)}{\partial z^2} = -\mathcal{E}.\frac{\partial c(z,t)}{\partial t} - (1-\mathcal{E}).\frac{\partial q(z,t)}{\partial t}$$

So, finally:

$$-D_L.\frac{\partial^2 c(z,t)}{\partial z^2} + v.\frac{\partial c(z,t)}{\partial z} + \frac{\partial c(z,t)}{\partial t} + \frac{(1-\mathcal{E})}{\mathcal{E}}.\frac{\partial q(z,t)}{\partial t} = 0$$

Annex 2. Complementary data for chapter 3

Determination of KOH impregnation solution concentration: example to obtain AC_850°C_3h impregnated at 10 wt.%

Data:

AC mass: 2.725 g
AC envelope density: 0.257 $g.cm^{-3}$
AC skeletal density: 2.113 $g.cm^{-3}$
KOH density: 2.120 $g.cm^{-3}$

Activated carbon porosity:

$$AC\ Porosity = \left(\frac{1}{0.257\ \frac{g}{cm^3}} - \frac{1}{2.113\ \frac{g}{cm^3}} \right) \times 2.725\ g = 9.313\ cm^3$$

Mass of KOH to impregnate the activated carbon with KOH at 10 wt.% on dry basis:

$$\%KOH = \frac{Mass\ of\ KOH}{Mass\ of\ KOH + Mass\ of AC}$$

$$\frac{10}{100} = \frac{Mass\ of\ KOH}{Mass\ of\ KOH + 2.725\ g}$$

$$Mass\ of\ KOH = 0.303\ g$$

The volume of the H_2O-KOH solution to be added should be equal to the pore volume of the activated carbon (9.313 cm^3).

Volume of KOH in the solution:

$$KOH\ volume = Mass\ of\ KOH \times \frac{1}{KOH\ density}$$

$$KOH\ volume = 0.303\ g \times \frac{1\ cm^3}{2.120\ g} = 0.143\ cm^3$$

Volume of H_2O in the solution:

$$H_2O\ volume = AC\ porosity - KOH\ volume$$

$$H_2O\ volume = 9.313\ cm^3 - 0.143\ cm^3 = 9.170\ cm^3$$

Determination of the H_2S separation equation from dynamic adsorption experiments

Nomenclature:

Q: Total gas flow rate ($mL \cdot min^{-1}$)
$C_{H_2S\ in}$: H_2S concentration in the inlet gas ($mg \cdot mL^{-1}$)
$C_{H_2S\ out}$: H_2S concentration in the outlet gas ($mg \cdot mL^{-1}$)
$C_{H_2S\ ads}$: H_2S adsorbed ($mg \cdot mL^{-1}$)
t_0: Initial time (min)
t_m: Final time (min)
q_{H_2S}: Amount of H_2S adsorbed (mg)

Mass balance on H_2S in the dynamic adsorption column (see **Figure A2.1a**):

$$Mass\ inlet - Mass\ outlet = Mass\ accumulation \tag{A2.1}$$

$$Q\ C_{H_2S\ in} - Q\ C_{H_2S\ out} = C_{H_2S\ ads} \tag{A2.2}$$

$$C_{H_2S\ ads} = Q\ (C_{H_2S\ in} - C_{H_2S\ out}) \tag{A2.3}$$

Since the amount of H_2S adsorbed varies continuously over time, the expression is integrated to account for the total accumulation throughout the process:

$$\int_{t_o}^{t_m} C_{H_2S\ ads}\ dt = \int_{t_o}^{t_m} Q\ (C_{H_2S\ in} - C_{H_2S\ out})\ dt \tag{A2.4}$$

The term $\int_{t_o}^{t_m} C_{H_2S\ ads}\ dt$ integrates the instantaneous accumulation rate over the duration of the adsorption run, which gives the total amount of H_2S adsorbed (q_{H_2S}):

$$q_{H_2S} = \int_{t_o}^{t_m} Q\ (C_{H_2S\ in} - C_{H_2S\ out})\ dt \tag{A2.5}$$

$$q_{H_2S} = Q \int_{t_o}^{t_m} (C_{H_2S\ in} - C_{H_2S\ out})\ dt \tag{A2.6}$$

Yet:

$$(C_{H_2S\ in} - C_{H_2S\ out}) = C_{H_2S\ in}\left(1 - \frac{C_{H_2S\ out}}{C_{H_2S\ in}}\right) \tag{A2.7}$$

Therefore:

$$q_{H_2S} = Q \int_{t_o}^{t_m} C_{H_2S\,in} \left(1 - \frac{C_{H_2S\,out}}{C_{H_2S\,in}}\right) dt \quad \text{(A2.8)}$$

$$q_{H_2S} = Q\, C_{H_2S\,in} \int_{t_o}^{t_m} \left(1 - \frac{C_{H_2S\,out}}{C_{H_2S\,in}}\right) dt \quad \text{(A2.9)}$$

The integral component of the equation is obtained from the breakthrough curve (**Figure A2.1b**) by plotting $1 - \frac{C_{H_2S\,out}}{C_{H_2S\,in}}$ vs time and calculating the area under this curve, as shown in **Figure A2.1c**.

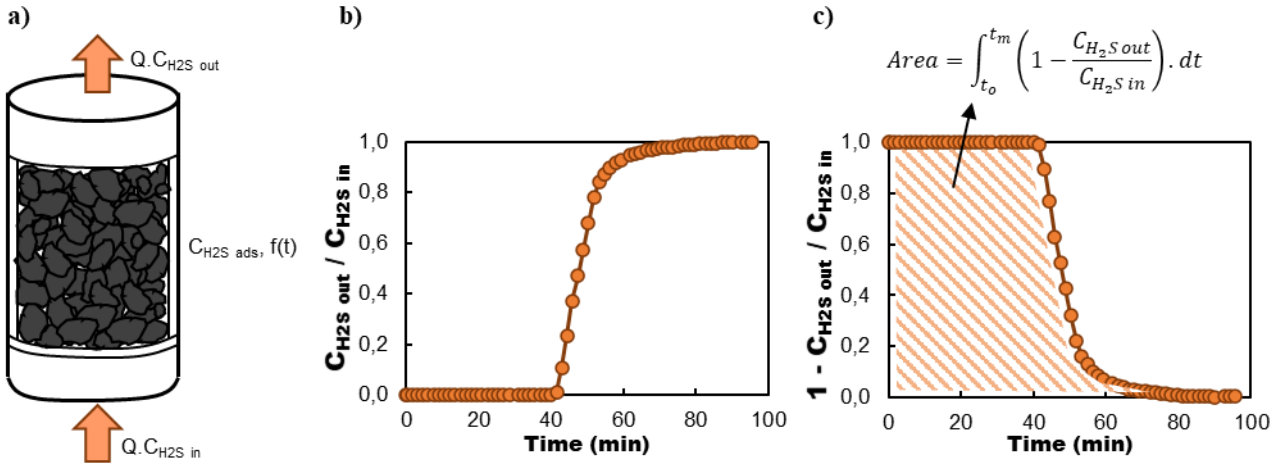

Figure A2.1 a) Packed bed system for mass balance of dynamic H_2S adsorption. b) Typical breakthrough curve of dynamic H_2S adsorption. c) Modification of the breakthrough curve for integral determination in Eq. (A2.9).

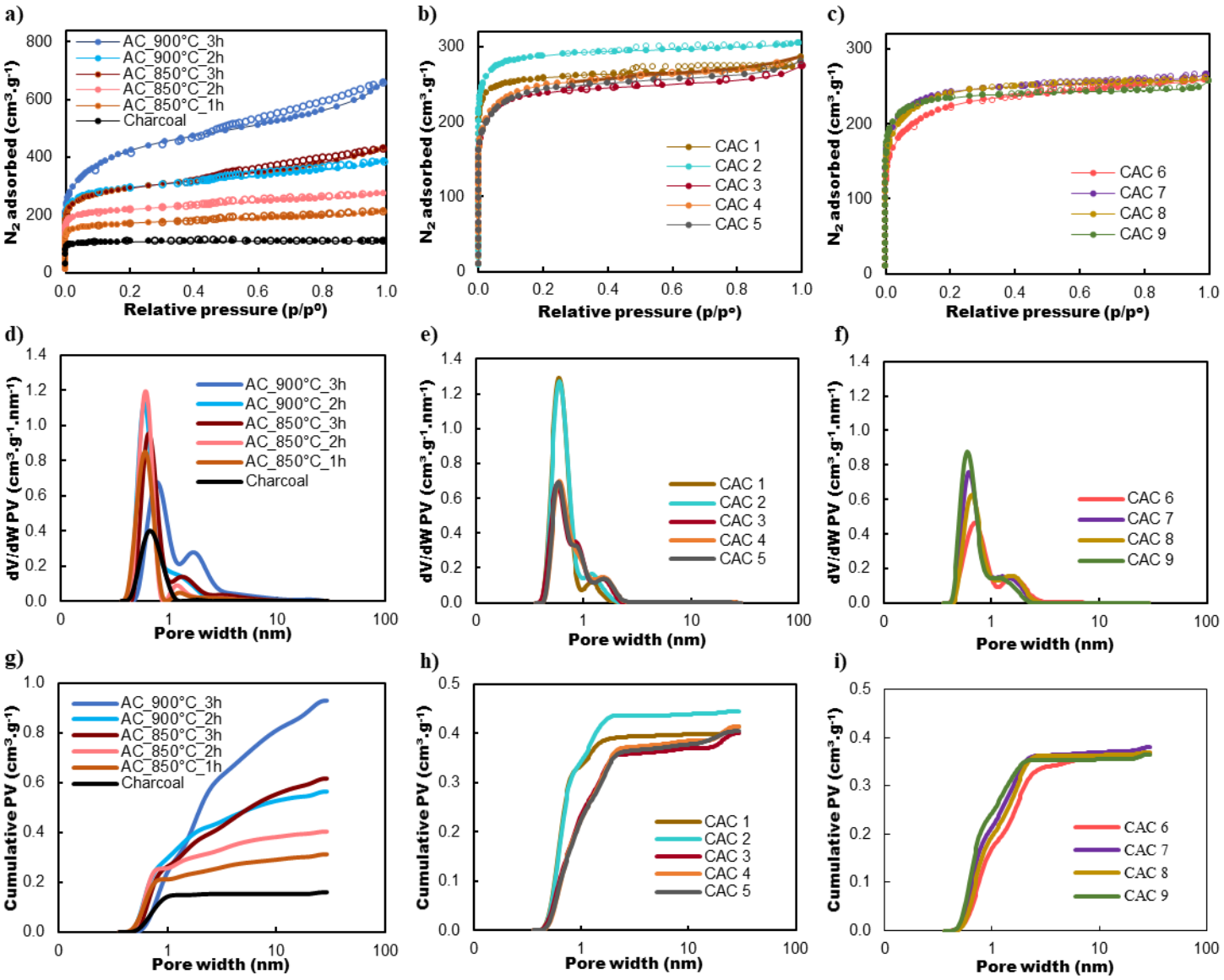

Figure A2.2 Nitrogen adsorption (solid symbols)-desorption (empty symbols) isotherms of a) pristine charcoal and charcoal-derived ACs, and b) and c) commercial ACs (CACs) after extensive washing, and corresponding pore size distributions (d, e and f) and cumulative pore volumes (g, h and i).

Table A2.1 Textural parameters of charcoal-derived ACs (as a function of activation time and temperature) and CACs and their pH and burn-offs.

Sample	BET, DR and V_{tot}			NLDFT					pH	Burn-off (%)
	A_{BET} ($m^2 \cdot g^{-1}$)	V_{DR} ($cm^3 \cdot g^{-1}$)	$V_{0.97}$ ($cm^3 \cdot g^{-1}$)	S_{NLDFT} ($m^2 \cdot g^{-1}$)	$V_{ultra-mic}$ ($cm^3 \cdot g^{-1}$)	$V_{<2nm}$ ($cm^3 \cdot g^{-1}$)	V_{mes} ($cm^3 \cdot g^{-1}$)	V_{tot} ($cm^3 \cdot g^{-1}$)		
Charcoal	400			428	0.08	0.15	0.01	0.16	9.3	-
AC_850°C_1h	655	0.26	0.33	785	0.18	0.24	0.07	0.31	10.2	31.0
AC_850°C_2h	840	0.33	0.43	967	0.22	0.31	0.10	0.41	10.4	47.0
AC_850°C_3h	1085	0.43	0.67	1045	0.17	0.38	0.24	0.62	10.8	62.1
AC_900°C_2h	1120	0.44	0.60	1166	0.22	0.41	0.15	0.56	10.4	52.3
AC_900°C_3h	1445	0.57	1.02	1181	0.08	0.50	0.43	0.93	10.5	73.9
CAC 1	1025	0.40	0.42	1177	0.26	0.39	0.02	0.41	10.2	-
CAC 2	1145	0.45	0.47	1235	0.26	0.44	0.01	0.45	9.0	-
CAC 3	925	0.36	0.41	900	0.14	0.35	0.05	0.40	9.7	-
CAC 4	940	0.37	0.43	885	0.14	0.36	0.06	0.41	7.4	-
CAC 5	920	0.36	0.43	876	0.13	0.35	0.05	0.40	9.4	-
CAC 6	830	0.31	0.40	705	0.08	0.30	0.07	0.37	8.1	-
CAC 7	920	0.36	0.41	855	0.14	0.35	0.03	0.38	8.9	-
CAC 8	885	0.38	0.40	785	0.11	0.34	0.03	0.37	9.0	-
CAC 9	900	0.36	0.38	920	0.17	0.35	0.02	0.37	9.1	-

A_{BET}: BET area
V_{DR}: Dubinin–Radushkevich micropore volume
$V_{0.97}$: Pore volume at relative pressure $P/P_o = 0.97$
S_{NLDFT}: Surface area from non-local density functional theory
$V_{ultra-mic}$: Ultramicropore volume (pore size < 0.7 nm)
$V_{<2nm}$: Micropore volume (pore size < 2 nm)
V_{mes}: Mesopore volume (2 < pore size < 50 nm)
V_{tot}: Total pore volume

Table A2.2 H_2S separation capacities of charcoal-derived activated charcoals.

H_2S concentration (ppm)	Sample	Mass (g)	H_2S separated at BTP. C/C_o 40 ppm		H_2S separated at saturation	
			($mg \cdot g^{-1}$)	($mg \cdot cm^{-3}$)	($mg \cdot g^{-1}$)	($mg \cdot cm^{-3}$)
400	Pristine charcoal	1.57	0.92	0.31	1.47	0.49
	AC_850°C_1H	1.42	1.46	0.45	2.05	0.63
	AC_850°C_2H	1.37	2.12	0.62	2.64	0.78
	AC_850°C_3H	1.13	3.11	0.76	3.44	0.84
	AC_900°C_2H	1.16	2.97	0.74	3.28	0.82
	AC_900°C_3H	1.06	3.19	0.72	3.60	0.82
4000	Pristine charcoal	1.55	1.94	0.42	4.01	1.33
	AC_850°C_1H	1.50	2.37	0.76	4.15	1.34
	AC_850°C_2H	1.35	3.29	0.95	5.66	1.64
	AC_850°C_3H	1.14	5.55	1.36	7.05	1.73
	AC_900°C_2H	1.19	5.26	1.34	7.46	1.90
	AC_900°C_3H	0.94	5.23	1.06	7.37	1.49

Table A2.3 H_2S (400 ppm) separation performance of KOH-impregnated activated carbons at breakthrough point (BTP: C/C_0 = 10%) and at saturation.

Sample	Mass (g)	H_2S separated at BTP. C/C_0 10%		H_2S separated at saturation	
		($mg \cdot g^{-1}$)	($mg \cdot cm^{-3}$)	($mg \cdot g^{-1}$)	($mg \cdot cm^{-3}$)
AC_900°C_3H_KOH 5%	1.18	5.71	1.45	6.40	1.63
AC_900°C_3H_KOH 10%	1.15	6.70	1.80	7.49	2.01
AC_900°C_3H_KOH 20%	1.36	6.08	2.08	7.14	2.44
AC_900°C_3H_KOH 30%	1.48	6.31	2.01	7.04	2.24
AC_850°C_3H_KOH 5%	1.33	5.84	1.67	6.42	1.84
AC_850°C_3H_KOH 10%	1.57	6.82	2.22	7.91	2.58
AC_850°C_3H_KOH 20%	1.66	6.51	2.32	7.31	2.60
AC_850°C_3H_KOH 30%	1.59	6.31	2.16	7.40	2.53
AC_850°C_2H_KOH 5%	1.47	5.20	1.64	6.28	1.97
AC_850°C_2H_KOH 10%	1.58	6.04	2.05	6.92	2.35
AC_850°C_2H_KOH 20%	1.58	5.61	1.90	6.86	2.33
AC_850°C_2H_KOH 30%	1.73	5.45	2.02	6.47	2.40

Table A2.4 Same as Table A1.3, but for KI-impregnated activated carbons.

Sample	Mass (g)	H_2S separated at BTP. C/C_0 10%		H_2S separated at saturation	
		($mg \cdot g^{-1}$)	($mg \cdot cm^{-3}$)	($mg \cdot g^{-1}$)	($mg \cdot cm^{-3}$)
AC_900°C_3H_KI 5%	1.12	5.53	1.33	6.05	1.45
AC_900°C_3H_KI 10%	1.19	6.19	1.59	7.46	1.91
AC_900°C_3H_KI 20%	1.32	6.21	1.76	7.07	2.01
AC_900°C_3H_KI 30%	1.53	5.10	1.68	5.74	1.89
AC_850°C_3H_KI 5%	1.22	5.18	1.36	5.70	1.49
AC_850°C_3H_KI 10%	1.31	5.66	1.60	6.74	1.90
AC_850°C_3H_KI 20%	1.43	6.05	1.86	7.16	2.20
AC_850°C_3H_KI 30%	1.49	6.10	1.96	7.08	2.27
AC_850°C_2H_KI 5%	1.32	4.04	1.14	5.85	1.66
AC_850°C_2H_KI 10%	1.28	5.41	1.49	6.50	1.78
AC_850°C_2H_KI 20%	1.49	4.44	1.42	5.72	1.84
AC_850°C_2H_KI 30%	1.51	4.99	1.62	6.26	2.03

Table A2.5 Same as Table A2.3, but for K_2CO_3-impregnated activated carbons.

Sample	Mass (g)	H_2S separated at BTP. C/C_0 10%		H_2S separated at saturation	
		($mg \cdot g^{-1}$)	($mg \cdot cm^{-3}$)	($mg \cdot g^{-1}$)	($mg \cdot cm^{-3}$)
AC_900°C_3H_K_2CO_3 5%	1.15	5.26	1.30	5.84	1.45
AC_900°C_3H_K_2CO_3 10%	1.16	6.45	1.61	6.90	1.72
AC_900°C_3H_K_2CO_3 20%	1.31	5.77	1.62	6.23	1.75
AC_900°C_3H_K_2CO_3 30%	1.44	5.67	1.76	6.65	2.06
AC_850°C_3H_K_2CO_3 5%	1.20	4.94	1.27	5.54	1.43
AC_850°C_3H_K_2CO_3 10%	1.29	6.17	1.71	6.96	1.93
AC_850°C_3H_K_2CO_3 20%	1.48	5.58	1.78	6.60	2.10
AC_850°C_3H_K_2CO_3 30%	1.60	4.62	1.48	5.74	1.84
AC_850°C_2H_K_2CO_3 5%	1.44	3.97	1.25	4.95	1.56
AC_850°C_2H_K_2CO_3 10%	1.35	4.92	1.42	5.71	1.65
AC_850°C_2H_K_2CO_3 20%	1.51	4.96	1.61	5.87	1.91
AC_850°C_2H_K_2CO_3 30%	1.49	3.62	1.16	4.51	1.44

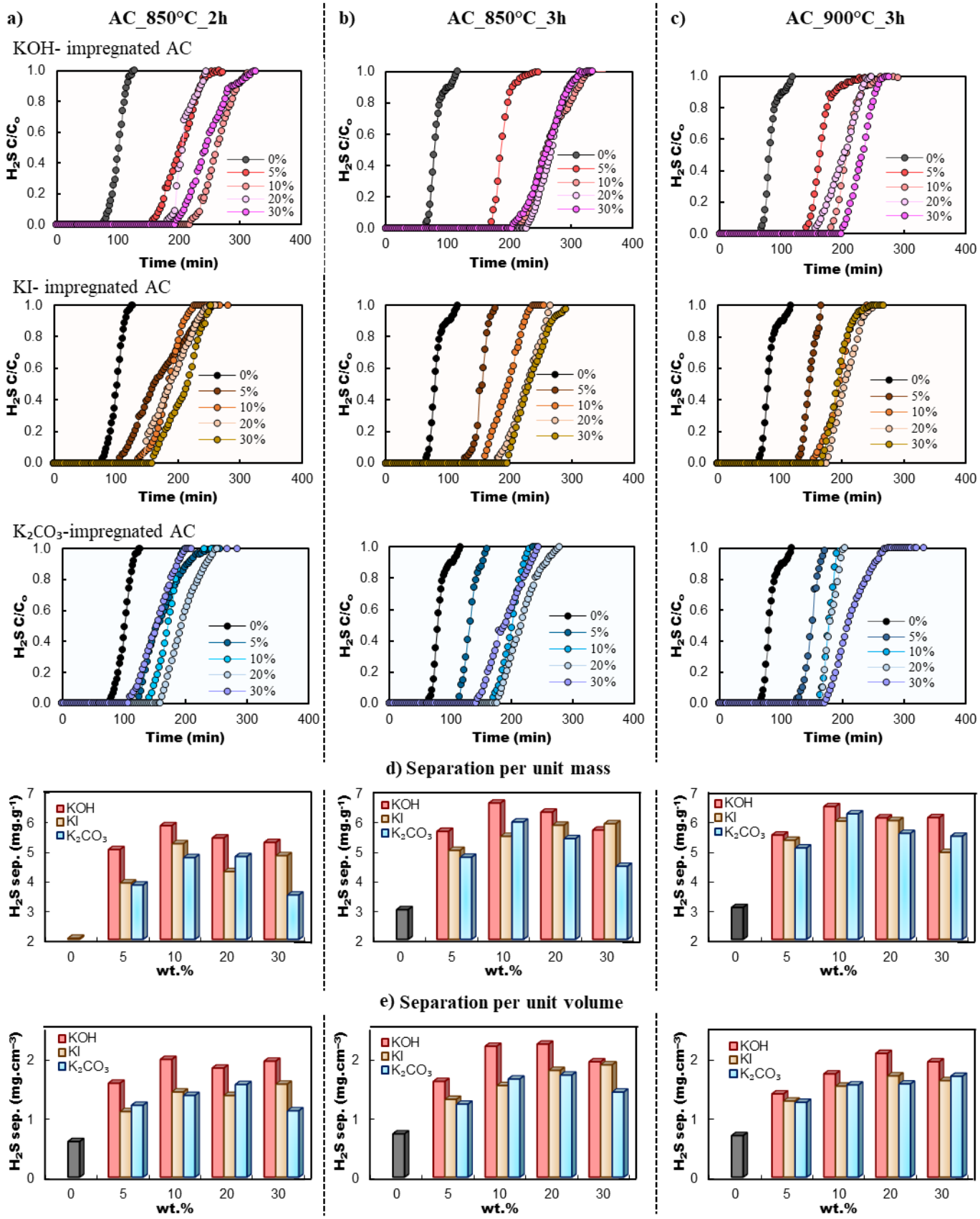
a) AC_850°C_2h
b) AC_850°C_3h
c) AC_900°C_3h
KOH- impregnated AC
KI- impregnated AC
K2CO3-impregnated AC
H2S C/Co
Time (min)
0%
5%
10%
20%
30%
d) Separation per unit mass
e) Separation per unit volume
H2S sep. (mg.g-1)
H2S sep. (mg.cm-3)
KOH
KI
K2CO3
wt.%

Figure A2.3 Effect of impregnating agent and impregnation ratio on H_2S (400 ppm) adsorption by a) AC_850°C_2h, b) AC_850°C_3h and c) AC_900°C_3h, and their separation capacities at BTP expressed per d) unit mass and e) unit volume

Table A2.6 H_2S (400 ppm) separated by AC_850°C_3H impregnated with 10 wt.% KOH under different humidification conditions, at breakthrough point (BTP: C/C_0 = 10%) and at saturation.

Sample	Mass (g)	H_2O adsorbed (wt.%)	H_2S separated at BTP. C/C_0 10%		H_2S separated at saturation	
			($mg \cdot g^{-1}$)	($mg \cdot cm^{-3}$)	($mg \cdot g^{-1}$)	($mg \cdot cm^{-3}$)
AC_850°C_3H_KOH10_RH_10%	1.24	4.21	5.35	1.42	6.86	1.82
AC_850°C_3H_ KOH10_RH_30%	1.33	11.88	6.04	1.72	7.68	2.19
AC_850°C_3H_ KOH10_RH_50%	1.51	22.18	6.82	2.22	7.91	2.58
AC_850°C_3H_ KOH10_RH_70%	1.56	26.85	7.15	2.39	8.12	2.72
AC_850°C_3H_ KOH10_RH_90%	1.70	31.51	7.07	2.58	8.08	2.95

Table A2.7 H_2S (4000 ppm) separation capacities of charcoal and its derived (non-impregnated) activated carbons at BTP (40 ppm), in the presence of O_2.

Sample	Mass (g)	H_2S separated at BTP, C/C_0 1%	
		($mg \cdot g^{-1}$)	($mg \cdot cm^{-3}$)
Charcoal	1.80	13.41	5.19
AC_850°C_1H	1.59	22.29	7.59
AC_850°C_2H	1.38	37.55	11.09
AC_850°C_3H	1.25	47.22	12.74
AC_900°C_2H	1.23	46.70	12.53
AC_900°C_3H	1.07	47.32	10.86

Table A2.8 H_2S (400 ppm concentration) separation capacities of commercial and our best charcoal-derived activated carbons for biogas desulfurization.

Sample	Mass (g)	H_2S separated at BTP. C/C_0 10%		H_2S separated at saturation	
		($mg \cdot g^{-1}$)	($mg \cdot cm^{-3}$)	($mg \cdot g^{-1}$)	($mg \cdot cm^{-3}$)
AC Com. 1	2.34	5.59	2.23	7.53	3.01
AC Com. 2	3.20	6.87	4.72	8.14	5.59
AC Com. 3	2.59	4.46	2.48	5.14	2.86
AC Com. 4	2.41	2.84	1.47	4.66	2.41
AC Com. 5	2.59	3.73	2.07	5.05	2.81
AC Com. 6	3.62	4.93	3.83	6.01	4.67
AC Com. 7	3.30	7.06	5.00	9.20	6.52
AC Com. 8	3.30	6.90	4.88	8.62	6.10
AC Com. 9	3.37	7.85	5.68	9.62	6.97
AC_850°C_3h_KOH 10	1.37	6.82	2.22	7.91	2.58

Table A2.9 Same as Table A1.8, but for an H_2S concentration of 4000 ppm.

Sample	Mass (g)	H_2S separated at BTP. C/C_0 1%		H_2S separated at saturation	
		($mg \cdot g^{-1}$)	($mg \cdot cm^{-3}$)	($mg \cdot g^{-1}$)	($mg \cdot cm^{-3}$)
AC Com. 1	2.41	6.51	3.37	8.74	4.53
AC Com. 2	3.20	8.73	6.01	12.05	8.29
AC Com. 3	2.60	6.77	3.79	8.38	4.68
AC Com. 4	2.72	8.21	4.80	12.62	7.38
AC Com. 5	2.80	8.92	5.35	10.54	6.33
AC Com. 6	3.51	5.60	4.22	9.76	7.35
AC Com. 7	3.56	9.69	7.41	12.43	9.50
AC Com. 8	3.28	9.18	6.46	12.85	9.05
AC Com. 9	3.33	9.58	6.85	12.30	8.79
AC_850°C_3h_KOH 10	1.40	8.36	2.41	10.27	2.96

Table A2.10 H_2S separation capacities at saturation under different H_2S concentrations for isotherm curve determination at 25°C for three different conditions of activated carbon.

	AC_850°C_3h		AC_850°C_3h_KOH 10		AC_850°C_3h_ KOH 10 - O_2 1.1%	
H_2S concentration (ppm)	Mass (g)	H_2S separated at saturation ($mg \cdot g^{-1}$)	Mass (g)	H_2S separated at saturation ($mg \cdot g^{-1}$)	Mass (g)	H_2S separated at saturation ($mg \cdot g^{-1}$)
100	1.18	1.64	1.25	3.95	-	-
400	1.13	3.44	1.52	7.91	1.41	68.86
700	1.21	4.87	1.39	8.94	-	-
1000	1.18	5.65	1.31	9.84	1.25	114.27
2000	1.17	6.50	1.53	10.97	1.20	161.07
3000	1.27	7.73	1.45	10.96	1.30	177.14
4000	1.14	7.30	1.34	10.62	1.47	185.13

Table A2.11 Equilibrium constants of the Langmuir isotherm.

Sample	q_s ($mol \cdot kg^{-1}$ - $mg \cdot g^{-1}$)	b ($m^3 \cdot mol^{-1}$)	R^2
AC_850°C_3h	0.25 - 8.5	65.8	0.96
AC_850°C_3h_KOH 10	0.34 - 11.6	200.7	0.96
AC_850°C_3h_KOH 10 - O_2 1.1%	6.50 - 221.5	37.5	0.97

Annex 3. Complementary data for chapter 4

Table A3.1 Proximate and elemental analysis of molasses and plant-based polyphenol for activated carbon pellet fabrication.

Binders	Proximate analysis (wt.%)				Elemental analysis (wt.%)				
	Humidity	Volatile matter	Ash	Fixed carbon	O	C	H	N	S
Cane 1	25.4	33.9	8.2	57.9	52.2	29.2	7.2	0.8	0.6
Cane 2	26.3	31.5	9.4	59.1	50.2	29.2	6.6	1.0	1.1
Beet	15.6	49.8	6.3	43.9	53.0	30.3	7.4	1.3	0.3
Polyphenols	6.4	45.3	1.4	53.3	39.5	55.3	5.0	0.2	0.0

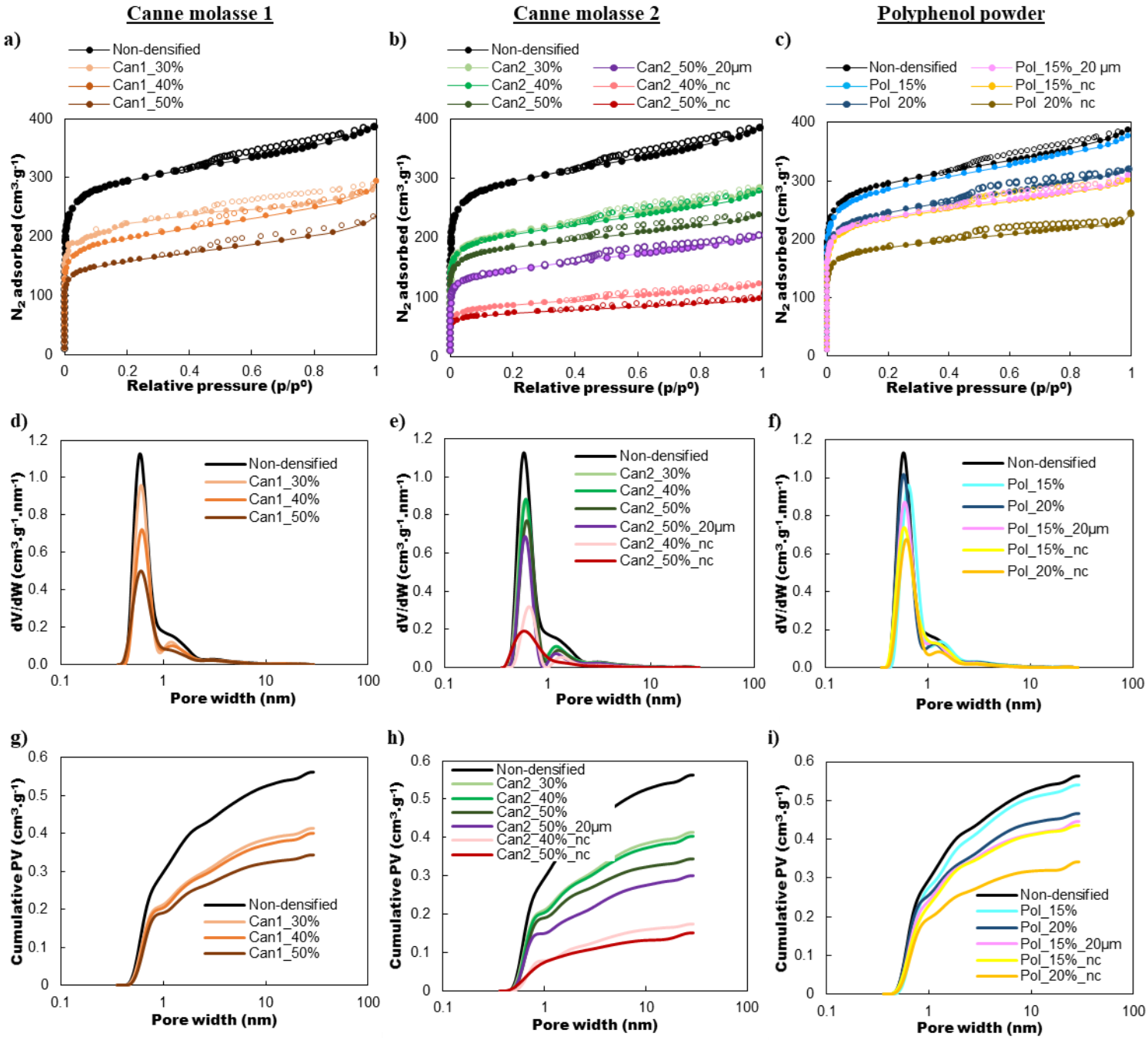

Figure A3.1 Nitrogen adsorption-desorption isotherms for: (a) Cane1-based ACs, (b) Cane2-based ACs and (c) Polyphenol-based ACs. Pore size distribution for (d) Cane1-based ACs, (e) Cane2-based ACs and (f) Polyphenol-based ACs. Cumulative pore volume distribution for (g) Cane1-based ACs, (h) Cane2-based ACs and (i) Polyphenol-based ACs.

dV: Differential pore volume
dW: Differential pore width
PV: Pore volume

Table A3.2 Textural parameters of densified activated carbons as a function of binder type and content (wt.%).

Sample	BET, DR and V_{tot}			NLDFT				
	A_{BET} ($m^2 \cdot g^{-1}$)	V_{mic} D-R ($cm^3 \cdot g^{-1}$)	$V_{0.97}$ ($cm^3 \cdot g^{-1}$)	S_{NLDFT} ($m^2 \cdot g^{-1}$)	$V_{ultra\text{-}mic}$ ($cm^3 \cdot g^{-1}$)	$V_{<2nm}$ ($cm^3 \cdot g^{-1}$)	V_{mes} ($cm^3 \cdot g^{-1}$)	V_{tot} ($cm^3 \cdot g^{-1}$)
BORDET AC ND	1120	0.44	0.60	1166	0.22	0.41	0.15	0.56
Can 1_30%	845	0.33	0.44	895	0.18	0.31	0.11	0.42
Can 1_40%	745	0.29	0.43	759	0.14	0.26	0.15	0.42
Can 1_50%	595	0.24	0.35	621	0.11	0.21	0.13	0.34
Can 2_30%	790	0.31	0.44	840	0.17	0.28	0.13	0.41
Can 2_40%	780	0.31	0.43	806	0.16	0.28	0.12	0.40
Can 2_50%	700	0.28	0.37	723	0.14	0.25	0.09	0.34
Can 2_50%_20µm	550	0.21	0.32	598	0.13	0.20	0.10	0.30
Can 2_40%_nc	325	0.13	0.19	313	0.05	0.11	0.06	0.18
Can 2_50%_nc	280	0.11	0.15	291	0.05	0.10	0.05	0.15
Pol_10%	1012	0.40	0.55	1065	0.20	0.37	0.16	0.52
Pol_15%	1075	0.42	0.58	1032	0.16	0.38	0.16	0.54
Pol_15%_20µm	910	0.36	0.48	933	0.17	0.33	0.12	0.45
Pol_20%	930	0.37	0.50	1006	0.20	0.34	0.13	0.47
Pol_10%_nc	800	0.31	0.41	840	0.17	0.29	0.09	0.38
Pol_15%_nc	895	0.35	0.47	904	0.15	0.33	0.11	0.44
Pol_20%_nc	710	0.28	0.35	728	0.13	0.26	0.08	0.34

ND: non densified
nc: non carbonized
A_{BET}: BET area
V_{DR}: Dubinin–Radushkevich micropore volume
$V_{0.97}$: Pore volume at relative pressure $P/P_0 = 0.97$
S_{NLDFT}: Surface area from non-local density functional theory
$V_{ultra\text{-}mic}$: Ultramicropore volume (pore size < 0.7 nm)
$V_{<2nm}$: Micropore volume (pore size < 2 nm)
V_{mes}: Mesopore volume (2 < pore size < 50 nm)
V_{tot}: Total pore volume

Table A3.3 H_2S (400 ppm) separation capacities of densified activated carbons.

Sample	Mass (g)	H_2S separated at BTP. C/C_0 40 ppm		H_2S separated at saturation	
		($mg \cdot g^{-1}$)	($mg \cdot cm^{-3}$)	($mg \cdot g^{-1}$)	($mg \cdot cm^{-3}$)
BORDET AC ND	1,16	2.97	0.74	3.28	0.82
Can1_30%	1,99	3.87	1.65	4.42	1.89
Can1_40%	1,98	3.66	1.56	4.13	1.76
Can1_50%	2,02	3.65	1.59	3.97	1.73
Can2_40%_nc	2,54	1.36	0.74	2.15	1.17
Can2_50%_nc	2,75	0.82	0.49	1.42	0.84
Can2_30%	2,01	4.97	2.14	5.42	2.34
Can2_40%	2,10	4.65	2.10	5.10	2.30
Can2_50%	2,03	4.17	1.82	4.67	1.73
Beet_50%	2.08	4.43	1.98	4.94	2.21
Pol_10%_nc	1,90	1.95	0.80	2.38	0.97
Pol_20%_nc	1,84	1.78	0.71	2.69	1.07
Pol_10%	1,81	2.53	0.98	3.11	1.21
Pol_20%	1,81	2.56	0.99	3.07	1.19

Table A3.4 Skeletal and grain densities of densified activated carbons for chemical impregnation.

Sample	Skeletal density ($g.cm^{-3}$)	Grain density ($g.cm^{-3}$)
Pol_15%	2.0119	0.5277
Pol_15%_nc	2.0009	0.5634
Can2_50%	1.9363	0.7003

Table A3.5 H_2S (4000 ppm) separation capacities of impregnated densified activated carbons.

Sample	Mass (g)	H_2S separated at BTP. C/C_o 40 ppm		H_2S separated at saturation	
		($mg \cdot g^{-1}$)	($mg \cdot cm^{-3}$)	($mg \cdot g^{-1}$)	($mg \cdot cm^{-3}$)
		Method 1			
Pol_15%_nc	2.01	3.65	1.58	4.97	2.15
Pol_15%_nc_KOH 5%	1.95	5.35	2.24	6.85	2.87
Pol_15%_nc_KOH 10%	2.20	6.33	2.99	8.32	3.93
Pol_15%_nc_KOH 15%	2.37	5.76	2.94	8.05	4.10
Pol_15%	1.88	5.06	2.04	6.45	2.61
Pol_15%_KOH 5%	2.00	6.68	2.87	8.03	3.45
Pol_15%	2.19	8.74	4.10	11.57	5.43
Pol_15%_KOH 15%	1.97	7.49	3.17	9.34	3.95
Can2_50%	2.28	5.91	2.89	7.19	3.52
Can2_50%_KOH 5%	2.21	7.14	3.39	9.02	4.29
Can2_50%_KOH 10%	2.29	8.75	4.30	9.88	4.86
Can2_50%_KOH 15%	2.52	7.40	4.00	8.83	4.77
		Method 2			
Pol_15%_nc	2.01	3.65	1.58	4.97	2.15
Pol_15%_nc_KOH 5%	2.12	5.23	2.38	7.97	3.63
Pol_15%_nc_KOH 10%	2.17	7.24	3.38	8.57	3.99
Pol_15%_nc_KOH 15%	2.34	6.28	3.16	9.01	4.53
Pol_15%	1.88	5.06	2.04	6.45	2.61
Pol_15%_KOH 5%	1.93	6.46	2.67	7.20	2.98
Pol_15%	2.01	8.82	3.81	11.21	4.84
Pol_15%_KOH 15%	2.13	7.71	3.53	9.12	4.17
Can2_50%	2.28	5.91	2.89	7.19	3.52
Can2_50%_KOH 5%	2.19	6.98	3.29	8.90	4.19
Can2_50%_KOH 10%	2.22	8.62	4.11	9.31	4.44
Can2_50%_KOH 15%	2.28	7.39	3.61	9.56	4.67

NI: Non-impregnated, but densified.

Table A3.6 H_2S (4000 ppm) separation capacities of impregnated (KOH) densified activated carbons.

Sample	Mass (g)	H_2S separated at BTP. C/C_0 40 ppm		H_2S separated at saturation	
		($mg \cdot g^{-1}$)	($mg \cdot cm^{-3}$)	($mg \cdot g^{-1}$)	($mg \cdot cm^{-3}$)
		Method 1			
Pol_15%_nc	2.01	3.65	1.58	4.97	2.15
Pol_15%_nc_KOH 5%	1.95	5.35	2.24	6.85	2.87
Pol_15%_nc_KOH 10%	2.20	6.33	2.99	8.32	3.93
Pol_15%_nc_KOH 15%	2.37	5.76	2.94	8.05	4.10
Pol_15%	1.88	5.06	2.04	6.45	2.61
Pol_15%_KOH 5%	2.00	6.68	2.87	8.03	3.45
Pol_15%_KOH 10%	2.19	8.74	4.10	11.57	5.43
Pol_15%_KOH 15%	1.97	7.49	3.17	9.34	3.95
Can2_50%	2.28	5.91	2.89	7.19	3.52
Can2_50%_KOH 5%	2.21	7.14	3.39	9.02	4.29
Can2_50%_KOH 10%	2.29	8.75	4.30	9.88	4.86
Can2_50%_KOH 15%	2.52	7.40	4.00	8.83	4.77
		Method 2			
Pol_15%_nc	2.01	3.65	1.58	4.97	2.15
Pol_15%_nc_KOH 5%	2.12	5.23	2.38	7.97	3.63
Pol_15%_nc_KOH 10%	2.17	7.24	3.38	8.57	3.99
Pol_15%_nc_KOH 15%	2.34	6.28	3.16	9.01	4.53
Pol_15%	1.88	5.06	2.04	6.45	2.61
Pol_15%_KOH 5%	1.93	6.46	2.67	7.20	2.98
Pol_15%_KOH 10%	2.01	8.82	3.81	11.21	4.84
Pol_15%_KOH 15%	2.13	7.71	3.53	9.12	4.17
Can2_50%	2.28	5.91	2.89	7.19	3.52
Can2_50%_KOH 5%	2.19	6.98	3.29	8.90	4.19
Can2_50%_KOH 10%	2.22	8.62	4.11	9.31	4.44
Can2_50%_KOH 15%	2.28	7.39	3.61	9.56	4.67

Annex 4. List of figures and tables

List of figures

Résumé de la thèse

Figure 1. Production de biométhane. 4
Figure 2. Sélectivité CO_2/CH_4 à l'équilibre, comparée pour différents adsorbants, à une composition gazeuse de 35 % CO_2 et 65 % CH_4 (en volume), sous 1 bar et à température ambiante. 4

Figure 3. Capacité d'adsorption de H_2S rapportée dans la littérature en utilisant des mélanges gaz inerte-H_2S. 5

Figure 4. a) Courbes de percée de H_2S, et capacités de séparation des charbons actifs commerciaux et du charbon actif dérivé de bois (850°C_3h_KOH 10) : b) par unité de masse, et c) par unité de volume. - Gaz analysé : N_2 60%, O_2 1,1%, H_2S 4000 ppm et équilibré avec CO_2. 6

Figure 5. a) Courbes de percée d'adsorption de H_2S, et capacités de séparation des charbons actifs commerciaux et du charbon actif dérivé de bois densifié avec des polyphénols (Pol_15%_KOH 10) et de mélasse de cane à sucre (Can_50%_KOH 10) : b) par unité de masse, et c) par unité de volume. - Gaz analysé : N_2 60%, O_2 1,1%, H_2S 4000 ppm et équilibré avec CO_2. 7

Figure 6. Profils de concentration dans une colonne d'adsorption à différentes concentrations d'entrée de H_2S pour le charbon actif développé densifié avec des polyphénols ajouté à 15 % en masse, et imprégné de KOH à 10 % en masse - Gaz analysé : N_2 60%, O2 1,1%, H_2S 4000 ppm et équilibré avec CO_2. 7

Chapter 1

Figure 1.1 Current[3] and potential production in 2030 and 2050[4] of biomethane per country from anaerobic digestion in Europe, expressed in billion cubic meters (bcm). NB: the natural gas consumption in the UE in 2020 was 400 bcm.[4] 15

Figure 1.2 Biomethane production and its applications. 18

Figure 1.3 Schematic diagrams of biogas upgrading methods: a) water scrubbing; b) chemical scrubbing (amine scrubbing); c) cryogenic distillation; d) membrane separation; e) pressure swing adsorption. 19

Figure 1.4 Efficient H_2S abatement technology according to the amount of H_2S and biogas in SCFM (standard cubic feet per minute).[38] 22

Figure 1.5 Conventional technologies for H_2S removal: a) absorption; b) adsorption in a column filter; c) membrane separation; d) biofilter: e) bioscrubber; f) biotrickling filter. 25

Figure 1.6 Reaction mechanisms for H_2S separation in activated carbons. The role of the impregnating agent is not shown. 36

Figure 1.7 Impregnated activated carbon. 38

Figure 1.8 Front view of the main pores of selected zeolites. The three-letter codes above each image are the official structure names from the International Zeolite Association, with common names in parentheses. 46

Chapter 2

Figure 2.1 Sequence steps for: a) basic Skarstrom PSA cycle; and b) EPSA cycle. *Product/PR*: pressurization with product; *ADS*: adsorption; *BD*: blowdown; *PG*: purge; *Intermediate DP*: intermediate depressurization; *DPE*: Depressurization pressure equalization; *PPE*: pressurization pressure equalization; *IDEL*: standby. 75

Figure 2.2 Comparison of CO_2/CH_4 equilibrium selectivity and PSA working capacity ratio for various adsorbents at a gas composition of CO_2 = vol. 35% and CH_4 = vol. 65%. a) Selectivity at 5 bar, b) PSA working capacity ratio at: P_a = 5 bar, P_d = 1bar. c) Selectivity at 1 bar, d) PSA working capacity ratio at: P_a =1 bar, P_d = 0.2bar. 82

Figure 2.3 1-z (1-Compressibility factor) for CO_2 and CH_4 as a function of temperature and pressure. 87

Figure 2.4 Purity, recovery, productivity and energy consumption plots for CO_2/CH_4 separation by EVSA and VSA: a) EVSA cycle, b) VSA cycle – Full symbols represent productivity and empty symbols represent energy consumption - ●: 2-bed Zeolite[42, 43, 54, 55] - ■: 2-bed CMS[54, 79] - ▲: 3-bed + 1tank CMS[81] - ●: 4-bed Zeolite [83] - ◆: 2-bed Zeolite + CMS[57] – ▼: 4-bed MOF + CO_2 production.[60] - ►: 6-bed CMS [84] - ▌Best PSA-adsorbent configuration. 95

Figure 2.5 Partition coefficient equation and typical breakthrough curve for dynamic H_2S adsorption. 99

Figure 2.6 Studies on H_2S removal from a gas mixture comprising CH_4, CO_2 and H_2S. a) H_2S adsorption capacity; b) Surface area of the sorbents presented in a). (See Tables 1.6 to 1.9 for reference). 102

Figure 2.7 Studies on H_2S removal from a gas mixture comprising air, H_2S and moisture. H_2S adsorption capacity for an H_2S inlet concentration of: a) 10000 ppm and a breakthrough point of 0.5% C/C_o, and b) between 500 and 3000 ppm at a breakthrough point of 1-17% C/C_o. H_2S adsorption capacity as a function of surface area for the materials shown: c) in Figure 2.7a, and d) in Figure 2.7b (See Tables 1.6 to 1.10 for reference). 105

Figure 2.8 Studies on H_2S removal from a gas mixture comprising an inert gas and H_2S. H_2S adsorption capacity at concentrations: a) between 100 to 2000 ppm, and b) of less than 100 ppm; H_2S adsorption capacity as a function of surface area for the materials shown: c) in Figure 2.8a, and d) in Figure 2.8b (See Tables 1.6 to 1.9 for reference). 107

Figure 2.9 1-*z* (*z* being the compressibility factor) for H_2S as a function of temperature and pressure. 115

Figure 2.10 H_2S separation capacity after each regeneration cycle and corresponding degradation of the separation capacity: a) Carbon-based materials; b) Zeolites and MOFs.. 119

Chapter 3

Figure 3.1 a) Experimental test bench for dynamic H_2S adsorption. MFC: mass flow controller; MFM: mass flow meter; GC: gas chromatograph. b) BET area and bulk density of lab-made wood-derived ACs and commercial ACs (CACs) for biogas desulfurization investigated here

(tables), as well as pore volume and bulk density vs BET area of ACs (solid discs) and CACs (crosses). 146

Figure 3.2 Breakthrough curves for dynamic H_2S adsorption in wood charcoal and non-impregnated wood-derived ACs at H_2S concentrations of a) 400 ppm and b) 4000 ppm. H_2S separation capacities at BTP expressed per c) unit mass and d) unit volume of AC, and as a function of micropore volume per e) unit mass and f) unit volume of AC. 151

Figure 3.3 Effect of impregnating agent and impregnation ratio on H_2S (400 ppm) adsorption by AC_850C_3h impregnated with: a) KOH b) KI and c) K_2CO_3, and separation capacities at BTP expressed per d) unit mass and e) unit volume. 153

Figure 3.4 Humidified and dried ACs for H_2S (400 ppm) separation: a) breakthrough curves, and separation capacity per b) unit mass and c) unit volume. Effect of humidity on H_2S (400 ppm) separation of AC_850°C_3h impregnated with 10 wt.% KOH: d) breakthrough curves, and separation capacity per e) unit mass and f) unit volume. 155

Figure 3.5 Effect of O_2 on H_2S (4000 ppm) separation performance of wood-derived (non-impregnated) ACs: a) breakthrough curves, and separation capacities per b)unit mass and c) unit volume. Effect of O_2 on H_2S (4000 ppm) separation of AC_850°C_3g impregnated at 10 wt.%: d) breakthrough curves, , and separation capacities per e) unit mass and f) unit volume. 157

Figure 3.6 H_2S breakthrough curves and separation capacities of commercial ACs and wood-derived AC_850°C_3h_KOH 10, using: a) 400 ppm H_2S, b) 4000 ppm H_2S, and c) 4000 ppm H_2S in the presence of O_2. 158

Figure 3.7 a) Experimental (solid discs) and simulated (dashed lines) breakthrough curves at different H_2S concentrations for AC_850°C_3h, AC_850°C_3h_KOH 10 and AC_850°C_3h_KOH 10 under the presence of O_2. b) H_2S equilibrium adsorption isotherms at 25 °C from experimental breakthrough curves: discs correspond to experimental data and dashed lines correspond to Langmuir fits. (Gas composition: 60% N_2, balanced with CO_2, and 1.1% O_2 when present). 161

Figure 3.8 Breakthrough curves and H_2S concentration profiles from simulations at H_2S concentrations of: a) 400 ppm, and b) 4000 ppm. 163

Chapter 4

Figure 4.1 a) Bulk density, source, modification and shape of Bordet and commercial Acs for biogas desulfurization. B) Experimental test bench for dynamic H_2S adsorption. C) Synthesis of lab-made densified-impregnated activated carbon. 174

Figure 4.2 Characterization of molasses: a) TGA curve, b) Ash content and c) XRD. 177

Figure 4.3 Bulk density (a) and pore volume variation by binder type and content for mesoporosity (b), microporosity (c) and ultra-microporosity (d) on densified ACs. 179

Figure 4.4 Breakthrough curve of densified activated carbons by binder type for H_2S (400 ppm) separation: a) Cane 1 and beet molasses, b) Cane molasses 2 and c) Polyphenol – Separation capacities at BTP per mass unit e) and per volume unit f). 181

Figure 4.5 Breakthrough curves for the separation of H_2S (4000 ppm), in the presence of O2, of densified ACs with (a) non-carbonized polyphenol binder and (b) cane molasses 2 binder,

all prepared by Method 2. Corresponding separation capacities: (c) per unit mass, and (d) per unit volume. NI means non-impregnated, still densified. 184

Figure 4.6 Breakthrough curves for the separation of H_2S (4000 ppm), without O2, of densified ACs with binders: (a) non-carbonized polyphenols, (b) carbonized polyphenols, and (c) cane molasses 2, prepared by Method 1 (full symbols) or Method 2 (empty symbols). Corresponding separation capacities: (d) per unit mass, and (e) per unit volume. 186

Figure 4.7 Breakthrough curves for the separation of H_2S (4000 ppm), in the presence of O2, of densified ACs impregnated with KOH at 10 wt.% (full symbols) and 15 wt.% (empty symbols), synthetized by (a) Method 1 and (b) Method 2. Corresponding separation capacities normalized by (c) unit mass and (d) unit volume of adsorbent. 187

Figure 4.8 (a) Bulk density of Pol_15%_20µm_KOH 10% and CACs for biogas desulfurization investigated here. (b) Pore volume vs BET area of Pol_15%_20µm (circles) and CACs (crosses). (c) H_2S breakthrough curves and separation capacities of CACs and Pol_15%_20µm_KOH 10% per (d) unit mass and (e) unit volume of sorbent. 190

Figure 4.9 (a) Experimental (dots) and simulated (dashed lines) breakthrough curves at different H_2S concentrations. (b) H_2S equilibrium adsorption isotherms at 25 °C based on experimental breakthrough curves (circles), along with Langmuir fit (dashed lines). (c) Breakthrough curves and H_2S concentration profiles from simulations. 192

Chapter 5

Figure 5.1 Nitrogen adsorption (solid symbols)-desorption (empty symbols) isotherms of a) AC_900°C_2h reference and activated charcoal 2 at different activation conditions, and d) commercial ACs for VOC removal (CAC_VOC), and their corresponding pore size distributions (b and e) and cumulative pore volumes (c and f). 200

Figure 5.2 Activated carbon impregnation procedure for pilot experiments. 203

Figure 5.3 H_2S removal from landfill gas. a) Biogas connection line and b) pilot adsorption column. 203

Figure 5.4 VOCs removal from landfill gas. a) Biogas connection line and b) xylene measurement using Dräger tubes calibrated to 400 ppm of xylene. 205

Figure 5.5 (a) Breakthrough curves of sample Pol_15%_ KOH 10 before (fresh) and after regeneration by Soxhlet washing or thermal regeneration with either air (150 °C) and or N_2 (300 °C). Breakthrough curves of sample (b) Pol_15%_ KOH 10 and (c) Can_50%_KOH 10 after thermal regeneration with N_2 at 500 °C and thermal regeneration with impregnation with KOH 10 wt.%. Separation capacities at BTP C/Co 1% corresponding to the regeneration methods of (d) Figure 5.4b, and (e) Figure 5.4c. 207

Annex 1

Figure A1.1 Control volume for axially dispersed plug flow model in adsorption columns. 219

Annex 2

Figure A2.1 a) Packed bed system for mass balance of dynamic H_2S adsorption. b) Typical breakthrough curve of dynamic H_2S adsorption. c) Modification of the breakthrough curve for integral determination in Eq. (S10). 227

Figure A2.2 Nitrogen adsorption (solid symbols)-desorption (empty symbols) isotherms of a) pristine charcoal and charcoal-derived ACs, and b) and c) commercial ACs (CACs) after extensive washing, and corresponding pore size distributions (d, e and f) and cumulative pore volumes (g, h and i). 228

Figure A2.3 Effect of impregnating agent and impregnation ratio on H_2S (400 ppm) adsorption by a) AC_850°C_2h, b) AC_850°C_3h and c) AC_900°C_3h, and their separation capacities at BTP expressed per d) unit mass and e) unit volume 233

Annex 3

Figure A3.1 Nitrogen adsorption-desorption isotherms for: (a) Cane1-based ACs, (b) Cane2-based ACs and (c) Polyphenol-based ACs. Pore size distribution for (d) Cane1-based ACs, (e) Cane2-based ACs and (f) Polyphenol-based ACs. Cumulative pore volume distribution for (g) Cane1-based ACs, (h) Cane2-based ACs and (i) Polyphenol-based ACs. 238

List of tables

Chapter 1

Table 1.1 Typical biogas composition (%).[5] 16

Table 1.2 Comparative table of gas desulfurization methods. 23

Table 1.3 Comparison of the properties of ACs, carbon molecular sieves, metal organic frameworks and zeolites. AC and CMS images were taken with permission from [55] and [56]. 26

Table 1.4 Main properties of adsorbents for CO_2/CH_4 separation. 28

Table 1.5 Properties of commercial activated carbons for biogas desulfurization. 34

Table 1.6 Activated carbons used for H_2S separation by dynamic adsorption and their H_2S removal properties. 41

Table 1.7 Waste-derived materials used for H_2S separation by dynamic adsorption and their H_2S removal properties. 44

Table 1.8 Zeolites used for H_2S separation by dynamic adsorption and their H_2S removal properties. 48

Table 1.9 Mesoporous silica used for H_2S separation by dynamic adsorption and their H_2S removal properties. 49

Table 1.10 MOFs used for H_2S separation by dynamic adsorption and their H_2S removal properties. 52

Table 1.11 Metal-based adsorbents used for H_2S separation by dynamic adsorption and their H_2S removal properties at room temperature (≈ 25 °C). 53

Table 1.12 Metal-based adsorbents used for H_2S separation by dynamic adsorption and their H_2S removal properties at high temperatures. 53

Chapter 2

Table 2.1 Activated carbons for CO_2/CH_4 separation in pressure swing adsorption (PSA) units evaluated at T ≈ 25°C. 77

Table 2.2 Carbon molecular sieves (CMS), metal organic frameworks (MOFs) and zeolites for CO_2/CH_4 separation in PSA units evaluated at T ≈ 25°C. 80

Table 2.3 Summary of dynamic models for CO_2/CH_4 separation through PSA systems. 84

Table 2.4 Single-bed PSA technologies for CO_2/CH_4 separation. 91

Table 2.5 Multi-bed PSA technologies for CO_2/CH_4 separation - experimental studies. 92

Table 2.6 Multi-bed PSA technologies for CO_2/CH_4 separation - simulation studies. 93

Table 2.7 H_2S/biogas separation studies. 101

Table 2.8 Performance parameters of adsorbents for biogas desulfurization. 111

Table 2.9 Dynamic models for biogas desulfurization through fixed-bed adsorption columns. 112

Table 2.10 Regeneration methods of H_2S-saturated sorbents. 118

Chapter 3

Table 3.1 Commercial activated carbons (CACs) for biogas desulfurization. 143

Table 3.2 Parameters used for simulation of dynamic H_2S adsorption. 148

Table 3.3 Mass transfer coefficients k (s^{-1}) estimated by fitting experimental and simulation data at different H_2S feed concentrations. 162

Chapter 4

Table 4.1 Parameters used for H_2S dynamic adsorption simulation. 191

Table 4.2 Mass transfer coefficients estimate by fitting experimental and simulation data at different H_2S feed concentrations. 193

Chapter 5

Table 5.1 Commercial activated carbons (CACs) for VOCs removal. 200

Table 5.2 Textural parameters of charcoal-derived ACs (as a function of activation time and temperature) and their burn-offs, and commercial ACs for VOC removal. 202

Annex 2

Table A2.1 Textural parameters of charcoal-derived ACs (as a function of activation time and temperature) and CACs and their pH and burn-offs. 229

Table A2.2 H_2S separation capacities of charcoal-derived activated charcoals. 229

Table A2.3 H_2S (400 ppm) separation performance of KOH-impregnated activated carbons at breakthrough point (BTP: C/C_0 = 10%) and at saturation. 230

Table A2.4 Same as Table A1.3, but for KI-impregnated activated carbons. 230

Table A2.5 Same as Table A2.3, but for K_2CO_3-impregnated activated carbons. 231

Table A2.6 H_2S (400 ppm) separated by AC_850°C_3H impregnated with 10 wt.% KOH under different humidification conditions, at breakthrough point (BTP: C/C_0 = 10%) and at saturation. 233

Table A2.7 H_2S (4000 ppm) separation capacities of charcoal and its derived (non-impregnated) activated carbons at BTP (40 ppm), in the presence of O_2. 233

Table A2.8 H_2S (400 ppm concentration) separation capacities of commercial and our best charcoal-derived activated carbons for biogas desulfurization. 233

Table A2.9 Same as Table A1.8, but for an H_2S concentration of 4000 ppm. 234

Table A2.10 H_2S separation capacities at saturation under different H_2S concentrations for isotherm curve determination at 25°C for three different conditions of activated carbon. 234

Table A2.11 Equilibrium constants of the Langmuir isotherm. 234

Annex 3

Table A3.1 Proximate and elemental analysis of molasses and plant-based polyphenol for activated carbon pellet fabrication. 237

Table A3.2 Textural parameters of densified activated carbons as a function of binder type and content (wt.%). 239

Table A3.3 H_2S (400 ppm) separation capacities of densified activated carbons. 240

Table A3.4 Skeletal and grain densities of densified activated carbons for chemical impregnation. 240

Table A3.5 H_2S (4000 ppm) separation capacities of impregnated densified activated carbons. 241

Table A3.6 H_2S (4000 ppm) separation capacities of impregnated (KOH) densified activated carbons. 242

Annex 5. Lists of scientific works derived from this thesis

List of scientific works derived from this thesis study

- **Publications in scientific journals:**

Published:

- Paz, L.; Gentil, S.; Fierro, V.; Celzard, A. Assessing the performance of adsorbents for CO_2/CH_4 separation in pressure swing adsorption units: a review, J. Environ. Chem. Eng. 12 (6) (**2024**) 114870, https://doi.org/10.1016/j.jece.2024.114870
- Paz, L.; Gentil, S.; Fierro, V.; Celzard, A. Activated Carbons Outperform Other Sorbents for Biogas Desulfurization. *Chemical Engineering Journal*, **2025**, *506*, 160304. https://doi.org/10.1016/j.cej.2025.160304
- Paz, L.; Selmi, T.; Fierro, V.; Celzard, A. Optimized wood-based activated charcoal for desulfurization under realistic biogas conditions. *Carbon*, **2026**, *247*, 120963. https://doi.org/10.1016/j.carbon.2025.120963

Submitted:

- Paz, L.; Selmi, T.; Fierro, V.; Celzard, A. Tailoring Wood-Based Activated Carbons and Assessing the Role of Impregnation and O_2 for Efficient H_2S Removal from Biogas. *Journal of Environmental Chemical Engineering*, **2025**.

- **Oral communications:**

- L. Paz, S. Gentil, V. Fierro, A. Celzard, Biogas upgrading by adsorption. 12emes Journées de l'Association Française de l'Adsorption, 26-27 january 2023, Université de Lorraine, Nancy FR.
- L. Paz, S. Gentil, V. Fierro, A. Celzard, Superiority of activated carbons over other adsorbents for biogas desulfurization. The World Conference on Carbon 2025, 29 June - 04 July 2025, Saint Malo FR.

- **Poster Communication**

- L. Paz, V. Fierro, A. Celzard, Wood based activated carbon for biogas desulfurization. Assemblée Générale du département N2EV & Journée doctorants, 5 december 2024, Nancy FR.

Abstract

This thesis evaluates adsorbents for biogas upgrading, with a particular focus on CO_2/CH_4 separation and H_2S removal from biogas with activated carbons (ACs). Through literature review, pressure swing adsorption systems were evaluated with various adsorbents for CO_2/CH_4 separation. Zeolites exhibited superior performance mainly due to their high selectivity. In terms of H_2S removal, ACs, when impregnated demonstrated the highest adsorption efficiencies. The experimental work focused on activation, densification and chemical impregnation of wood-based charcoal for biogas desulfurization. Densification and subsequent impregnation proved most effective when cane molasses or plant-based polyphenol were used in combination with 10 wt.% KOH. Comparative testing against commercial ACs for biogas desulfurization confirmed superior performance in terms of mass-based adsorption capacity and highly competitive volumetric performance. Additionally, a validated one-dimensional dynamic model was developed to simulate breakthrough behavior under realistic biogas conditions, enabling accurate prediction and design optimization.

Résumé

Cette thèse évalue des adsorbants pour l'épuration du biogaz, en mettant particulièrement l'accent sur la séparation du CO_2/CH_4 et l'élimination du H_2S à l'aide de charbons actifs (ACs). À travers une revue de la littérature, les systèmes d'adsorption modulée en pression (PSA) ont été étudiés avec différents adsorbants pour la séparation du CO_2/CH_4. Les zéolithes ont montré des performances supérieures, principalement en raison de leur sélectivité. Concernant l'élimination du H_2S, les ACs imprégnés ont démontré les meilleures efficacités d'adsorption. Le travail expérimental s'est concentré sur l'activation, la densification et l'imprégnation chimique de charbons de bois pour la désulfuration du biogaz. La densification suivie de l'imprégnation s'est révélée particulièrement efficace lorsque de la mélasse de canne ou des polyphénols d'origine végétale ont été utilisés en combinaison avec 10 wt.% KOH. Des tests comparatifs avec des ACs commerciaux pour la désulfuration du biogaz ont confirmé des performances supérieures en termes de capacité d'adsorption massique et des performances volumiques très compétitives. De plus, un modèle dynamique unidimensionnel validé a été développé pour simuler le comportement de percée dans des conditions réalistes de biogaz, permettant une prédiction précise et une optimisation de la conception.